# FINAL REPORT

**WY-2307F**

# IMPROVING DESIGN AND CONSTRUCTION OF TRANSPORTATION INFRASTRUCTURE THROUGH BEDROCK CHARACTERIZATION


Prepared by:

Kam Ng, Ph.D., P.E., Professor

Lokendra Khatri, Master's Graduate

Esraa Alomari, Ph.D. Student

Department of Civil & Architectural Engineering and Construction Management

Department of Mathematics & Statistics

University of Wyoming

1000 E. University Avenue

Laramie, Wyoming 82071



September 2023

# DISCLAIMER

## Notice

This document is disseminated under the sponsorship of the Wyoming Department of Transportation (WYDOT) in the interest of information exchange. WYDOT assumes no liability for the use of the information contained in this document. WYDOT does not endorse products or manufacturers. Trademarks or manufacturers' names appear in this report only because they are considered essential to the objective of the document.

## Quality Assurance Statement

WYDOT provides high-quality information to serve government, industry, and the public in a manner that promotes public understanding. Standards and policies are used to ensure and maximize the quality, objectivity, utility, and integrity of its information. WYDOT periodically reviews quality issues and adjusts its programs and processes to ensure continuous quality improvement.

## Copyright

No copyrighted material, except that which falls under the "fair use" clause, may be incorporated into a report without permission from the copyright owner, if the copyright owner requires such. Prior use of the material in a WYDOT or governmental publication does not necessarily constitute permission to use it in a later publication.

- Courtesy – Acknowledgment or credit will be given by footnote, bibliographic reference, or a statement in the text for use of material contributed or assistance provided, even when a copyright notice is not applicable.
- Caveat for Unpublished Work – Some material may be protected under common law or equity even though no copyright notice is displayed on the material. Credit will be given and permission will be obtained as appropriate.
- Proprietary Information – To avoid restrictions on the availability of reports, proprietary information will not be included in reports, unless it is critical to the understanding of a report and prior approval is received from WYDOT. Reports containing such proprietary information will contain a statement on the Technical Report Documentation Page restricting availability of the report.

## Creative Commons

The report is covered under a Creative Commons, CC-BY-SA license. When drafting an adaptive report or when using information from this report, ensure you adhere to the following:

- Attribution – You must give appropriate credit, provide a link to the license, and indicate if changes were made. You may do so in any reasonable manner, but not in any way that suggests the licensor endorses you or your use.
- ShareAlike – If you remix, transform, or build upon the material, you must distribute your contributions under the same license as the original.
- No additional restrictions – You may not apply legal terms or technological measures that legally restrict others from doing anything the license permits.

You do not have to comply with the license for elements of the material in the public domain or where your use is permitted by an applicable exception or limitation. No warranties are given. The license may not give you all of the permissions necessary for your intended use. For example, other rights such as publicity, privacy, or moral rights may limit how you use the material.

TECHNICAL REPORT DOCUMENTATION PAGE

<table>
<tr><td colspan="2">1. Report No. WY-2307F</td><td>2. Government Accession No.</td><td colspan="2">3. Recipient’s Catalog No.</td></tr>
<tr><td colspan="3" rowspan="2">4. Title and Subtitle<br><br>Improving Design and Construction of Transportation Infrastructure through Bedrock Characterization</td><td colspan="2">5. Report Date<br>September 2023</td></tr>
<tr><td colspan="2">6. Performing Organization Code:</td></tr>
<tr><td colspan="3">7. Author(s)<br><br>Kam W. Ng (0000-0001-5099-5454), Lokendra Khatri (0000-0002-5951-3252), Esraa Alomari (0000-0001-5117-886X)</td><td colspan="2">8. Performing Organization Report No.</td></tr>
<tr><td colspan="3" rowspan="2">9. Performing Organization Name and Address<br>Department of Civil and Architectural Engineering and Construction Management<br>University of Wyoming<br>1000 E. University Avenue, Dept. 3295<br>Laramie, WY 82071-2000</td><td colspan="2">10. Work Unit No.</td></tr>
<tr><td colspan="2">11. Contract or Grant No. RS09220</td></tr>
<tr><td colspan="3" rowspan="2">12. Sponsoring Agency Name and Address<br>Wyoming Department of Transportation<br>5300 Bishop Blvd.<br>Cheyenne, WY 82009-3340<br>WYDOT Research Center (307) 777-4182</td><td colspan="2">13. Type of Report and Period<br>Final Report</td></tr>
<tr><td colspan="2">14. Sponsoring Agency Code<br><br>WYDOT</td></tr>
<tr><td colspan="5">15. Supplementary Notes<br>WYDOT Project Champion: David Vanderveen</td></tr>
<tr><td colspan="5">16. Abstract<br>Tertiary bedrock formations are commonly encountered during the design and construction of transportation infrastructure in Wyoming. The engineering properties of these bedrocks are highly variable due to the geological processes to which they have been subjected including deposition, cementation, weathering and erosion. Furthermore, comprehensive experimental investigations on these bedrocks are rarely performed in the past due to the absence of advanced rock testing equipment, and hence their strength and deformation behaviors are not well understood. However, our transportation infrastructure, such as bridges, slopes, and roadways, is either constructed on or associated with these bedrock formations in Wyoming. The overall objective of the proposed research is to understand the strength and deformation behaviors of Wyoming bedrocks to improve the resilience of our transportation infrastructure to disaster. The research objectives are achieved by completing six major tasks: literature review, assessment of WYDOT electronic database and rock inventory, geotechnical investigation and rock sampling, laboratory rock testing, data analysis and correlation development, and outcomes recommendations and reporting. The research results will yield many beneficial outcomes pertinent to design and construction of transportation infrastructure.</td></tr>
<tr><td colspan="2">17. Key Words<br>Bedrock, unconfined compressive strength, modulus, shear strength, porosity, density, water content, triaxial, uniaxial</td><td colspan="3">18. Distribution Statement<br><br>No restrictions. This document is available through the National Transportation Library and the Wyoming State Library. </td></tr>
<tr><td>19. Security Classif. (of this report)<br>Unclassified</td><td colspan="2">20. Security Classif. (of this page)<br>Unclassified</td><td>21. No. of Pages:<br>215</td><td>22. Price</td></tr>
</table>

Form DOT F 1700.7 (8-72) Reproduction of completed page authorized.

# SI* (MODERN METRIC) CONVERSION FACTORS

## APPROXIMATE CONVERSIONS TO SI UNITS

| Symbol | When You Know | Multiply By | To Find | Symbol |
|---|---|---|---|---|
| | | **LENGTH** | | |
| in | inches | 25.4 | millimeters | mm |
| ft | feet | 0.305 | meters | m |
| yd | yards | 0.914 | meters | m |
| mi | miles | 1.61 | kilometers | km |
| | | **AREA** | | |
| $in^2$ | square inches | 645.2 | square millimeters | $mm^2$ |
| $ft^2$ | square feet | 0.093 | square meters | $m^2$ |
| $yd^2$ | square yard | 0.836 | square meters | $m^2$ |
| ac | acres | 0.405 | hectares | ha |
| $mi^2$ | square miles | 2.59 | square kilometers | $km^2$ |
| | | **VOLUME** | | |
| fl oz | fluid ounces | 29.57 | milliliters | mL |
| gal | gallons | 3.785 | liters | L |
| $ft^3$ | cubic feet | 0.028 | cubic meters | $m^3$ |
| $yd^3$ | cubic yards | 0.765 | cubic meters | $m^3$ |
| | NOTE: volumes greater than 1000 L shall be shown in $m^3$ | | | |
| | | **MASS** | | |
| oz | ounces | 28.35 | grams | g |
| lb | pounds | 0.454 | kilograms | kg |
| T | short tons (2000 lb) | 0.907 | megagrams (or "metric ton") | Mg (or "t") |
| | | **TEMPERATURE (exact degrees)** | | |
| $^oF$ | Fahrenheit | 5 (F-32)/9<br>or (F-32)/1.8 | Celsius | $^oC$ |
| | | **ILLUMINATION** | | |
| fc | foot-candles | 10.76 | lux | lx |
| fl | foot-Lamberts | 3.426 | $candela/m^2$ | $cd/m^2$ |
| | | **FORCE and PRESSURE or STRESS** | | |
| lbf | poundforce | 4.45 | newtons | N |
| $lbf/in^2$ | poundforce per square inch | 6.89 | kilopascals | kPa |

## APPROXIMATE CONVERSIONS FROM SI UNITS

| Symbol | When You Know | Multiply By | To Find | Symbol |
|---|---|---|---|---|
| | | **LENGTH** | | |
| mm | millimeters | 0.039 | inches | in |
| m | meters | 3.28 | feet | ft |
| m | meters | 1.09 | yards | yd |
| km | kilometers | 0.621 | miles | mi |
| | | **AREA** | | |
| $mm^2$ | square millimeters | 0.0016 | square inches | $in^2$ |
| $m^2$ | square meters | 10.764 | square feet | $ft^2$ |
| $m^2$ | square meters | 1.195 | square yards | $yd^2$ |
| ha | hectares | 2.47 | acres | ac |
| $km^2$ | square kilometers | 0.386 | square miles | $mi^2$ |
| | | **VOLUME** | | |
| mL | milliliters | 0.034 | fluid ounces | fl oz |
| L | liters | 0.264 | gallons | gal |
| $m^3$ | cubic meters | 35.314 | cubic feet | $ft^3$ |
| $m^3$ | cubic meters | 1.307 | cubic yards | $yd^3$ |
| | | **MASS** | | |
| g | grams | 0.035 | ounces | oz |
| kg | kilograms | 2.202 | pounds | lb |
| Mg (or "t") | megagrams (or "metric ton") | 1.103 | short tons (2000 lb) | T |
| | | **TEMPERATURE (exact degrees)** | | |
| $^oC$ | Celsius | 1.8C+32 | Fahrenheit | $^oF$ |
| | | **ILLUMINATION** | | |
| lx | lux | 0.0929 | foot-candles | fc |
| $cd/m^2$ | $candela/m^2$ | 0.2919 | foot-Lamberts | fl |
| | | **FORCE and PRESSURE or STRESS** | | |
| N | newtons | 0.225 | poundforce | lbf |
| kPa | kilopascals | 0.145 | poundforce per square inch | $lbf/in^2$ |

## TABLE OF CONTENT

## LIST OF FIGURES

## LIST OF TABLES

## LIST OF ABBREVIATIONS

| | |
|---|---|
| LRFD | Load and Resistance Factor Design |
| GSI | Geological Strength Index |
| WYDOT | Wyoming Department of Transportation |
| RQD | Rock Quality Designation |
| ISRM | International Society of Rock Mechanics |
| UCS | Unconfined Compressive Strength |
| UC | Unconfined Compression |
| MC | Mohr-Coulomb |
| HB | Hoek-Brown |
| CT | Computed Tomography |
| RMR | Rock Mass Rating |
| LVDT | Linear Variable Differential Transformers |
| TS | Tensile Splitting |
| MTS | Multiple Tensile Splitting |
| NA | Not Available |
| COV | Coefficient of Variation |
| RMSE | Root Mean Square Error |
| MAD | Mean Absolute Deviation |
| RSE | Residual Standard Error |
| AIC | Akaike Information Criterion |
| BIC | Bayesian Information Criterion |

# CHAPTER 1: INTRODUCTION

## 1.1 Background

Bedrock is the underlying relatively hard and solid rock beneath the soil, gravel, and other unconsolidated material. The bedrocks are either igneous, metamorphic, or sedimentary, depending on the formation process they undergo. The rock can be formed by the lithification of loose sediments over time, cooling and hardening of magma, or changing form. Thus, these underlying bedrocks have different strengths based on their formation, age, type, and depth. The age of the bedrock ranging from Precambrian to Cenozoic differs in strength and deformation properties. These bedrocks are the parent material for soil materials and take up the loads from the civil infrastructure during the design and construction. It is, therefore, essential to perform comprehensive experimental investigations on these bedrocks to understand their strength and deformation properties.

In the case of transportation infrastructure in Wyoming, especially bridges, slopes, and roadways, different bedrock formations, such as White River, Wasatch, Fort Union, Green River, and Arikaree are often encountered. The engineering properties such as shear strength, elastic properties, failure parameters, stiffness, and bedrock quality of these bedrock formations are lacking due to the absence of advanced rock testing equipment. The lack of understanding rock behaviors and measured engineering parameters has created challenges in the design and construction of the transportation infrastructures in Wyoming. Although the correlations developed and published by researchers have been used to estimate some of these engineering properties, in the absence of measured properties of Wyoming bedrock, the applicability of these correlations has yet to be verified.

A site investigation is performed by The Wyoming Department of Transportation (WYDOT) to determine the subsurface profile and geomaterial properties. The lithology of the Wyoming bedrock formations consists predominantly of shale, sandstone, siltstone, claystone, mudstone, and conglomerate. A standard penetration test, rock quality designation, geological strength index, and unconfined compressive strength (UCS) are measured and logged in the bedrock properties database. However, the shear strength properties of these bedrocks (internal friction angle and cohesion) and elastic properties (Young's modulus and Poisson's ratio) are usually estimated but not measured. Understanding and characterizing these properties of Wyoming bedrocks will yield prediction equations that are more representative of local bedrocks,

contribute a more significant economic benefit in the design and construction of transportation infrastructure, and increase the reliability of these infrastructures.

## 1.2 Problem Statement

The underlying bedrocks have natural variability depending upon the formation process they undergo. This creates increased uncertainty in the subsurface condition for the design and construction of the transportation infrastructures. The limited understanding of the bedrock behaviors and absence of strength and elastic properties leads to unforeseen construction challenges, especially in the case of deep foundation design in soft rocks (Mokwa and Brooks 2008). This research includes measuring the rock properties of different lithology and locations within the state of Wyoming to advance the development of a geomaterial classification system (Adhikari et al. 2019). A comprehensive test data of the bedrock will reduce the uncertainties and discrepancy between design outcomes and construction performance by improving the engineering design efficiency.

- During the construction of driven piles, especially in soft rocks, AASHTO (2020) recommends that the pile be driven in the same manner as soil. The static analysis method for soft rocks is not readily available for pile resistance estimation; hence, pile resistances are usually under-predicted (Ng and Sullivan 2017). The piles don't satisfy the Load and Resistance Factor Design (LRFD) strength limit at the end of driving and occasionally at the beginning of the last strike. Significant discrepancies between estimated and measured pile resistances were reported (Ng et al., 2015). This high uncertainty in pile performance could lead to construction challenges, especially in the case of a bridge project where foundation construction is critical. This research, therefore, can provide a database of bedrock properties that can be utilized to calibrate the static analysis method to improve the pile resistance estimation and decrease the discrepancy between the estimated and measured pile resistance in soft rocks. This will reduce the design and construction costs.
- The empirical correlations for the Hoek-Brown (HB) parameters are developed based on general bedrocks that might not represent the Wyoming bedrocks. The measured properties of intact rock samples along with the UCS and geological strength index (GSI) records in the WYDOT Bedrock Properties Database can be used to calibrate the HB parameters, improve the unit end bearing ($q_p$) estimation, and increase the reliability of drilled shaft design and construction in Wyoming. This improvement can reduce the depth of the bedrock socket, and eventually the overall construction cost.

- Landslides and rock falls are common occurrences in Wyoming. This research will generate measured shear strength properties (internal friction angle and cohesion) and elastic properties (Young's modulus and Poisson's ratio) of Wyoming bedrocks used in rock stability evaluation and mitigation strategies for rock slope stabilization. This will increase the stability and reduce the cost of rock slope stabilization.
- The design of spread footing on shallow bedrock requires the determination of HB parameters (Carter and Kulhawy 1988) or shear strength properties (Goodman 1989). Due to the challenges with determining the nominal bearing resistance on rocks, a shallow footing may be over-designed or under-designed leading to unforeseen changes in cost and design. This research will provide the necessary parameters to reduce the need for an expensive plate load test to determine the nominal bearing resistance.
- Rock rippability or the ease of mechanical evacuation of rock is commonly encountered during road construction. The rock rippability depends on the geology and engineering properties of the bedrock. Seismic lines are run at sites to correlate drilling characteristics and seismic velocities to the rippability of the rock. Still, high torque and horsepower drills have made the comparison more difficult. The measured bedrock properties from this research will provide the technical background to improve rock rippability evaluation and excavation effort prediction, enhancing the preparation of the construction schedule and cost estimation.
- Bedrock is a parent material of base aggregates used in flexible and rigid pavements. Although the laboratory-measured properties and resilient modulus of the local base materials in Wyoming have been recently quantified (Ng et al. 2019), little is known about the Wyoming bedrock as the parent material. A study by the Virginia Department of Transportation (DOT) concluded that limestone aggregates have a higher resilient modulus than granite aggregates (Hossain and Lane 2015). Hence, this research will provide the basis for future assessment of suitable bedrock sources for base aggregates in terms of degradation behavior, particle breakage, and mechanical properties.

## 1.3 Research Objectives

The main objective of this research was to understand the strength and deformation behaviors of Wyoming bedrock to improve the design and construction of transportation infrastructure. The research outcomes also look to address the strategic goals of WYDOT: acquiring and responsibly managing resources, providing a safe, reliable, and effective transportation system, and encouraging and supporting innovation to increase the efficiency in the design and

construction of the transportation infrastructures. This research also aimed at reducing the design and construction challenges due to the lack of measured engineering properties of bedrock representing Wyoming formations. The objectives of the research were as follows:

- To determine the strength and deformation properties of the bedrock. This includes the shear strength properties (internal friction angle and cohesion) and elastic properties (Young's modulus and Poisson's ratio).
- To develop locally calibrated relationships for bedrock properties in terms of index parameters, rock quality, and UCS. These parameters will be used to better define the HB criterion to achieve a more cost-effective design of drilled shafts and driven piles.
- To expand WYDOT database of rock properties. This database currently has 2,100 project and rock test records, and 523 were identified as tertiary formations. The database has measured bedrock density, percentage recovery, Rock Quality Designation (RQD), and Geological Strength Index (GSI) but lacks shear strength and elastic properties.
- To improve the understanding between Wyoming geology and bedrock behaviors.

## 1.4 Research Plan

The research objectives were accomplished by completing five research tasks. The first research task was to conduct a literature review pertinent to rock mechanics and bedrock properties. This task included a review of documents, books, papers, reports, catalogs, manuals, notes, and presentation slides about bedrock quality and properties relevant to civil engineering applications. This task also included documentation and reviewing the current knowledge and practice related to bedrock classification, description, testing, and properties. This research task also identified gaps in the knowledge and review of current specifications and guidelines by DOTs, AASHTO, and other agencies.
The second research task included assessing the WYDOT electronic database and rock inventory data. In this task, a review and analysis of usable records like rock quality description, $q_u$ value, and geology description from the WYDOT database was conducted for subsequent studies. This task helped identify relevant cores and usable rock samples from the WYDOT geology storage for laboratory testing.

The third task included obtaining new rock samples from the geotechnical investigation of highway projects. The geology program performed a geotechnical investigation to obtain standard rock cores of diameters of about 1.91 inches. The geotechnical reports and subsurface

profiles of the projects were assessed to determine the underlying bedrock characteristics, stratigraphy, geological formation, and discontinuity. A minimum of three rock samples with a diameter-to- height ratio of 1:2 was obtained for laboratory testing.

The fourth task was to conduct laboratory testing of the collected rock samples from Task 3. The laboratory testing included uniaxial and triaxial compressive tests following the ASTM D7012 (2014) using the servo-controlled testing system (GCTS RTR-1500). This task included testing 50 rock samples, i.e., at least 150 specimens, collected from all around Wyoming. These 50 rock samples consisted of the typical lithology of Wyoming bedrock formations, predominantly shale, sandstone, siltstone, claystone, mudstone, and conglomerate.

The fifth task included data analysis and prediction equation development using the data collected from the literature review in Task 1, collected data from the database in Task 2, and the laboratory-measured data from Task 4. This task focused on understanding bedrock failure and deformation behaviors. Combining uniaxial and triaxial test results, HB parameters and Mohr-Coulomb shear strength parameters were determined. The measured rock properties and the rock quality description were compiled for each Wyoming bedrock formation and lithology. The properties were presented with model comparison criteria.

## 1.5 Report Focus and Organization

This report aims to better understand the mechanical and deformation behavior of Wyoming bedrock to improve the design of WYDOT transportation infrastructures. Chapter 1 presents the background, objectives, and tasks of this research. A literature review follows in Chapter 2. Chapter 3 focuses on laboratory rock testing and sample preparation. Chapter 4 describes the summary of experimental testing of different rock types. Chapters 5, 6, 7, 8, and 9 present the analysis results in predicting the mechanical properties under uniaxial and triaxial conditions for sandstone, siltstone, shale, claystone, and carbonate rocks, respectively. Finally, summary and conclusions are given in Chapter 10, which is followed by the references.

# CHAPTER 2: LITERATURE REVIEW

## 2.1 Mechanical Properties of Rocks

Based on the process of formation, rocks are of three types: igneous, sedimentary, or metamorphic. The mechanical properties of these rocks, like the stress and strain, the compressive strength, and elastic constants (Young's modulus, shear modulus, bulk modulus, and Poisson's ratio), are affected by numerous factors. The compressive strength and Young's modulus are affected by the constitutive properties of the rock and test conditions. The constitutive properties include porosity, mineralogy, anisotropy, geological age, and density, whereas the test conditions are the confinement, strain rate, temperature, and sample condition.

### *2.1.1 Mechanical Anisotropy*

Rock masses are complex materials that consist of intact rock pieces, fractures, and bedding planes at different orientations. These characteristics of rock masses affect their mechanical behaviors and cause anisotropy. Anisotropy is the variations of properties concerning the directions in analyzing the rock structure. The anisotropic nature of rocks creates variation in strength and deformation behaviors in different directions. The strength envelopes of these rocks vary significantly with axial and confining pressures. Anisotropy is generally observed in sedimentary rocks because of the orientation of clay, aligned fractures, cracks and pores, and fine layering (Nasseri et al. 2003). Rock anisotropy can be described as intrinsic and induced. The intrinsic anisotropy is caused by bedding planes, discontinuities, and constituting minerals whereas the induced anisotropy is caused by overburden pressure and sediment changes.

Anisotropy plays an important role when microstructural observations are made of argillaceous rocks like shale and claystone. These rocks consist of porous fine-grained clay with embedded silt/sand grains. Therefore, the mechanical properties are altered by the ratio of these contents. The anisotropic properties of these rocks are rarely available or measured from small rock samples as they don't contain fractures with varying sizes, orientations, and bedding at large scales. Therefore, evaluating the anisotropic nature of the rocks is still a challenge in rock mechanics. Mechanical properties like Young's modulus and Poisson's ratio often describe the rocks' anisotropic behaviors.

### *2.1.2 Young's Modulus*

Young's modulus is defined as the measure of rock's stiffness or resistance to elastic deformation under the applied load. The lower the Young's modulus, the more ductile the rock, and the higher the Young's modulus, the more brittle the rock. Young's modulus is a critical parameter in describing the rock behavior under loading due to the quasi-brittle nature of rocks (Bieniawski 1989, Hoek & Brown 1980). The International Society of Rock Mechanics (ISRM) has described three methods for determining Young's modulus: the tangent, secant, and average methods. Young's modulus determined in this research is calculated by plotting the axial stress in the y-axis and the axial strain as a percentage in the x-axis as shown in Figure 2.2 as an example. The linear portion of the curve given as a straight line is identified, and the gradient of this line is calculated. To express Young's modulus in the same unit as the stress, the gradient is then multiplied by 100 so that the strain is in dimensionless decimal instead of percentage. Figure 2.1 represents the equation for the calculation of Young's modulus.

$$\varepsilon = \frac{Axial\ Stress}{Axial\ Strain\ (\%)} \times 100$$

**Figure 2.1: Equation. Young's modulus calculation**

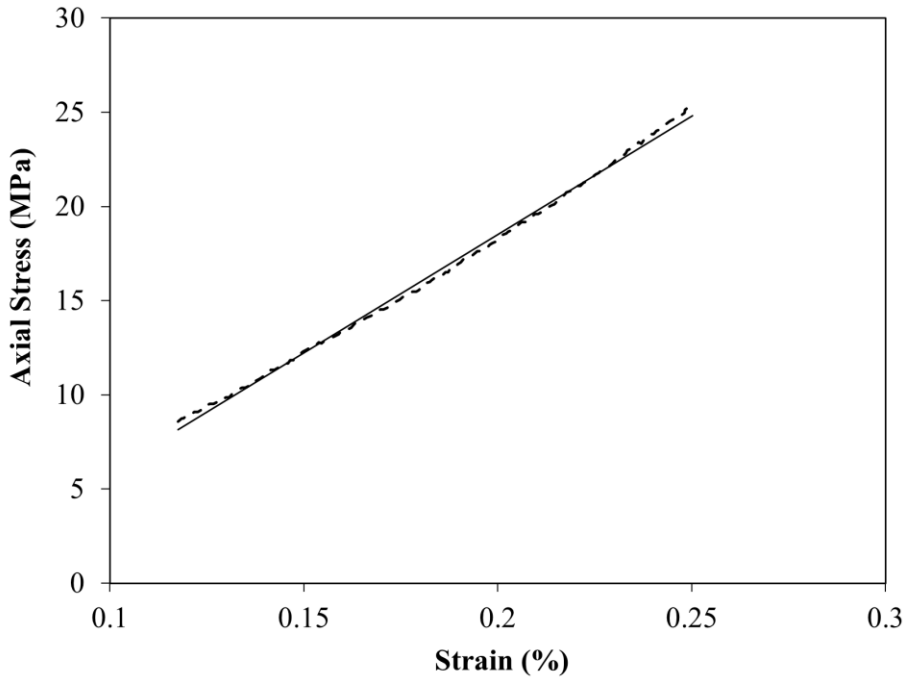


**Figure 2.2: Stress-strain curve to determine Young's modulus.**

### *2.1.3 Poisson's Ratio*

Poisson's ratio is a ratio of change in width (radial deformation) to the change in length (axial deformation) of the rock under loading. Poisson's ratio measures the compressibility of rocks and provides a valuable measure of how much a material deforms under stress. The maximum value of Poisson's ratio for rocks is considered 0.5. Rock will have a Poisson's ratio of 0.5 if it deforms elastically at a low strain rate. Poisson's ratio of a rock core subjected to axial load is expressed in a dimensionless ratio of lateral strain to axial strain shown in Figure 2.4 (a) and the method of calculation from the unconfined compression test is shown in Figure 2.4 (b).
Poisson's ratio ($\nu$) calculated according to the equation shown in Figure 2.3 has a negative sign because the material will contract in the transverse direction when compressed or expand when stretched.

$$\nu = -\frac{\Delta R/R}{\Delta L/L} = -\frac{\varepsilon_l}{\varepsilon_a}$$

**Figure 2.3: Equation. Poisson's ratio formula.**

Where, $\varepsilon_l$ is the lateral strain, and $\varepsilon_a$ is the axial strain.

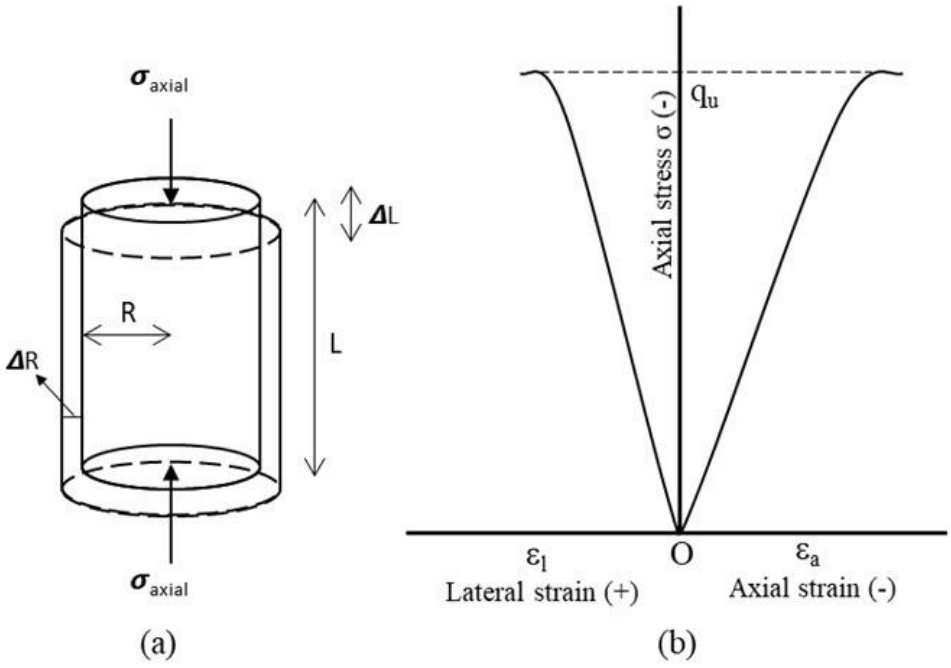


**Figure 2.4: (a) Deformation of cylindrical specimen under uniaxial stress; (b) Unconfined compression test results to illustrate calculation method of Poisson's ratio (ASTM D7012, 2014).**

## 2.2 Shear Strength

The shear strength of intact rock developed along a potential rupture surface is described by two parameters: internal friction angle ($\varphi$) and cohesion ($c$). When the cohesion becomes zero, i.e., when a planar, clean fracture occurs in rocks with no infilling material, the shear strength of the rock is a function of internal friction angle. The cohesion and internal friction angle are determined from a Mohr-Coulomb envelope given by the equation shown in Figure 2.5 plotted against a series of Mohr's circles as shown in Figure 2.6. Mohr's circle is defined as the locus of points that represent the state of stress on individual planes at all their orientations.

$$\tau = c + \sigma \tan \varphi$$

**Figure 2.5: Equation. Mohr- Coulomb envelope.**

Where $\tau$ is the shear stress, $c$ is the y-intercept, $\sigma$ is the normal stress, and $\varphi$ is the internal friction angle.

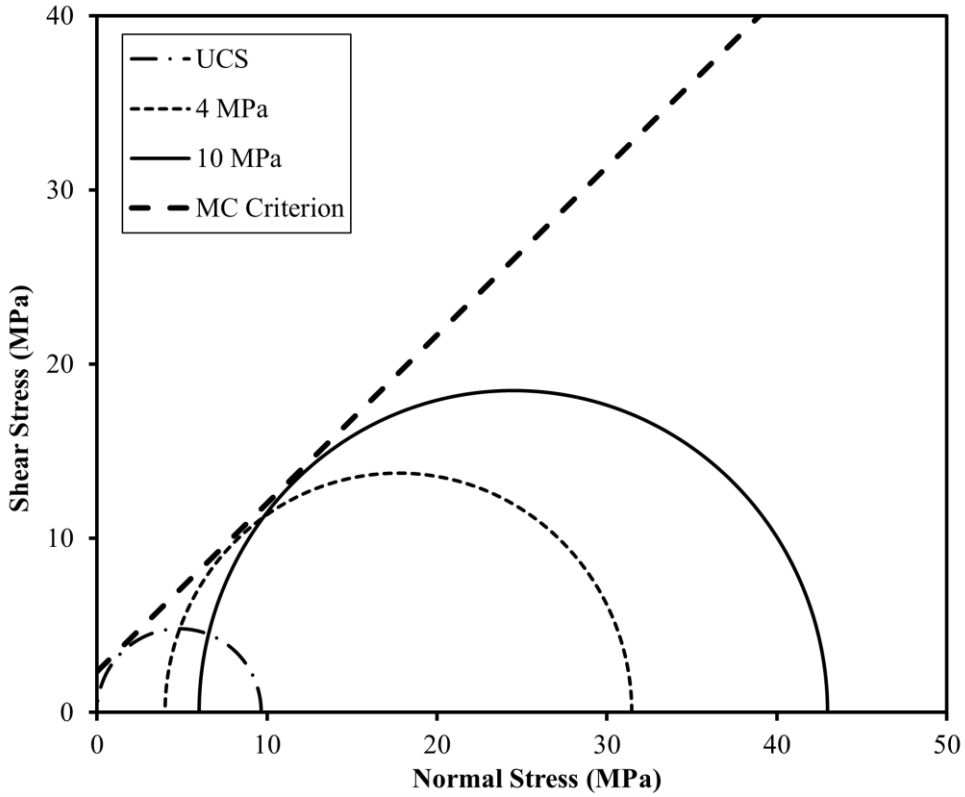


**Figure 2.6: Plot of series of Mohr circle for the determination of cohesion and internal friction angle.**

The strength and stiffness of intact rocks depend on factors like the rock type, degree of weathering, and mineralogy. Therefore, the strength of intact rock can vary across different rocks, and sometimes within the same rock type if the rock is anisotropic.

### *2.2.1 Cohesion (c)*

Cohesion is an integral part of shear strength independent of inter-particle friction. The cohesion of rock is also known as inherent strength and is represented by the y-intercept of the Mohr-Coulomb (MC) criterion (Figure 2.5). Table 2.1 shows the cohesion of some typical rock types reported in the literature (Goodman 1980). These cohesion values can only be used as a reference while laboratory testing of individual rock types is recommended.

**Table 2.1: Typical range of internal friction angle for a variety of rock types (Goodman, 1980).**

| Rock Type | Cohesion (MPa) |
|---|---|
| Berea Sandstone | 27.2 |
| Muddy Shale | 38.4 |
| Stone Mt. Granite | 21.2 |
| Georgia Marble | 21.2 |
| Sioux Quartzite | 70.6 |
| Indiana Limestone | 6.7 |

### *2.2.2 Internal Friction Angle ($\varphi$)*

The size and shape of particle grains exposed on a fracture surface during failure determine the internal friction angle of the rock. Granular rocks like sandstone and siltstone have different friction angles depending on their grain size. Rocks can be categorized into three groups based on their grain sizes (fine, medium, and coarse). Fine-grained rocks like schists and shales generally have low internal friction angles. Medium-grained rocks like sandstones, siltstones, and gneiss have medium internal friction angles, and coarse-grained rocks like basalt, granite, limestone, and conglomerate have high internal friction angles. Table 2.2 shows a typical range of internal friction angles for various rock types (Barton 1973, and Jaeger and Cook 1976). Besides grain size, asperity, surface roughness, and shape of grains can also affect the internal friction angle. Hence, laboratory testing of rocks should be conducted to determine the internal friction angle precisely.

**Table 2.2: Typical range of internal friction angles for various rock types (Wyllie et al., 1996).**

| Rock Class | φ Range (Degree) | Typical Rock Type |
|---|---|---|
| Low Friction | 20 to 27 | Schists, Shale, Marl |
| Medium Friction | 27 to 34 | Sandstones, Siltstones, Gneiss, Chalk, Slate |
| High Friction | 34 to 40 | Basalt, Granite, Limestone, Conglomerate |

## 2.3 Failure Criteria Overview

The rock failure criterion describes the shear strength of rock under different normal stresses. A failure criterion, either linear or nonlinear, describes the maximum shear stress at maximum normal stress $\sigma_n$ at which the rock will fail. The failure behavior depends upon the rock type, applied confinement, and rock mass discontinuities. Some other principal factors are mineral composition, bedding, water content, and state of stress in the rock mass. Rock failure criteria can be classified as isotropic or anisotropic depending on their application on rocks that exhibit anisotropic behavior or not. In the case of anisotropic rocks like shale, Ambrose et al. (2014) from the computed tomography (CT) scans reported that shales at bedding angles ($\beta$) of 0 degree to 10 degrees and at 90 degrees show tensile failure, shales at 45 degrees to 75 degrees show shear failure along the plane of weakness, and shales between 15 degrees to 30 degrees show transitional failure i.e., mixed failure mode of tensile and shear. Similar findings were reported by Tien et al. (2006) for reconstituted argillaceous rocks under unconfined conditions. The failure mode is also found to be dependent on confining pressure as most unconfined compression tests showed brittle failure and as the confinement is increased, the failure mode gradually changed to ductile failure.

Many failure criteria have been proposed by researchers over the decades. The failure criteria discussed in this research are the Mohr-Coulomb (MC) failure criterion and the HB failure criterion because of their wide acceptance in engineering practice, mainly due to their simplicity and the sheer volume of experimental data available. The MC and HB are linear and nonlinear failure criteria, respectively.

### *2.3.1 Mohr-Coulomb (MC) Failure Criterion*

The MC criterion is a linear failure criterion most widely used for quasi-brittle material like rocks. This criterion is commonly used in engineering practice because its material parameters have a clear physical meaning in terms of cohesion and internal friction angle. This criterion assumes that failure is controlled by maximum shear stress and the shear stress at failure depends on

the normal stress. It also assumes that the intermediate principal stress ($\sigma_2$) doesn't affect the failure. The MC failure line is a straight line that best touches the Mohr circles as shown in Figure 2.7 and given by the equation in Figure 2.10. The MC failure criterion can be written as a function of major and minor principal stresses or normal and shear stresses. MC can be plotted in the major and minor principal stress plane or a normal and shear stress plane (Jaeger and Cook 1979). The derivation of the Mohr-Coulomb failure criterion in the normal stress ($\sigma$) vs shear stress ($\tau$) 2D plane is described by the equations presented in Figures 2.8, 2.9, and 2.10.

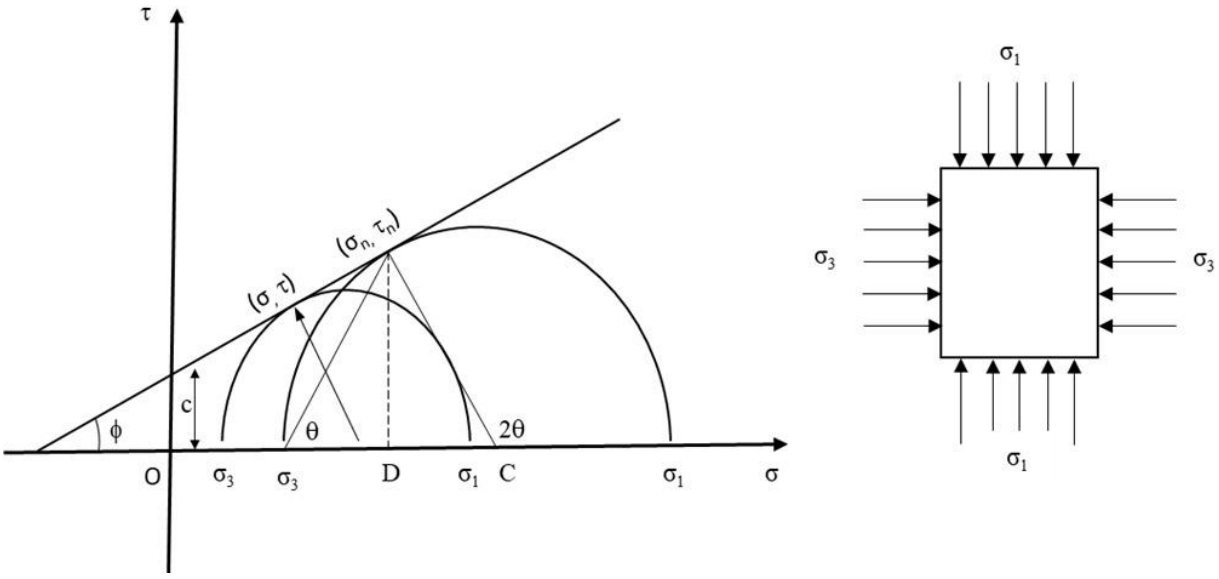


**Figure 2.7: Illustration of Mohr-Coulomb failure criterion in 2D.**

From the Mohr circles we have,

$$\sigma = \sigma_m - \tau_m \sin\phi$$

**Figure 2.8: Equation. Normal stress.**

$$\tau = \tau_m \cos\phi$$

**Figure 2.9: Equation. Shear stress.**

Where $\tau_m$ is the maximum shear stress; $\sigma_m$ is the mean principal stress; $\sigma_1$ and $\sigma_3$ are the major and minor principal stresses respectively.

The Mohr-coulomb criterion can therefore be written as.

$$\tau_m = \sigma_m \sin\emptyset + c\cos\emptyset$$

**Figure 2.10: Equation. Mohr- Coulomb criterion.**

The normal stress ($\sigma_n$) and shear stress ($\tau_n$) on a failure plane (Figure 2.13) are given by the equations shown in Figures 2.11 and 2.12, respectively.

$$\sigma_n = \frac{\sigma_1 + \sigma_3}{2} + \frac{\sigma_1 - \sigma_3}{2}\cos(2\theta)$$

**Figure 2.11: Equation. The normal stress on a failure plane.**

$$\tau_n = \frac{\sigma_1 - \sigma_3}{2}\sin(2\theta)$$

**Figure 2.12: Equation. The shear stress on a failure plane.**

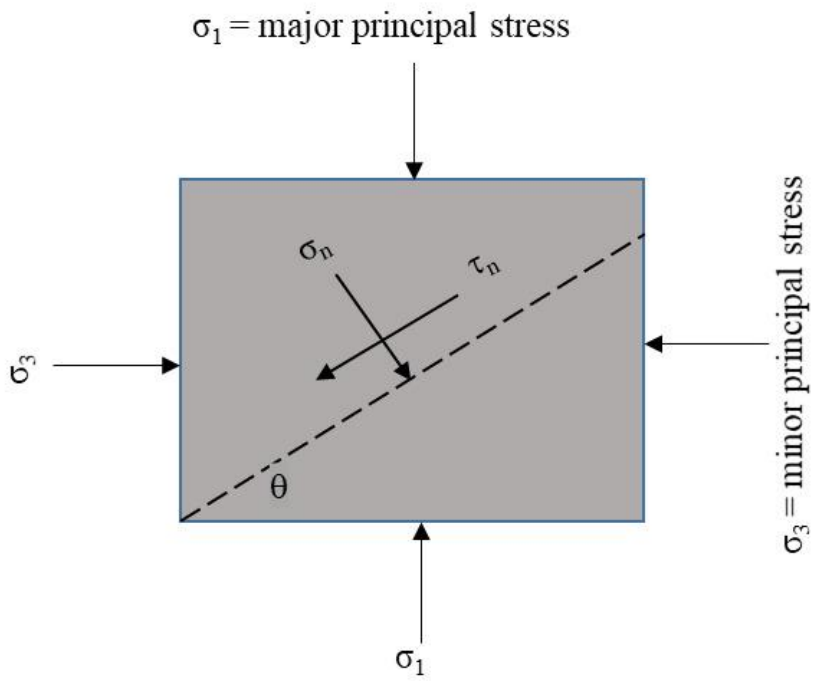


**Figure 2.13: $\sigma_n$ and $\tau_n$ are the normal and shear stresses acting on the failure plane.**

### *2.3.2 HB Failure Criterion*

HB failure criterion (1980) is a nonlinear failure criterion that was derived from the brittle fracture criterion of intact and jointed rock mass (Griffith 1924). Hoek focused on rock fracture propagation and failure of rock samples following fracture initiation in the compression stress field, whereas Griffith's theory predicted failure strength in the tensile stress field.

The HB criterion given by the equation in Figure 2.14 is based on the major principal stress ($\sigma_1$) and minor principal stress ($\sigma_3$) at failure and is a function of UCS or $\sigma_{ci}$, the rock mass constant $m_{b,}$ and HB fitting coefficients $a$ and $s$, which depend upon the characteristics of the rock mass

(Hoek and Brown 1980). This criterion assumes that the rock is isotropic and doesn't consider tensile failure, i.e., neglects the value of confining pressure less than 0.

The rock material constants $a$, $s$, and $m_b$ can be calculated using the equations shown in Figures 2.15, 2.16, and 2.17, respectively, based on the geological strength index ($GSI$) and disturbance factor ($D$). The $m_b$ constant for a rock mass is also related to the constant $m_i$ for an intact rock.

$$\sigma_1 = \sigma_3 + \sigma_{ci} \sqrt[a]{m_b \frac{\sigma_3}{\sigma_{ci}} + s}$$

**Figure 2.14: Equation. The HB criterion.**

$$a = \frac{1}{2} + \frac{1}{6}\left(e^{\frac{-GSI}{15}} - e^{\frac{-20}{3}}\right)$$

**Figure 2.15: Equation. The material constant (a).**

$$s = exp\left(\frac{GSI - 100}{9 - 3D}\right)$$

**Figure 2.16: Equation. The material constant (s).**

$$m_b = m_i \exp\left(\frac{GSI - 100}{28 - 14D}\right)$$

**Figure 2.17: Equation. The material constant ($m_b$).**

The *GSI* can be estimated directly from Rock Mass Rating (RMR), and the $D$ factor depends on the degree of disturbance that the rock suffers during blast damage and stress relaxation. The generalized HB criterion (Figure 2.18) for an intact rock can be derived by substituting the constants $s = 1$ and $a = 0.5$.

$$\sigma_1 = \sigma_3 + \sqrt{m\sigma_{ci}\sigma_3 + s{\sigma_{ci}}^2}$$

**Figure 2.18: Equation. The generalized HB criterion for intact rock.**

# CHAPTER 3: LABORATORY ROCK TESTING AND MEASUREMENTS

## 3.1 Introduction

Mechanical properties of natural rocks vary significantly due to rock texture, discontinuities, bedding, and mineral composition. This variation is due to their mineralogy, geological age, formations, and other natural processes. Anisotropic rocks have highly variable mechanical properties which cannot be easily reproduced (Jaeger et al. 2007). Laboratory measurement of the mechanical properties of different rock types is necessary to evaluate their failure behavior, mechanical properties, and strength parameters.

This study included various rock types (sandstone, siltstone, shales, etc.), tested at varying confining pressure. The rock samples collected from Wyoming include both drilled cores and surface boulders. Intact rock samples were tested for at least one unconfined compression test and several triaxial compression tests at different confinements. Uniaxial and triaxial compression tests were performed at the Engineering laboratory of the University of Wyoming in accordance with the ASTM D7012 (2014). For the compression triaxial tests, the stress condition of $\sigma_1 > \sigma_2 = \sigma_3$ is applied.

## 3.2 Preparation of Rock Specimens

According to the ASTM standard, a specific specimen size must be attained before proceeding with the mechanical testing of the rock specimen. The height-to-diameter ratio of the tested specimen should be equal to or greater than two but not less than two.

### *3.2.1 Drilling of Rock Specimens from Surface Rock Boulders*

The drilling equipment used for rock coring is a 1200 hp top drive table drill from Ancker drilling company. Figure 3.1 shows a schematic representation of the drilling process using the Ancker drill. For the top drive drill, thrust (force) was applied from the top and the torque generated due to the spinning of the drill bit cuts through the rock boulder as shown in Figure 3.1c and Figure 3.1b. Once the drill bit passed through the rock, the drill bit is lifted with the drilled rock core inside it as shown in Figure 3.1c. Figure 3.2 shows the drill used to core rock specimens from surface rock boulders. It has four adjustable drilling speeds of 250 rpm, 500 rpm, 800 rpm, and 1400 rpm. Drill bits with outer diameters of 32mm and 57mm were used for drilling 25mm and 50mm diameter rock specimens, respectively. The drill bits are especially designed for wet

drilling using a sufficient supply of water during the drilling to prevent the damage of the drill bits by overheating. The dry drilling can be done on soft rocks that break with water.

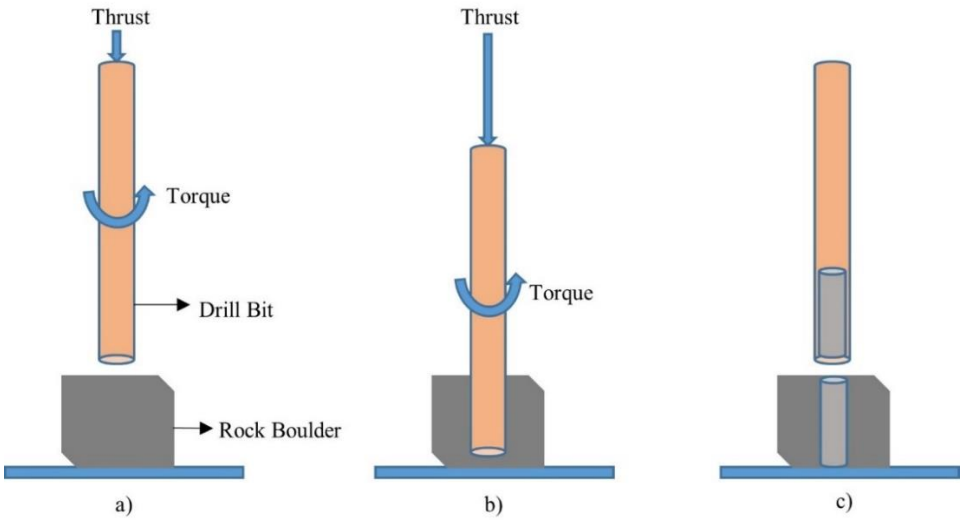


**Figure 3.1: Rotary drilling of cores from rock boulders.**

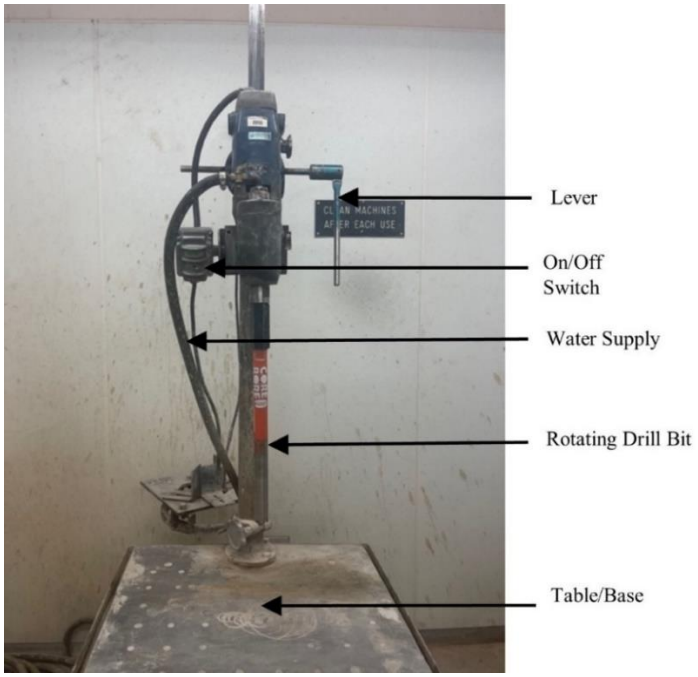


**Figure 3.2: Drilling equipment and setup for rocks.**

The rock boulder to be drilled must be fastened tightly on the table before drilling. Although many setups can be used to fasten the rock onto the table, 2×4 Irwin quick grip clamps and C-clamps as shown in Figure 3.3a were found to be adequate. The drilling process could encounter several problems if the rock boulder was not held properly. First, if the boulder is not

fastened properly, it might get thrown off the table during drilling. Second, if the rock is allowed to move during a high-speed rotation, the drill bit could hit the rock and cause rock vibration, preventing the drilling through the rock. This could break the rock specimen as shown in Figure 3.3b. Lastly, if the boulder moves or shifts during the drilling process, a perfectly vertical and straight cylindrical rock specimen cannot be obtained. A similar setup was made when drilling smaller diameter cores from large diameter rock cores.

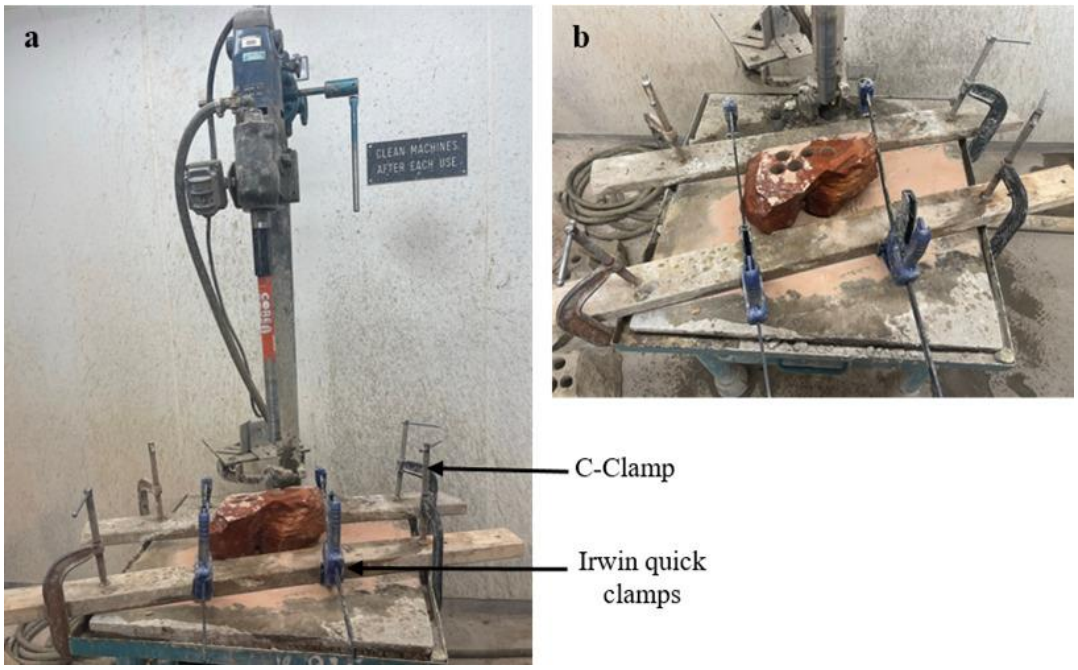


**Figure 3.3: (a) Fastening the rock boulder on the table using clamps, and (b) broken rock sample.**

After fastening the rock boulder on the table underneath the drill bit, a rotation speed of the drill bit was chosen depending on the rock's hardness. For hard rocks like the gneiss and volcanic breccia, a slower drilling speed of 250-500 rpm with a full supply of water to cool the drill bit is recommended. Using a higher rotation speed risks damaging the drill bit and takes a lot more effort to push the drill bit through the rock. On the other hand, a higher drilling speed of 850-1400 rpm with a controlled water supply is recommended for soft rocks like sandstones and shales. The longer the soft rocks are subjected to the vibration effect from the rotatory drill, the more likely breakage will occur.

After fastening the rock boulder and determining the drilling speed, the drill bit was lowered using the lever control shown in Figure 3.3. For soft rocks, the lever should be held to maintain a constant force and achieve smooth drilling through the rock. For hard rocks, force should be

applied to the lever to facilitate rock drilling and prevent idle rotation in one place. Before and after the drilling process, the lever should be held tightly and fixed in place to avoid sudden falling of the drill setup and risk of breakage of the drill bit, bottom table, rock sample, or injury. The operation process produces deafening sounds and splashes of water, so it is important to wear ear and eye protection gear during drilling. The drill bit rotates at very high speed to produce the torque required for drilling the rock, it is thus very important to not wear loose clothing during the drilling process as it might get in contact with the rotating drill and cause injuries. Figure 3.4a shows the drilled sandstone sample and Figure 3.4b shows four long cylindrical rock cores obtained from the rock boulder.


**Figure 3.4: (a) Drilled rock boulder, and (b) drilled rock cores.**

### *3.2.2 Cutting of Rock Cores*

After the rock cores were extracted from the rock boulder, the rock core length was cut to obtain a length-to-diameter ratio (L/D) equal to 2. The rock cutting was accomplished using the 178mm portable wet cutting saw equipment shown in Figure 3.5. The cutting equipment has a 178mm continuous rim diamond blade, and water was used during the cutting process to keep the blade cool. The excess water from the tabletop was collected in a tray. The cutting equipment has a scale printed on the top and an adjustable linear guide that can be fixed at the desired distance from the saw to get a precise cut. The equipment can reach a saw cutting speed of up to 3400

rpm. The housing is made from anti-fire plastic material, and the tabletop is stainless steel. The equipment must be cleaned before and after each cutting operation to ensure the best cutting performance. The sample should be held tightly during cutting to get a smooth and even cut. Care should be taken while cutting as the blades of the cutting saw are exposed and injuries may occur if the hands touch the running blade. During the cutting process, a lot of water is splashed onto the body and eyes, thus wearing proper safety gear is highly recommended.

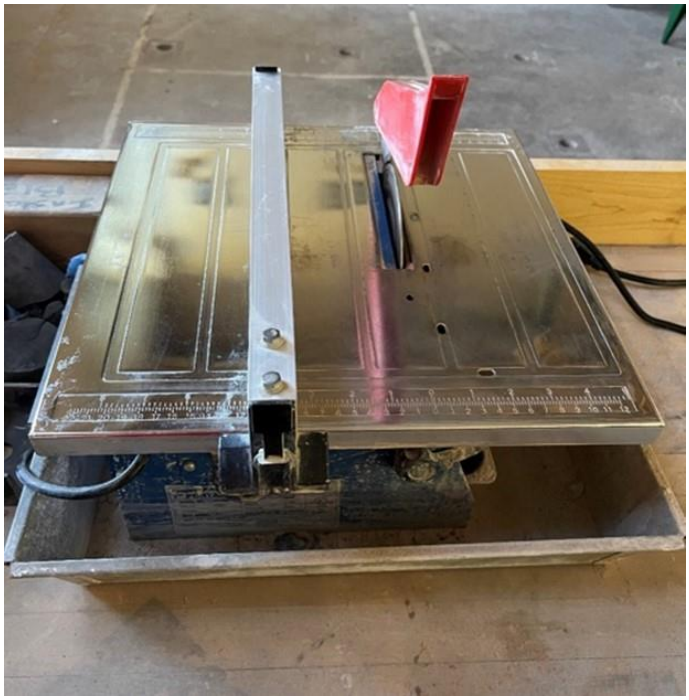

**Figure 3.5: Equipment for cutting and trimming rock specimens.**

### *3.2.3 Rock Trimming and Polishing*

After the rock specimens were cut to their desired lengths, both ends of the rock specimens were trimmed and polished to obtain a uniformly planar surface for testing as the top and bottom of the test specimen should be parallel to each other and perpendicular to the longitudinal axis. The finished top and bottom surfaces should not exceed the tolerance of 0.0254 mm (ASTM D4543 2008). Care should be taken while polishing softer rocks like sandstone to avoid breaking at the edges or making it too short. The polishing is accomplished by rotating the rock specimen and the milter gauge worktable assembly with an attached sanding belt shown in Figure 3.6. The aluminum worktable can be tilted from 0 to 45 degrees, and the sanding belt sander is 10×91 cm. There are two cast aluminum worktables for vertical and horizontal polishing. The maximum disc speed is 3450 rpm. A milter gauge is provided to fix the rock

specimen's proper angle, and a vacuum is connected to the machine to collect the produced dust particles.


**Figure 3.6: Polishing equipment with a sanding belt.**

## 3.3 Rock Testing System

There were two types of rocks tested in the laboratory. Hard rocks were tested using the GCTS rapid Triaxial rock testing equipment RTR-1500, and soft soil-based rocks were tested using the GeoJac triaxial equipment.

### *3.3.1 GCTS Rapid Triaxial Rock (RTR-1500) Testing Equipment*

The GCTS Rapid Triaxial Rock (RTR-1500) testing equipment shown in Figure 3.7 was used for the unconfined compression test and the triaxial test of the hard rock specimens. An automatic hydraulic lift and sliding base, a triaxial cell made of stainless steel, and two pressure intensifiers for controlling the cell and pore pressures are provided in the setup. The triaxial cell can accommodate cylindrical specimens of up to 75 mm. The equipment has a load frame with a stiffness of 1.75 MN/mm. This equipment is a digitally regulated closed-loop servo control of the axial actuator and is operated using a computer as shown in Figure 3.8. The setup includes a fully integrated SCON-2000 digital signal controller and CATS-TRX-ROCKS software. GCTS RTR-1500 has a rapid, easy, and safe operation with automated cell assembly and meets the specifications of the ISRM and ASTM standards for triaxial testing of the rock samples.

The axial load actuator has a capacity ranging up to 1500 kN and the triaxial cell can apply a maximum confining pressure of 140 MPa. The confinement was applied using an oil-filled stainless-steel chamber inside the frame. For confinement, a pressure intensifier for cell pressure was used. The pressure intensifier is housed inside a metal cabinet and includes a 20-liter fluid reservoir, precise analog gauges, high pressure valves, and flow indicators. Both the cell and pore pressure intensifiers have a pressure transducer and linear variable differential transformer (LVDT) connected allowing for the servo control as a function of pressure, fluid volume control, or any other measured or calculated test parameter. A heat-shrink membrane was used to protect and separate the rock specimen from the oil. The connected computer controls the testing system and can be programmed for testing at different ASTM testing standards. The equipment was set up for testing 25 mm and 50 mm diameter rock specimens.

Two axial and one radial strain linear variable differential transformers (LVDTs) were used for strain measurements. At the bottom, feed-through lines from the radial LVDT, axial LVDT's and top & bottom platen were connected to measure the deformation and post-failure behavior studies. The equipment is also equipped with an ultrasonic measurement capacity to yield P-wave and S-wave velocities. The high-performance equipment has a servo-controlled axial actuator used to control the maximum deformation of the axial strain for automatically completing the triaxial test.


**Figure 3.7: GCTS RTR-1500 triaxial testing equipment.**


**Figure 3.8: Computer operated SCON controller for RTR 1500 triaxial testing equipment.**

### *3.3.2 GeoJac Triaxial Equipment*

The GeoJac triaxial equipment shown in Figure 3.9 is a compact and lightweight automated testing system for the mechanical testing of soil-based rock specimens. The machine has an axial load capacity of 9 kN and a 0.38 m stroke that can be configured to perform various triaxial tests. The setup is operated using a computer system that can be programmed to perform unconsolidated undrained (UU), consolidated undrained (CU), and consolidated drained (CD) tests. The test setup consists of a load actuator mounted on two vertical stands which can be used to automate the three triaxial test types. The GeoJac equipment can perform testing under a closed-loop control of axial deformation, load, or pressure.

The triaxial tests were mainly conducted under a controlled axial deformation, with 15 percent as the peak strain As the rock specimens are soil-like, it undergoes bulging when the load was applied, hence for the safety of equipment and to avoid the destruction of samples, the test was stopped at a 15 percent strain limit. The specimen can be sheared in various modes like constant deformation rate, constant rate of loading, or a series of step loads to reach the final axial deformation value. The GeoJac device has a cylindrical glass side wall placed on the base part with a bottom pedestal to place the rock specimen. The top of the cylindrical sidewall is mounted with the piston setup. Water is used to apply uniform confining pressure to the specimen during the test, and the device can withstand a confining pressure of up to 0.55 MPa. A plastic membrane was used to protect the rock specimen from the water. A cell pressure

sensor was placed on the top part of the cell chamber to take the Stress-strain measurements during the shearing stage.

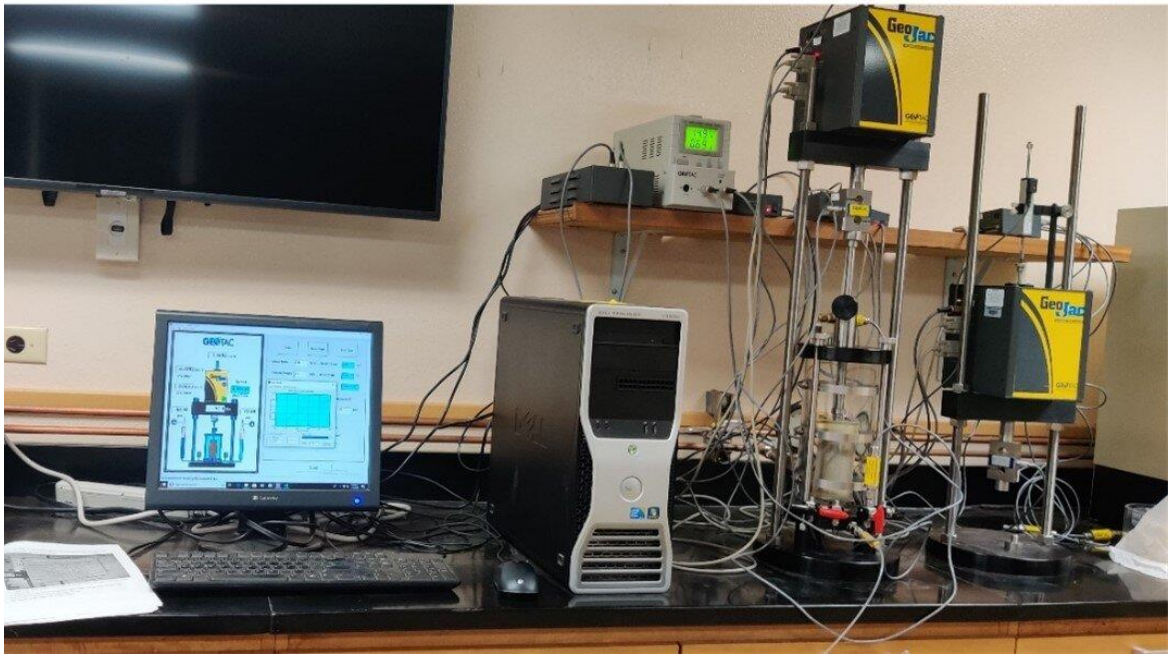


**Figure 3.9: GeoJac equipment setup in UW laboratory.**

## 3.4 Rock Testing Procedure

### *3.4.1 GCTS Rapid Triaxial Rock Testing Procedure*

The height, diameter, and weight of each rock specimen were measured as shown in Figure 3.10. The specimen was then placed between the bottom and top platens. A heat-shrink tubing was then wrapped on the rock specimen using a heat gun. A steel chain for the radial LVDT sensor was wrapped around the mid depth of the rock specimen. For the measurement of the axial deformation of the specimen, two axial LVDTs are inserted vertically through the two rings, and for the measurement of the radial deformation, the radial LVDT was inserted horizontally through the chain as shown in Figure 3.11.

The installed specimen setup was then slid into the loading frame and beneath the cylindrical cell wall, and the cell wall was lowered and closed. The cell wall was then filled with oil, and the desired confining pressure was applied to the rock specimen. The initial seating pressure of 50 psi was applied before the shearing stage. The rock was then subjected to an axial shearing stage using a controlled axial strain setup at a constant strain rate of 0.1 percent per minute for hard rocks and 0.05 percent per minute for softer rocks. The rock failed, and the test was

stopped. After that, the specimen's failure plane and failure angle were determined as shown in Figure 3.12. The results of the confining stage and the shearing stage were stored in two separate files for analysis.


**Figure 3.10: Measurement of height, diameter, and weight of each rock specimen.**


**Figure 3.11: Triaxial setup with three LVDT sensors.**

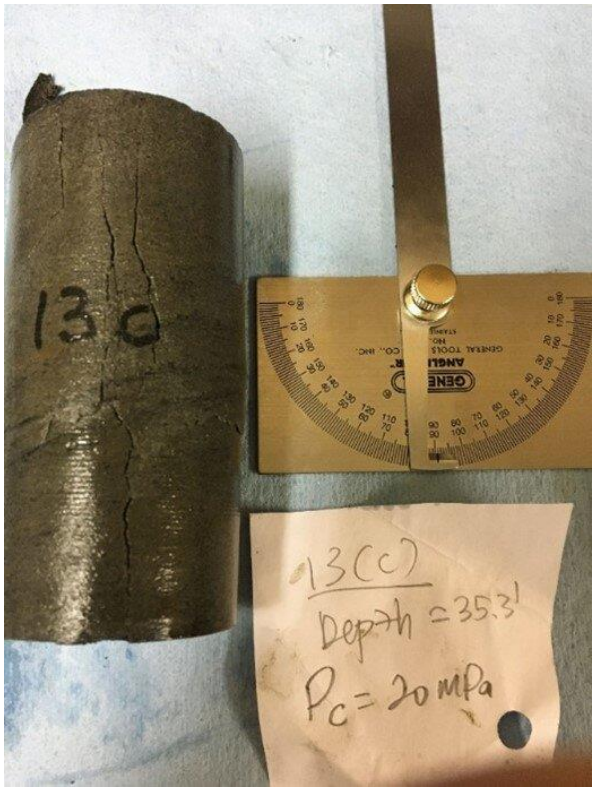


**Figure 3.12: Rock specimen after testing.**

### *3.4.2 GeoJac Triaxial Procedure*

The height, diameter, and weight of the specimen were measured. A porous stone was placed on the base pedestal, followed by filter paper. The rock specimen was placed on top of filter paper followed by a top filter paper and the top pedestal. The specimen was wrapped in a rubber membrane that was held tightly against the top and bottom platens using O-rings. The specimen was enclosed in the cylindrical glass cell wall, and a piston was placed on the top of the cell wall, which was fixed in place using three rods as shown in Figure 3.13a. The cell was then filled with water, and the cell pressure was changed to confining pressure using the valve in a red circle (Figure 3.13b). We then unlocked the top piston to allow the application of axial load and the specimen was then sheared until the axial strain reached the maximum limit of 15 percent. The applied strain rate should fall between 0.3 percent to 1 percent per minute so that failure occurs in more than 15 minutes. The specimen during loading and at failure is shown in Figure 3.14a and Figure 3.14b. The experimental data was then recorded and saved for further analysis.

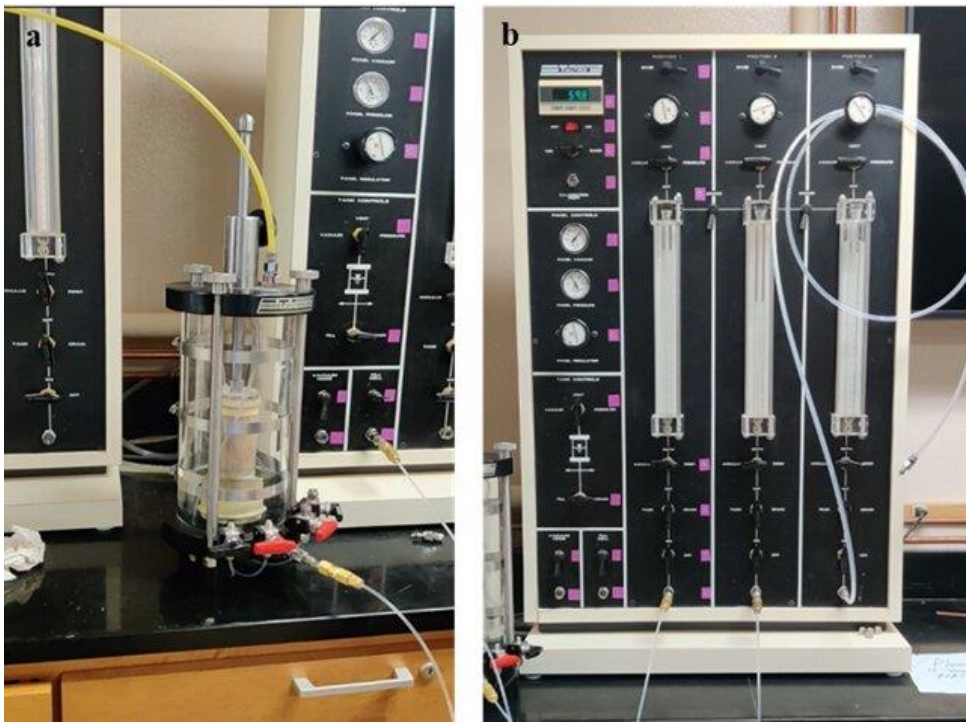


**Figure 3.13: (a) GeoJac triaxial setup, and (b) switchboard for applying confining pressure.**


**Figure 3.14: (a) Application of axial load during the shearing stage, and (b) final deformed shape of the specimen.**

## 3.5 Determination of Porosity

The porosity (*n*) is the total volume inside a rock for the passage and storage of fluid and gas. It can be represented as $1 - (V_s/V)$ , where $V_s$ is the volume of rock solid, and $V$ is the total volume of the rock. The porosity of a rock is intrinsic to the rock's bulk matrix, which controls the flow and transport processes inside the rock that typically decreases with age and depth of burial and differs with rock type, pore distribution, and composition. Depending upon the rock type, porosity can be determined using the saturation method or calculated using the measured specific gravity of rock solid. The saturation method is suitable for harder rocks that would not break or integrate in water while the specific gravity method is recommended for softer rocks that break or disintegrate on the action of the water.

### *3.5.1 Porosity Determination Using the Specific Gravity Method*

To determine a rock's porosity using this method, we first determine the specimen specific gravity ($G_s$) and water content. The specific gravity was determined using the AASHTO-100 standard test method. The rock specimen was ground into solid particles and tested using the calibrated 250 ml Pycnometer. The dry weight, weight of Pycnometer filled with de-aired water,

and temperature were noted. The weight of the Pycnometer with water at 2 degrees above and below the measured temperature was calculated. Solid particles between 30-40 gm are added to ¾ full Pycnometer and vacuumed for 10 minutes as shown in Figure 3.19 left. The Pycnometer was then filled up to the mark, and its weight was measured. The whole mix was then transferred onto an evaporating dish, leaving no solid particles in the Pycnometer. The flow of the mixture coming out from the Pycnometer was controlled by lowering the lip above the water as shown in Figure 3.19 right. The evaporating dish with the mixture was placed inside the oven for at least 24 hours to dry out the water completely. The weight of the evaporating dish with the remaining solids was measured and deducted from the empty weight of the dish to get the weight of the solids. The calculation of the specific gravity is then given by Figure 3.15 below.

$$G_{s,T} = \frac{W_o}{[W_o + (W_a - W_b)]}$$

**Figure 3.15: Equation. Specific gravity formula.**

The specific gravity can be calculated using the equation below for $K$ selected based on temperature $T_o$ using the equation shown in Figure 3.16.

$$G_{s,20C} = K \times G_{s,T_x} = \frac{K \times W_o}{[W_o + (W_a - W_b)]}$$

**Figure 3.16: Equation. Specific gravity calculation at temperature of 20°C.**

Where $K$ is the correlation factor, $W_o$ is the dry weight of solids, $W_a$ is the weight of Pycnometer and de-aired water, $W_b$ is the weight of Pycnometer, solid, and de-aired water.
After Specific gravity, we determined the water content of the rock specimen. The moist weight of the rock was measured and oven-dried for at least 24 hours before measuring the dry weight. Then we calculated water content from these two weights using the equation shown in Figure 3.17,

$$Water\ Content\ (\%) = \frac{W_2 - W_3}{W_2 - W_1} \times 100\%$$

**Figure 3.17: Equation. Water content formula.**

Where $W_1$ = empty weight of a can, $W_2$ = weight of the can and moist rock specimen before drying, and $W_3$ = weight of the can and rock specimen after oven-drying.

When the porosity and water content of the rock had been measured, we then measured the height (L) and diameter (D) of an intact rock specimen in inches and the moist weight of the rock specimen ($W_m$) in grams. We calculate the intact rock's volume, dry weight, and dry bulk density ($\rho$) and determine the porosity of the intact rock by

$$Porosity\ (\%) = \frac{1 - Dry\ Bulk\ Density}{Specific\ Gravity} \times 100$$

**Figure 3.18: Equation. porosity of intact rock formula.**

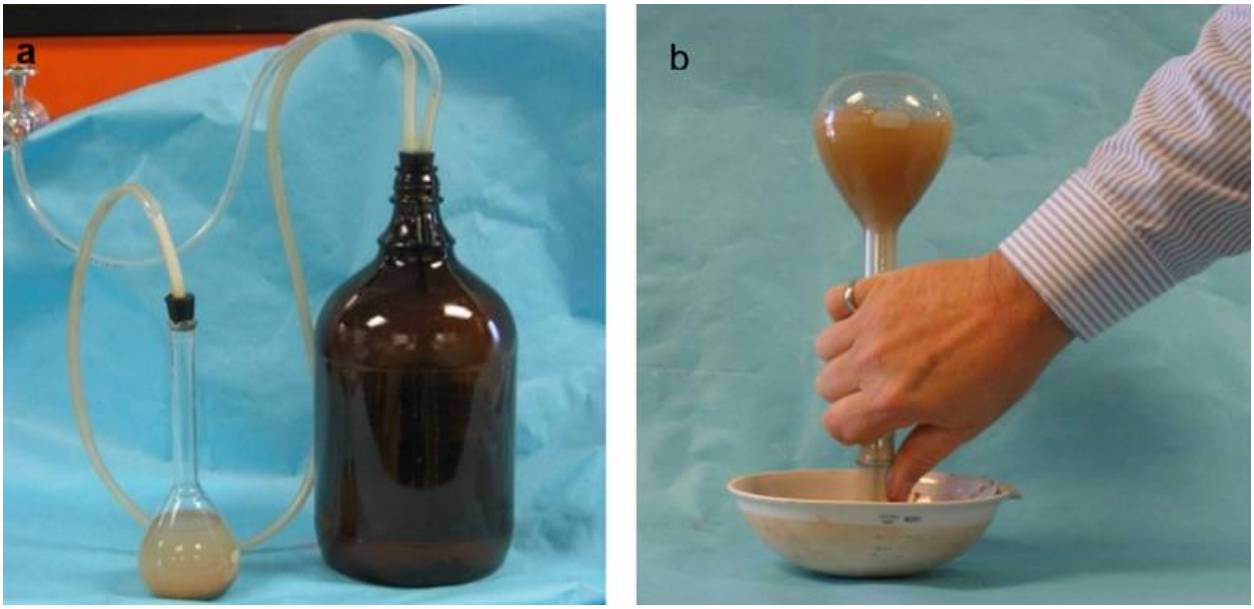


**Figure 3.19: (a) Vacuuming the sample and deaired water mix, and (b) pouring the mix into evaporating dish for drying.**

### *3.5.2 Porosity Determination Using the Saturation Method*

The rock specimen is prepared to be tested with length ($L$) and diameter ($D$) such that $\frac{L}{D} \geq 2$. The rock specimen is then placed inside an oven to dry for at least 24 hours, and the dry weight of the rock ($W_d$) is measured. The oven-dried sample is then placed inside the saturation vessel as shown in Figure 3.21 left, and the vacuum is turned on for 24 hours as shown in Figure 3.21 right. After 24 hours, the first saturated weight is taken, and the vacuum is turned on again for the next 24 hours. This process is repeated until the difference in the last two consecutive weights is less than 1 percent. The previous weight measurement is noted as $W_s$. From the

length and diameter, the volume of the intact rock specimen is calculated, and the porosity of the rock is calculated using the equation shown in Figure 3.20,

$$Porosity\ (\%) = \frac{W_s - W_d}{D_w\ (gm/cc) \times V\ (in\ cc)} \times\ 100\%$$

**Figure 3.20: Equation. The porosity of rock.**

Where, $W_s$ is the saturated weight, $W_d$ is the dry weight, $D_w$ is the density of water and $V$ is the volume of the rock.

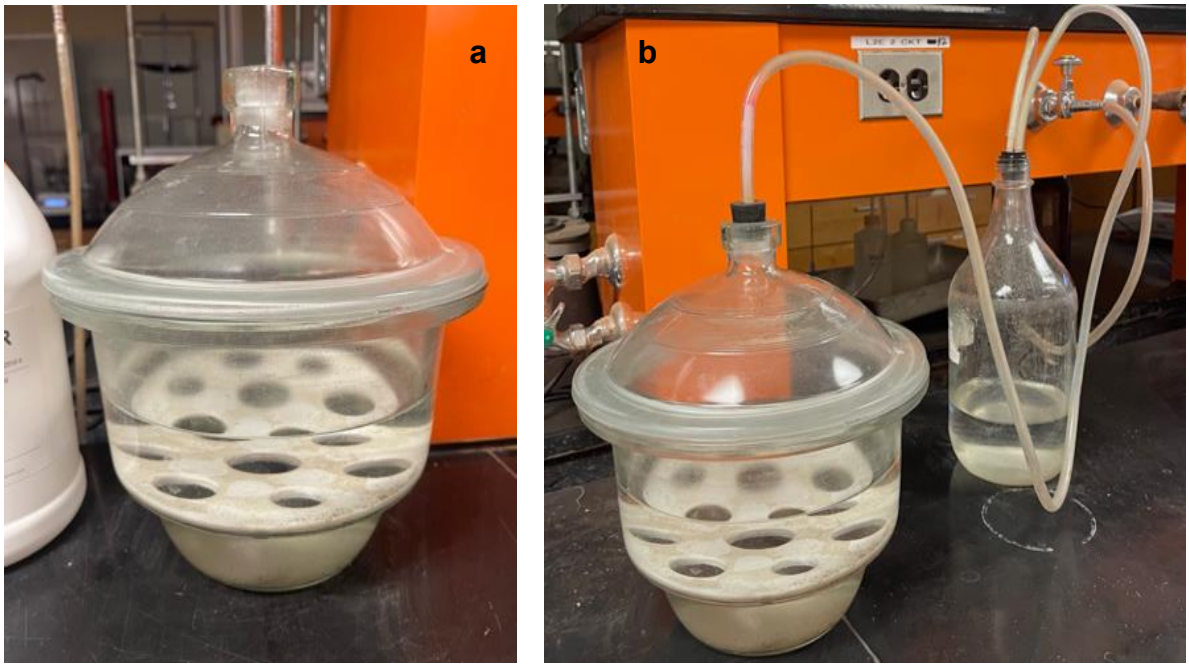


**Figure 3.21: (a) Saturation vessel, and (b) saturation vessel connected to vacuum.**

# CHAPTER 4: BEDROCK DATABASE AND TEST RESULTS

Fifty-six rock samples were collected from different locations around the State of Wyoming. These samples were a mix of different rock types, formations, geologic ages, and depths. Figure 4.1 shows the location of the individual samples on the geographical map of Wyoming. Each sample was identified with an identification number from 1 to 56. Among the 56 samples, six samples (3, 7, 8, 26, 38, and 52) were not usable for various reason ns indicated in Table 4.1, and hence, 50 rock samples are considered usable.

## 4.1 Master Summary of Tested Samples

The information about individual samples obtained is shown in Table 4.1. Representative rocks from all four geological eras; Precambrian, Paleozoic, Mesozoic, and Cenozoic were collected and tested in this project. The samples also represent all three geological rock types: Igneous, Sedimentary, and Metamorphic. The samples collected were a mixture of surface boulders and rock cores obtained from a depth up to 65 m so that the strength properties of rocks can be compared for all major civil engineering applications.

The number of samples based on rock types, ages, and depths are shown in Tables 4.2, 4.3, and 4.4, respectively. Table 4.2 shows 13 rock types collected and tested in this project, their geological type, and the count of each rock type. Table 4.3 shows the list of geological ages, their respective geological era, and the count of rock samples from each geological age. Table 4.4 shows the number of rock samples that are obtained either as a surface boulder or from a subsurface depth by various coring methods.

Table 4.2 shows that sandstone (30.36 percent), siltstone (23.24 percent), and shale (14.29 percent) made up the majority of rock samples used in this study; hence most of the rock samples are sedimentary rocks. Other notable rock types encountered were limestone (7.14 percent), granite (5.36 percent), and claystone (5.36 percent). Other less notable rock types were amphibolite (1.79 percent), anorthosite (1.79 percent), conglomerate (3.57 percent), dolostone (1.79 percent), gneiss (1.79 percent), volcanic breccia (1.79 percent), and welded tuff (1.79 percent).

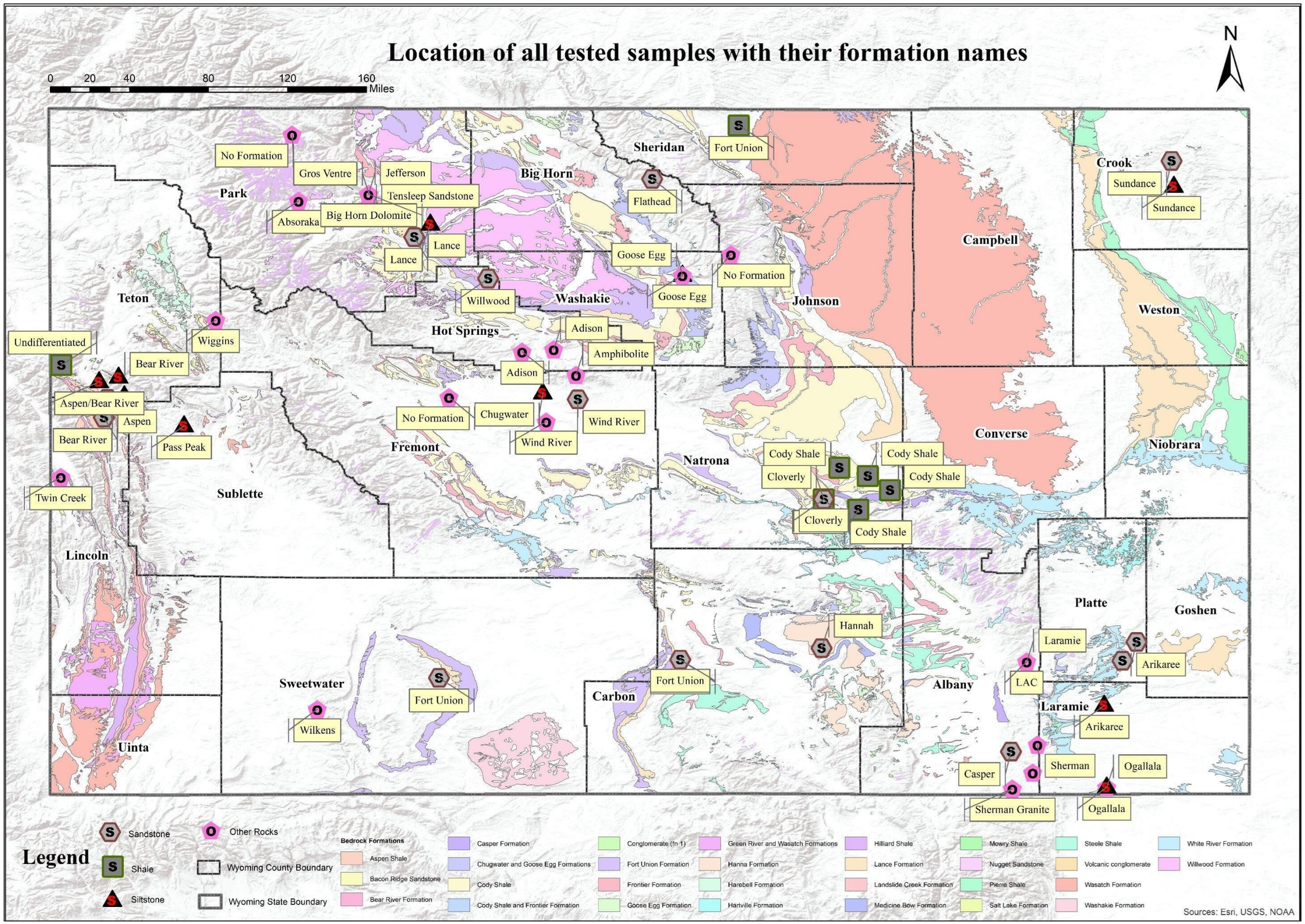


**Figure 4.1: Location of tested samples with their formation names (Esri ArcGIS 10.3).**

**Table 4.1: Summary of 56 rock samples with different identifications, ages, formations, types, depths, and locations.**

| Sample ID | Period | Formation | Rock Type | Depth (m) | Location | Comments |
|---|---|---|---|---|---|---|
| 1 | Miocene | Ogallala | Claystone | 19.82-20.20 | Terry Ranch Road | |
| 2 | Cretaceous | Cody Shale | Shale | 15.55-16.16 | Walsh Drive, Casper | |
| 3 | Jurassic | Morrison | Shale | 1.92-2.80 | Narrow Backslope | Dried out and short length of cores |
| 4 | Cretaceous | Undifferentiated | Shale | 13.11-13.72 | Mail Cabin Landslide | |
| 5 | Permian | Goose Egg | Siltstone | 3.57-3.96 | Toms Pit | |
| 6 | Jurassic | Sundance | Siltstone | 8.08-10.06 | Lower Red Canyon Slide | |
| 7 | Cretaceous | Aspen/Bear River | Siltstone | 12.04-13.48 | Bear River Slide 3 | Dried out and short length of cores |
| 8 | Eocene | Pass Peak | Clayey Siltstones | 13.72-17.62 | Spud Slide | Dried out and short length of cores |
| 9 | Oligocene | Wiggins | Volcanic Breccia | 64.82-65.43 | The Rock, Togwotee Pass | |
| 10 | Cretaceous | Cloverly | Conglomerate | 28.02-29.09 | Narrows Backslope | |
| 11 | Eocene | Wasatch | Siltstone | 17.80-21.80 | | |
| 12 | Paleogene | White River | Siltstone | 21.68-23.05 | | |
| 13 | Cretaceous | Aspen/Bear River | Siltstone | 10.43-11.04 | Swinging Bridge | |
| 14 | Cretaceous | Cody Shale | Shale | 17.93-23.78 | North Platte River Bridge | |
| 15 | Cretaceous | Cody Shale | Shale | 13.11-16.16 | Walsh Drive | |
| 16 | Cambrian | Flathead | Sandstone | 3.05-19.97 | Ski Area Slide | |
| 17 | Cretaceous | Cloverly | Sandstone | 29.88-30.55 | Narrows Backslope | |
| 18 | Jurassic | Sundance | Sandstone | 0.91-17.68 | Lower Red Canyon Slide | |
| 19 | Cretaceous | Aspen/Bear River | Sandstone | 6.10-12.50 | Hoback Jct. Bridge | |
| 20 | Cretaceous | Aspen/Bear River | Sandstone | 8.08-10.73 | Hoback Jct. Bridge | |
| 21 | Paleocene | Fort Union | Shale | 14.63-16.16 | Tongue River Bridge | |
| 22 | Cretaceous | Cody Shale | Shale | 15.55-18.14 | F-St. Bridge over North Platte | |
| 23 | Cretaceous | Lance | Graywacke Sandstone | Surface | MP 65.8, US 120, South of Cody | |
| 24 | Cretaceous | Lance | Siltstone | Surface | MP 65.8, US 120, South of Cody | |
| 25 | Mississippian | Madison Limestone | Limestone | Surface | MP 122.5, US20/WY789, Wind River Canyon | |

| Sample ID | Period | Formation | Rock Type | Depth (m) | Location | Comments |
|---|---|---|---|---|---|---|
| 26 | Eocene | Willwood | Sandstone | Surface | Paddy Pit, Hot Springs County | Rock boulder broke during drilling and no cores were extracted |
| 27 | Permian | Goose Egg | Limestone | Surface | Toms Pit, Washakie County | |
| 28 | Precambrian | No Designation | Granite | Surface | MP 7.6, WY 296 | |
| 29 | Archeon | No Designation | Hornblende Gneiss | Surface | MP 56, US16, Powder River Basin | |
| 30 | Cretaceous | Bear River | Siltstone | 11.59-13.41 | Bear River Slide | |
| 31 | Pennsylvanian | Tensleep Sandstone | Sandstone | Surface | MP 44.3, US16/14/20 West of Cody | |
| 32 | Lower Miocene | Arikaree | Coarse Sandstone | Surface | TY Bluff Road | |
| 33 | Lower Miocene | Arikaree | Medium Sandstone | Surface | I25 cut at Chugwater | |
| 34 | Lower Miocene | Arikaree | Siltstone | Surface | East I25 Frontage Road, MP 38 | |
| 35 | Paleogene | Hanna | Siltstone | 57.01-57.93 | Hanna Power Pole | |
| 36 | Triassic | Chugwater | Siltstone | Surface | US20/WY789, MP 112.9, Red Bed Slide | |
| 37 | Miocene | Ogallala | Siltstone | 24.70-29.27 | Terry Ranch Road, Cheyenne | |
| 38 | Paleogene | Hanna | Claystone | 9.45-13.41, 20.12-22.56 | Hanna Power Pole | Only two testable samples, other cores were too short for testing |
| 39 | Paleogene | Hanna | Fine Sandstone | 43.60-47.87 | Hanna Power Pole | |
| 40 | Paleogene | Hanna | Shale | 32.32-35.37 | Hanna Power Pole | |
| 41 | Paleogene | Hanna | Coarse Sandstone | 23.17-26.22 | Hanna Power Pole | |
| 42 | Jurassic | Twin Creek | Limestone | Surface | MP 94.7, US89, North of Afton | |
| 43 | Eocene | Wind River | Medium Sandstone | Surface | MP 95.5, US20/26, East of Shoshoni | |
| 44 | Eocene | Wind River | Silty Claystone | Surface | MP 95.5, US20/26, East of Shoshoni | |
| 45 | Ordovician | Big Horn Dolomite | Dolostone | Surface | MP 45.05, US14/16/20 | |

| Sample ID | Period | Formation | Rock Type | Depth (m) | Location | Comments |
|---|---|---|---|---|---|---|
| 46 | Cambrian | Gros Ventre | Limestone Pebble Conglomerate | Surface | MP 45.1, US14/16/21 | |
| 47 | Devonian | Jefferson Formation | Limestone | Surface | MP 44.84, US14/16/22 | |
| 48 | Eocene | Absoraka Supergroup | Welded Tuff | Surface | MP 23.6, US 14/16/23 | |
| 49 | Eocene | Bridger | Medium Sandstone | Surface | MP 3.0, WY530 | |
| 50 | Paleocene | Fort Union | Medium Sandstone | Surface | MP 131, I-80 | |
| 51 | Paleocene | Fort Union | Fine Sandstone | Surface | MP 206, I-80 | |
| 52 | Proterozoic | Sherman Granite | Granite Pegmatite | Surface | MP 422.6, US 287 | Rock boulder broke during drilling and no cores were extracted |
| 53 | Proterozoic | Lac Wheatland | Anorthosite | Surface | MP 25, WY34 | |
| 54 | Archeaon | No Designation | Amphibolite | Surface | MP 116.6, US20 | |
| 55 | Proterozoic | Sherman Granite | Granite | Surface | MP 28.8, WY210 | |
| 56 | Permian | Casper | Sandstone | Surface | MP 323.6, I-80 | |

Note: M–Medium; MP–Mile post.

**Table 4.2: Summary of rock sample counts based on rock types.**

| Rock Type | Geological Rock Type | Count | Weightage (Percent) |
|---|---|---|---|
| Amphibolite | Metamorphic | 1 | 1.79 |
| Anorthosite | Igneous | 1 | 1.79 |
| Claystone | Sedimentary | 3 | 5.36 |
| Conglomerate | Sedimentary | 2 | 3.57 |
| Dolostone | Sedimentary | 1 | 1.79 |
| Gneiss | Metamorphic | 1 | 1.79 |
| Granite | Igneous | 3 | 5.36 |
| Limestone | Sedimentary | 4 | 7.14 |
| Sandstone | Sedimentary | 17 | 30.36 |
| Shale | Sedimentary | 8 | 14.29 |
| Siltstone | Sedimentary | 13 | 23.21 |
| Volcanic Breccia | Igneous | 1 | 1.79 |
| Welded Tuff | Igneous/Sedimentary (Pyroclastic) | 1 | 1.79 |

Based on the geological age of rocks summarized in Table 4.3, most rock samples were from the Cretaceous Period (26.79 percent), followed by Eocene (12.5 percent), Paleogene (10.71 percent), Miocene (8.93 percent), Jurassic (7.14 percent), Permian (5.36 percent), and Paleocene (5.36 percent). This suggests that most rock samples were from the Mesozoic era (252-66 million years ago) and the Cenozoic era (66 million years ago to present). The details of the geological time scale are discussed in Table 4.3

**Table 4.3: Summary of rock sample counts based on geological ages and eras.**

| Geological Period | Geological Era | Count | Weightage (Percent) |
|---|---|---|---|
| Miocene | Cenozoic | 5 | 8.93 |
| Cretaceous | Mesozoic | 15 | 26.79 |
| Jurassic | Mesozoic | 4 | 7.14 |
| Permian | Paleozoic | 3 | 5.36 |
| Eocene | Cenozoic | 7 | 12.50 |
| Oligocene | Cenozoic | 1 | 1.79 |
| Paleogene | Cenozoic | 6 | 10.71 |
| Paleocene | Cenozoic | 3 | 5.36 |
| Mississipian | Paleozoic | 1 | 1.79 |
| Precambrian | Precambrian | 1 | 1.79 |
| Archeon | Precambrian | 2 | 3.57 |
| Pennsylvanian | Paleozoic | 1 | 1.79 |
| Triassic | Mesozoic | 1 | 1.79 |
| Ordovician | Paleozoic | 1 | 1.79 |
| Cambrian | Paleozoic | 1 | 1.79 |
| Devonian | Paleozoic | 1 | 1.79 |
| Proterozoic | Precambrian | 3 | 5.36 |

The rock samples were collected either as surface boulders or rock cores from drilling. One or two-inch diameter rock specimens were drilled out from the surface boulders using the drilling machine for testing described in Chapter 3. Table 4.4 indicates that the number of rock samples collected as surface boulders and rock cores were almost equal at 48.21 percent and 51.79 percent, respectively. The stress-strain plots of all tested specimens in addition to the post failure pictures are given in Appendices A (Khatri 2022).

**Table 4.4: Summary of rock sample counts based on rock depths.**

| Sample No. | Rock Depth | Count | Weightage (Percent) |
|---|---|---|---|
| 1 | Surface | 27 | 48.21 |
| 2 | Rock cores from subsurface drilling | 29 | 51.79 |

## 4.2 Sandstones

Among the 17 sandstone samples tested, ten samples were obtained as surface boulders, and 7 samples were obtained as rock cores drilled out from various projects around the state. Figure 4.3 shows the description of the tested sandstone samples, and Figure 4.4 shows the location map of the sandstone samples. The specimens were prepared at either 25mm diameter or 50mm diameter. The length to diameter ratio (L/D) ratio of the test specimen was maintained between 2 to 2.5 and the top and bottom of the test specimen should be parallel to each other and perpendicular to the longitudinal axis. The finished top and bottom surfaces should not exceed the tolerance of 0.0254 mm (ASTM D4543 2008). The length and diameter of all the specimens are provided in Figure 4.3.

The water content of the tested sandstones ranged from 0.14 percent to 6.58 percent. It is desirable to have the lowest possible water content as the presence of moisture in a sedimentary rock like sandstone can cause a drastic reduction in its compressive strength by the reduction of the fracture toughness and friction coefficient (Corentin Noël 2021). In a study of 35 British sandstones by Hawkins & McConnell (1992), they found that the sensitivity of sandstone to the effect of water content depends on the quartz and clay mineral content. Sandstones with higher amounts of quartz, a principal constituent of the sandstone, and low clay content were found to be less susceptible to moisture.

The amount of quartz also affected the specific gravity of sandstones. The higher the quartz content, the closer the specific gravity of sandstone to 2.65, which is the specific gravity of quartz. The specific gravity of the tested sandstones is found to be between 2.556 to 2.725. The

compressive strength of sandstones reduces as the porosity of the rock increases (Martin and Chandler 1994, Hoek and Martin 2014, Eremin 2020, and Corentin Noël 2021). The porosity of the tested sandstones in this project ranged from a minimum of 3.73 percent to a maximum of 25.86 percent.

### *4.2.1 Individual Test Results*

A series of uniaxial and triaxial compressive strength, porosity, and specific gravity tests were conducted on these samples, and the results in terms of Mohr-Coulomb failure parameters, HB failure parameters, elastic properties, particle size effect, and crack thresholds are discussed in the following subsections. Figure 4.5 consists of the test results of the sandstone samples. The confinement, peak stress, *β*, strain rate while loading, failure mode, failure behavior, and failure angle of each tested specimen are provided in Figure 4.5. The Specimen ID nomenclature is not in alphabetical order as not all prepared test specimens were used for testing. $\epsilon_a$, $\epsilon_r$, and $\epsilon_v$ in the figure legends represent the axial, radial, and volumetric strains, respectively. Some of the tests ended in a few seconds generating very few data points and thus, an unusual stress-strain plot. The reason for the sudden failure had been attributed to the strain rate, which was too high for some specimens.

### *4.2.2 Mohr-Coulomb Parameters*

The UCS ranged from 2.54 MPa to 84.48 MPa, the cohesion (*c*) ranged from 1.1 MPa to 20.34 MPa, and the internal friction angle ranged from 8 to 56 degrees. The lowest UCS, cohesion, and internal friction angle were observed in sandstone from Cretaceous Lance Formation. Table 4.5 shows the variation of UCS for all sandstone samples. The greatest difference between the UCS and cohesion is observed in Wind River Formation of Eocene age (81.17 percent) whereas the least difference is seen in Sundance Formation of Jurassic age (32.79 percent). This difference is due to the contribution of the internal friction angle. For comparison, we calculate the UCS using the equation shown in Figure 4.2 and compare the calculated value with the measured UCS.

$$\widehat{UCS} = \frac{2c\cos\varphi}{1-\sin\varphi}$$

**Figure 4.2: Equation. Uniaxial Compressive Strength (UCS).**

The calculated UCS is higher than the measured UCS in all sandstone formations except the Cloverly Formation (Sample ID 17) as shown in Table 4.5. The greatest difference between the

measured and calculated UCS values at about 25 percent is seen in Fort Union Formation (Sample ID 51) and the least difference at about 3 percent is observed in Lance Formation (Sample ID 23). Comparing cohesion with the calculated UCS, the greatest difference increased to about 85 percent in Wind River Formation and the lowest difference is seen in Lance Formation at about 57 percent.

| Sample ID | Period | Formation | Sandstone Type | Specimen ID | Depth (m) | Specimen Diameter (mm) | Specimen Height (mm) | Water content (%) | Specific Gravity | Porosity (%) | Grain Size (mm) |
|---|---|---|---|---|---|---|---|---|---|---|---|
| 16 | Cambrian | Flathead | Medium | 16a | 4.60 | 50.29 | 103.63 | 1.24 | - | 1.613 | ¼ to ½ |
| | | | | 16b | 4.76 | 50.29 | 103.63 | 1.24 | | 2.200 | |
| | | | | 16f | 5.61 | 50.29 | 104.65 | 1.86 | | 5.353 | |
| | | | | 16d | 5.85 | 50.29 | 105.41 | 2.36 | | 9.432 | |
| | | | | 16e | 6.04 | 50.29 | 105.66 | 1.24 | | 3.059 | |
| | | | | 16h | 7.13 | 50.29 | 104.14 | 1.24 | | 3.023 | |
| 17 | Cretaceous | Cloverly | Medium | 17a | 29.88 | 41.66 | 97.79 | 0.14 | 2.639 | 19.488 | ¼ to ½ |
| | | | | 17b | 30.03 | 41.66 | 98.30 | 0.14 | | 17.794 | |
| | | | | 17c | 30.18 | 41.66 | 97.54 | 0.14 | | 19.474 | |
| | | | | 17d | 30.34 | 41.66 | 93.98 | 0.14 | | 21.228 | |
| 18 | Jurassic | Sundance | Fine | 18a | 0.91 | 50.29 | 104.90 | 0.74 | 2.603 | 22.861 | ⅛ to ¼ |
| | | | | 18b | 3.35 | 50.29 | 103.38 | 0.74 | | 22.538 | |
| | | | | 18c | 3.66 | 50.29 | 103.63 | 0.74 | | 25.155 | |
| | | | | 18d | 4.27 | 50.29 | 100.84 | 0.74 | | 27.997 | |
| | | | | 18e | 4.57 | 50.04 | 102.11 | 0.74 | | 21.286 | |
| | | | | 18f | 5.49 | 50.55 | 104.39 | 0.74 | | 23.200 | |
| | | | | 18g | 6.40 | 50.29 | 105.16 | 0.74 | | 26.665 | |
| | | | | 18h | 6.49 | 50.29 | 104.14 | 0.74 | | 26.518 | |
| 19 | Cretaceous | Aspen/Bear River | Medium | 19a | 6.10 | 49.53 | 100.84 | 1.32 | - | 3.430 | ¼ to ½ |
| | | | | 19b | 6.40 | 49.28 | 99.06 | 1.72 | | 4.400 | |
| | | | | 19c | 6.55 | 49.78 | 100.33 | 1.46 | | 3.690 | |
| | | | | 19d | 6.19 | 49.02 | 102.11 | 1.36 | | 3.410 | |
| 20 | Cretaceous | Aspen/Bear River | Fine | 20a | 11.52 | 48.51 | 103.12 | 1.87 | 2.725 | 5.620 | ⅛ to ¼ |
| | | | | 20b | 11.65 | 48.77 | 106.68 | 1.85 | | 7.715 | |
| 23 | Cretaceous | Lance | Fine | 23a | Surface | 24.89 | 51.56 | 0.68 | 2.562 | 13.821 | ⅛ to ¼ |
| | | | | 23b | Surface | 24.64 | 48.26 | 0.72 | | 12.180 | |
| | | | | 23c | Surface | 24.64 | 52.07 | 0.75 | | 9.311 | |
| 26 | Eocene | Willwood | Fine | N/A | Surface | N/A | N/A | N/A | N/A | N/A | ⅛ to ¼ |
| 31 | Pennsylvanian | | Medium | 31a | Surface | 25.15 | 52.07 | 2.21 | - | 12.960 | ¼ to ½ |

**Figure 4.3: Summary of tested sandstone samples.**

| Sample ID | Period | Formation | Sandstone Type | Specimen ID | Depth (m) | Specimen Diameter (mm) | Specimen Height (mm) | Water content (%) | Specific Gravity | Porosity (%) | Grain Size (mm) |
|---|---|---|---|---|---|---|---|---|---|---|---|
| | | Tensleep Sandstone | | 31b | Surface | 25.15 | 52.07 | 2.21 | | 13.180 | |
| | | | | 31c | Surface | 25.15 | 52.07 | 2.21 | | 12.800 | |
| | | | | 31d | Surface | 24.89 | 53.09 | 2.21 | | 12.210 | |
| | | | | 31e | Surface | 24.89 | 52.07 | 2.21 | | 13.430 | |
| 32 | Lower Miocene | Arikaree | Medium | 32a | Surface | 24.64 | 52.07 | 5.12 | - | 11.650 | ¼ to ½ |
| | | | | 32b | Surface | 24.38 | 50.04 | 5.01 | | 10.940 | |
| | | | | 32c | Surface | 24.64 | 52.58 | 5.06 | | 13.980 | |
| 33 | Lower Miocene | Arikaree | Medium | 33a | Surface | 24.64 | 51.56 | 1.09 | - | 12.220 | ¼ to ½ |
| | | | | 33b | Surface | 24.13 | 51.31 | 1.12 | | 11.130 | |
| | | | | 33c | Surface | 24.38 | 50.04 | 1.15 | | 12.050 | |
| 39 | Paleogene | Hanna | Fine | 39a | 43.96 | 24.13 | 51.31 | 5.99 | 2.540 | 13.791 | ⅛ to ¼ |
| | | | | 39b | 44.15 | 24.13 | 49.53 | 5.95 | | 13.158 | |
| | | | | 39c | 44.60 | 24.38 | 50.80 | 5.87 | | 13.410 | |
| 41 | Paleogene | Hanna | Medium | 41a | 23.26 | 24.38 | 50.04 | 7.16 | 2.556 | 13.663 | ¼ to ½ |
| | | | | 41b | 23.32 | 24.64 | 52.58 | 6.86 | | 13.510 | |
| | | | | 41c | 24.09 | 24.64 | 51.56 | 6.58 | | 16.276 | |
| | | | | 41d | 25.06 | 24.38 | 50.80 | 6.56 | | 16.482 | |
| | | | | 41e | 26.22 | 24.38 | 50.80 | 5.96 | | 16.420 | |
| 43 | Eocene | Wind River | Medium | 43a | Surface | 24.89 | 51.05 | 8.21 | - | 14.490 | ¼ to ½ |
| | | | | 43b | Surface | 24.89 | 51.56 | 8.21 | | 13.550 | |
| 49 | Eocene | Bridger | Medium | 49a | Surface | 25.15 | 51.82 | 13.45 | - | 27.180 | ¼ to ½ |
| | | | | 49b | Surface | 25.15 | 51.82 | 13.29 | | 26.190 | |
| | | | | 49c | Surface | 25.15 | 52.07 | 12.10 | | 24.220 | |
| | | | | 49d | Surface | 25.15 | 50.80 | 13.13 | | 26.320 | |
| 50 | Paleocene | Fort Union | Medium | 50a | Surface | 24.38 | 49.53 | 2.44 | 2.562 | 13.821 | ¼ to ½ |
| | | | | 50b | Surface | 24.64 | 52.58 | 2.46 | | 12.180 | |
| 51 | Paleocene | Fort Union | Medium | 51a | Surface | 25.40 | 51.05 | 2.51 | - | 3.920 | ¼ to ½ |
| | | | | 51b | Surface | 25.65 | 51.56 | 1.23 | | 3.300 | |
| | | | | 51c | Surface | 25.65 | 51.56 | 1.50 | | 5.920 | |
| | | | | 51d | Surface | 25.40 | 51.31 | 2.28 | | 4.530 | |
| | | | | 51e | Surface | 25.40 | 51.05 | 2.22 | | 3.956 | |

**Figure 4.3 (Continued): Summary of tested sandstone samples.**

| Sample ID | Period | Formation | Sandstone Type | Specimen ID | Depth (m) | Specimen Diameter (mm) | Specimen Height (mm) | Water content (%) | Specific Gravity | Porosity (%) | Grain Size (mm) |
|---|---|---|---|---|---|---|---|---|---|---|---|
| 56 | Permian | Casper | Medium | 56a | Surface | 25.15 | 52.07 | 2.51 | - | 9.370 | ¼ to ½ |
| | | | | 56b | Surface | 25.15 | 53.34 | 2.55 | | 11.065 | |
| | | | | 56c | Surface | 25.15 | 52.07 | 2.48 | | 10.205 | |

Note: N/A–Unavailable test specimen.

**Figure 4.3 (Continued): Summary of tested sandstone samples.**

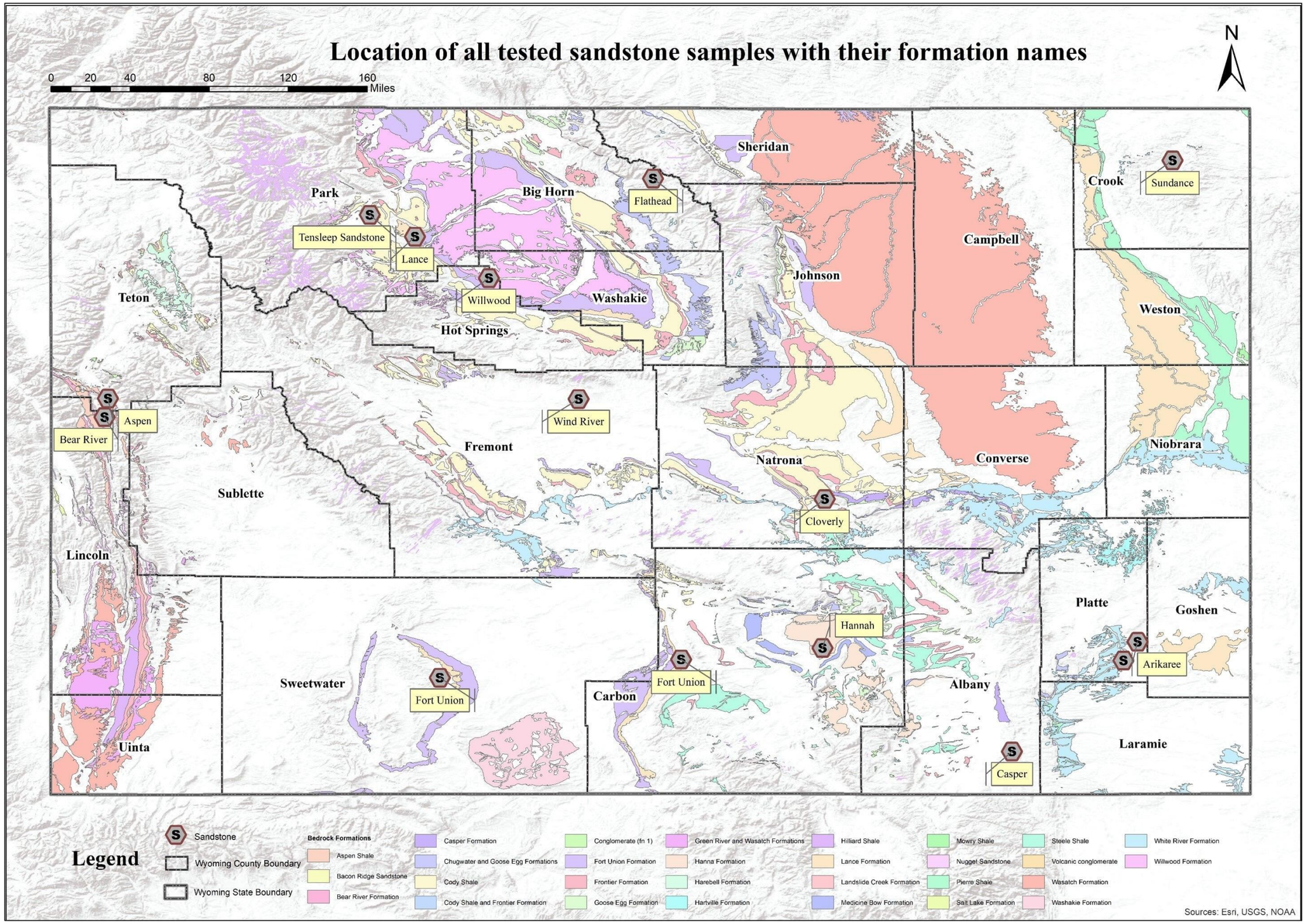


**Figure 4.4: Location of tested sandstone samples with their formation names (Esri ArcGIS 10.3).**

| Sample ID | Formation | S ID | $\sigma_c$ (MPa) | $\sigma_p$ (MPa) | $\beta$ (deg) | SR (%/min) | Failure Mode | Failure Behavior | Failure Angle (deg) |
|---|---|---|---|---|---|---|---|---|---|
| 16 | Flathead | 16a | 1.00 | 118.86 | 90 | 0.1 | TS | Brittle | 90 |
| | | 16b | 4.00 | 95.61 | 90 | 0.1 | TS | Brittle | 90 |
| | | 16d | 9.97 | 120.15 | 25 | 0.1 | MTS | Ductile | 90 |
| | | 16e | 0.00 | 20.32 | 45 | 0.1 | TS | Brittle | 90 |
| | | 16f | 8.00 | 35.90 | 30 | 0.1 | MTS | Ductile | 90 |
| | | 16h | 1.99 | 87.59 | 90 | 0.1 | TS | Brittle | 90 |
| 17 | Cloverly | 17a | 6.00 | 62.21 | 45 | 0.1 | TS | Brittle | 90 |
| | | 17b | 10.00 | 31.91 | 15 | 0.1 | TS | Brittle | 90 |
| | | 17c | 4.00 | 15.89 | 20 | 0.1 | TS | Brittle | 90 |
| | | 17d | 0.00 | 11.61 | 15 | 0.1 | S | Ductile | 60 |
| 18 | Sundance | 18d | 39.98 | 90.30 | N/A | 0.1 | S | Brittle | 60 |
| | | 18h | 0.00 | 13.88 | N/A | 0.1 | TS | Brittle | 90 |
| | | 18i | 2.00 | 21.66 | N/A | 0.1 | TS | Brittle | 60 |
| | | 18j | 5.99 | 25.77 | N/A | 0.1 | S | Brittle | 30 |
| | | 18k | 30.14 | 74.57 | N/A | 0.1 | S | Brittle | 60 |
| | | 18l | 20.01 | 55.67 | N/A | 0.1 | S | Brittle | 60 |
| 19 | Aspen/ Bear River | 19a | 10.00 | 98.84 | 90 | 0.1 | TS | Brittle | 90 |
| | | 19f | 0.00 | 22.60 | 30 | 0.1 | S | Brittle | 20 |
| | | 19g | 6.00 | 114.86 | 90 | 0.1 | S | Brittle | 90 |
| 20 | Aspen/ Bear River | 20a | 4.00 | 45.86 | 90 | 0.1 | S | Brittle | 30 |
| | | 20b | 10.05 | 99.56 | 90 | 0.1 | S | Brittle | 45 |
| 23 | Lance | 23a | 0.00 | 2.47 | N/A | 0.1 | S | Brittle | 80 |
| | | 23b | 2.00 | 5.08 | N/A | 0.1 | S | Brittle | 60 |
| | | 23c | 4.00 | 36.52 | N/A | 0.1 | S | Ductile | 50 |
| 26 | Willwood | N/A | N/A | N/A | N/A | N/A | N/A | N/A | N/A |
| 31 | Tensleep Sandstone | 31a | 1.00 | 70.26 | N/A | 0.05 | TS | Brittle | 90 |
| | | 31b | 0.00 | 55.91 | N/A | 0.05 | TS | Brittle | 90 |
| | | 31c | 4.00 | 59.90 | N/A | 0.05 | MTS | Brittle | 90 |
| | | 31e | 8.00 | 120.42 | N/A | 0.05 | S | Brittle | 65 |
| 32 | Arikaree | 32a | 4.00 | 45.88 | N/A | 0.1 | S | Ductile | 75 |

**Figure 4.5: Summary of test results of sandstones.**

| Sample ID | Formation | S ID | $\sigma_c$ (MPa) | $\sigma_p$ (MPa) | $\beta$ (deg) | SR (%/min) | Failure Mode | Failure Behavior | Failure Angle (deg) |
|---|---|---|---|---|---|---|---|---|---|
| | | 32b | 0.00 | 12.19 | N/A | 0.1 | TS | Brittle | 90 |
| | | 32c | 10.07 | 93.83 | N/A | 0.1 | S | Brittle | 60 |
| 33 | Arikaree | 33a | 4.00 | 46.50 | N/A | 0.1 | T | Ductile | 90 |
| | | 33b | 10.00 | 111.06 | N/A | 0.1 | TS | Ductile | 70 |
| | | 33c | 0.00 | 17.01 | N/A | 0.1 | S | Brittle | 60 |
| 39 | Hanna | 39a | 0.00 | 9.39 | N/A | 0.05 | TS | Brittle | 90 |
| | | 39b | 4.00 | 33.19 | N/A | 0.05 | S | Brittle | 20 |
| | | 39c | 10.00 | 70.74 | N/A | 0.05 | S | Ductile | 45 |
| 41 | Hanna | 41a | 0.00 | 9.65 | N/A | 0.1 | S | Brittle | 30 |
| | | 41b | 4.00 | 31.48 | N/A | 0.1 | MTS | Ductile | 90 |
| | | 41e | 6.00 | 42.97 | N/A | 0.1 | S | Ductile | 90 |
| 43 | Wind River | 43a | 4.00 | 70.46 | N/A | 0.05 | S | Ductile | 60 |
| | | 43b | 0.00 | 47.61 | N/A | 0.05 | TS | Brittle | 90 |
| | | 43c | 10.00 | 160.68 | N/A | 0.05 | S | Ductile | 60 |
| 49 | Bridger | 49a | 4.00 | 34.69 | N/A | 0.1 | S | Ductile | 60 |
| | | 49b | 0.00 | 13.92 | N/A | 0.1 | S | Brittle | 20 |
| | | 49c | 10.00 | 42.45 | N/A | 0.1 | S | Ductile | 20 |
| 50 | Fort Union | 50a | 0.00 | 6.00 | N/A | 0.1 | S | Ductile | 30 |
| | | 50b | 4.00 | 31.49 | N/A | 0.1 | S | Ductile | 60 |
| 51 | Fort Union | 51a | 0.00 | 26.09 | N/A | 0.1 | TS | Brittle | 90 |
| | | 51b | 8.00 | 147.03 | N/A | 0.1 | S | Ductile | 60 |
| | | 51c | 6.00 | 89.71 | N/A | 0.1 | TS | Ductile | 90 |
| 56 | Casper | 56a | 0.00 | 39.01 | N/A | 0.1 | TS | Brittle | 90 |
| | | 56b | 4.00 | 72.58 | N/A | 0.1 | S | Ductile | 60 |
| | | 56c | 10.00 | 132.26 | N/A | 0.1 | TS | Ductile | 90 |

Note: S ID– Specimen ID; $\sigma_c$ – Confining pressure (MPa); $\sigma_p$ –Peak stress (MPa); $\beta$– Bedding angle (deg); SR– Strain rate (%/min); S–Shear; TS–Tensile Splitting; MTS–Multiple Tensile Splitting.

**Figure 4.5 (Continued): Summary of test results of sandstones.**

**Table 4.5: Mohr-Coulomb results of tested sandstones.**

| Sample ID | Formation | Measured UCS, (MPa) | Calculated UCS, (MPa) | Cohesion, *c* (MPa) | Internal friction Angle, $\varphi$ (deg) |
|---|---|---|---|---|---|
| 16 | Flathead | N/A | 81.61 | 20.34 | 37 |
| 17 | Cloverly | 11.61 | 10.23 | 3.45 | 22 |
| 18 | Sundance | 9.03 | 16.70 | 6.07 | 18 |
| 19 | Aspen/Bear River | 22.60 | 28.77 | 5.38 | 49 |
| 20 | Aspen/Bear River | N/A | 84.48 | 5.52 | 49 |
| 23 | Lance | 2.47 | 2.54 | 1.10 | 8 |
| 26 | Willwood | N/A | N/A | N/A | N/A |
| 31 | Tensleep Sandstone | 55.91 | 68.27 | 13.10 | 48 |
| 32 | Arikaree | 12.19 | 15.58 | 2.76 | 51 |
| 33 | Arikaree | 17.01 | 19.10 | 3.10 | 54 |
| 39 | Hanna | 9.39 | 12.29 | 2.48 | 46 |
| 41 | Hanna | 9.65 | 11.05 | 2.34 | 44 |
| 43 | Wind River | 47.61 | 58.65 | 8.97 | 56 |
| 49 | Bridger | 13.92 | 15.22 | 4.48 | 29 |
| 50 | Fort Union | 6.00 | 7.00 | 1.38 | 47 |
| 51 | Fort Union | 26.09 | 35.00 | 5.52 | 55 |
| 56 | Casper | 39.01 | 47.41 | 7.93 | 53 |

Note: UCS– Unconfined compressive strength (MPa); N/A –Unavailable specimen for testing.

Comparing the measured with the calculated UCS (Figure 4.2), we observed that for the UCS less than 20 MPa, the data points were on or near the one-to-one line; whereas, for UCS greater than 20 MPa, the calculated UCS was higher than the measured ones as indicated by the points above the one-to-one line in Figure 4.6. This indicated that UCS is likely over predicted above 20 MPa.

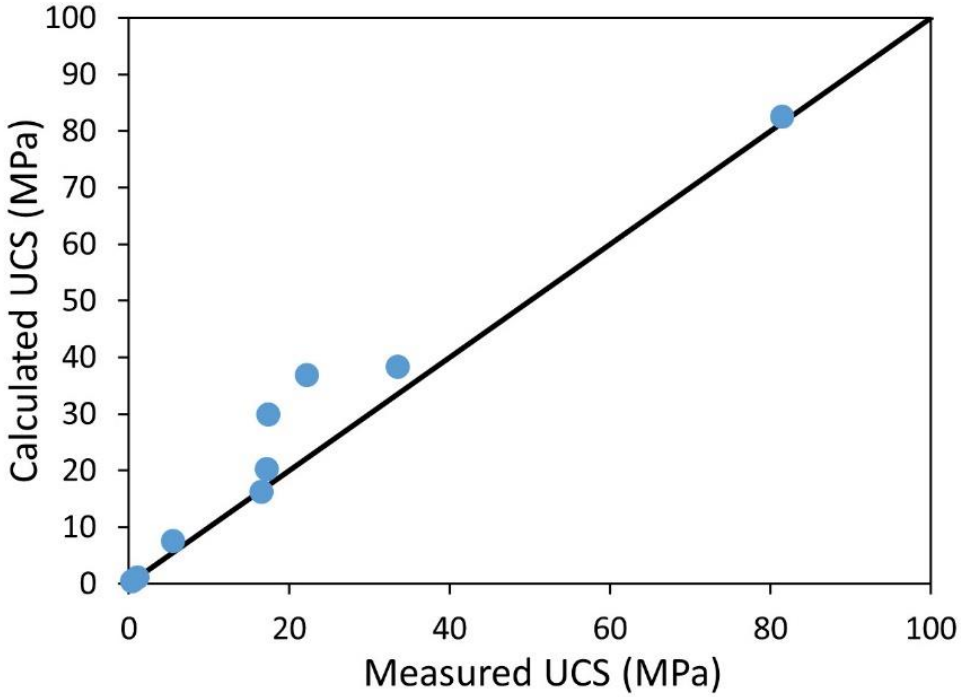


**Figure 4.6: Comparison of measured and calculated UCS values.**

### *4.2.3 HB Parameters*

The non-linear failure criterion proposed by Hoek and Brown (1997) was used to calculate the non-linear shear strength of the tested samples. The HB material constant for intact rock ($m_i$) was calculated using the statistical method proposed by Hoek and Brown (2019) based on test results on a principal axes plane. The HB criterion was applied on the intact rock taking the HB parameters $a = 0.5$ and $s = 1$, to estimate the cohesion and internal friction angle. Tensile strength ($\sigma_t$) of each rock sample was also back-calculated as discussed in Chapter 2. The HB criterion fitting to Mohr circles is presented in Appendices B (Khatri 2022).

The calculation of the material constant $m_i$ was conducted from a series of uniaxial and triaxial tests performed on intact rock specimens for each sample. In this process, the major and minor principal stresses of the tested specimens were plotted, and a curve HB line was fitted through the points by substituting $a = 0.5$, $s = 1$, and $m_b$= $m_i$ in the generalized HB criterion given by the equation in Figure 4.7 in terms of major and minor principal stresses ($\sigma_1$ and $\sigma_3$) and $\sigma_c$ is the UCS value. The only unknown in the equation is the $m_i$, which can be easily back calculated. The determination of $m_i$ from the back calculation method was found to provide results that are comparable to the values proposed by Hoek and Brown (1997) for sandstones, and hence was

preferred in the calculations of the cohesion and internal friction angle. The $\sigma_1$- $\sigma_3$ plots for the determination of $m_i$ values are presented in Appendices C (Khatri 2022).

$$\sigma_1 = \sigma_3 + \sigma_c \left( m_i \frac{\sigma_3}{\sigma_c} + 1 \right)^{0.5}$$

**Figure 4.7: Equation. The generalized HB criterion.**

At least one UCS and two triaxial tests are required for the determination of $m_i$ value. Samples with fewer than two triaxial tests were not reported.

Hoek & Brown (1997) and Marinos & Hoek (2000) recommended the range of $m_i$ values of sandstone as $17 \pm 4$. However, we observed that the calculated $m_i$ values range from 2.97 to 66.38, significantly varying from the proposed range. Hoek & Brown (1997) reported that the $m_i$ value can vary significantly with different rock $\beta$ angles as the failure could occur along a weakness plane. The difference in $m_i$ values could be attributed to the effect of bedding of the intact rock specimens while the tested intact rock specimens in this study did not show any apparent beddings.

Bandyopadhyay et al. (2013) reported that the indirect tensile strengths of weak and strong sandstones measured using the Brazilian method are 1 MPa and 1.40 MPa, respectively. They also reported that the UCS and tensile strength are directly proportional to each other. Table 4.6 shows that the tensile strengths of Arikaree, Fort Union, Aspen/bear River, and Hanna Formations were lower than 1 MPa and the rest of the formations were within the range reported by Bandyopadhyay et al. (2013). The experimental results except for Sundance and Cloverly Formations shown in Figure 4.8 confirmed the direct relationship between UCS and tensile strength.

**Table 4.6: HB results of tested sandstones.**

| Sample ID | Formation | $m_i$ (measured) | $c$ (MPa) | $\varphi$ (deg) | $\sigma_t$ (MPa) |
|---|---|---|---|---|---|
| 16 | Flathead | 6.34 | 22.81 | 35.00 | 12.86 |
| 17 | Cloverly | 2.97 | 3.52 | 16.00 | 3.44 |
| 18 | Sundance | 4.18 | 5.27 | 17.00 | 3.32 |
| 19 | Aspen/Bear River | 44.57 | 4.79 | 48.00 | 0.51 |
| 20 | Aspen/Bear River | 26.36 | 4.58 | 51.00 | 0.88 |
| 23 | Lance | - | - | - | - |
| 26 | Willwood | N/A | N/A | N/A | N/A |
| 31 | Tensleep Sandstone | 21.60 | 11.30 | 50.00 | 2.59 |
| 32 | Arikaree | 49.03 | 2.40 | 51.00 | 0.25 |
| 33 | Arikaree | 46.88 | 3.00 | 55.00 | 0.37 |

| Sample ID | Formation | $m_i$ (measured) | *c* (MPa) | $\varphi$ (deg) | $\sigma_t$ (MPa) |
|---|---|---|---|---|---|
| 39 | Hanna | 32.80 | 2.09 | 46.00 | 0.28 |
| 41 | Hanna | 20.03 | 2.54 | 39.00 | 0.48 |
| 43 | Wind River | 33.64 | 7.92 | 57.00 | 1.41 |
| 49 | Bridger | 7.76 | 4.41 | 28.00 | 1.79 |
| 50 | Fort Union | - | - | - | - |
| 51 | Fort Union | 66.38 | 4.48 | 56.00 | 0.39 |
| 56 | Casper | 30.56 | 7.48 | 52.00 | 1.28 |

Note: *c*–Cohesion; $\sigma_t$–Tensile strength; $\varphi$ – Internal friction angle; $m_i$–HB parameter; N/A–Unavailable specimen for testing; - –Not enough tests for calculation.

The cohesion (*c*) and internal friction angle ($\varphi$) obtained from the linear MC criterion and the non-linear HB criterion were comparable as illustrated in Figure 4.9 and 4.10, respectively. Figure 4.9 showed that most of the cohesion values fell along the one-to-one line while few cohesion values from HB criterion were higher than that from MC criterion. A similar agreement was observed between the internal friction angles from both criteria while several internal friction angles from HB criterion were higher than that from MC criterion.

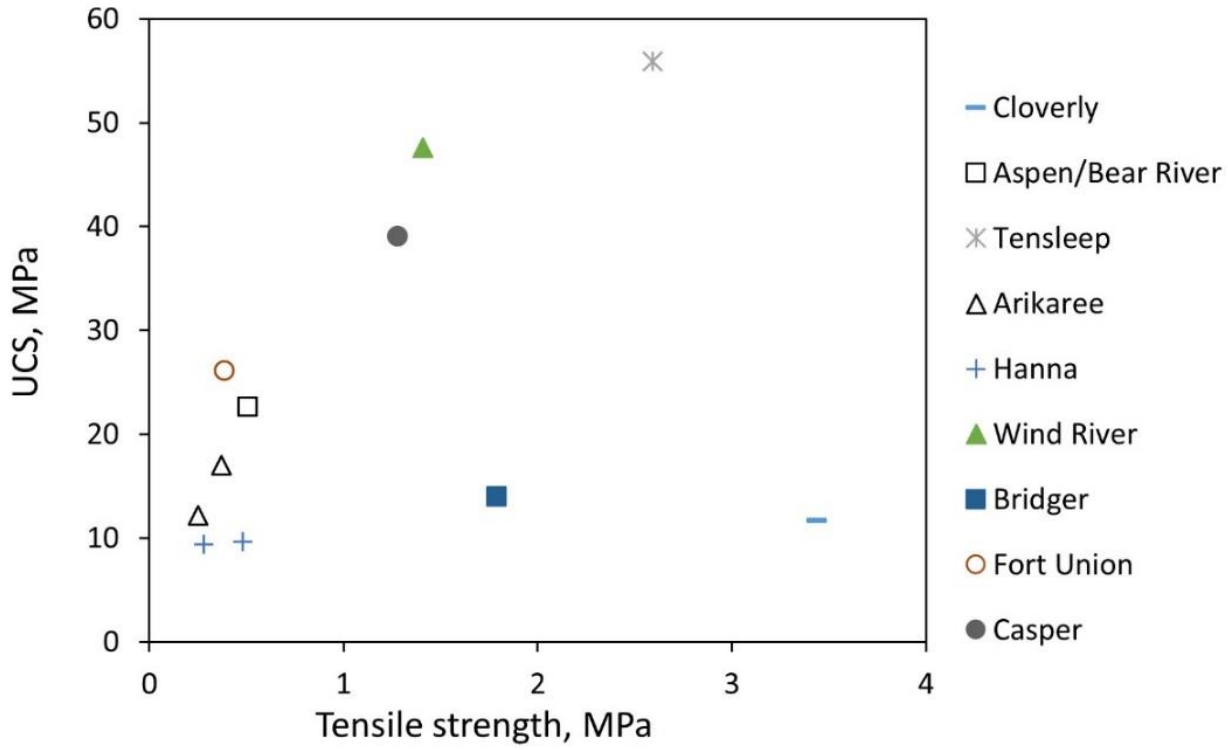


**Figure 4.8: Comparison of UCS values from measured and MC Criteria for all sandstones.**

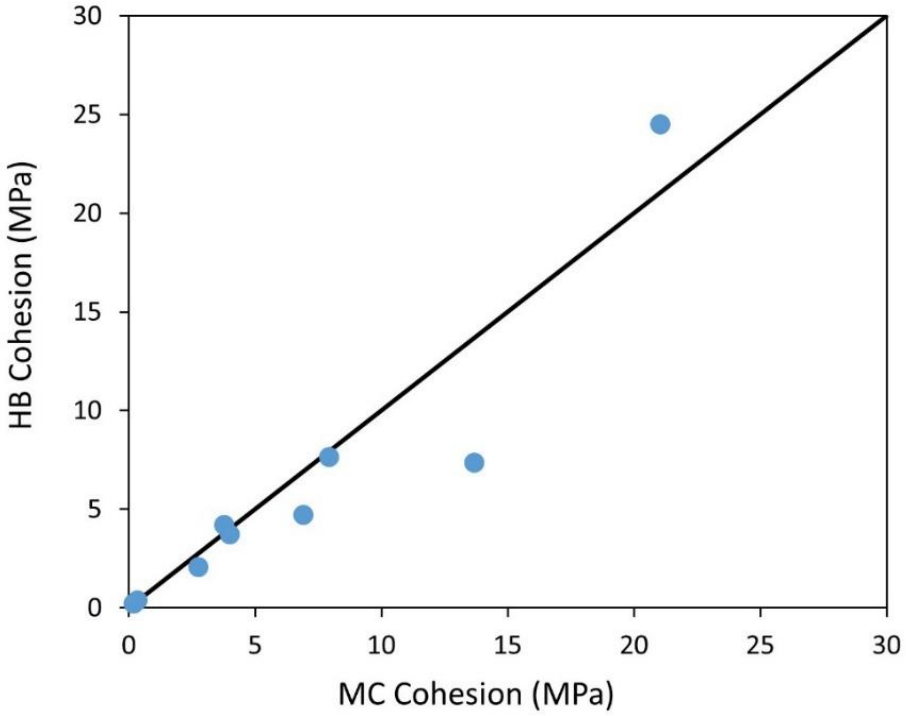


**Figure 4.9: Comparison of Cohesion values from HB and MC Criteria for all sandstones.**

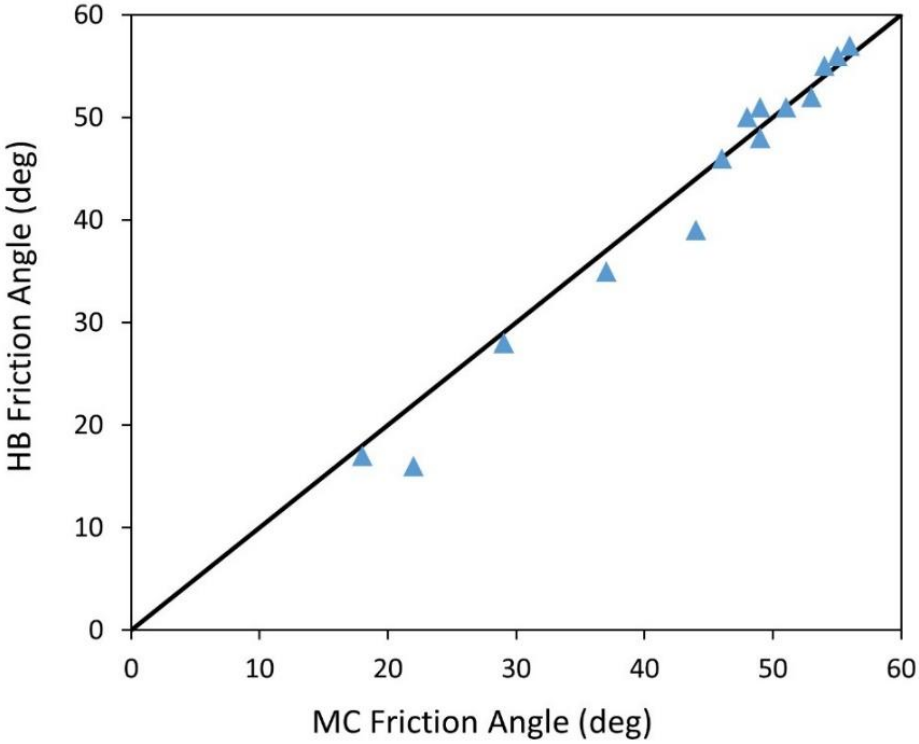


**Figure 4.10: Comparison of internal friction Angle values from HB and MC Criteria for all sandstones.**

### *4.2.4 Elastic Properties*

Figure 4.11 summarizes the calculated Young's modulus ($E$) and Poisson's ratio ($\nu$) of the sandstone samples. The $E$ value of the tested sandstones varied from 2.34 GPa for Fort Union Formation to 137.39 GPa for Flathead Formation of the Cambrian, the oldest geological period of the sandstone samples. About 50 percent of sandstone samples had Young's modulus values that fell within the typical $E$ values between 11.03 GPa and 39.99 GPa (Xu Hao et al. 2016). Similarly, the $\nu$ value of the rocks under compression ranged between 0.03 for Fort Union Formation Sample 51 to 0.42 for Clovery Formation.

| Sample ID | Formation | S ID | $E$ (GPa) | $\nu$ | Avg $E$ (GPa) | Avg $\nu$ |
|---|---|---|---|---|---|---|
| 16 | Flathead | 16a | 65.86 | 0.09 | 50.76 | 0.21 |
| | | 16b | 61.32 | 0.22 | | |
| | | 16d | 41.02 | 0.26 | | |
| | | 16f | 67.51 | 0.22 | | |
| | | 16h | 18.05 | 0.26 | | |
| 17 | Cloverly | 17a | 5.74 | 0.17 | 17.79 | 0.42 |
| | | 17b | 36.57 | 0.50 | | |
| | | 17c | 27.33 | 0.50 | | |
| | | 17d | 1.51 | 0.50 | | |
| 18 | Sundance | 18a | 4.75 | 0.16 | 16.45 | 0.40 |
| | | 18c | 7.24 | 0.50 | | |
| | | 18d | 24.08 | 0.50 | | |
| | | 18e | 6.03 | 0.50 | | |
| | | 18f | 2.72 | 0.31 | | |
| | | 18k | 7.19 | 0.25 | | |
| | | 18i | 55.50 | 0.50 | | |
| | | 18h | 24.08 | 0.50 | | |
| 19 | Aspen/ Bear River | 19a | 34.31 | 0.36 | 137.39 | 0.25 |
| | | 19b | 88.10 | 0.50 | | |
| | | 19c | 23.51 | 0.04 | | |
| | | 19d | 403.60 | 0.09 | | |
| 20 | Aspen/ Bear River | 20a | 53.51 | 0.50 | 27.46 | 0.30 |
| | | 20b | 1.40 | 0.09 | | |
| 23 | Lance | 23a | 3.06 | 0.19 | 3.14 | 0.20 |
| | | 23b | 1.72 | 0.21 | | |
| | | 23c | 4.63 | 0.19 | | |
| 26 | Willwood | N/A | N/A | N/A | N/A | N/A |
| 31 | Tensleep Sandstone | 31a | 18.67 | 0.20 | 14.30 | 0.15 |
| | | 31b | 17.25 | 0.08 | | |
| | | 31c | 12.79 | 0.04 | | |
| | | 31d | 8.47 | 0.27 | | |
| | | 31e | N/A | N/A | | |
| 32 | Arikaree | 32a | 33.99 | 0.31 | 19.19 | 0.21 |

**Figure 4.11: Mohr-Coulomb results of tested sandstones.**

| Sample ID | Formation | S ID | $E$ (GPa) | $\nu$ | Avg $E$ (GPa) | Avg $\nu$ |
|---|---|---|---|---|---|---|
| | | 32b | 4.39 | 0.11 | | |
| | | 32c | N/A | N/A | | |
| 33 | Arikaree | 33a | 8.95 | 0.37 | 4.58 | 0.33 |
| | | 33b | 0.33 | 0.37 | | |
| | | 33c | 4.44 | 0.26 | | |
| 39 | Hanna | 39a | 2.20 | 0.10 | 3.72 | 0.13 |
| | | 39b | 3.13 | 0.16 | | |
| | | 39c | 5.81 | 0.14 | | |
| 41 | Hanna | 41a | 1.90 | 0.30 | 3.39 | 0.39 |
| | | 41b | 4.08 | 0.40 | | |
| | | 41c | 4.17 | 0.48 | | |
| | | 41d | N/A | N/A | | |
| | | 41e | N/A | N/A | | |
| 43 | Wind River | 43a | 17.90 | 0.03 | 12.77 | 0.27 |
| | | 43b | 7.64 | 0.50 | | |
| 49 | Bridger | 49a | 29.59 | 0.09 | 11.23 | 0.19 |
| | | 49b | 6.83 | 0.40 | | |
| | | 49c | 4.40 | 0.07 | | |
| | | 49d | 4.10 | 0.19 | | |
| 50 | Fort Union | 50a | 1.15 | 0.13 | 2.34 | 0.19 |
| | | 50b | 3.52 | 0.25 | | |
| 51 | Fort Union | 51a | 5.03 | 0.06 | 4.67 | 0.03 |
| | | 51b | 2.74 | 0.02 | | |
| | | 51c | 7.69 | 0.01 | | |
| | | 51e | 4.05 | 0.01 | | |
| | | 51f | 3.83 | 0.07 | | |
| 56 | Casper | 56a | 9.54 | 0.12 | 13.64 | 0.09 |
| | | 56b | 14.37 | 0.05 | | |
| | | 56c | 16.99 | 0.09 | | |

Note: S ID– Specimen ID; $E$– Young's modulus (GPa); $\nu$– Poisson's ratio; Avg –Average.

**Figure 4.11 (Continued): Mohr-Coulomb results of tested sandstones.**

## 4.3 Siltstones

Among the 13 siltstone samples tested, three samples were obtained as surface boulders, and ten samples were obtained as rock cores drilled out from various projects around the state. The prepared test specimens were either 25mm in diameter or 50mm in diameter. The length to diameter ratio (L/D) of the test specimens was maintained between 2 to 2.5. The top and bottom of the test specimen should be parallel to each other and perpendicular to the longitudinal axis. The finished top and bottom surfaces should not exceed the tolerance of 0.001 (ASTM D4543 2008). The description of the tested samples is shown in Figure 4.12 and their location map is shown in Figure 4.13.

The water content of the tested siltstones ranged from 0.57 percent to 22.25 percent. A decreasing trend of rock strength with the increase in water content was observed by other researchers (Yang et al. 2011, Zhang et al. 2011, Al-Bazali 2013, and Yang Qi. 2016). These researchers reported that the effect of particle size on the cohesion and compressive strength values of the siltstones was not apparent.

### *4.3.1 Individual Test Results*

A series of uniaxial and triaxial compressive strength, porosity, and specific gravity tests were conducted on these samples, and the results in terms of Mohr-Coulomb failure parameters, HB failure parameters, and elastic properties are discussed in the following subsections. Figure 4.14 summarizes the test results of the siltstone samples. The confinement, peak stress, $\beta$, strain rate while loading, failure mode, failure behavior, and failure angle of each tested specimen were summarized. The Specimen ID nomenclature is not in alphabetical order as not all test specimens prepared were used for testing. $\epsilon_a$, $\epsilon_r$, and $\epsilon_v$ in the figure legends represent the axial, radial, and volumetric strains, respectively. The failure behaviors were categorized as ductile, transitional, and brittle.

| Sample ID | Age | Formation | Specimen ID | Depth (m) | Specimen Diameter (mm) | Specimen Height (mm) | Water Content (%) | Specific Gravity | Porosity (%) |
|---|---|---|---|---|---|---|---|---|---|
| 5 | Permian | Goose Egg | 5a | 3.56 | 50.29 | 101.09 | 0.57 | 2.67 | 21.660 |
| | | | 5b | 3.69 | 50.29 | 104.90 | 0.57 | | 20.600 |
| 6 | Jurassic | Sundance | 6a | 7.92 | 46.73 | 105.15 | 5.32 | 2.62 | 24.086 |
| | | | 6b | 8.04 | 46.99 | 105.66 | 5.32 | | 25.491 |
| | | | 6c | 9.45 | 49.53 | 99.06 | 5.32 | | 28.486 |
| | | | 6d | 9.57 | 50.54 | 103.37 | 5.32 | | 26.202 |
| 7 | Cretaceous | Aspen / Bear River | N/A | N/A | N/A | N/A | N/A | N/A | N/A |
| 8 | Eocene | Pass Peak | N/A | N/A | N/A | N/A | N/A | N/A | N/A |
| 11 | Eocene | Wasatch | 11a | 17.68 | 51.56 | 107.44 | 22.25 | 2.69 | 36.158 |
| | | | 11b | 17.80 | 51.56 | 106.17 | 22.25 | | 35.572 |
| | | | 11c | 17.95 | 51.81 | 105.91 | 22.25 | | 35.944 |
| | | | 11d | 18.10 | 51.30 | 107.69 | 22.25 | | 31.340 |
| | | | 11e | 18.41 | 51.81 | 107.69 | 22.25 | | 31.811 |
| | | | 11f | 18.87 | 51.81 | 104.64 | 22.25 | | 31.786 |
| | | | 11g | 18.71 | 52.07 | 106.68 | 22.25 | | 32.487 |
| | | | 11h | 19.05 | 51.81 | 105.64 | 22.25 | | 31.619 |
| | | | 11i | 19.23 | 52.07 | 104.39 | 22.25 | | 31.813 |
| 12 | Paleogene | White River | 12a | 21.67 | 46.73 | 108.71 | N/A | N/A | N/A |
| | | | 12b | 22.46 | 45.46 | 107.18 | N/A | | N/A |
| | | | 12c | 23.04 | 45.21 | 107.95 | N/A | | N/A |
| 13 | Cretaceous | Aspen/Bear River | 13a | 10.42 | 50.54 | 104.90 | 1.48 | N/A | 2.943 |
| | | | 13b | 10.57 | 50.54 | 104.90 | 1.48 | | 5.729 |
| | | | 13c | 10.76 | 50.54 | 104.90 | 1.48 | | 2.227 |
| | | | 13d | 10.91 | 50.54 | 104.64 | 1.48 | | 2.096 |
| 24 | Cretaceous | Lance | 24a | Surface | 25.40 | 53.59 | 1.30 | N/A | 3.430 |
| | | | 24b | Surface | 25.14 | 53.34 | 1.69 | | 4.400 |
| | | | 24c | Surface | 24.89 | 53.34 | 1.34 | | 3.690 |
| 30 | Cretaceous | Bear River | 30a | 11.61 | 25.14 | 52.57 | 1.32 | N/A | 1.490 |
| | | | 30b | 11.76 | 24.89 | 50.54 | 1.10 | | 1.820 |

**Figure 4.12: Summary of tested siltstone samples.**

| Sample ID | Age | Formation | Specimen ID | Depth (m) | Specimen Diameter (mm) | Specimen Height (mm) | Water Content (%) | Specific Gravity | Porosity (%) |
|---|---|---|---|---|---|---|---|---|---|
| | | | 30b | 11.76 | 24.89 | 50.54 | 1.10 | | 1.820 |
| | | | 30c | 12.01 | 24.89 | 51.30 | 1.23 | | 1.740 |
| 34 | Lower Miocene | Arikaree | 34a | Surface | 24.63 | 52.07 | 1.95 | N/A | 12.960 |
| | | | 34b | Surface | 24.38 | 52.32 | 3.01 | | 13.180 |
| | | | 34c | Surface | 24.63 | 51.81 | 3.00 | | 12.800 |
| 35 | Paleogene | Hanna | 35a | 57.07 | 24.89 | 52.07 | 1.53 | N/A | 4.250 |
| | | | 35b | 57.25 | 24.63 | 51.05 | 1.55 | | 4.540 |
| | | | 35c | 57.38 | 24.63 | 51.56 | 1.73 | | 4.380 |
| | | | 35d | 57.53 | 24.38 | 50.80 | 1.75 | | 4.050 |
| | | | 35e | 57.71 | 24.89 | 49.78 | 1.68 | | 4.020 |
| 36 | Triassic | Chugwater | 36a | Surface | 24.63 | 49.78 | 0.67 | N/A | 7.810 |
| | | | 36b | Surface | 24.63 | 51.30 | 0.58 | | 6.700 |
| | | | 36c | Surface | 24.63 | 51.81 | 0.62 | | 6.970 |
| 37 | Miocene | Ogallala | 37a | 25.06 | 47.75 | 97.79 | 21.29 | N/A | 43.480 |
| | | | 37b | 25.24 | 48.26 | 97.79 | 21.29 | | 42.660 |
| | | | 37c | 25.67 | 47.49 | 97.02 | 21.29 | | 42.630 |

Note: N/A –Unavailable specimen for testing

**Figure 4.12 (Continued): Summary of tested siltstone samples.**

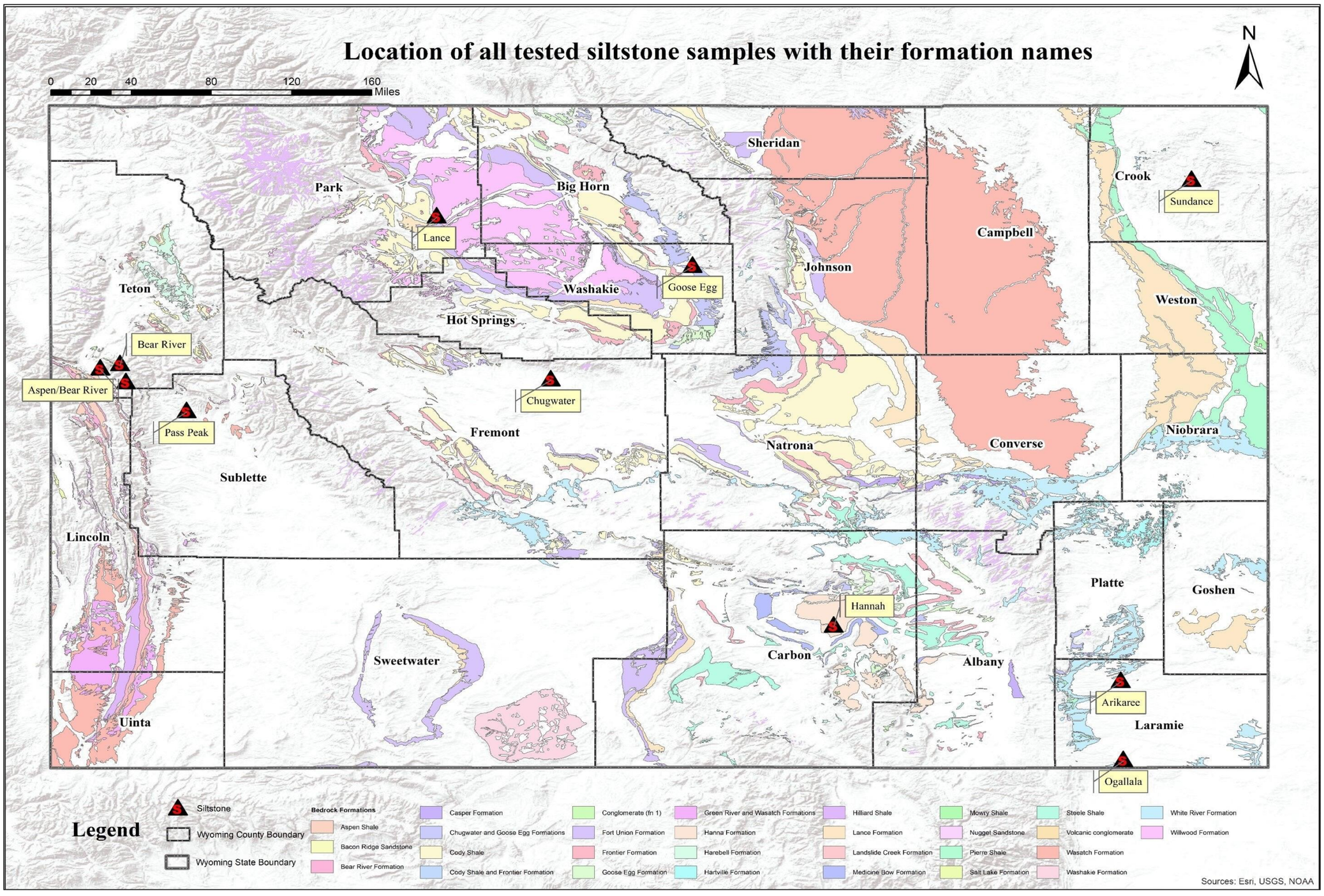


**Figure 4.13: Location of tested siltstone samples with their formation names (Esri ArcGIS 10.3).**

### *4.3.2 Mohr-Coulomb Parameters*

The UCS ranged from 0.43 MPa to 122.28 MPa, the cohesion (*c*) ranged from 0.2 MPa to 27.58 MPa, and the internal friction angle ranged from 5 to 49 degrees. The lowest UCS of 0.43 MPa and cohesion of 0.2 MPa were observed for the Eocene Wasatch Formation, and the lowest internal friction angle of 5 degrees was observed for the Permian Goose Egg Formation. Figure 4.15 shows the variation of UCS for all siltstone samples. The largest difference of 94.69 MPa between UCS and cohesion was observed in the Cretaceous Aspen/Bear River Formation whereas the least difference of 0.23 MPa was seen in the Eocene Wasatch Formation. This difference was due to the contribution of the internal friction angle. Hence, UCS is calculated using the equation shown in Figure 4.2 and compared to the measured UCS in Figure 4.15.

The calculated values were higher than the measured UCS for all siltstone formations except for the Chugwater Formation (Sample ID 36). The largest difference between the measured and calculated UCS value at about 12.49 MPa was seen for the Goose Egg Formation (Sample ID 5) and the smallest difference at about 0.006 MPa was observed for the White River Formation (Sample ID 12). Comparing the cohesion with the calculated UCS, the largest difference increases to about 30 MPa in the Lance Formation and the smallest difference seen was in the Goose Egg Formation of 16.18 MPa.

All the formations with larger internal friction angles had higher cohesion values (Table 4.7). Forbes (2011) reported that the typical range of internal friction angles for dry siltstones is 31 to 33 degrees. The tested siltstones in this study had internal friction angles ranging from 5 to 49 degrees, which significantly vary from the ones reported in the literature.

Comparing the measured with the calculated UCS, the UCS less than 17 MPa and above 68 MPa agreed well following the one-to-one line. For UCS values between 17 and 68 MPa, the calculated UCS was higher than the measured UCS as shown in Figure 4.15.

| Sample ID | Formation | S ID | $\sigma_c$ (MPa) | $\sigma_p$ (MPa) | $\beta$ (deg) | SR (%/min) | Failure Mode | Failure Behavior | Failure Angle (deg) |
|---|---|---|---|---|---|---|---|---|---|
| 5 | Goose Egg | 5a | 0.99 | 31.12 | 90 | 0.20 | TS | Brittle | 75 |
| | | 5b | 9.99 | 41.74 | 90 | 0.20 | TS | Brittle | 70 |
| 6 | Sundance | 6a | 0.99 | 9.22 | 90 | 0.20 | TS | Brittle | 80 |
| | | 6b | 10.00 | 19.50 | 90 | 0.10 | TS | Brittle | 60 |
| | | 6c | 4.00 | 17.17 | 90 | 0.10 | TS | Brittle | 60 |
| | | 6d | 10.00 | 23.23 | 90 | 0.10 | TS | Brittle | 70 |
| 7 | Aspen/ Bear River | N/A | N/A | N/A | N/A | N/A | N/A | N/A | N/A |
| 8 | Pass Peak | N/A | N/A | N/A | N/A | N/A | N/A | N/A | N/A |
| 11 | Wasatch | 11a | 0.00 | 0.43 | N/A | 0.10 | S | Ductile | 30 |
| | | 11b | 0.29 | 0.82 | N/A | 0.10 | S | Ductile | 30 |
| | | 11c | 0.00 | 0.26 | N/A | 0.10 | S | Ductile | 30 |
| | | 11d | 0.54 | 1.23 | N/A | 0.10 | S | Ductile | 45 |
| | | 11e | 0.00 | 0.72 | N/A | 0.10 | S | Ductile | 30 |
| | | 11f | 2.21 | 3.05 | N/A | 0.10 | S | Ductile | 60 |
| | | 11g | 1.10 | 1.60 | N/A | 0.10 | S | Ductile | 45 |
| | | 11h | 9.97 | 11.12 | N/A | 0.10 | S | Ductile | 45 |
| | | 11i | 1.10 | 1.91 | N/A | 0.10 | S | Ductile | 60 |
| 12 | White River | 12a | 0.72 | 2.68 | N/A | 0.10 | N/A | Ductile | N/A |
| | | 12b | 0.14 | 1.36 | N/A | 0.10 | N/A | Ductile | N/A |
| | | 12c | 0.28 | 1.68 | N/A | 0.10 | N/A | Ductile | N/A |
| 13 | Aspen/Bear River | 13a | 10.00 | 136.97 | 45 | 0.20 | TS | Brittle | 90 |
| | | 13b | 3.99 | 163.28 | 15 | 0.20 | S | TN | 45 |
| | | 13c | 19.99 | 221.78 | 90 | 0.20 | TS | TN | 90 |
| | | 13d | 0.99 | 122.86 | 90 | 0.20 | TS | Brittle | 90 |
| 24 | Lance | 24a | 0.00 | 22.21 | N/A | 0.10 | TS | Brittle | 90 |
| | | 24b | 4.00 | 76.25 | N/A | 0.10 | S | TN | 45 |
| | | 24c | 10.00 | 105.72 | N/A | 0.10 | S | Ductile | 45 |
| 30 | Bear River | 30a | 1.00 | 80.79 | N/A | 0.05 | TS | Brittle | 90 |
| | | 30b | 4.00 | 95.29 | N/A | 0.05 | TS | Brittle | 90 |
| | | 30c | 0.00 | 81.46 | N/A | 0.05 | TS | Brittle | 90 |

**Figure 4.14: Summary of test results of siltstone.**

| | | | | | | | | | |
|---|---|---|---|---|---|---|---|---|---|
| 34 | Arikaree | 34a | 4.00 | 44.86 | N/A | 0.10 | S | Ductile | 45 |
| | | 34b | 10.00 | 82.49 | N/A | 0.10 | S | Ductile | 45 |
| | | 34c | 0.00 | 17.14 | N/A | 0.10 | TS | Brittle | 90 |
| 35 | Hanna | 35a | 0.00 | 7.73 | N/A | 0.10 | S | Brittle | 45 |
| | | 35b | 4.08 | 57.25 | N/A | 0.01 | S | Brittle | 60 |
| | | 35c | 0.00 | 33.53 | N/A | 0.01 | TS | Brittle | 90 |
| | | 35d | 10.00 | 93.19 | N/A | 0.05 | MTS | Ductile | 90 |
| | | 35e | 4.00 | 28.36 | N/A | 0.10 | MTS | Ductile | 45 |
| 36 | Chugwater | 36a | 0.00 | 16.52 | N/A | 0.10 | TS | Brittle | 90 |
| | | 36b | 10.00 | 61.88 | N/A | 0.10 | TS | TN | 90 |
| | | 36c | 4.00 | 35.36 | N/A | 0.10 | TS | TN | 90 |
| 37 | Ogallala | 37a | 0.41 | 0.50 | N/A | 0.10 | S | Ductile | N/A |
| | | 37b | 0.28 | 0.37 | N/A | 0.10 | S | Ductile | N/A |
| | | 37c | 0.45 | 0.59 | N/A | 0.10 | S | Ductile | N/A |

Note: S ID– Specimen ID; $\sigma_c$ – Confining pressure (MPa); $\sigma_p$ – Peak stress (MPa); $\beta$– Bedding angle (deg); SR– Strain rate (%/min); S–Shear; TS–Tensile Splitting; MTS–Multiple Tensile Splitting; TN– Transitional; N/A– Test data not available.

**Figure 4.14 (Continued): Summary of test results of siltstone.**

**Table 4.7: Mohr-Coulomb results of tested siltstones.**

| Sample ID | Formation | Measured UCS (MPa) | Calculated UCS (MPa) | Cohesion, *c* (MPa) | Internal Friction Angle, $\varphi$ (deg) |
|---|---|---|---|---|---|
| 5 | Goose Egg | 17.38 | 29.88 | 13.69 | 5 |
| 6 | Sundance | 5.52 | 7.46 | 2.76 | 17 |
| 7 | Aspen/Bear River | N/A | N/A | N/A | N/A |
| 8 | Pass Peak | N/A | N/A | N/A | N/A |
| 11 | Wasatch | 0.43 | 0.46 | 0.20 | 8 |
| 12 | White River | 1.06 | 1.06 | 0.35 | 23 |
| 13 | Aspen/Bear River | 122.28 | 126.89 | 27.59 | 43 |
| 24 | Lance | 22.21 | 36.89 | 6.90 | 49 |
| 30 | Bear River | 81.46 | 82.57 | 21.03 | 36 |
| 34 | Arikaree | 17.14 | 20.31 | 4.00 | 47 |
| 35 | Hanna | 33.53 | 38.30 | 7.93 | 45 |
| 36 | Chugwater | 16.53 | 16.27 | 3.79 | 40 |
| 37 | Ogallala | N/A | N/A | N/A | N/A |

Note: UCS –Unconfined compressive strength (MPa); N/A – Unavailable specimen for testing.

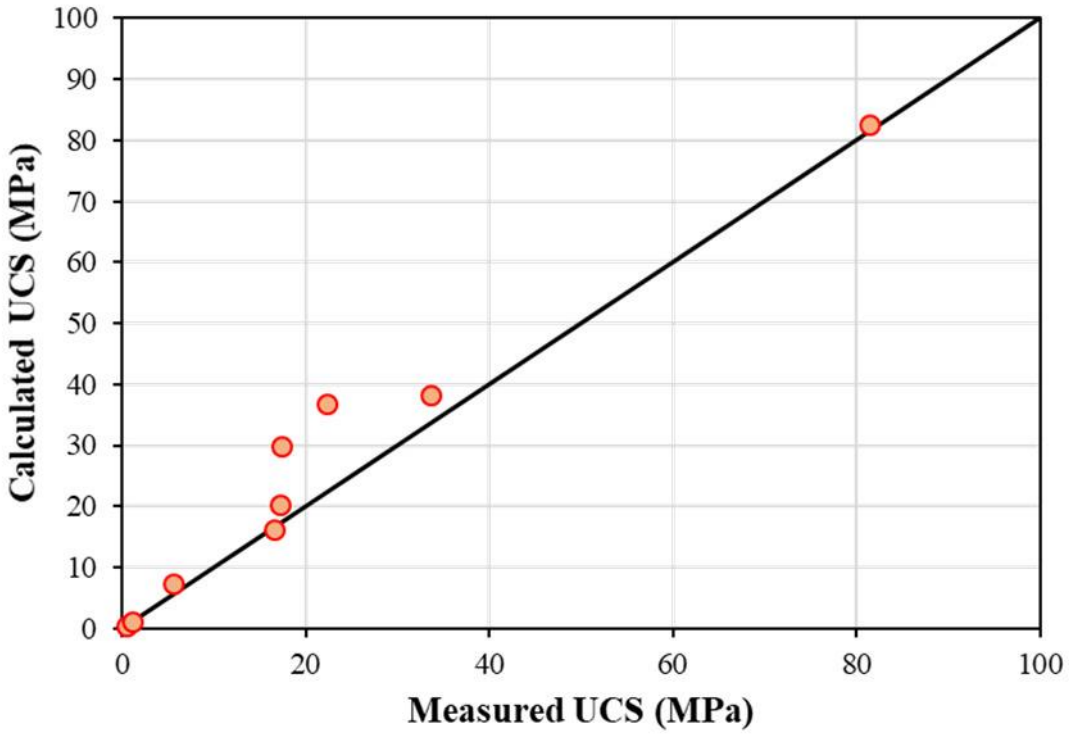


**Figure 4.15: Comparison of measured and calculated UCS values of siltstones.**

### *4.3.3* HB *Parameters*

The non-linear failure criterion proposed by Hoek and Brown (1997) was used to calculate the non-linear shear strength of the tested samples. The HB material constant for intact rock ($m_i$) was calculated using the statistical method proposed by Hoek and Brown (2019) based on test results on a principal stress plane. The HB criterion was applied by taking the HB parameters $a = 0.5$ and $s = 1$, to estimate the cohesion and internal friction angle. The calculated $m_i$ values in were comparable to the values proposed by Hoek and Brown (1997) for siltstones as 7$\pm$ 2 and hence were used in the calculation of the cohesions and internal friction angles.

The major and minor principal stresses of the tested specimens were plotted, and HB curve line was fitted through the points by substituting$a = 0.5$, $s = 1$, and $m_b$= $m_i$ in the generalized HB equation given by the equation in Figure 4.7. The only unknown in the equation is the value of $m_i$, which can be back calculated. At least one UC and two triaxial tests were required for the determination of $m_i$ value. Samples with fewer than two triaxial tests were not reported.

**Table 4.8: HB results of tested siltstones.**

| Sample ID | Formation | $m_i$ | *c* (MPa) | $\varphi$ (deg) | $\sigma_t$ (MPa) |
|---|---|---|---|---|---|
| 5 | Goose Egg | 4.73 | 7.37 | 11.00 | 3.68 |
| 6 | Sundance | 3.55 | 2.06 | 18.00 | 1.55 |
| 7 | Aspen/Bear River | N/A | N/A | N/A | N/A |
| 8 | Pass Peak | N/A | N/A | N/A | N/A |
| 11 | Wasatch | 0.73 | 0.20 | 2.00 | 0.58 |
| 12 | White River | 2.86 | 0.37 | 21.00 | 0.37 |
| 13 | Aspen/Bear River | 8.39 | 32.26 | 38.00 | 14.56 |
| 24 | Lance | 42.67 | 4.71 | 48.00 | 0.52 |
| 30 | Bear River | 4.61 | 24.50 | 31.00 | 17.67 |
| 34 | Arikaree | 26.42 | 3.72 | 47.00 | 0.65 |
| 35 | Hanna | 16.04 | 7.63 | 45.00 | 2.09 |
| 36 | Chugwater | 12.47 | 4.19 | 39.00 | 1.32 |
| 37 | Ogallala | N/A | N/A | N/A | N/A |

Note: *c*–Cohesion; $\sigma_t$–Tensile strength; $\varphi$ – Internal friction angle; $m_i$–HB parameter; N/A–Unavailable specimen for testing.

The $m_i$ values of siltstone samples are summarized in Table 4.8 along with the cohesion (*c*), internal friction angle ($\varphi$), and tensile strength ($\sigma_t$). Hoek & Brown (1997) and Marinos & Hoek 2001 recommend the range of $m_i$ values of siltstone as 7 $\pm$ 2, which were determined based on rock specimens tested normal to bedding. However, the calculated $m_i$ values ranged from 0.73 to 42.67, which were significantly different from the recommended range. Hoek & Brown (1997)

reported that the $m_i$ value can change significantly due to the rock bedding plane as failure could occur along a weakness plane, the compressive and shear strength are directly affected by the bedding plane. However, the intact rock specimens tested in the study did not have any apparent bedding.

The cohesion ($c$) and internal friction angle ($\varphi$) obtained from the linear MC criterion and non-linear HB criterion were comparable as illustrated in Figure 4.16 and 4.17, respectively. Figure 4.16 shows that most of the cohesion values fell on the one-to-one line while a few cohesion values from HB criterion were higher than those from MC criterion. A similar agreement was observed between internal friction angles from both criteria while several internal friction angles from HB criterion were higher than those from MC criterion.

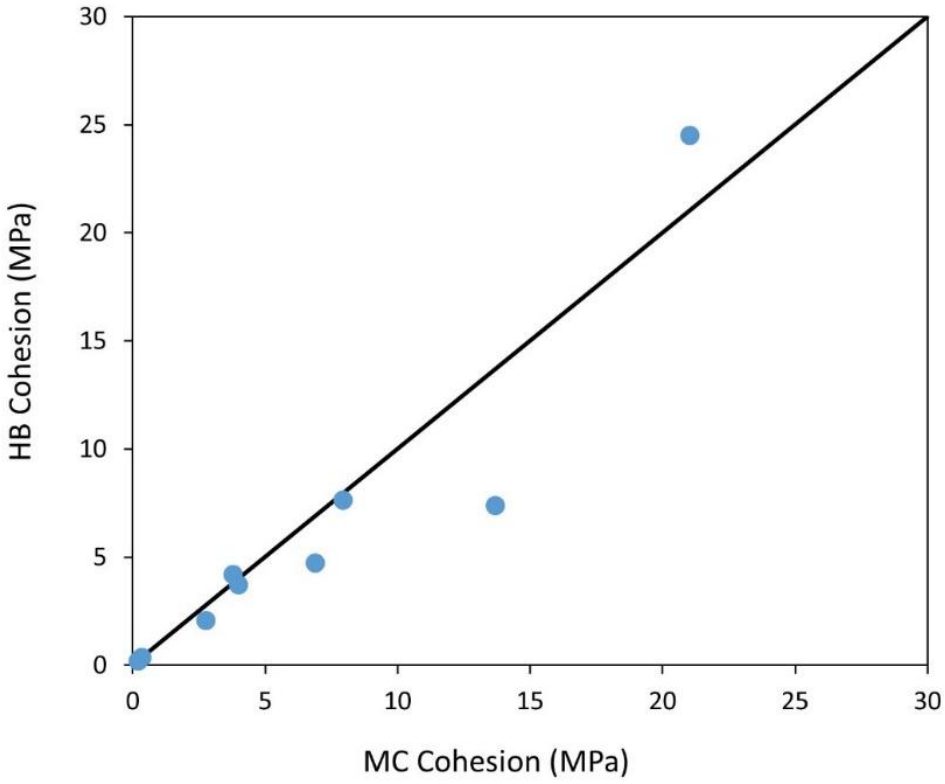


**Figure 4.16: Comparison of Cohesion values from HB and MC Criteria for all siltstones.**

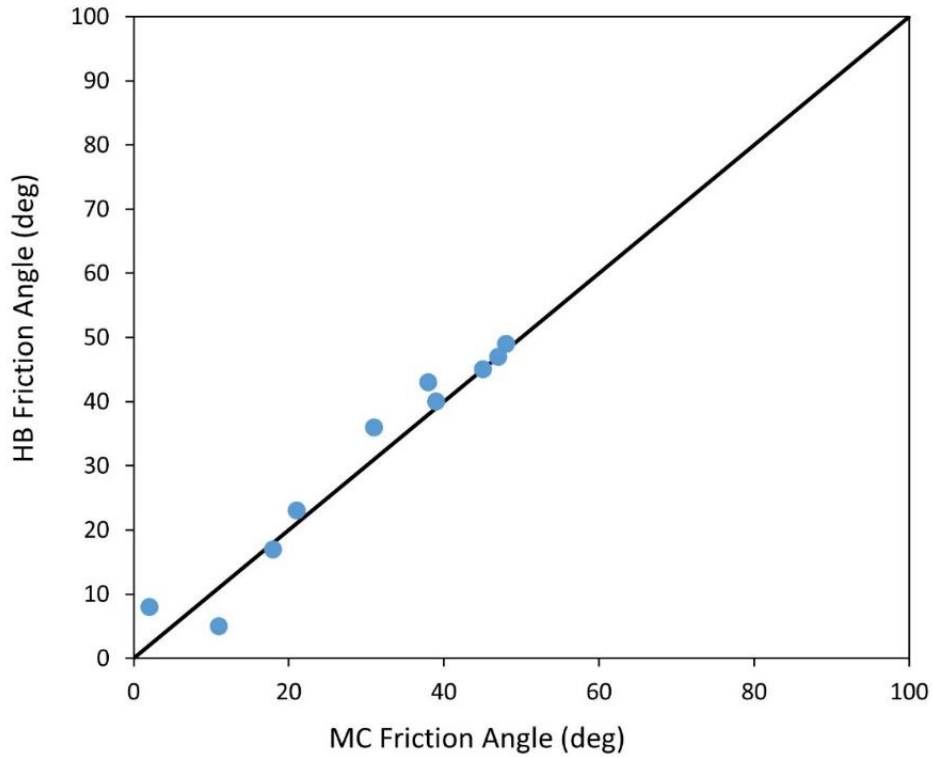


**Figure 4.17: Comparison of internal friction angle values from HB and MC Criteria for all siltstones.**

### *4.3.4 Elastic Properties*

Figure 4.18 summarizes the calculated Young's modulus ($E$) and Poisson's ratio ($\nu$) of the siltstone samples. Young's modulus values of the tested siltstones varied from 0.12 GPa for White River Formation to 41.03 GPa for Cretaceous Aspen/Bear River Formations. About 50 percent of the siltstone samples had $E$ values that fell within the typical range between 6.56 GPa and 93.50 GPa (Davarpanah et al. 2020). Similarly, Poisson's value, or the deformability of the rocks under stress ranged between 0.03 for Bear River Formation and 0.47 for Sundance Formation. About 50 percent of the siltstone samples with $\nu$ values fell between the typical range of 0.06 and 0.27 (Davarpanah et al. 2020).

| Sample ID | Formation | S ID | $E$ (GPa) | $\nu$ | Avg $E$ (GPa) | Avg $\nu$ |
|---|---|---|---|---|---|---|
| 5 | Goose Egg | 5a | 8.748 | 0.44 | 10.27 | 0.39 |
| | | 5b | 11.789 | 0.33 | | |
| 6 | Sundance | 6a | 12.796 | 0.5 | 7.83 | 0.47 |
| | | 6b | 4.869 | 0.44 | | |
| | | 6c | 7.655 | 0.5 | | |
| | | 6d | 5.983 | 0.45 | | |
| 7 | Aspen/Bear River | N/A | N/A | N/A | N/A | N/A |
| 8 | Pass Peak | N/A | N/A | N/A | N/A | N/A |
| 11 | Wasatch | 11a | 14.017 | 0.34 | 20.94 | 0.38 |
| | | 11b | 12.802 | 0.44 | | |
| | | 11c | 13.293 | 0.33 | | |
| | | 11d | 7.624 | 0.50 | | |
| | | 11e | 10.477 | 0.50 | | |
| | | 11f | 14.178 | 0.37 | | |
| | | 11g | 33.175 | 0.33 | | |
| | | 11h | 68.117 | 0.13 | | |
| | | 11i | 14.735 | 0.50 | | |
| 12 | White River | 12a | 0.095 | 0.41 | 0.12 | 0.39 |
| | | 12b | 0.103 | 0.45 | | |
| | | 12c | 0.160 | 0.31 | | |
| 13 | Aspen/Bear River | 13a | 50.229 | 0.32 | 41.03 | 0.26 |
| | | 13b | 44.994 | 0.38 | | |
| | | 13c | 29.795 | 0.23 | | |
| | | 13d | 39.118 | 0.10 | | |
| 24 | Lance | 24a | 6.224 | 0.07 | 11.21 | 0.21 |
| | | 24b | 11.327 | 0.5 | | |
| | | 24c | 16.065 | 0.07 | | |
| 30 | Bear River | 30a | 17.320 | 0.03 | 17.41 | 0.03 |
| | | 30b | 14.862 | 0.05 | | |
| | | 30c | 20.043 | 0.02 | | |
| 34 | Arikaree | 34a | 7.219 | 0.38 | 17.99 | 0.46 |
| | | 34b | 42.346 | 0.50 | | |
| | | 34c | 4.394 | 0.50 | | |
| 35 | Hanna | 35a | N/A | 0.50 | 7.08 | 0.22 |
| | | 35b | N/A | 0.50 | | |
| | | 35c | 6.272 | 0.50 | | |
| | | 35d | 11.326 | 0.15 | | |
| | | 35e | 3.641 | 0.02 | | |
| 36 | Chugwater | 36a | 5.650 | 0.05 | 5.71 | 0.07 |
| | | 36b | 5.191 | 0.07 | | |
| | | 36c | 6.297 | 0.09 | | |
| 37 | Ogallala | 37a | N/A | N/A | N/A | N/A |
| | | 37b | N/A | N/A | | |
| | | 37c | N/A | N/A | | |

Note: S ID– Specimen ID; $E$– Young's modulus (ksf); $\nu$ – Poisson's ratio; Avg – Average.

**Figure 4.18: Elastic properties of tested siltstones.**

## 4.4 Shales

Among the 8 shale samples tested, all samples were obtained as rock cores drilled out from various projects around the state. Figure 4.19 shows the description of the tested shale samples, and Figure 4.20 shows the location map of the samples. The test specimens were prepared at either 25mm diameter or 50mm diameter. The length to diameter ratio (L/D) ratio of the test specimen was maintained between 2 to 2.5. The top and bottom of the test specimen should be parallel to each other and perpendicular to the longitudinal axis. The finished top and bottom surfaces should not exceed the tolerance of 0.001 (ASTM D4543 2008). The length and diameter of all the specimens tested are provided in Figure 4.19. A series of uniaxial and triaxial compressive strength, porosity, and specific gravity tests were conducted on these samples, and the results in terms of Mohr-Coulomb failure parameters, HB failure parameters, elastic properties, the effect of particle size and crack thresholds are discussed in the following subsections.

### *4.4.1 Individual Test Results*

Table 4.9 consists of the test results of shale samples. Information about the confinement, peak stress, $\beta$, strain rate while loading, failure mode, failure behavior, and failure angle of each tested specimen is provided in the table. The Specimen ID nomenclature is not in alphabetical order as not all test specimens prepared were used for testing. $\epsilon_a$, $\epsilon_r$, and $\epsilon_v$ in the figure legends represent the axial, radial, and volumetric strains, respectively. The failure behavior is categorized as ductile, transitional, and brittle.

| Sample ID | Period/Epoch | Formation | Specimen ID | Depth (m) | Specimen Diameter (mm) | Specimen Height (mm) | Water Content (%) | Specific Gravity | Porosity (%) |
|---|---|---|---|---|---|---|---|---|---|
| 2 | Cretaceous | Cody Shale | 2a | 15.55 | 52.07 | 104.90 | 12.47 | 2.730 | 31.000 |
| | | | 2b | 15.67 | 51.82 | 104.90 | 12.47 | | 30.000 |
| | | | 2c | 15.79 | 51.56 | 104.14 | 12.47 | | 29.000 |
| | | | 2d | 15.30 | 50.80 | 107.95 | 12.47 | | 30.000 |
| 3 | Jurassic | Morrison | N/A | N/A | N/A | N/A | N/A | N/A | N/A |
| 4 | Cretaceous | Undifferentiated | 4a | 13.41 | 52.07 | 105.16 | 10.16 | 2.650 | 29.200 |
| | | | 4b | 13.11 | 51.05 | 105.16 | 10.16 | | 27.800 |
| | | | 4c | 13.23 | 51.82 | 104.14 | 10.16 | | 35.500 |
| 14 | Cretaceous | Cody Shale | 14a | 22.48 | 51.31 | 100.08 | 20.37 | 2.477 | 23.800 |
| | | | 14b | 22.64 | 51.56 | 101.09 | 20.37 | | 23.800 |
| | | | 14c | 23.17 | 51.56 | 104.90 | 20.37 | | 23.200 |
| | | | 14d | 23.55 | 51.82 | 104.90 | 20.37 | | 24.700 |
| | | | 14e | 23.78 | 51.56 | 105.41 | 20.37 | | 24.100 |
| | | | 14f | 23.91 | 51.82 | 105.16 | 20.37 | | 24.500 |
| | | | 14g | 21.49 | 51.31 | 104.65 | 20.37 | | 23.800 |
| 15 | Cretaceous | Cody Shale | 15a | 13.29 | 51.56 | 104.39 | 13.26 | 2.529 | 26.900 |
| | | | 15b | 14.18 | 50.80 | 104.14 | 13.26 | | 21.900 |
| | | | 15c | 14.33 | 51.05 | 100.58 | 13.26 | | 21.000 |
| | | | 15d | 14.57 | 50.80 | 104.39 | 13.26 | | 20.100 |
| | | | 15e | 15.21 | 50.29 | 103.63 | 13.26 | | 24.400 |
| | | | 15f | 15.52 | 51.56 | 104.39 | 13.26 | | 23.100 |
| | | | 15g | 15.73 | 51.31 | 103.89 | 13.26 | | 24.100 |
| | | | 15h | 15.91 | 51.82 | 103.63 | 13.26 | | 23.800 |
| 21 | Paleocene | Fort Union | 21a | 14.64 | 51.05 | 101.85 | 22.24 | 2.536 | 36.240 |
| | | | 21b | 14.88 | 51.31 | 102.11 | 22.24 | | 36.500 |
| | | | 21c | 15.00 | 51.05 | 102.87 | 22.24 | | 38.280 |
| 22 | Cretaceous | Cody Shale | 22a | Surface | 51.56 | 105.16 | 11.59 | 2.624 | 24.397 |
| | | | 22b | Surface | 48.26 | 104.14 | 11.59 | | 21.417 |
| | | | 22c | Surface | 52.07 | 102.87 | 11.59 | | 22.954 |
| | | | 22d | Surface | 51.31 | 102.11 | 11.59 | | 22.242 |

**Figure 4.19: Summary of tested shale samples.**

| Sample ID | Period/Epoch | Formation | Specimen ID | Depth (m) | Specimen Diameter (mm) | Specimen Height (mm) | Water Content (%) | Specific Gravity | Porosity (%) |
|---|---|---|---|---|---|---|---|---|---|
| | | | 22e | Surface | 51.82 | 102.87 | 11.59 | | 22.654 |
| 40 | Paleogene | Hanna | 40a | 32.44 | 51.31 | 24.64 | 5.01 | N/A | 12.940 |
| | | | 40b | 32.68 | 50.80 | 24.64 | 5.01 | | 13.200 |
| | | | 40c | 33.02 | 51.56 | 24.64 | 5.01 | | 12.760 |

Note: N/A– Unavailable specimen for testing

**Figure 4.19 (Continued): Summary of tested shale samples.**

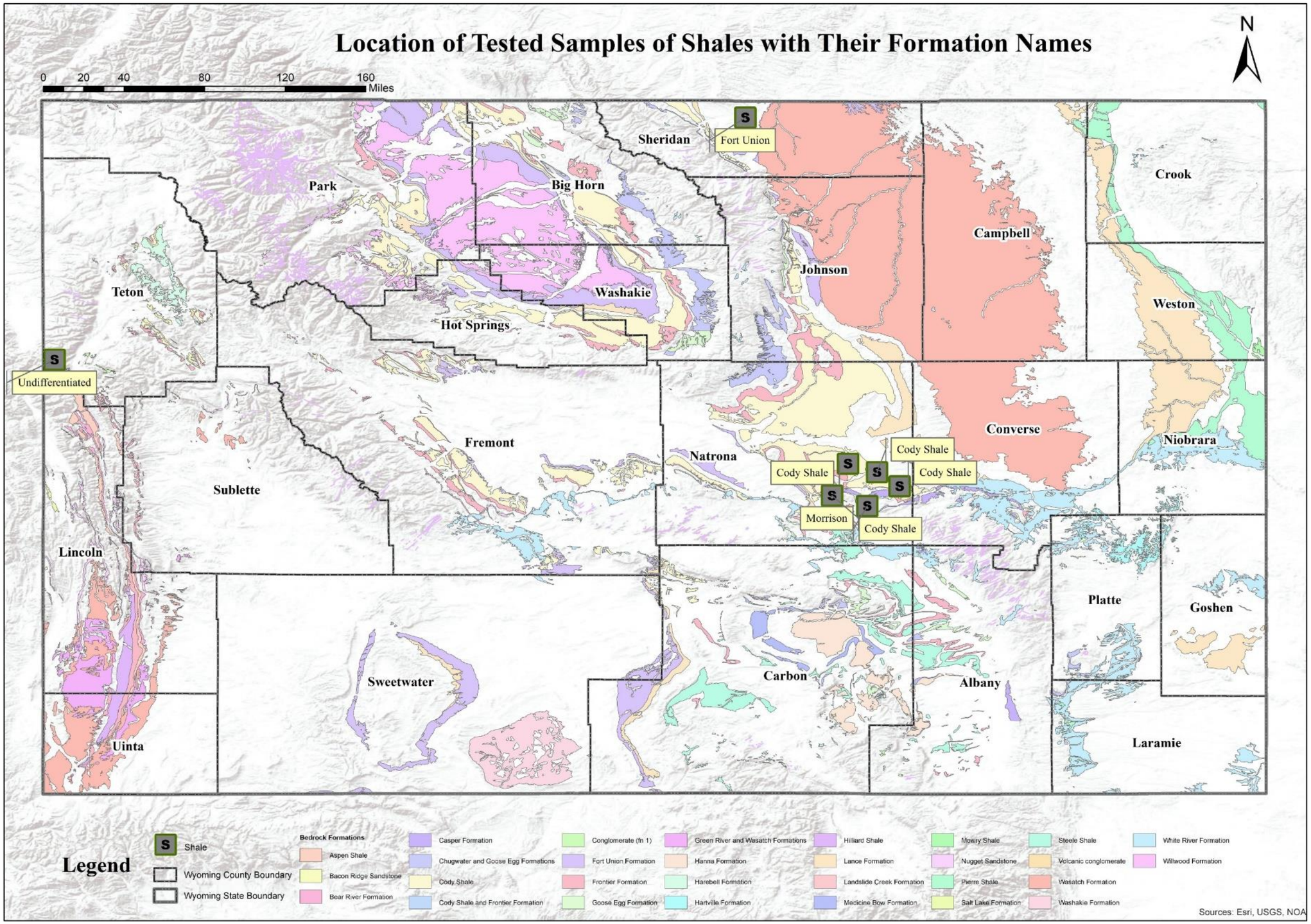


**Figure 4.20: Location of tested shale samples with their formation names (Esri ArcGIS 10.3).**

### *4.4.2 Mohr-Coulomb Parameters*

The UCS ranged from 0.32 MPa to 32.21 MPa, the cohesion (*c*) ranged from 0.16 MPa to 7.93 MPa, and the internal friction angle ranged from 2 to 44 degrees. The lowest UCS and cohesion were observed in shale from an undifferentiated formation of Cretaceous age and the internal friction angle was lowest for the Cretaceous Cody Shale Formation. The greatest difference between the UCS and cohesion was observed for the Paleogene Hanna Formation whereas the least difference was seen for the undifferentiated formation of Cretaceous age. This difference was due to the contribution of the internal friction angle. For comparison, we calculate the UCS (Figure 4.2) and compare the calculated value with the measured UCS.

The calculated UCS was higher than the measured UCS in all shale formations except for the Cody Shale Formation (Sample ID 15). The greatest difference between the measured and calculated value was seen in undifferentiated Cretaceous formation (Sample ID 4) at about 20 percent and the least difference was observed in Cody Shale Formation (Sample ID 2) at about 0.7 percent. All the formations had higher cohesion for higher internal friction angles.

**Table 4.9: Mohr-Coulomb results of tested shales.**

| Sample ID | Formation | Measured UCS, (MPa) | Calculated UCS, (MPa) | Cohesion, *c* (MPa) | Internal Friction Angle, $\varphi$ (deg) |
|---|---|---|---|---|---|
| 2 | Cody Shale | 1.06 | 1.06 | 0.35 | 23 |
| 3 | Morrison | N/A | N/A | N/A | N/A |
| 4 | Undifferentiated | 0.32 | 0.40 | 0.16 | 13 |
| 14 | Cody Shale | 1.86 | 1.91 | 0.88 | 5 |
| 15 | Cody Shale | 1.00 | 0.41 | 0.31 | 2 |
| 21 | Fort Union | N/A | 0.46 | 0.05 | N/A |
| 22 | Cody Shale | 1.35 | 1.61 | 0.68 | 10 |
| 40 | Hanna | 32.21 | 37.37 | 7.93 | 44 |

Note: N/A– Unavailable specimen for testing.

Comparing the measured UCS with the calculated UCS presented in Table 4.9 we observed that for the UCS less than 14 MPa, the data points were on or near the one-to-one line; whereas, for UCS greater than 14 MPa, the calculated UCS was higher than the measured one as indicated by one point above the one-to-one line in Figure 4.21. This indicated that there was over prediction of the UCS value above 14 MPa.

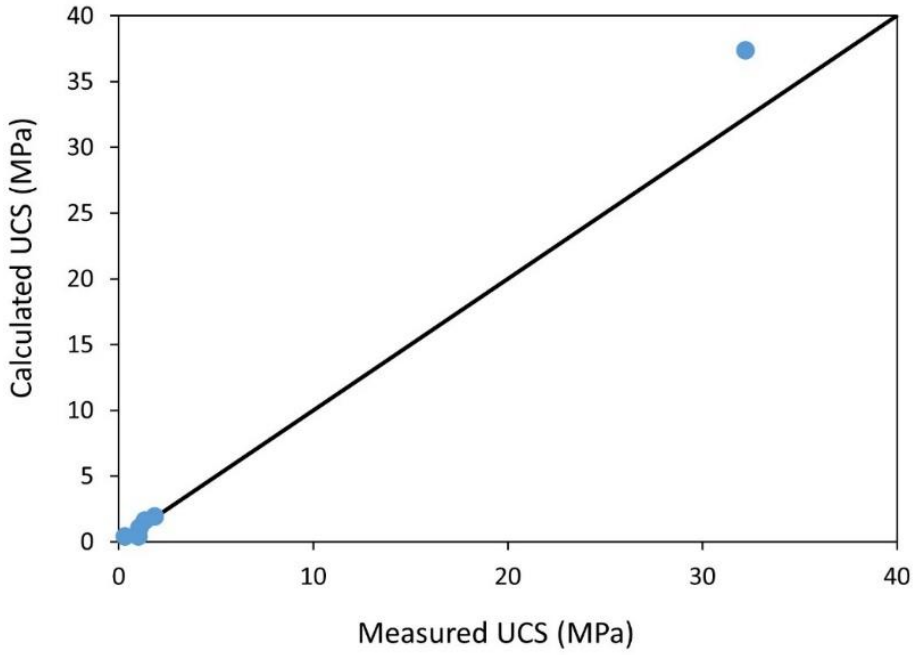


**Figure 4.21: Comparison of measured and calculated UCS values.**

### *4.4.3* HB *Parameters*

The non-linear failure criterion proposed by Hoek and Brown (1997) was used to calculate the non-linear shear strength of the tested samples. The HB material constant for intact rock ($m_i$) was calculated using the statistical method proposed by Hoek (2019) based on test results on a principal axes plane. The HB criterion was applied on the intact rock taking the HB parameters $a$=0.5 and $s$=1, to estimate the cohesion and internal friction angle. The determination of $m_i$ from the back calculation method was found to provide results that were comparable to the values proposed by Hoek and Brown (1997) for sandstones and hence was preferred in the calculations of the cohesion and internal friction angle.

The calculation of the material constant $m_i$ was conducted from a series of uniaxial and triaxial tests performed on intact rock specimens for each sample. In this process, the major and minor principal stresses of the tested specimens were plotted, and a curve HB line was fitted through the points by substituting $a = 0.5$, $s = 1$, and $m_b$= $m_i$ in the generalized HB criterion (Figure 4.7) in terms of major and minor principal stresses ($\sigma_1$ and $\sigma_3$) and $\sigma_c$ is the UCS value. The only unknown in the equation is the $m_i$, which can be easily back calculated. At least one UCS and two triaxial tests were required for the determination of $m_i$ value. Samples with fewer than two triaxial tests were not reported.

| Sample ID | Formation | S ID | $\sigma_c$ (MPa) | $\sigma_p$ (MPa) | $\beta$ (deg) | SR (%/min) | Failure Mode | Failure Behavior | Failure Angle (deg) |
|---|---|---|---|---|---|---|---|---|---|
| 2 | Cody Shale | 2a | 0.29 | 1.37 | 0 | 0.20 | S | Ductile | 90 |
| | | 2b | 0.57 | 1.72 | 0 | 0.20 | TS | Ductile | 30 |
| | | 2c | 0.41 | 1.51 | 0 | 0.20 | S | Ductile | 90 |
| | | 2d | 0.00 | 1.09 | 0 | 0.20 | S | Ductile | 90 |
| 3 | Morrison | N/A | N/A | N/A | N/A | N/A | N/A | N/A | N/A |
| 4 | Undifferentiated | 4a | 0.30 | 1.27 | N/A | 0.20 | S | Ductile | 60 |
| | | 4b | 0.54 | 1.26 | N/A | 0.20 | S | Ductile | 90 |
| | | 4c | 0.41 | 1.05 | N/A | 0.20 | S | Ductile | 90 |
| 14 | Cody Shale | 14a | 1.00 | 2.68 | N/A | 0.10 | S | Brittle | 50 |
| | | 14b | 4.00 | 5.93 | N/A | 0.10 | S | Brittle | 50 |
| | | 14c | 0.00 | 3.34 | N/A | 0.10 | S | Brittle | 10 |
| | | 14d | 2.00 | 4.37 | N/A | 0.10 | T | Brittle | 75 |
| | | 14e | 8.00 | 11.45 | N/A | 0.10 | T | Brittle | 90 |
| | | 14f | 10.00 | 12.58 | N/A | 0.10 | S, T | Brittle | 80 |
| | | 14g | 0.00 | 1.86 | N/A | 0.10 | S | Brittle | 80 |
| 15 | Cody Shale | 15a | 0.99 | 1.73 | N/A | 0.20 | S | Ductile | 80 |
| | | 15b | 3.99 | 5.78 | N/A | 0.20 | S | Transitional | 60 |
| | | 15c | 1.99 | 4.79 | N/A | 0.20 | S | Transitional | 50 |
| | | 15d | 1.99 | 4.80 | N/A | 0.20 | S | Transitional | 45 |
| | | 15e | 3.99 | 5.03 | N/A | 0.20 | S | Ductile | 65 |
| | | 15f | 3.00 | 3.84 | N/A | 0.20 | S | Brittle | 20 |
| | | 15g | 7.99 | 9.16 | N/A | 0.20 | S | Transitional | 45 |
| | | 15h | 9.99 | 11.01 | N/A | 0.20 | T | Transitional | 75 |
| 21 | Fort Union | 21a | 0.14 | 0.57 | N/A | 0.30 | S | Ductile | 60 |
| | | 21b | 0.17 | 0.69 | N/A | 0.30 | S | Ductile | 60 |
| | | 21c | 0.41 | 0.78 | N/A | 0.30 | S | Ductile | 60 |
| 22 | Cody Shale | 22a | 4.00 | 6.01 | 90 | 0.05 | MTS | Transitional | 60 |
| | | 22b | 10.00 | 12.86 | 90 | 0.05 | S | Brittle | 45 |
| | | 22c | 0.99 | 5.75 | 90 | 0.05 | S | Brittle | 60 |
| | | 22d | 6.00 | 10.02 | 90 | 0.05 | S, T | Brittle | 65 |

**Figure 4.22: Summary of test results of tested shales.**

| Sample ID | Formation | S ID | $\sigma_c$ (MPa) | $\sigma_p$ (MPa) | $\beta$ (deg) | SR (%/min) | Failure Mode | Failure Behavior | Failure Angle (deg) |
|---|---|---|---|---|---|---|---|---|---|
| | | 22e | 0.99 | 2.94 | 90 | 0.05 | S | Transitional | 80 |
| 40 | Hanna | 40a | 0.00 | 32.21 | N/A | 0.10 | TS | Brittle | 70 |
| | | 40b | 4.00 | 81.67 | N/A | 0.10 | TS | Brittle | 80 |
| | | 40c | 10.00 | 88.92 | N/A | 0.10 | S | Brittle | 45 |

Note: S ID– Specimen ID; $\sigma_c$ – Confining pressure (MPa); $\sigma_p$ – Peak stress (MPa); $\beta$– Bedding angle (deg); SR– Strain rate (%/min); S– Shear; TS– Tensile Splitting; MTS– Multiple Tensile Splitting.

**Figure 4.22 (Continued): Summary of test results of tested shales.**

**Table 4.10: HB results of tested shales.**

| Sample ID | Formation | $m_i$ (measured) | *c* (MPa) | $\varphi$ (deg) | $\sigma_t$ (MPa) |
|---|---|---|---|---|---|
| 2 | Cody Shale | 2.86 | 0.37 | 21.00 | 0.37 |
| 3 | Morrison | N/A | N/A | N/A | N/A |
| 4 | Undifferentiated | 2.32 | 0.13 | 13.00 | 0.14 |
| 14 | Cody Shale | 0.28 | 0.91 | 1.00 | 6.63 |
| 15 | Cody Shale | 1.64 | 0.21 | 48.00 | 0.61 |
| 21 | Fort Union | N/A | N/A | N/A | N/A |
| 22 | Cody Shale | 1.74 | 0.56 | 12.00 | 0.78 |
| 40 | Hanna | 21.05 | 7.50 | 44.00 | 1.52 |

Note: *c*– Cohesion; $\sigma_t$– Tensile strength; $\varphi$ – Internal friction angle; $m_i$– HB parameter; N/A– Unavailable specimen for testing.

The intact rock material constant ($m_i$) values for all shale samples are provided in Table 4.10 along with the cohesion (*c*), internal friction angle ($\varphi$), and tensile strength ($\sigma_t$). Hoek & Brown (1997), and Marinos & Hoek (2001) provided the range of $m_i$ value of shale as $6 \pm 2$. However, we observed that the calculated values of $m_i$ ranged from 0.28 to 21.05, significantly lower and higher than the proposed range. Hoek & Brown (1997) reported that the value of $m_i$ can change significantly with variations in the rock *β* angle as the failure will occur along a weakness plane. The reason for the variation observed could be because the values reported are for intact rock specimens tested normal to bedding whereas the intact rock specimens tested in the project do not show any apparent beddings.

Comparing the values of the cohesion (*c*) and internal friction angle ($\varphi$) obtained from the linear MC criterion and non-linear HB criterion, the values were comparable as illustrated by Figure 4.23 and 4.24, respectively. Figure 4.23 shows that most values fell along the one-to-one line and some values from the HB criterion are lower than those from MC criterion. A similar agreement was observed between the internal friction angles from both criteria while several internal friction angles from HB criterion were higher than that from MC criterion.

### *4.4.4 Elastic Properties*

Figure 4.25 summarizes the calculated Young's modulus ($E$) and Poisson's ratio ($\nu$) of the shale samples. The $E$ value of the tested shales varied from 0.02 GPa for undifferentiated formation Sample 4 to 280.31 GPa for Cody Shale Formation sample 14 of the Cretaceous, the oldest geological age of the shale samples. Similarly, Poisson's value or the deformability of the rocks under stress ranged between 0.03 for Hanna Formation sample 40 to 0.50 for Cody Shale Formation sample 22.

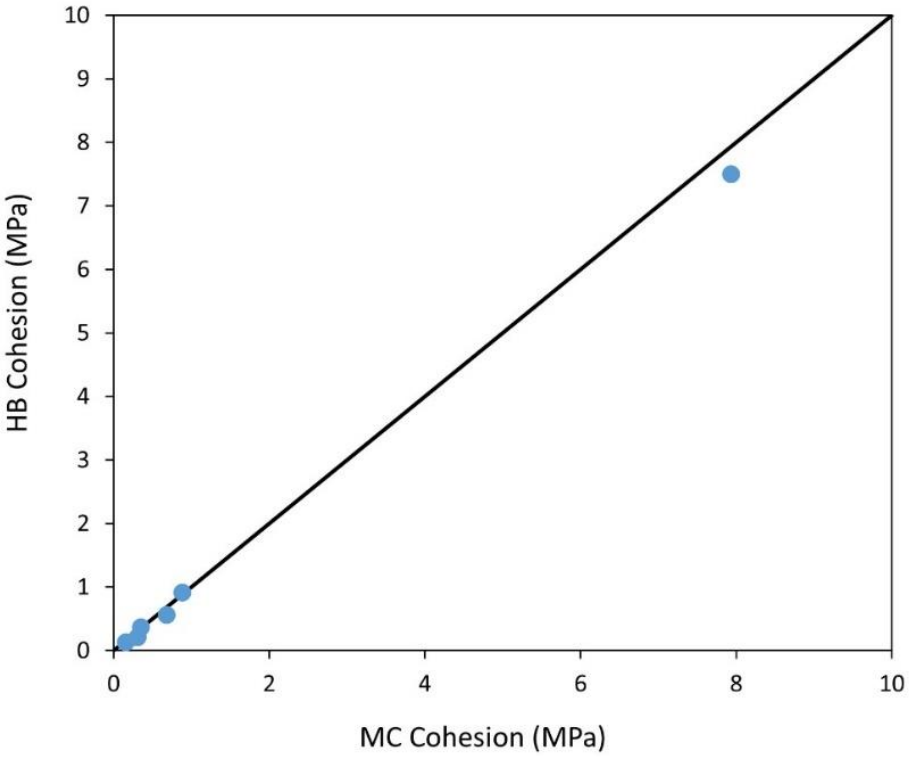


**Figure 4.23: Comparison of cohesion values from HB and MC Criteria for all shales.**

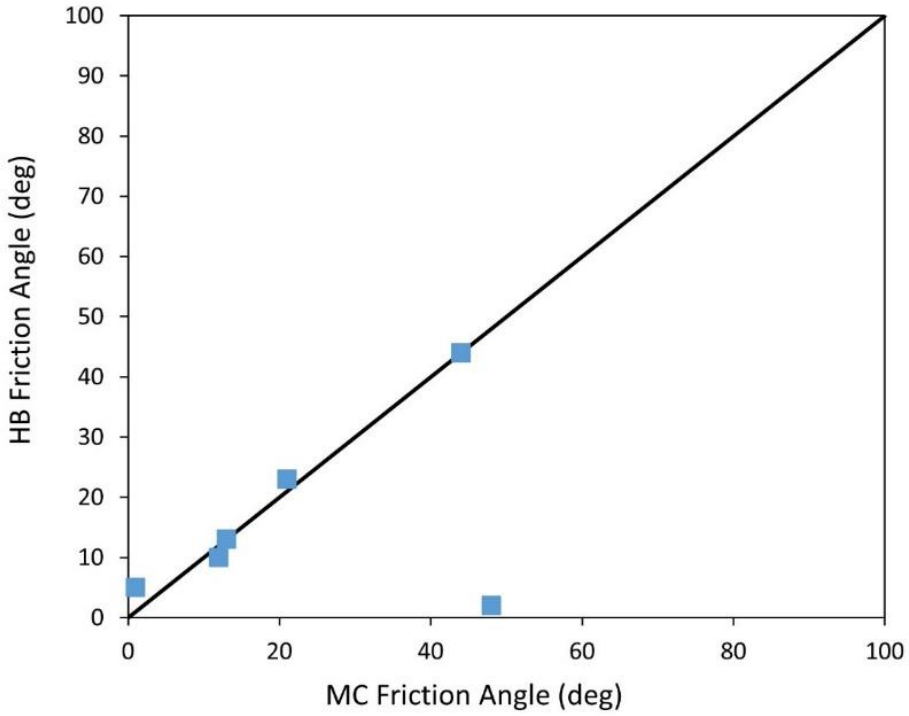


**Figure 4.24: Comparison of the internal friction angle values from HB and MC Criteria for all shales.**

| Sample ID | Formation | S ID | $E$ (GPa) | $\nu$ | Avg $E$ (GPa) | Avg $\nu$ |
|---|---|---|---|---|---|---|
| 2 | Cody Shale | 2a | 0.05 | 0.39 | 0.04 | 0.26 |
| | | 2b | 0.04 | 0.16 | | |
| | | 2c | 0.04 | 0.26 | | |
| | | 2d | 0.02 | 0.24 | | |
| 3 | Morrison | N/A | N/A | N/A | N/A | N/A |
| 4 | Undifferentiated | 4a | 0.07 | 0.20 | 0.04 | 0.19 |
| | | 4b | 0.03 | 0.24 | | |
| | | 4c | 0.02 | 0.14 | | |
| 14 | Cody Shale | 14a | 200.47 | 0.10 | 185.83 | 0.35 |
| | | 14b | 171.91 | 0.40 | | |
| | | 14c | 212.81 | 0.34 | | |
| | | 14d | 199.96 | 0.50 | | |
| | | 14e | 280.31 | 0.50 | | |
| | | 14f | 151.68 | 0.26 | | |
| | | 14g | 83.70 | 0.35 | | |
| 15 | Cody Shale | 15a | 10.17 | 0.50 | 80.36 | 0.38 |
| | | 15b | 77.48 | 0.34 | | |
| | | 15c | 190.95 | 0.42 | | |
| | | 15d | 205.81 | 0.42 | | |
| | | 15e | 66.26 | 0.28 | | |
| | | 15f | 28.82 | 0.31 | | |
| | | 15g | 34.78 | 0.44 | | |
| | | 15h | 28.61 | 0.33 | | |
| 21 | Fort Union | 21a | N/A | N/A | N/A | N/A |
| | | 21b | N/A | N/A | | |
| | | 21c | N/A | N/A | | |
| 22 | Cody Shale | 22a | 0.10 | 0.50 | 0.17 | 0.49 |
| | | 22b | 0.21 | 0.50 | | |
| | | 22c | 0.22 | 0.50 | | |
| | | 22d | 0.25 | 0.50 | | |
| | | 22e | 0.07 | 0.48 | | |
| 40 | Hanna | 40a | 7.70 | 0.08 | 7.63 | 0.12 |
| | | 40b | 5.38 | 0.25 | | |
| | | 40c | 9.83 | 0.03 | | |

Note: S ID– Specimen ID; $E$– Young's modulus (GPa); $\nu$– Poisson's ratio; Avg – Average.

**Figure 4.25: Elastic properties of tested shales.**

## 4.5 Other Rocks

Among the 17 rock samples tested, fourteen samples were obtained as surface boulders, and three samples were obtained as rock cores drilled out from various projects around the state. Figure 4.26 shows the description of the tested rock samples, and Figure 4.27 shows the location map of the rock samples. Test specimens were prepared at either 25mm diameter or 50mm diameter. The length-to-diameter ratio (L/D) ratio of the test specimen was maintained between 2 to 2.5. The top and bottom of the test specimen should be parallel to each other and

perpendicular to the longitudinal axis. The finished top and bottom surfaces should not exceed the tolerance of 0.001 *(*ASTM D4543 2008*).* The length and diameter of all the specimens tested are provided in Figure 4.26. A series of uniaxial and triaxial compressive strength, porosity, and specific gravity tests were conducted on these samples, and the results in terms of Mohr-Coulomb failure parameters, HB failure parameters, and elastic properties, are discussed in the following subsections.

| Sample ID | Period/Epoch | Formation | Rock Type | Specimen ID | Depth (m) | Specimen Diameter (mm) | Specimen Height (mm) | Water Content (%) | Specific Gravity | Porosity (%) |
|---|---|---|---|---|---|---|---|---|---|---|
| 1 | Miocene | Ogallala | Claystone | 1a | 19.82 | 51.31 | 106.43 | 15.90 | 2.580 | 28.00 |
| | | | | 1b | 19.94 | 51.82 | 103.63 | 15.90 | | 28.00 |
| | | | | 1c | 20.06 | 50.80 | 101.60 | 15.90 | | 28.00 |
| 9 | Oligocene | Wiggins | Volcanic Breccia | 9a | 64.88 | 41.66 | 92.71 | 3.83 | 2.680 | 23.95 |
| | | | | 9b | 65.00 | 40.89 | 98.04 | 3.83 | | 19.23 |
| | | | | 9c | 65.12 | 41.15 | 98.55 | 3.83 | | 20.52 |
| | | | | 9d | 65.30 | 41.15 | 97.79 | 3.83 | | 24.29 |
| 10 | Cretaceous | Cloverly | Conglomerate | 10a | 28.02 | 41.66 | 98.81 | 1.69 | 2.560 | 13.24 |
| | | | | 10b | 28.14 | 41.66 | 95.50 | 1.69 | | 15.34 |
| | | | | 10c | 28.26 | 41.66 | 99.57 | 1.69 | | 13.25 |
| | | | | 10d | 28.96 | 42.16 | 96.77 | 1.69 | | 14.39 |
| 25 | Mississippian | Madison Limestone | Limestone | 25a | Surface | 24.89 | 49.53 | 2.18 | N/A | 7.93 |
| | | | | 25b | Surface | 24.89 | 51.56 | 2.18 | | 2.60 |
| | | | | 25c | Surface | 24.38 | 52.07 | 2.18 | | 3.23 |
| 27 | Permian | Goose Egg | Limestone | 27a | Surface | 24.89 | 50.29 | 1.84 | N/A | 12.41 |
| | | | | 27b | Surface | 25.15 | 59.69 | 1.84 | | 11.96 |
| | | | | 27c | Surface | 24.89 | 50.29 | 1.84 | | 12.18 |
| | | | | 27d | Surface | 25.15 | 50.29 | 1.84 | | 12.23 |
| 28 | Precambrian | No Designation | Granite | 28a | Surface | 24.64 | 51.56 | 0.23 | N/A | 0.81 |
| | | | | 28b | Surface | 48.26 | 101.60 | 0.23 | | 0.72 |
| | | | | 28c | Surface | 48.51 | 99.57 | 0.23 | | 0.98 |
| 29 | Archeaon | No Designation | Hornblende Gneiss | 29a | Surface | 24.38 | 51.31 | 0.38 | N/A | 1.08 |
| | | | | 29b | Surface | 24.89 | 51.05 | 0.38 | | 0.74 |
| | | | | 29c | Surface | 24.89 | 51.05 | 0.38 | | 0.89 |
| 38 | Paleogene | Hanna | Claystone | 38a | Surface | 24.64 | 51.31 | 6.58 | N/A | 7.86 |
| | | | | 38b | Surface | 24.38 | 52.07 | 6.58 | | 7.45 |
| 44 | Eocene | Wind River | Silty Claystone | 44a | Surface | 25.40 | 51.31 | 7.85 | N/A | 5.41 |
| | | | | 44b | Surface | 26.42 | 51.31 | 7.85 | | 5.03 |
| | | | | 44c | Surface | 24.89 | 50.29 | 7.85 | | 4.96 |
| 45 | Ordovician | Big Horn Dolomite | Dolostone | 45a | Surface | 25.65 | 52.83 | 1.41 | N/A | 8.50 |
| | | | | 45b | Surface | 26.16 | 52.07 | 1.41 | | 8.27 |
| | | | | 45c | Surface | 26.16 | 52.83 | 1.41 | | 8.09 |
| 46 | Cambrian | Gros Ventre | Limestone Pebble Conglomerate | 46a | Surface | 25.40 | 53.34 | 2.23 | N/A | 0.82 |
| | | | | 46b | Surface | 25.91 | 52.07 | 2.23 | | 1.01 |
| | | | | 46c | Surface | 26.67 | 53.34 | 2.23 | | 1.47 |
| | | | | 46d | Surface | 25.40 | 51.82 | 2.23 | | 1.10 |
| 47 | Devonian | Jefferson Formation | Limestone | 47a | Surface | 25.65 | 52.07 | 1.87 | N/A | 2.12 |
| | | | | 47b | Surface | 25.91 | 52.58 | 1.87 | | 1.55 |
| | | | | 47c | Surface | 26.42 | 53.34 | 1.87 | | 1.90 |
| 48 | Eocene | Absoraka Supergroup | Welded Tuff | 48a | Surface | 50.55 | 101.35 | 0.15 | N/A | 13.62 |
| | | | | 48b | Surface | 50.29 | 100.33 | 0.15 | | 13.08 |
| | | | | 48c | Surface | 50.29 | 103.12 | 0.15 | | 13.01 |
| 52 | Proterozoic | Sherman Granite | Granite Pegmatite | N/A | Surface | N/A | N/A | N/A | N/A | N/A |
| 53 | Proterozoic | LAC | Anorthosite | 53a | Surface | 25.15 | 51.05 | 3.15 | N/A | 5.07 |
| | | | | 53b | Surface | 24.89 | 51.31 | 3.15 | | 4.56 |
| | | | | 53c | Surface | 25.15 | 51.05 | 3.15 | | 4.68 |
| 54 | Archeaon | No Designation | Amphibolite | 54a | Surface | 25.65 | 51.31 | 2.46 | N/A | 5.26 |
| | | | | 54b | Surface | 25.65 | 51.56 | 2.46 | | 7.42 |
| | | | | 54c | Surface | 25.91 | 51.31 | 2.46 | | 5.78 |

**Figure 4.26: Summary of tested rock samples.**

| Sample ID | Period/Epoch | Formation | Rock Type | Specimen ID | Depth (m) | Specimen Diameter (mm) | Specimen Height (mm) | Water Content (%) | Specific Gravity | Porosity (%) |
|---|---|---|---|---|---|---|---|---|---|---|
| 55 | Proterozoic | Sherman Granite | Granite | 55a | Surface | 25.15 | 52.07 | 1.24 | N/A | 3.49 |
| | | | | 55b | Surface | 25.91 | 51.82 | 1.24 | | 4.85 |
| | | | | 55c | Surface | 25.65 | 51.31 | 1.24 | | 4.38 |

**Figure 4.26 (Continued): Summary of tested rock samples.**

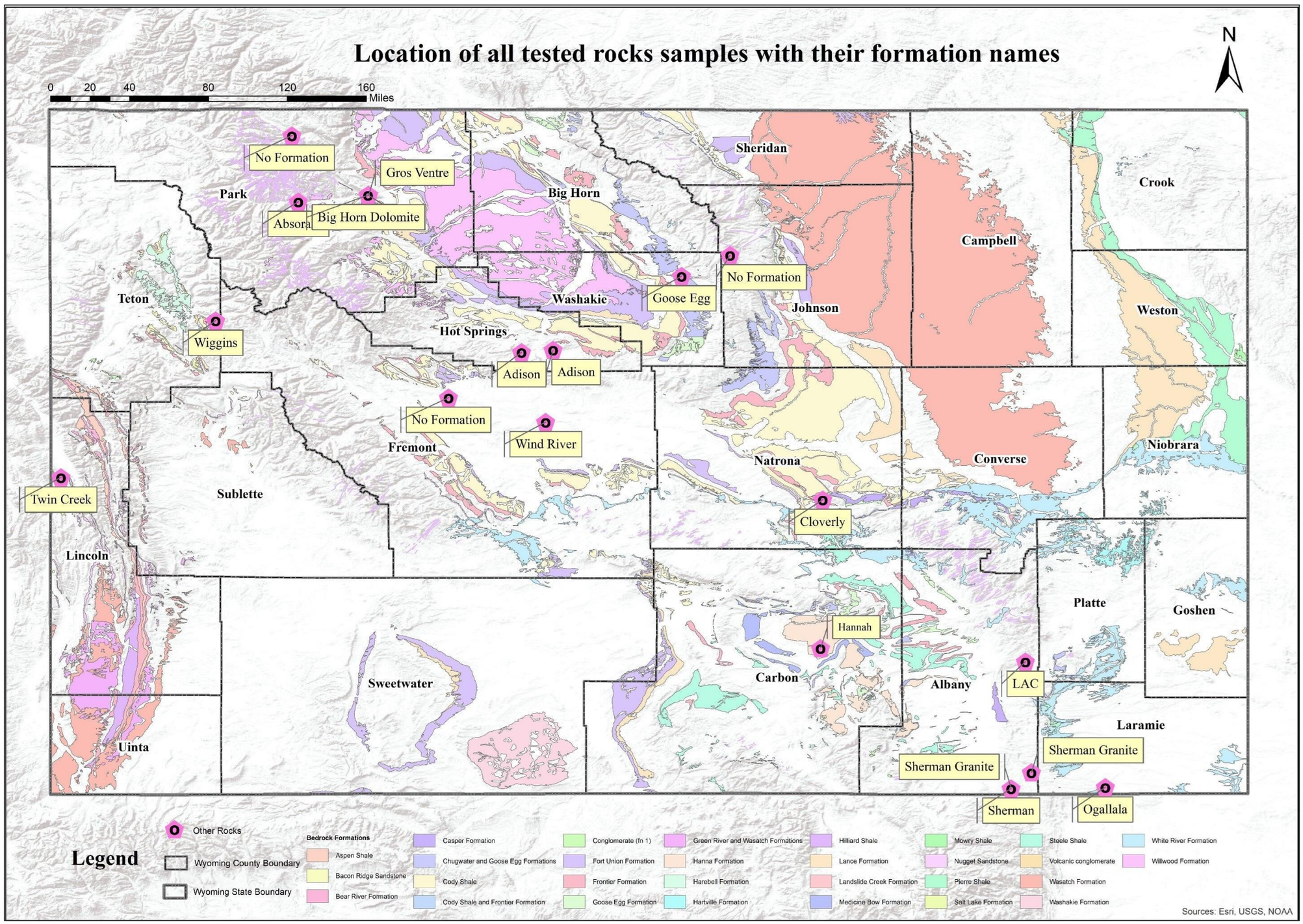


**Figure 4.27: Location of other rock samples with their formation names (Esri ArcGIS 10.3).**

### *4.5.1 Individual Test Results*

A series of uniaxial and triaxial compressive strength, porosity, and specific gravity tests were conducted on these samples, and the results in terms of Mohr-Coulomb failure parameters, Hoek and Brown (HB) failure parameters, and elastic properties are discussed in the following subsections. Figure 4.28 consists of the test results of the tested rock samples. Information about the confinement, peak stress, *β*, strain rate while loading, failure mode, and failure behavior and failure angle of each tested specimen is provided in the table. The Specimen ID nomenclature is not in alphabetical order as not all test specimens prepared were used for testing. $\epsilon_a$, $\epsilon_r$, and $\epsilon_v$ in the figure legends represent the axial, radial, and volumetric strains, respectively. The failure behavior is categorized as ductile, transitional, and brittle.

### *4.5.2 Mohr-Coulomb Parameters*

The UCS ranged from 11.33 MPa to 61.27 MPa, the cohesion (*c*) ranged from 3.10 MPa to 11.86 MPa, and the internal friction angle ($\varphi$) ranged from 6 to 58 degrees for limestone. Similarly, UCS ranged from 0.41 MPa to 20.61 MPa, c ranged from 0.089 MPa to 5.51 MPa, and $\varphi$ ranged from 25 to 46 degrees for claystone. The UCS, *c*, and $\varphi$ for other rock types are summarized in Table 4.11. The lowest UCS and cohesion in Limestone were observed for the Devonian Jefferson Formation, and the lowest internal friction angle was observed for Mississippian Madison Formation. Similarly, for claystone, the lowest UCS, cohesion, and internal friction angle were observed for Miocene Ogallala Formation. The greatest difference between the UCS and cohesion for limestone was observed for the Madison Formation, with cohesion being 85 percent lower than UCS. In the Jefferson Formation cohesion was 75 percent lower than UCS. Similarly, for claystone, the greatest difference between the UCS and cohesion was observed for the Ogallala Formation (78 percent) and the least difference for the Eocene Wind River Formation (71 percent). The difference was due to the contribution of the internal friction angle. For comparison, we calculated the UCS (Figure 4.2) and compared it with the measured UCS.

| Sample ID | Formation | Rock Type | $\sigma_c$ (MPa) | $\sigma_p$ (MPa) | SR (%/min) | Failure Mode | Failure Behavior | Failure Angle, (deg) |
|---|---|---|---|---|---|---|---|---|
| 1 | Ogallala | Claystone | 0.00 | 0.41 | 0.20 | S | Ductile | 45 |
| | | | 0.32 | 0.99 | 0.20 | S | Ductile | 45 |
| | | | 0.57 | 1.28 | 0.20 | S | TN | 65 |
| 9 | Wiggins | Volcanic Breccia | 0.00 | 7.66 | 0.08 | S | Brittle | 55 |
| | | | 0.79 | 9.12 | 0.08 | MTS | Brittle | 90 |
| | | | 3.99 | 29.37 | 0.08 | S | Brittle | 25 |
| | | | 10.00 | 56.96 | 0.10 | TS | Brittle | 90 |
| 10 | Cloverly | Conglomerate | 0.00 | 11.26 | 0.08 | TS | Brittle | 60 |
| | | | 1.01 | 21.34 | 0.10 | TS | Brittle | 90 |
| | | | 4.00 | 33.99 | 0.08 | TS | Brittle | 90 |
| | | | 10.00 | 28.39 | 0.10 | TS | Brittle | 90 |
| 25 | Madison Limestone | Limestone | 0.99 | 38.61 | 0.10 | TS | TN | 90 |
| | | | 4.00 | 90.05 | 0.10 | TS | TN | 90 |
| | | | 10.00 | 31.68 | 0.10 | TS | Brittle | 90 |
| 27 | Goose Egg | Limestone | 0.00 | 61.27 | 0.05 | MTS | Brittle | 90 |
| | | | 0.99 | 67.03 | 0.05 | TS | TN | 90 |
| | | | 2.00 | 63.00 | 0.05 | TS | TN | 90 |
| | | | 8.00 | 119.54 | 0.05 | MTS | Brittle | 90 |
| 28 | No Designation | Granite | 0.00 | 87.97 | 0.10 | MTS | Brittle | 90 |
| | | | 6.00 | 154.61 | 0.10 | TS | TN | 90 |
| | | | 10.00 | 200.28 | 0.10 | S | TN | 80 |
| 29 | No Designation | Hornblende Gneiss | 0.00 | 36.68 | 0.10 | TS | Brittle | 90 |
| | | | 0.99 | 65.19 | 0.10 | S | Brittle | 70 |
| | | | 10.00 | 153.78 | 0.10 | S | Brittle | 90 |
| 38 | Hanna | Claystone | 0.00 | 20.61 | 0.05 | TS | TN | 90 |
| | | | 4.00 | 50.52 | 0.05 | TS | TN | 90 |
| 44 | Wind River | Silty Claystone | 0.00 | 8.50 | 0.10 | S | TN | 45 |
| | | | 4.00 | 50.50 | 0.10 | S | Brittle | 60 |
| | | | 10.00 | 69.63 | 0.10 | S | TN | 75 |
| 45 | Big Horn Dolomite | Dolostone | 0.00 | 23.13 | 0.10 | TS | TN | 90 |
| | | | 4.00 | 79.56 | 0.10 | S | Brittle | 60 |

**Figure 4.28: Summary of test results of tested rocks.**

| Sample ID | Formation | Rock Type | $\sigma_c$ (MPa) | $\sigma_p$ (MPa) | SR (%/min) | Failure Mode | Failure Behavior | Failure Angle, (deg) |
|---|---|---|---|---|---|---|---|---|
| | | | 10.00 | 38.55 | 0.10 | MTS | Brittle | 90 |
| 46 | Gros Ventre | Limestone Pebble Conglomerate | 0.00 | 40.70 | 0.05 | TS | Brittle | 90 |
| | | | 4.02 | 41.04 | 0.05 | S | Brittle | 60 |
| | | | 6.00 | 95.02 | 0.05 | S | Brittle | 60 |
| | | | 10.00 | 27.08 | 0.05 | TS | TN | 90 |
| 47 | Jefferson Formation | Limestone | 0.00 | 11.33 | 0.05 | TS | Brittle | 90 |
| | | | 4.00 | 52.77 | 0.05 | MTS | Brittle | 90 |
| | | | 10.00 | 146.74 | 0.05 | MTS | TN | 90 |
| 48 | Absoraka Supergroup | Welded Tuff | 0.00 | 21.13 | 0.10 | MTS | TN | 90 |
| | | | 4.00 | 53.74 | 0.10 | TS | Brittle | 90 |
| | | | 10.00 | 74.58 | 0.10 | MTS | Brittle | 90 |
| 52 | Sherman Granite | Granite Pegmatite | N/A | N/A | N/A | N/A | N/A | N/A |
| 53 | Lac Wheatland | Anorthosite | 0.00 | 44.26 | 0.10 | S | Brittle | 45 |
| | | | 4.00 | 63.03 | 0.10 | TS | Ductile | 90 |
| | | | 10.00 | 144.66 | 0.10 | S | TN | 60 |
| 54 | No Designation | Amphibolite | 0.00 | 60.52 | 0.10 | TS | Brittle | 90 |
| | | | 4.00 | 114.54 | 0.10 | TS | TN | 90 |
| | | | 10.00 | 184.61 | 0.10 | MTS | TN | 90 |
| 55 | Sherman Granite | Granite | 0.00 | 26.77 | 0.10 | TS | Brittle | 90 |
| | | | 4.00 | 66.26 | 0.10 | MTS | Ductile | 90 |
| | | | 10.00 | 125.28 | 0.10 | S | TN | 60 |

Note: S ID– Specimen ID; $\sigma_c$ – Confining pressure (MPa); $\sigma_p$ – Peak stress (MPa); SR– Strain rate (%/min); S– Shear; TS– Tensile Splitting; MTS– Multiple Tensile Splitting; TN– Transitional; N/A– Unavailable specimen for testing.

**Figure 4.28 (Continued): Summary of test results of tested rocks.**

The calculated UCS was higher than the measured UCS for all rock types except claystone from the Ogallala Formation, breccia from Wiggin's Formation, and limestone from Madison Formation. Except for these three formations, the greatest difference between the measured UCS and calculated UCS was seen in limestone for the Jefferson Formation, 204.80 MPa, and the least difference was also observed in limestone for Madison Formation, 3.91 MPa. Barton & Choubey (1977), reported the internal friction angle of dry limestone as 31-37 degrees, conglomerate as 35, Amphibolite as 32, and Gneiss as 26-29 degrees. The observed values for these rocks were much higher than the ones reported by Barton & Choubey (1977). Comparing the measured with the UCS calculated, we observed that the calculated UCS was much higher than the measured UCS in Figure 4.29. For all rock types, the mean bias was 0.91 and the coefficient of variation (COV) of 0.72. Limestone had a mean bias of 1.33 and COV of 1.13. Similarly, mean bias and COV for claystone, conglomerate, and granite were 0.97 & 0.43, 0.80 & 0.17, and 0.74 & 0.08 respectively. Among all the rocks, limestone had the most variation among the three limestone samples.

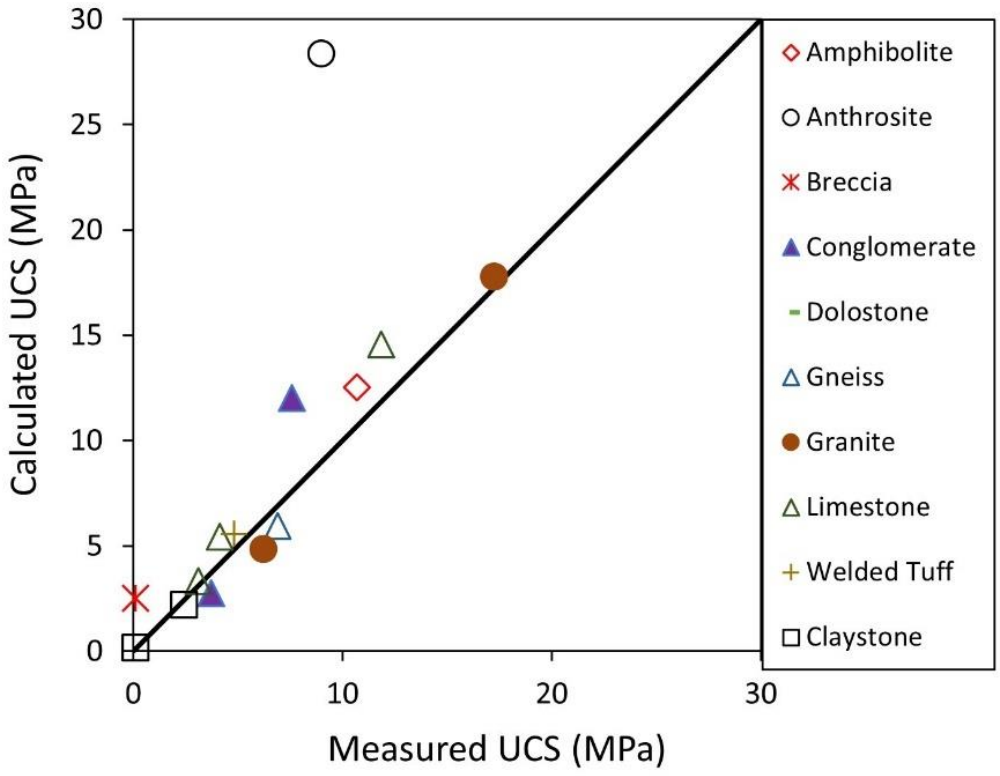


**Figure 4.29: Comparison of measured and calculated UCS values.**

**Table 4.11: Mohr-Coulomb results of tested rocks.**

| Sample ID | Age | Rock Type | Measured UCS, (MPa) | Calculated UCS, (MPa) | Cohesion, *c* (MPa) | Internal friction Angle, $\varphi$ (deg) |
|---|---|---|---|---|---|---|
| 1 | Miocene | Claystone | 0.41 | 0.28 | 0.09 | 25 |
| 9 | Oligocene | Breccia | 7.66 | 5.71 | 1.24 | 43 |
| 10 | Cretaceous | Conglomerate | 11.26 | 15.97 | 3.72 | 40 |
| 25 | Mississippian | Limestone | 27.59 | 9.19 | 4.14 | 6 |
| 27 | Permian | Limestone | 61.27 | 65.18 | 11.86 | 50 |
| 28 | Precambrian | Granite | 87.97 | 112.79 | 17.24 | 56 |
| 29 | Archaeon | Gneiss | 36.68 | 46.57 | 6.90 | 57 |
| 38 | Paleogene | Claystone | 20.61 | 27.31 | 5.52 | 46 |
| 44 | Eocene | Claystone | 8.50 | 11.95 | 2.41 | 46 |
| 45 | Ordovician | Dolostone | 23.13 | 32.21 | 5.86 | 50 |
| 46 | Cambrian | Conglomerate | 40.69 | 45.34 | 7.59 | 53 |
| 47 | Devonian | Limestone | 11.33 | 216.13 | 3.10 | 58 |
| 48 | Eocene | Welded Tuff | 21.13 | 22.74 | 4.83 | 44 |
| 52 | Proterozoic | Granite | N/A | N/A | N/A | N/A |
| 53 | Proterozoic | Anorthosite | 44.26 | 53.59 | 8.97 | 53 |
| 54 | Archeaon | Amphibolite | 60.52 | 74.56 | 10.69 | 58 |
| 55 | Proterozoic | Granite | 26.77 | 38.21 | 6.21 | 54 |

Note: N/A –Unavailable specimen for testing.

### *4.5.3* HB *Parameters*

The non-linear failure criterion proposed by Hoek and Brown (1997) was used to calculate the non-linear shear strength of the tested samples. The HB material constant for intact rock ($m_i$) was calculated using the statistical method proposed by Hoek (2019) based on test results on a principal axes plane. The HB criterion was applied on the intact rock taking the HB parameters $a = 0.5$ and $s = 1$, to estimate the cohesion and internal friction angle. The determination of $m_i$ from the back calculation method was found to provide results that are comparable to the values proposed by Hoek and Brown (1997) for sandstones and hence was preferred in the calculations of the cohesion and internal friction angle.

The calculation of the material constant $m_i$ was conducted from a series of uniaxial and triaxial tests performed on the intact rock specimens for each sample. In this process, the major and minor principal stresses of the tested specimens were plotted, and a curve HB line was fitted through the points by substituting $a = 0.5$, $s = 1$, and $m_b = m_i$ in the generalized HB criterion (Figure 4.7) in terms of major and minor principal stresses ($\sigma_1$ and $\sigma_3$) and $\sigma_c$ is the UCS value. The only unknown in the equation is the $m_i$, which can be easily back calculated. At least one UCS and two triaxial tests were required for the determination of $m_i$ value.

**Table 4.12: HB results of tested rocks.**

| Sample ID | Age | Rock Type | $m_i$ | *c* (MPa) | $\varphi$ (deg) | $\sigma_t$ (MPa) |
|---|---|---|---|---|---|---|
| 1 | Miocene | Claystone | 1.63 | 0.17 | 14.00 | 0.26 |
| 9 | Oligocene | Breccia | 24.18 | 2.52 | 26.00 | 0.32 |
| 10 | Cretaceous | Conglomerate | 18.33 | 2.74 | 42.00 | 0.61 |
| 25 | Mississippian | Limestone | 53.80 | 5.43 | 51.00 | 0.51 |
| 27 | Permian | Limestone | 17.42 | 14.57 | 43.00 | 3.52 |
| 28 | Precambrian | Granite | 30.55 | 17.77 | 50.00 | 2.88 |
| 29 | Archaeon | Gneiss | 54.02 | 5.92 | 58.00 | 0.68 |
| 38 | Paleogene | Claystone | N/A | N/A | N/A | N/A |
| 44 | Eocene | Claystone | 46.27 | 2.20 | 39.00 | 0.19 |
| 45 | Ordovician | Dolostone | 39.40 | 5.14 | 46.00 | 0.59 |
| 46 | Cambrian | Conglomerate | 13.30 | 12.02 | 32.00 | 3.05 |
| 47 | Devonian | Limestone | 125.00 | 3.10 | 58.00 | 1.44 |
| 48 | Eocene | Welded Tuff | 19.19 | 5.57 | 38.00 | 1.10 |
| 52 | Proterozoic | Granite | N/A | N/A | N/A | N/A |
| 53 | Proterozoic | Anorthosite | 28.39 | 7.37 | 57.00 | 1.56 |
| 54 | Archeaon | Amphibolite | 41.99 | 12.53 | 49.00 | 1.44 |
| 55 | Proterozoic | Granite | 41.93 | 4.86 | 54.00 | 0.64 |

Note: *c*– Cohesion; $\sigma_t$– Tensile strength; $\varphi$ – Internal friction angle; $m_i$– HB parameter; N/A– Unavailable specimen for testing.

The intact rock material constant ($m_i$) values for all the tested rock samples are summarized in Table 4.12 along with the cohesion (*c*), internal friction angle ($\varphi$), and tensile strength ($\sigma_t$). Hoek & Brown (1997) and Marinos & Hoek (2001) recommended the range of $m_i$ values of limestone as $12 \pm 3$, claystone $4 \pm 2$, granite $32 \pm 3$, and gneiss $28 \pm 5$. However, we observed that the calculated values of $m_i$ ranged from 17.42 to 125 for limestone, 1.63 to 46.27 for claystone, significantly varying from the proposed range. Hoek & Brown (1997) reported that the value of $m_i$ can vary significantly with variations in the rock $\beta$ angle as the failure will occur along a weakness plane. The reason for the variation observed could be because the values reported are for intact rock specimens tested normal to bedding whereas the intact rock specimens tested in the project do not show any apparent beddings.

The cohesion (*c*) and internal friction angle ($\varphi$) obtained from the linear MC criterion and non-linear HB criterion some values were comparable with each other while some show significant variation as illustrated in Figure 4.30 and 4.31, respectively. c and $\varphi$ values from the HB criterion were potted on the Y-axis and the values from the MC criterion were on the X-axis. Figure 4.30 shows that the cohesion values fell along the one-to-one line while few cohesion values from the HB criterion were higher than that from the MC criterion. A similar agreement was observed between the internal friction angles from both criteria.

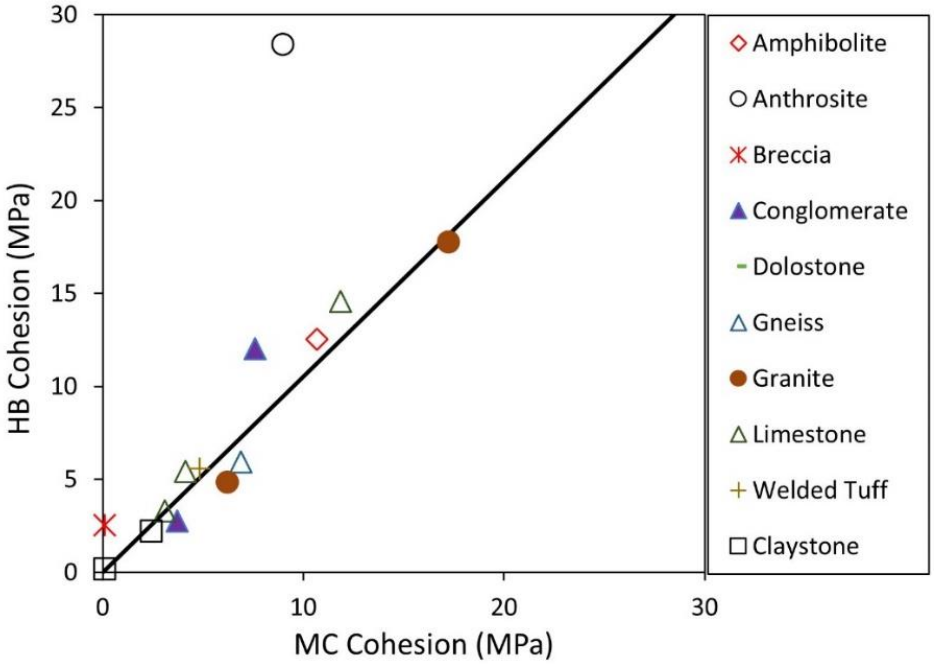


**Figure 4.30: Comparison of cohesion values from HB and MC Criteria for all rocks.**

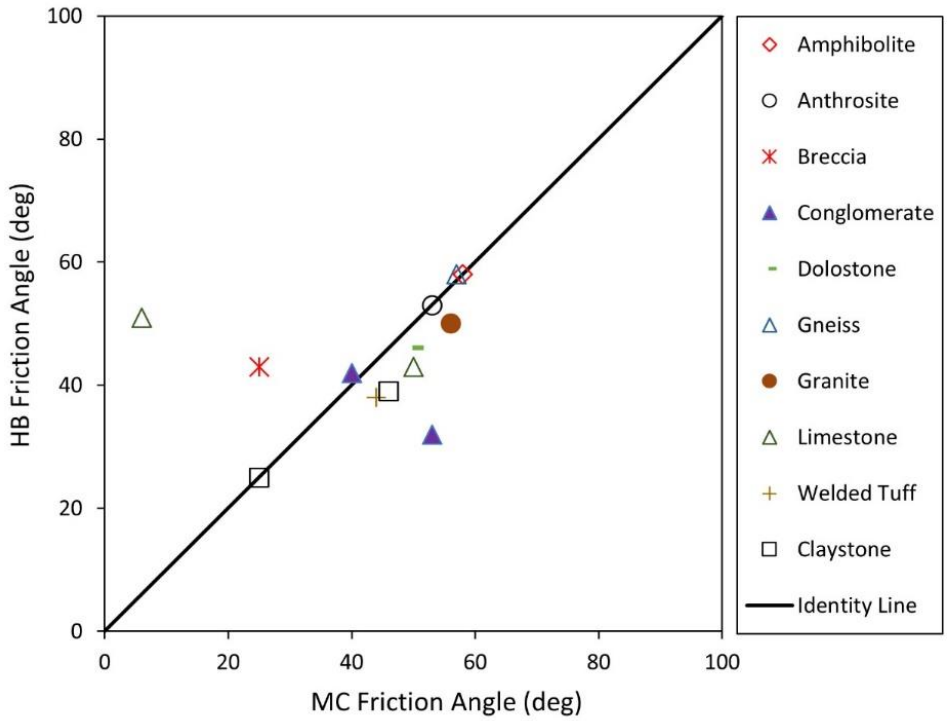


**Figure 4.31: Comparison of internal friction angle values from HB and MC Criteria for all rocks.**

### *4.5.4 Elastic Properties*

Table 4.24 summarizes the calculated Young's modulus ($E$) and Poisson's ratio ($\nu$) of the rock samples. The $E$ value of the tested limestones varied from 14.08 GPa for the Jefferson Formation (Sample 47) to 35.75 GPa for the Madison Formation (Sample 25). For Claystone, Young's modulus ranged from 0.01 GPa for the Ogallala Formation (Sample 1) to 0.42 GPA for the Wind River Formation (Sample 44). Similarly, the $\nu$ value or the deformability of the rocks under stress ranged between 0.09 for Madison Formation (Sample 25) to 0.11 for the Jefferson Formation (Sample 47). For Claystone, $\nu$ ranged from 0.07 for the Hanna Formation (Sample 38) to 0.33 for the Ogallala Formation (Sample 1).

| Sample ID | Formation | S ID | $E$ (GPa) | $\nu$ | Avg $E$ (GPa) | Avg $\nu$ |
|---|---|---|---|---|---|---|
| 1 | Claystone | 1a | 0.01 | 0.45 | 0.01 | 0.33 |
| | | 1b | 0.01 | 0.33 | | |
| | | 1c | 0.02 | 0.22 | | |
| 9 | Volcanic Breccia | 9a | 18.28 | 0.14 | 14.59 | 0.29 |
| | | 9b | 13.43 | 0.17 | | |
| | | 9c | 15.56 | 0.50 | | |
| | | 9d | 11.10 | 0.34 | | |
| 10 | Conglomerate | 10a | 11.80 | 0.28 | 13.41 | 0.29 |
| | | 10b | 8.81 | 0.22 | | |
| | | 10c | 18.55 | 0.39 | | |
| | | 10d | 14.48 | 0.27 | | |
| 25 | Limestone | 25a | 15.30 | 0.04 | 35.75 | 0.09 |
| | | 25b | 13.98 | 0.15 | | |
| | | 25c | 77.96 | 0.08 | | |
| 27 | Limestone | 27a | 29.61 | 0.27 | 27.52 | 0.10 |
| | | 27b | 15.66 | 0.01 | | |
| | | 27c | 32.55 | 0.03 | | |
| | | 27d | 32.25 | 0.08 | | |
| 28 | Granite | 28a | 34.41 | 0.10 | 30.27 | 0.22 |
| | | 28b | 21.42 | 0.48 | | |
| | | 28c | 34.97 | 0.08 | | |
| 29 | Hornblende Gneiss | 29a | 44.86 | 0.33 | 54.23 | 0.28 |
| | | 29b | 101.01 | 0.23 | | |
| | | 29c | 16.82 | 0.28 | | |
| 38 | Claystone | 38a | 4.57 | 0.08 | 4.07 | 0.07 |
| | | 38b | 3.58 | 0.05 | | |
| 44 | Silty Claystone | 44a | 3.91 | 0.07 | 4.26 | 0.09 |
| | | 44b | 4.38 | 0.09 | | |
| | | 44c | 4.49 | 0.12 | | |
| 45 | Dolostone | 45a | 9.83 | 0.05 | 8.37 | 0.007 |
| | | 45b | 7.59 | 0.07 | | |
| | | 45c | 7.70 | 0.08 | | |
| 46 | Limestone Pebble Conglomerate | 46a | 14.50 | 0.07 | 15.00 | 0.23 |
| | | 46b | 16.74 | 0.25 | | |
| | | 46c | 8.61 | 0.25 | | |
| | | 46d | 20.14 | 0.34 | | |
| 47 | Limestone | 47a | 15.37 | 0.20 | 14.08 | 0.11 |
| | | 47b | 6.72 | 0.08 | | |
| | | 47c | 20.14 | 0.04 | | |
| 48 | Welded Tuff | 48a | 19.05 | 0.01 | 22.09 | 0.19 |
| | | 48b | 20.88 | 0.30 | | |
| | | 48c | 26.34 | 0.25 | | |
| 52 | Granite Pegmatite | N/A | N/A | N/A | N/A | N/A |
| 53 | Anorthosite | 53a | 21.18 | 0.07 | 18.42 | 0.08 |

**Figure 4.32: Elastic properties of tested rocks.**

| Sample ID | Formation | S ID | $E$ (GPa) | $\nu$ | Avg $E$ (GPa) | Avg $\nu$ |
|---|---|---|---|---|---|---|
| | | 53b | 19.49 | 0.09 | | |
| | | 53c | 14.60 | 0.07 | | |
| 54 | Amphibolite | 54a | 43.84 | 0.05 | 31.89 | 0.10 |
| | | 54b | 18.61 | 0.22 | | |
| | | 54c | 33.24 | 0.04 | | |
| 55 | Granite | 55a | 17.01 | 0.08 | 10.23 | 0.06 |
| | | 55b | 5.68 | 0.02 | | |
| | | 55c | 8.00 | 0.07 | | |

Note: S ID– Specimen ID; $E$– Young's modulus (GPa); $\nu$– Poisson's ratio; Avg – Average.

**Figure 4.32 (Continued): Elastic properties of tested rocks.**

## 4.6 Effect of Rock Specimen Size

The selection of specimen size for experimental studies and determining rock strength properties depends on various factors such as design requirements, sample geometry and size, rock condition, and cost. The International Society of Rock Mechanics (ISRM) suggests using a length-to-diameter ratio (L/D) ratio of the test specimen is proposed between 2 and 2.5. Hoek and Brown (1997) derived the equation shown in Figure 4.33 based on UCS results of different rock types to correct the UCS value for the specimen diameter ($d$) to an equivalent UCS $_{50}$ value of a 50-mm diameter specimen. The empirically derived constant ($k$) is suggested as 0.18 by Hoek and Brown (1997).

$$\frac{UCS}{UCS_{50}} = \left(\frac{d}{50}\right)^{k}$$

**Figure 4.33: Equation. Corrected UCS value.**

Hoek and Brown (1997) found that the UCS increases with the decrease in the specimen diameter. Many other researchers have studied the effect of specimen size and reported similar findings (Broch and Franklin 1972, Thuro et al. 2001, and Prakoso et al. 2011). To determine the sample size effect, two rock types (granite of Sample 29 and sandstone of Sample 39) were selected for the preparation of 25mm and 50mm diameter specimens. Triaxial tests at a confining pressure of 10 MPa were conducted on the granite specimens and UC tests were

performed on the sandstone specimens. The test results and the strength ratio (the ratio of compressive strengths for the 25mm specimen to the 50mm specimen) are shown in Figure 4.34.

| Rock Type | Confinement (MPa) | Compressive Strength (MPa) | | Strength ratio |
|---|---|---|---|---|
| | | 25mm diameter | 50mm diameter | |
| Granite | 10 | 200.27 | 73.18 | 2.74 |
| Sandstone | 0 | 9.39 | 5.37 | 1.74 |

**Figure 4.34: Effect of specimen sizes.**

Granite exhibited a greater size effect as suggested by the strength ratio of 2.74. Under a UC condition, the UCS of sandstone increased when the specimen diameter reduced from 50mm to 25mm, but the strength ratio was lower at 1.74. The results confirmed the effect of specimen sizes on compressive strengths under both UC and triaxial conditions.

# CHAPTER 5: MECHANICAL PROPERTIES OF SANDSTONE UNDER UNIAXIAL AND TRIAXIAL CONDITIONS

Sandstone is a common sedimentary rock that is widely distributed on the crust surface of the earth (Huang et al. 2021). An understanding of the strength and deformation behaviors of sandstone is essential for the design and simulation of geotechnical structures for underground environments and underground reservoirs for mineral extraction and subsurface storage (Hua et al. 2018). Although the mechanical behaviors of sandstone have been investigated in past studies, a more comprehensive study that involves a wide variety of sandstone formations under different loading conditions is important to understand sandstone behaviors and application in engineering designs and constructions.

## 5.1 Research Methods and Analysis

A total of 17 sandstone samples of different formations and porosities from Wyoming were tested under uniaxial and triaxial compression conditions and at room temperature. Most sandstone samples were collected from depths of 3 to 44m, and nine surface samples were also collected for testing. The sandstones had water contents ($w$) ranging from 0.14 to 13.30 percent and porosity ($n$) from 2.20 to 31.20 percent. In addition, historical UCS test data from the Wyoming Department of Transportation (WYDOT) for four sandstone formations were also included in the analysis.

The selected model can be evaluated by comparing the observed values of the response variable $(y_i)$ to the predicted values of the response variable $(\hat{y}_i)$. Two commonly used measures for this comparison are the Root Mean Square Error (RMSE) given by the equation shown in Figure 5.1 and the Mean Absolute Deviation (MAD) given by the equation shown in Figure 5.2.

$$\mathrm{RMSE} = \sqrt{\frac{\sum\left(y_{(i)} - \hat{y}_{(i)}\right)^2}{num}}$$

**Figure 5.1: Equation. Root Mean Square Error (RMSE).**

$$\mathrm{MAD} = \frac{\sum\left|y_{(i)} - \hat{y}_{(i)}\right|}{num}$$

**Figure 5.2: Equation. Mean Absolute Deviation (MAD).**

Where *num* is the number of observations. It is desirable to have a small RMSE and MAD for a reasonable candidate model. Predictions were generated for both the training dataset and the testing dataset. Predictions based on the training dataset were used to assess the goodness-of-fit of a set of initially proposed models. Predictions based upon the testing dataset were used to assess the predictive ability of models proposed by this research and those models appearing in the literature.

## 5.2 Mechanical Properties under Uniaxial Compression

UCS is one of the most commonly measured rock parameters in rock engineering (Yagiz 2009). Compressive strength generally decreases with the increase in water content, porosity, and mean grain size. Based on statistical results using R Studio software version 2022.02.2, the recommended model for the true mean UCS was linear in the predictors mean grain size ($d_m$ in mm), porosity (*n* in percentage), and water content ($w$ in percentage) as shown in Figure 5.4 and given by the equation in Figure 5.5 based on the training dataset that contained 193 data points with 31 formations from literature and 4 formations from Wyoming. Figure 5.3 and Table 5.1 represent uniaxial compression test results of Wyoming sandstone and sandstone collected from a historical database developed by WYDOT, respectively. Figure 5.6 represents experimental data for sandstones collected from the literature.

| Sample ID | Formation | Geological Period | Depth, m | D, mm | n, % | w, % | UCS, MPa | *E*, GPa |
|---|---|---|---|---|---|---|---|---|
| 16 | Flathead | Cambrian | 6.04 | 50 | 3.06 | 0 | 20.31 | 2.60 |
| 17 | Cloverly | Cretaceous | 30.34 | 50 | 21.20 | 0 | 11.61 | 1.51 |
| 18 | Sundance | Jurassic | 6.49 | 50 | 23.20 | 0 | 13.88 | 24.08 |
| 19 | Aspen | Cretaceous | 6.19 | 50 | 3.69 | 0 | 22.59 | NA |
| 23 | Lance | Cretaceous | Surface | 50 | 13.82 | 0 | 2.47 | 3.067 |
| 31 | Tensleep | Pennsylvanian | Surface | 50 | 12.80 | 0 | 55.90 | 12.79 |
| 32 | Arikaree | Lower Miocene | Surface | 50 | 10.90 | 0 | 12.18 | 4.39 |
| 33 | | | | 50 | 12.10 | 0 | 17.00 | 4.44 |
| 39 | Hanna | Paleogene | 43.96 | 25 | 13.80 | 0 | 9.39 | 2.21 |
| 41 | | | 23.26 | 25 | 15.40 | 0 | 9.65 | 1.91 |
| 43 | Wind River | Eocene | Surface | 25 | 13.60 | 0 | 47.59 | 7.64 |
| 49 | Bridger | Eocene | Surface | 25 | 26.20 | 0 | 13.91 | 6.83 |
| 50 | Fort Union | Paleocene | Surface | 25 | 13.80 | 0 | 6.00 | 1.15 |
| 51 | | | | 25 | 3.92 | 0 | 26.08 | 2.75 |
| 56 | Casper | Permian | Surface | 25 | 9.37 | 0 | 39.00 | 9.54 |

Note: D– Specimen diameter (mm); n– Porosity (%); w– water content (%); UCS– Unconfined compressive strength (MPa); *E*– Young's modulus (GPa).

**Figure 5.3: Summary of the UC test results of sandstone formations in Wyoming.**

**Table 5.1: A summary of UC test data from historical WYDOT database.**

| Formation | Geological Period | D, mm | *n*, Percent | Number of UC test | *w*, Percent | UCS, MPa |
|---|---|---|---|---|---|---|
| Flathead | Cambrian | 50 | 2.10 | 12 | 4.49 - 8.88 | 1.86 – 12.79 |
| Cloverly | Cretaceous | 50 | 18.00 | 10 | 0.27 – 5.33 | 10.56 – 61.21 |
| Sundance | Jurassic | 50 | 23.00 | 5 | 3.44 – 5.74 | 14.38 – 38.62 |
| Aspen | Cretaceous | 50 | 3.40 | 9 | 0.51 – 3.19 | 11.43 – 161.43 |

Note: D– Specimen diameter (mm); *n*– Porosity (Percent); *w*– Water content (Percent); UCS– Unconfined compressive strength (MPa).

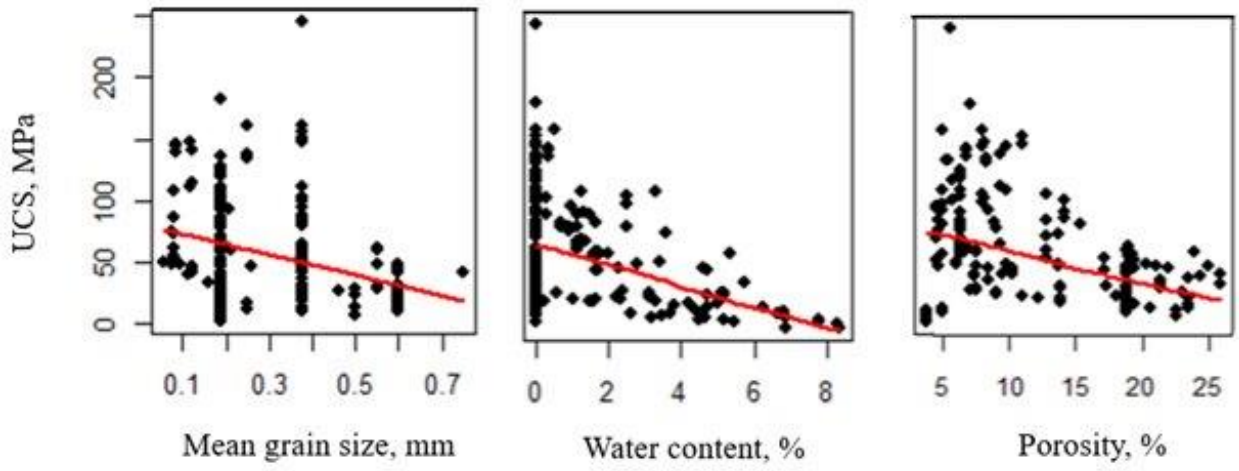


**Figure 5.4: Linear trend associated with the predictor variables on the true mean of the response UCS.**

*Relationship between the rock's physical properties and* UCS

The relationship between UCS and physical properties such as porosity, water content, and mean grain size was investigated, in addition to the relationship between UCS and Young's modulus.

$$\widehat{UCS}\ (MPa) = 109.87 - 2.39\, n - 9.12\, w - 33.74\, d_m$$

**Figure 5.5: Equation. The estimated Uniaxial Compressive Strength (UCS).**

| Formation, (Location) | D, mm | n, % | w, % | UCS, MPa | *E*, GPa | Reference |
|---|---|---|---|---|---|---|
| Shanxi, (Huaibei and Xuzhou mining areas) | 25 | 7.90 | 0-2.96 | 66.45-40.62 | 10.17-5.24 | Lu et al. (2017) |
| NA, (Chuxiong) | 50 | 8.50 | 0-2.29 | 71.91-50.48 | 7.05-5.52 | Cai et al. (2019) |
| Red Sandstone, (Hunan) | 50 | 11.60 | 0-3.40 | 108.00-55.50 | 16.80-11.30 | Tang et al. (2018) |
| NA, (Linyi) | 50 | 6.00 | 0-5.13 | 60.85-29.11 | NA | Geng and Cao (2020) |
| Red Sandstone, (Yichang) | 50 | 12.69 | 0-6.25 | 32.00-19.00 | 5.00-2.30 | Huang et al. (2021) |
| Gosford, (Sydney basin) | 42 | 18.00 | 0-6.90 | 43.98-11.69 | 6.58-1.98 | Masoumi et al. (2017) |
| NA, (Cauvery basin) | 28 | 3.00-25.00 | 0 | 48.00-10.60 | 30.00-8.50 | Chatterjee and Mukhopadhyay (2002) |
| NA, (France, Germany, USA, UK) | 20 | 6.50-28.00 | 0 | 161.40-30.10 | NA | Baud et al. (2014) |
| NA, (Dholpur) | 50 | 21.00 | 0 | 31.14-37.68 | 11.98-7.48 | Sirdesai et al. (2018) |
| Jiaozuo, (Henan) | 50 | 5.30-16.00 | 0.38 | 140.00-54.00 | 34.50-6.25 | Wu et al. (2013) |
| NA, (Longchang) | 50 | 4.70 | 0-1.61 | 127.45-61.17 | 20.98-12.34 | Shibin Tang (2018) |
| Black Sandstone, (NA) | 50 | 1.50 | 0 | 93.64 | 19.47 | Zhou et al. (2018) |
| Red Sandstone, (NA) | 50 | 2.00 | 0 | 43.32 | 8.52 | |
| Buntsandstein, (Pfinztal) | 40 | 8.00 | 0 | 114.00-142.00 | 16.70-26.40 | Egert et al. (2018) |
| Buntsandstein, (Tennenbach) | 40 | 9.00 | 0 | 42.00-47.00 | 11.60-11.50 | |
| NA, (Atovgvia da Baleia) | 50 | 3.60-18.60 | 0 | 135.70-17.60 | NA | Ludovico-Marques et al. (2012) |
| NA, (NA) | 50 | 3.00-7.60 | 0 | 87.20-27.90 | 20.00-6.40 | Huamin et al. (2018) |
| Red Sandstone, (Hunan) | 50 | 5.20-5.30 | 0 | 60.73-64.62 | 10.53-10.36 | Lin et al. (2020) |
| Red Sandstone, (Ganzhou) | 50 | 2.80 | 0-2.77 | 96.58-53.07 | 16.00-10.60 | Zhao et al. (2021) |
| NA, (Perth and Sydney basin) | 38 | 13.00-16.00 | 0 | 65.01-32.37 | 13.34 | Wasantha et al. (2018) |
| Red, Berea, and Buff Sandstone, (Utah and Ohio) | 55 | 5.60-23.00 | 0 | 183.00-75.00 | 25.00-11.60 | Kim et al. (2017) |
| NA, (Hongliulin coal mine) | 50 | 4.70 | 0-3.63 | 111.12-76.47 | 18.84-15.15 | Chen et al. (2021) |
| Red Sandstone, (Hongyang) | 50 | 6.48 | 0 | 101.28-107.38 | NA | Wu et al. (2018) |
| NA, (Rizhao) | 50 | 6.88 | 0 | 134.45-137.99 | 28.78-27.16 | Sheng-Qi Yang (2011) |
| Buntsandstein, (France) | 20 | 3.40-18.50 | 0 | 242.70-58.20 | 39.60-16.10 | Heap et al. (2019) |
| NA, (Chongqing) | 25 | 8.10 | 0 | 42.40 | 7.23 | Xu et al. (2017) |
| Red Sandstone, (Yunnan) | 50 | 8.50 | 0, 3.3 | 147.3, 112 | NA | Li et al. (2019) |

**Figure 5.6: Summary of UC test results of sandstones from literature.**

| Formation, (Location) | D, mm | n, % | w, % | UCS, MPa | *E*, GPa | Reference |
|---|---|---|---|---|---|---|
| Red Sandstone, (Hunan) | 50 | 12.60 | 0-4.70 | 75.00-48.00 | 10.95-7.70 | Yu et al. (2019) |
| Hawkesbury Sandstone (Australia) | 42 | 12.50 | 0 | 38.81-77.22 | 8.00-11.60 | Roshan et al. (2018) |

Note: NA–Unavailable; D– Specimen diameter (mm); n– Porosity (%); w– Water content (%); UCS– Unconfined compressive strength (MPa); *E*– Young's modulus (GPa).

**Figure 5.6 (Continued): Summary of UC test results of sandstones from literature.**

The negative linear trend in water content on predicting UCS from the equation shown in Figure 5.5 was consistent with past findings that explain the water weakening effect as a combination of mechanical and chemical processes that occur at a microscopic scale (Noël et al. 2021). The water weakening effect includes the dissolution of cement inside the rock that leads to the loosening of the internal microstructure (Geng & Cao 2020). Furthermore, the increase in water saturation means more voids are occupied with water and increases the likelihood of slippage between solid particles. For example, the UCS of Shanxi Sandstone in Figure 5.6 with a porosity of 7.90 percent decreases from 66.45 to 40.62 MPa or 39 percent when the water content increases from 0 to 2.96 percent, emphasizing the weakening effect of saturation (Lu et al. 2017).

Similarly, an increase in porosity reduced the predicted UCS values of both dry and saturated sandstones because pores are considered weak points within a rock matrix that induces stress concentration. Hence, more porous sandstones have more voids and higher porosity, reducing the strength of the rock skeleton (Ludovico-Marques et al. 2012). The negative linear trend of the mean grain size on the predicted UCS (Figure 5.5) was consistent with the past findings on artificial sandstones (Fattahpour et al. 2014). This observation can be explained by the fact that larger grains have longer grain boundaries which provide more flaws for the nucleation of cracks and stress concentration (Qi et al. 2022).

Table 5.2 summarizes several relationships for predicting the UCS of specific sandstone formations reported in the literature. These relationships were developed based on a single predictor variable of either water content ($w$) or porosity ($n$) in percentage. According to the independent testing dataset that contains 78 data points and includes 19 sandstone formations from literature and four sandstone formations from Wyoming, the proposed equation for UCS prediction fitted the testing dataset better than other equations according to the lowest RMSE and MAD values summarized in Table 5.3.

**Table 5.2: Assessment of prediction equations for UCS based on the testing dataset.**

| Sandstone Formation | Sandstone Location | Equation | RMSE | MAD | Reference |
|---|---|---|---|---|---|
| Tables 5.1, 5.2, and Figure 5.5 | Wyoming and literature data | $\widehat{UCS} = 109.87 - 2.39\,n\% - 9.12\,w\% - 33.74\,d_m$ | 31.60 | 22.13 | This study |
| Red Sandstone | Jiangxi Province, China | $\widehat{UCS} = 70.8734\,e^{-0.3188\,w\%} + 26.84$ | 37.01 | 26.59 | Zhao et al. (2021) |
| Red Sandstone | Hunan Province, China | $\widehat{UCS} = 55.21\,e^{-0.7502\,w\%} + 51.6$ | 40.63 | 29.82 | Tang et al. (2018) |
| Black Sandstone | Sichuan Province, China | $\widehat{UCS} = 80.604\,e^{-0.9044\,w\%} + 43.17$ | 46.44 | 34.11 | Shibin Tang (2018) |
| Gosford Sandstone | Sydney Basin, Australia | $\widehat{UCS} = 43.63\,e^{-0.20\,w\%}$ | 48.50 | 36.60 | Masoumi et al. (2017) |
| NA | Shanxi Province, China | $\widehat{UCS} = 44.6\,e^{-0.399\,w\%} + 66.60$ | 46.80 | 37.24 | Chen et al. (2021) |
| NA | Krishna-Godavari Basin, India | $\widehat{UCS} = -2.16\,n\% + 52.84$ | 50.91 | 38.72 | Chatterjee and Mukhopadhyay (2002) |
| NA | Atouguia da Baleia, Portugal | $\widehat{UCS} = 206.7\,e^{-0.129\,n\%}$ | 50.55 | 38.64 | Ludovico-Marques et al. (2012) |
| NA | Cauvery Basin, India | $\widehat{UCS} = -0.79\,n\% + 30.88$ | 58.31 | 45.55 | Chatterjee and Mukhopadhyay (2002) |

Note: NA–Unavailable; UCS –Unconfined compressive strength (MPa); $w$–water content (Percent); n–rock porosity (Percent); RMSE-Root Mean Square Error; MAD-Mean Absolute Deviation.

*Relationship between Young's Modulus and* UCS

The data presented in Table 5.1 and Figures 5.3 and 5.5, and Figure 5.5 were split randomly into training and testing datasets. The relationship between Young's modulus and UCS according to the training dataset is shown in Figure 5.7. The plot illustrated a linear increase in $E$ as UCS increases with $R^2$of 0.87.

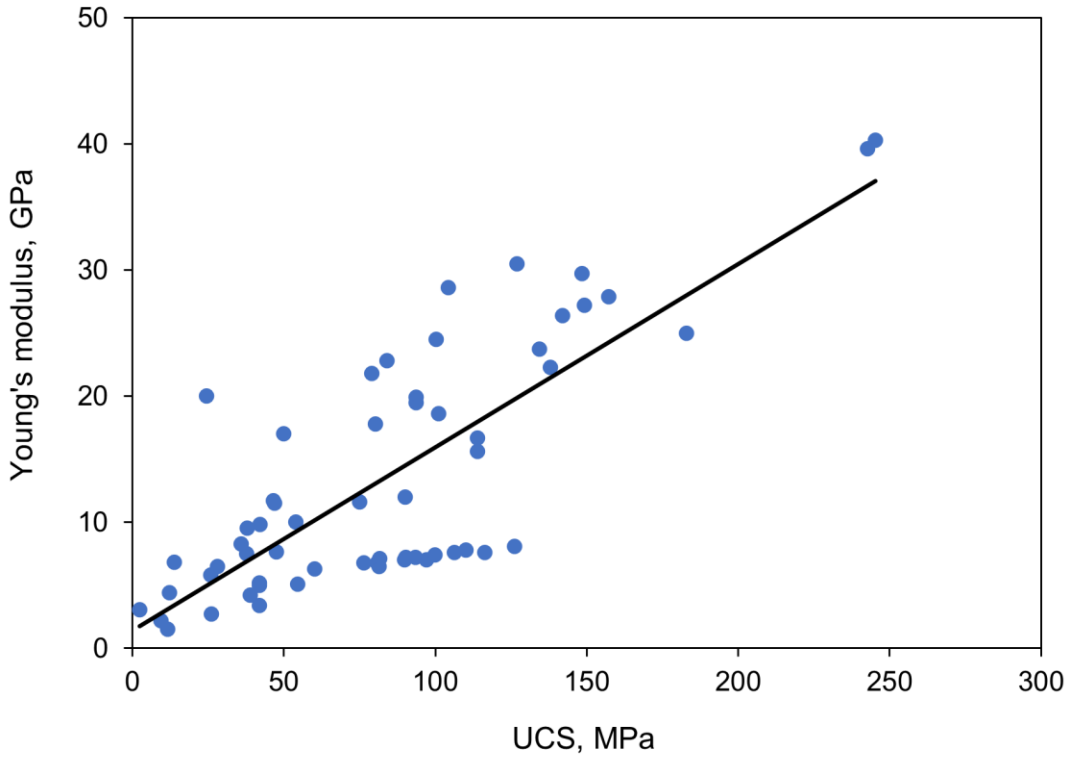


**Figure 5.7: Relationship between UCS and Young's modulus *E* of the training dataset.**

The prediction equation (Figure 5.8) described a linear increase in predicted Young's modulus with an increase in UCS according to the training dataset that contained 90 UC data points with 16 sandstone formations from literature and 12 sandstone formations from Wyoming. Other studies related the predicted UCS linearly to $E$ as summarized in Table 5.3 (Rohde and Feng 1990, Chatterjee & Mukhopadhyay 2002, and Malkowski et al. 2018).

$$\hat{E}(GPa) = 0.1455 \times UCS(MPa) + 1.3802$$

**Figure 5.8: Equation. The predicted Young's modulus of sandstone.**

A comparison of the proposed equation with other relationships reported in the literature is presented in Table 5.3. According to the testing dataset that contained 39 data points with 13 sandstone formations from literature and one sandstone formation from Wyoming, the proposed equation (Figure 5.8) had the lowest RMSE of 9.79 and MAD of 7.05 compared to those from literature, indicating a better prediction of Young's modulus.

**Table 5.3: Assessment of prediction equations for Young's modulus based on the testing dataset.**

| Sandstone Formation | Sandstone Location | Equation | Reference | RMSE | MAD |
|---|---|---|---|---|---|
| Tables 5.1 and Figure 5.5 | Wyoming and literature data | $\hat{E} = 0.1455\ UCS + 1.3802$ | This study | 9.79 | 7.05 |
| Island Creek | US Bureau of Mines | $\hat{E} = 0.05\ UCS + 20.6$ | Rohde and Feng (1990) | 12.17 | 10.59 |
| Krishna-Godavari and Cauvery basin | India | $\hat{E} = 0.73\ UCS + 0.17$ | Chatterjee and Mukhopadhyay (2002) | 33.35 | 26.90 |
| Upper Silesia Basin | Poland | $\hat{E} = 0.17\ UCS + 2.907$ | Malkowski et al. (2018) | 9.81 | 8.13 |

Note: RMSE–Root mean square error; MAD–Mean absolute deviation; UCS –Unconfined compressive strength (MPa); *E*–Young's modulus (GPa).

## 5.3 Mechanical Properties under Triaxial Compression

Conventional triaxial compression tests were conducted on 17 samples from 13 sandstone formations. GCTS RTR-1500 equipment has rapid, easy, and safe operation with automated cell assembly and meets the specifications of the ISRM and ASTM standards for triaxial testing of the rock samples. The axial load actuator has a capacity ranging up to 1500 kN and the triaxial cell can apply a maximum confining pressure of 140 MPa. The confinement was applied using an oil-filled stainless-steel chamber inside the frame. The initial seating pressure of 0.345 MPa is applied before the shearing stage. A summary of the triaxial compression test results of Wyoming Sandstone is given in Figure 5.10. Additional test results collected from the literature are summarized in Figure 5.11.

The mean $\sigma_1$ decreased with the increase in *n*. An increase in the internal surface area per unit rock volume resulting from a higher $\mathrm{n}$ decreases the predicted integrity of the rock and hence reduces its strength (Atapour and Mortazavi 2018a). On the other hand, the mean $\sigma_1$ generally increases linearly with an increase in the confining pressure $(\sigma_3)$ due to the strengthening effect of confinement on compressive strength.

Statistical results indicate that both $\mathrm{n}$ and $\sigma_3$ are important predictors of mean $\sigma_1$. The proposed equation (Figure 5.9) contains a polynomial of order two to capture the nonlinear relationship between n in percentage, $\sigma_3$ in MPa, and the true mean $\sigma_1$ in MPa based on the training dataset that contained 61 data points with 17 sandstone formations from literature and 13 sandstone formations from Wyoming.

$$\widehat{\sigma_1} = 90.68 + 1.63\, n\% + 2.9\, \sigma_3 - 0.12\, n\%^2 + 0.0042\, {\sigma_3}^2$$

**Figure 5.9: Equation. Predicted compressive strength of sandstone.**

Previously published relationships related $\sigma_1$ to $\sigma_3$ without considering the effect of porosity (Table 5.4). Having the lowest RMSE and MAD values based on an independent testing dataset that contained 27 data points and included 13 sandstone formations from literature and five sandstone formations from Wyoming, the combined effect of *n* and $\sigma_3$ (Figure 5.9) provided a better prediction of the $\sigma_1$.

| Sample ID | Formation | Geological Period/Epoch | Depth m | D, mm | n, % | $\sigma_3$, MPa | $\sigma_1$, MPa | *E*, GPa | c, MPa | $\varphi$, Degree |
|---|---|---|---|---|---|---|---|---|---|---|
| 16 | Flathead | Cambrian | 4.76 | 50 | 2.20 | 4 | 95.59 | 61.33 | 20.34 | 37 |
| | | | 5.85 | 50 | 5.35 | 10 | 120.12 | 41.027 | | |
| 17 | Cloverly | Cretaceous | 30.18 | 50 | 17.80 | 4 | 15.89 | 36.57 | 3.45 | 22 |
| | | | 30.03 | 50 | 19.50 | 10 | 31.90 | 27.34 | | |
| 18 | Sundance | Jurassic | 3.35 | 50 | 22.50 | 8 | 38.58 | 13.91 | 6.07 | 18 |
| 19 | Aspen | Cretaceous | 6.10 | 50 | 3.43 | 10 | 98.89 | 34.31 | 5.38 | 49 |
| 20 | Aspen | Cretaceous | 11.52 | 50 | 5.62 | 4 | 45.85 | 53.52 | 5.52 | 49 |
| | | | 11.65 | 50 | 7.18 | 10 | 99.53 | 1.41 | | |
| 21 | Denver and Arapahoe | NA | NA | 50 | 30.40 | 1 | 8.71 | 0.097 | 2.62 | 18 |
| | | | | 50 | 30.00 | 4 | 15.57 | 1.095 | | |
| | | | | 50 | 31.20 | 10 | 25.92 | 0.21 | | |
| 23 | Lance | Cretaceous | Surface | 50 | 9.31 | 2 | 5.07 | 1.72 | 11 | 8 |
| | | | | 50 | 12.18 | 4 | 36.50 | 4.64 | | |
| 31 | Tensleep | Pennsylvanian | Surface | 50 | 13.00 | 1 | 70.24 | 18.67 | 13.1 | 48 |
| | | | | 50 | 13.20 | 4 | 59.88 | 17.25 | | |
| | | | | 50 | 13.11 | 8 | 120.39 | 8.48 | | |
| 32 | Arikaree | Lower Miocene | Surface | 50 | 11.70 | 4 | 45.86 | 33.99 | 2.76 | 51 |
| | | | | 50 | 14.00 | 10 | 93.80 | NA | | |
| 33 | Arikaree | Lower Miocene | Surface | 50 | 12.20 | 4 | 46.49 | 8.95 | 3.1 | 54 |
| | | | | 50 | 11.10 | 10 | 111.03 | 0.34 | | |
| 39 | Hanna | Paleocene | 44.15 | 25 | 13.10 | 4 | 33.19 | 3.14 | 2.48 | 46 |
| | | | 44.60 | 25 | 15.20 | 10 | 70.72 | 5.82 | | |
| 41 | Hanna | Paleocene | 23.32 | 25 | 14.80 | 4 | 31.47 | 4.09 | 2.34 | 44 |
| | | | 24.09 | 25 | 16.80 | 6 | 42.96 | 4.17 | | |
| 43 | Wind River | Eocene | Surface | 25 | 14.50 | 4 | 14.00 | 17.90 | 8.96 | 56 |
| | | | | 25 | 14.00 | 10 | 21.11 | 7.70 | | |
| 49 | Bridger | Eocene | Surface | 25 | 27.20 | 4 | 34.68 | 29.59 | 4.48 | 29 |
| | | | | 25 | 24.20 | 10 | 42.44 | 4.40 | | |
| 50 | Fort Union | Paleocene | Surface | 25 | 12.20 | 4 | 31.48 | 3.52 | 1.38 | 47 |
| 51 | Fort Union | Paleocene | Surface | 25 | 5.92 | 6 | 89.69 | 5.03 | 5.52 | 55 |
| | | | | 25 | 3.92 | 8 | 147.00 | 7.70 | | |
| 56 | Casper | Permian | Surface | 25 | 11.10 | 4 | 72.56 | 14.38 | 7.93 | 53 |

**Figure 5.10: Summary of triaxial compression test results of sandstones from Wyoming.**

| Sample ID | Formation | Geological Period/Epoch | Depth m | D, mm | n, % | $\sigma_3$, MPa | $\sigma_1$, MPa | *E*, GPa | c, MPa | $\varphi$, Degree |
|---|---|---|---|---|---|---|---|---|---|---|
| | | | | 25 | 14.00 | 10 | 21.11 | 7.70 | | |

Note: NA– Unavailable; D– Specimen diameter (mm); n– Porosity (%); $\sigma_3$– Confining pressure (MPa); $\sigma_1$– Compressive Strength (MPa); *E*– Young's modulus (GPa); c-Cohesion (MPa); $\varphi$ – Internal friction angle.

**Figure 5.10 (Continued): Summary of triaxial compression test results of sandstones from Wyoming.**

| Formation, (Location) | D, mm | n, % | w, % | $\sigma_3$, MPa | $\sigma_1$, MPa | *E*, GPa | c, MPa | $\varphi$, Degree | Reference |
|---|---|---|---|---|---|---|---|---|---|
| Red Sandstone, (Yunnan) | 50 | 8.50 | 0 | 10-40 | 147.00-245.00 | 19.00-17.00 | 28.07 | 38.38 | Li et al. (2019) |
| | | 8.50 | 3.30 | 10-40 | 112.00-175.00 | 16.30-15.20 | 25.68 | 32.89 | |
| Red Sandstone, (Yichang) | 50 | 12.69 | 0-6.25 | 10 | 121.00-86.00 | 12.00-8.45 | NA | NA | Huang et al. (2021) |
| Buntsandstein, (Pfinztal) | 40 | 8.00 | 0 | 50-90 | 337.00-471.00 | 11.80-13.00 | 40 | 35 | Egert et al. (2018) |
| Buntsandstein, (Tennenbach) | 40 | 9.00 | 0 | 50-90 | 251.00-358.00 | 10.90-10.20 | 24 | 31 | |
| Hawkesbury, (Sydney basin) | 50 | 16.00 | 0 | 10-30 | 109.90-172.40 | NA | 22.6 | 31.5 | Roshan et al. (2017) |
| Black Sandstone, (NA) | 50 | 1.50 | 0 | 10-60 | 131.86-241.81 | 19.89-21.71 | 22.5 | 33.5 | Zhou et al. (2018) |
| Red Sandstone, (NA) | 50 | 2.00 | 0 | 10-60 | 93.40-131.49 | 10.76-9.90 | 13 | 23 | |
| NA, (Chongqing) | 25 | 8.10 | 0 | 5-40 | 77.00-219.09 | 8.03-16.07 | 30.16 | 38.4 | Xu et al. (2017) |
| NA, (Yunnan) | 50 | 8.50 | 0 | 2-10 | 110.02-185.97 | 26.71-30.97 | 13.86 | 56.29 | Kegang et al. (2016) |
| NA, (Rizhaou) | 50 | 6.88 | 0 | 8-35 | 198.92-316.38 | 29.03-33.69 | 30.58 | 45.7 | Sheng-Qi Yang (2016) |
| Shanxi, (Henan) | 50 | 6.53 | 0 | 10-50 | 187.81-283.93 | NA | 40 | 32 | Wang and Cui (2018) |
| Hawkesbury, (Sydney) | 54 | 13.00 | 0 | 4-25 | 58.00-116.00 | NA | 16.5 | 28 | Wasantha and Ranjith (2014) |
| Yellow Sandstone, (Zunyi) | 50 | 16.20 | 0 | 10-60 | 123.57-254.58 | 20.52-26.13 | 28 | 29.5 | Yang et al. (2020) |
| NA, (Xiangjiaba) | 50 | 2.64 | 0 | 3-20 | 144.81-266.08 | 27.18-31.12 | 32 | 44 | Wang et al. (2020) |
| Red Sandstone, (Shandong) | 55 | 6.48 | 0 | 5-35 | 115.10-242.90 | 18.81-23.80 | 22.42 | 37.8 | Yang and Jing (2013) |
| NA, (Qinghai) | 50 | 1.63 | 0 | 1-3 | 120.00-127.60 | NA | 27.74 | 38.32 | Liping et al. (2019) |
| | 50 | 1.92 | 0 | 1-3 | 109.30-122.30 | NA | 20.74 | 46.32 | |
| Yellow Sandstone, (Meishan) | 50 | 21.00 | 0 | 2-8 | 106.12-164.23 | NA | NA | NA | Huang et al. (2021) |
| Vosges Sandstone (France) | 50 | 22.00 | 0 | 0.1-60 | 32.10-175.00 | NA | NA | NA | Bésuelle et al. (2000) |

Note: NA– Unavailable; D– Specimen diameter (mm); n– Porosity (%); w– water content (%); $\sigma_3$– Confining pressure (MPa); $\sigma_1$– Compressive Strength (MPa); *E*– Young's modulus (GPa); c-Cohesion (MPa); $\varphi$– Internal friction angle (degree).

**Figure 5.11: Summary of triaxial compression test results of sandstones from literature.**

**Table 5.4: Assessment of prediction equations based on the testing dataset.**

| Formation | Location | Equation | Reference | RMSE | MAD |
|---|---|---|---|---|---|
| Figures 5.9 and 5.10 | Wyoming and literature data | $\widehat{\sigma_1} = 36.57 + 39.46\, n\% - 5.84\, n\%^2 + 0.29\, n\%^3 - 0.0047\, n\%^4 + 2.99\, \sigma_3$ | This study | 50.10 | 38.70 |
| Red Sandstone | Shandong | $\widehat{\sigma_1} = 3.9766\, \sigma_3 + 109.1850$ | Wu et al. (2018) | 53.88 | 45.02 |
| Yellow Sandstone | Zunyi | $\widehat{\sigma_1} = 4.36\, \sigma_3 + 77.33$ | Yang et al. (2020) | 51.52 | 43.00 |
| NA | Linyi | $\widehat{\sigma_1} = 9.008\, \sigma_3 + 83.56$ | Gong et al. (2019) | 146.46 | 104.18 |

Note: NA– Unavailable; $\sigma_1$– Compressive strength (MPa); $\sigma_3$– Confining pressure (MPa); *n*– Porosity (Percent); RMSE– Root mean square error; MAD–Mean Absolute Deviation.

# CHAPTER 6: MECHANICAL PROPERTIES OF SILTSTONE UNDER UNIAXIAL AND TRIAXIAL CONDITIONS

Siltstones may be massive or laminated, composed of quartz and clay minerals, but unlike shales, they show little effect of bedding on their compressive strength. Siltstones are generally interbedded with shales or fine-grained sandstones and rarely form thick deposits like shale and sandstone. Independent studies of the mechanical properties of siltstone like compressive strength and deformability are not commonly found. These properties are often deemed similar to other commonly occurring sedimentary rocks like sandstone. Although siltstones are not found in abundance, the effect of factors like temperature, confining pressure, mineral composition, porosity, and water content on their mechanical properties should be studied to improve the design of our civil infrastructures.

## 6.1 Research Methods and Analysis

A total of 42 siltstone samples from eleven locations in Wyoming were tested for UCS and used in the triaxial tests. Most siltstone samples were collected from depths of 6 to 28 m, and three surface samples were collected for testing. The siltstones had water contents (w) ranging from 0.57 percent to 21 percent and the porosity (*n*) ranged from 1.5 percent to 43.5 percent. In addition, historical UC test data from the Wyoming Department of Transportation (WYDOT) for eleven siltstone formations were also included in the analyses. Akaike Information Criterion (AIC) (Akaike 1974) and Bayesian Information Criterion (BIC) (Schwarz 1978) were selected as the comparison criteria for evaluating and selecting nonlinear prediction models. The Residual standard error (RSE) was also determined to improve the assessment of the nonlinear models. Mean bias, the ratio of measured over predicted, and coefficient of variation (COV) were also used to measure the relationship between the measured and predicted values. COV provides a statistical measure of dispersion of values around the mean and was calculated as a ratio of standard deviation to mean bias.

## 6.2 Mechanical Properties under Uniaxial Compression

The UC test results described in this chapter were primarily based on unpublished test data of siltstone rock cores obtained from the WYDOT. The analysis comprised two parts: first considering all siltstone data from literature and Wyoming, and later considering only the Wyoming Siltstone data. A summary of the Wyoming Siltstones used for UC tests is shown in

Table 6.1. The geological ages were listed from youngest to oldest. The porosity and water content of samples from younger ages were higher than that from older ages while samples from younger ages exhibited lower UCS than that from older ages.

**Table 6.1: UC test data for different siltstone formations in Wyoming and literature.**

| Siltstone Formation | Avg Depth (m) | Avg *n* (Percent) | Avg *w* (Percent) | Avg UCS (MPa) | Reference |
|---|---|---|---|---|---|
| White River | 23.84 | 49.88 | 35.28 | 0.60 | WYDOT |
| Ogallala | 28.33 | 51.05 | 37.29 | 0.15 | WYDOT |
| Green River | 15.29 | 31.95 | 18.31 | 3.56 | WYDOT |
| Upper Lance Creek | 14.14 | 30.08 | 16.89 | 1.55 | WYDOT |
| Frontier | 6.05 | 5.76 | 2.22 | 19.74 | WYDOT |
| Aspen | 6.95 | 7.41 | 3.08 | 14.25 | WYDOT |
| Bear River | 22.83 | 19.18 | 9.52 | 11.28 | WYDOT |
| Cody | 9.28 | 15.50 | 6.80 | 13.86 | WYDOT |
| Cloverly | 12.27 | 16.00 | 2.29 | 27.92 | WYDOT |
| Chugwater | 20.62 | 15.70 | 7.31 | 12.54 | WYDOT |
| Goose Egg | 25.28 | 24.62 | 12.29 | 0.30 | WYDOT |
| Eidsvold Basin | - | - | 0.0 | 61.58 | Wanniarachchi et al. (2018) |
| Zhungdong | - | - | 1.60 | 56.76 | Li et al. (2019) |

Note: Avg– Average; *n*– Porosity (Percent); *w*– Water content (Percent); UCS – Unconfined compressive strength; WYDOT– Wyoming Department of Transportation.

UCS of siltstone was related to easily measured physical properties such as water content, porosity, and $\rho$. Also, UCS was related to mechanical properties such as Young's modulus and axial strain at the peak stress.

*Water Content (w)*

A study on siltstone from Zhundong coalmine, China by Li et al. (2019) showed that the UCS varies nonlinearly with water content, and saturation of siltstone resulted in up to 50 percent reduction in UCS. The relationships between UCS in MPa and water content in percentage for siltstones reported by various researchers are summarized in Figure 6.1.

| Prediction Model for UCS (MPa) | Source | Location of Siltstone | Statistical Summary | | Comparison of Model | | |
|---|---|---|---|---|---|---|---|
| | | | Mean Bias | COV | RSE | AIC | BIC |
| $17.71e^{-0.383w} + 57.44$ | Li et al. 2019 | Xinjiang, China | 1.2 | 1.4 | 18.9 | 1712.7 | 1722.5 |
| $67.35 \times 0.77^{w}$ | This Study | World | 0.8 | 1.1 | 18.6 | 1705.9 | 1715.8 |
| $39.18 \times 0.83^{w}$ | This Study (All) | Wyoming, USA | 1.0 | 0.7 | 9.6 | 746.9 | 754.7 |
| $42.99 \times 0.81^{w}$ | This Study (Cretaceous) | Wyoming, USA | 0.9 | 0.6 | 12.5 | 398.5 | 404.2 |
| $69.40 \times 0.7^{w}$ | This Study (Triassic) | Wyoming, USA | 1.7 | 0.5 | 5.1 | 259.9 | 265.1 |

Note: UCS– Uniaxial compression test (MPa); COV– Coefficient of variation; w– Water content (%); RSE– Residual standard error; AIC– Akaike Information Criterion; BIC– Bayesian Information Criterion.

**Figure 6.1: Comparison of nonlinear models for UCS based on water content for siltstones.**

Figure 6.6 shows a comparison of UCS and $w$ for siltstones from literature and Wyoming. A power model was given by the equation in Figure 6.2 to describe this relationship. The UCS decreased with the increase in water content. The mean bias and coefficient of variation (COV) for the models from literature and the proposed models are provided in Figure 6.1. The COV for the model by Li et al. (2019) is 1.4 and the proposed model had a COV of 1.1 for all data and 0.7 for data from Wyoming Siltstones only. The RSE, AIC and BIC values for the proposed power model (Figure 6.2) for all siltstone data were lower than the model proposed by Li et al. (2019), and thus the proposed model yielded a better prediction of UCS.

A similar trend between UCS and $w$ was observed based on Wyoming Siltstone data, and a nonlinear power model given by the equation shown in Figure 6.3 can be used to describe this relationship (Figure 6.3). This proposed power model had RSE, AIC and BIC values of 9.573, 746.90, and 754.75, respectively, which were lower than the power model considering all literature data. This was expected as we limit the data to certain formations or geological ages, the mechanical properties of siltstones were similar to each other. The comparison based on statistical indices suggested that the proposed power models had lower AIC and BIC values and provided a more accurate UCS prediction than the model from the literature.

$$\widehat{UCS} = 67.35 \times 0.77^{w}$$

**Figure 6.2: Equation. Predicted UCS for siltstone from literature and Wyoming.**

$$\widehat{UCS} = 39.18 \times 0.83^{w}$$

**Figure 6.3 : Equation. Predicted UCS for Wyoming siltstone only.**

Wyoming Siltstones were from different formations and geological ages. The two most prominent geological ages of Wyoming Siltstones were the Cretaceous (135-66 million years ago) and the Triassic (250-205 million years ago). Figure 6.88a and 6.8b compare the UCS and water content for siltstones with the geological ages of Cretaceous and Triassic, respectively.

The power models for the Cretaceous and Triassic periods are given by the equations in Figures 6.4 and 6.5, respectively. For the Cretaceous period, the RSE, AIC, and BIC values were 12.51, 398.50, and 404.24, respectively. For the Triassic period, the RSE, AIC, and BIC values were 5.09, 259.89, and 265.10 respectively. The RSE, AIC, and BIC values of equation in Figure 6.4 for Cretaceous Siltstone and equation in Figure 6.5 for Triassic Siltstone were much lower than the model comprising of all siltstone data (Figure 6.2). This was expected as

the siltstones from the same age and location have similar physical properties and show similar trends in compressive strength. This was evident by the decreasing value of AIC and BIC from all data to Wyoming data followed by Wyoming data from individual geological ages. The higher AIC and BIC values of the equation in Figure 6.2 were attributed to a wider scatteredness of data from different geological ages and locations.

$$\widehat{UCS} = 42.99 \times 0.81^{w} \qquad (for\ Cretaceous\ Siltstone)$$

**Figure 6.4: Equation. Predicted UCS for Cretaceous siltstone.**

$$\widehat{UCS} = 69.40 \times 0.7^{w} \qquad (for\ Triassic\ Siltsone)$$

**Figure 6.5: Equation. Predicted UCS for Triassic siltstone.**

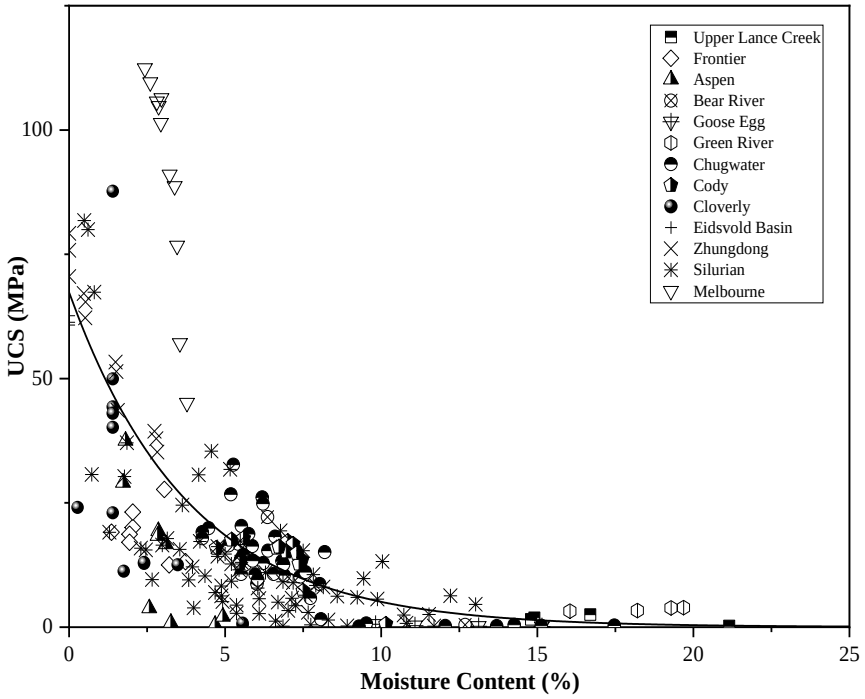


**Figure 6.6: UCS vs water content for siltstone.**

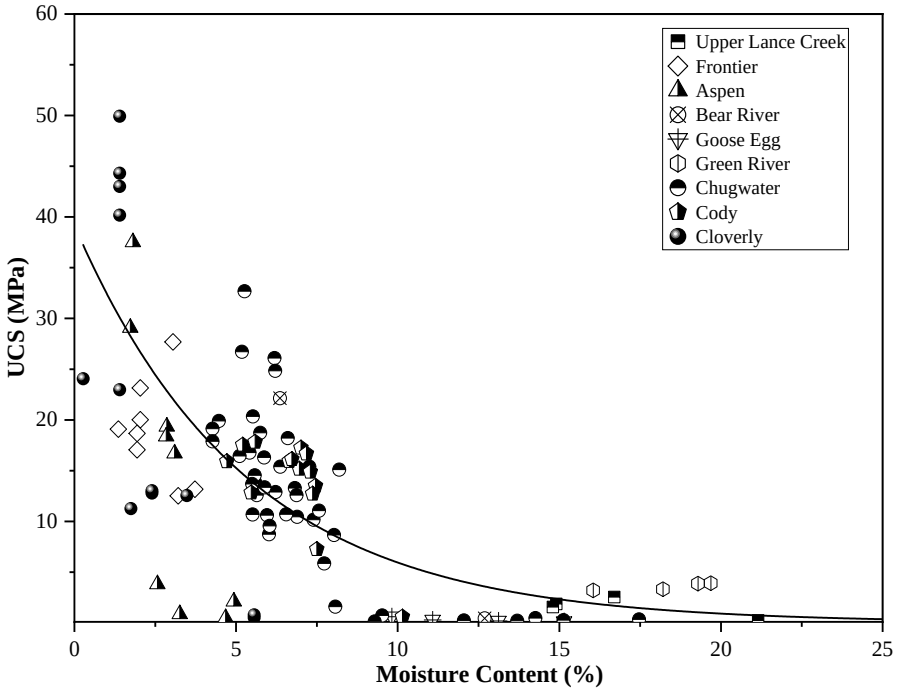


**Figure 6.7: UCS vs water content for Wyoming Siltstone.**

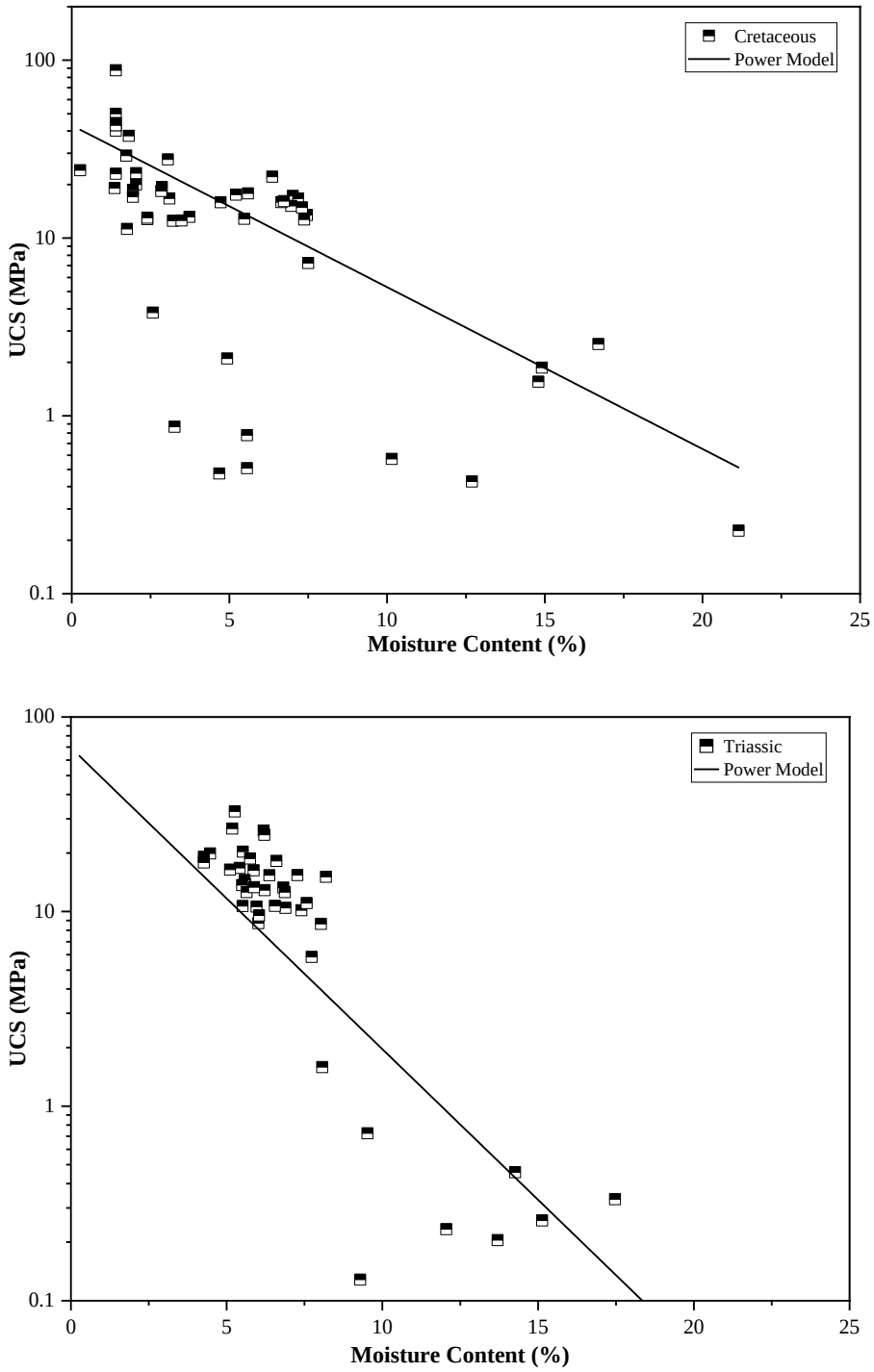


**Figure 6.8: (a) UCS vs water content for Wyoming Siltstones with the geological ages of Cretaceous, and (b) Triassic.**

Li et al. (2019) reported a gradual decrease in Young's modulus with increasing water content in siltstones. He reported a 35 percent reduction in Young's modulus of saturated siltstone when

compared to dry siltstone. Young's modulus was found to reduce nonlinearly and could be described by an exponential equation given by the equation shown in Figure 6.9. Erguler and Ulusay (2009), Hu et al. (2014), and Bian et al. (2019) have reported a loss of UCS and Young's modulus of about 90 percent on siltstones. Figure 6.11 shows the observed relationship between Young's modulus and water content for Wyoming Siltstones given by the equation in Figure 6.10. The RSE, AIC, and BIC of Li et al. (2019) model and the power model from this study are provided in Figure 6.12.

$$\hat{E} = 9.79 + 6.35e^{-0.796w}$$

**Figure 6.9: Equation. Predicted Young's modulus (Li et al. 2019).**

$$\hat{E} = 4.4725w^{-1.45}$$

**Figure 6.10: Equation. Predicted Young's modulus for Wyoming siltstone.**

The mean bias of Li et al. (2019) was low at 0.1 because of the constant 9.79 GPa value in the model. The observed value of Young's modulus in Wyoming Siltstones was very low at 0.08 to 2.85 GPa. The equation in Figure 6.9 over predicted the Young's modulus value. Although the mean bias of the equation in Figure 6.9 was lower, the COV, RSE, AIC and BIC values of equation in Figure 6.10 developed based on Wyoming Siltstones were lower indicating that the power model was the best in describing Young's modulus based on water content.

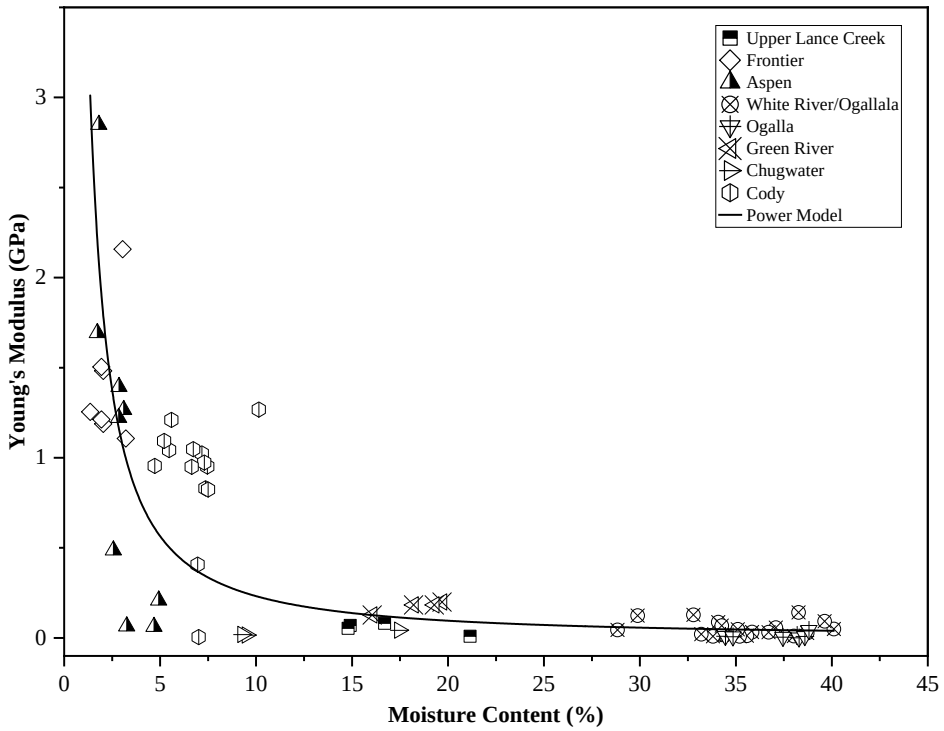


**Figure 6.11: Young's modulus vs water content for Wyoming Siltstones.**

| Prediction Model for $E$ (GPa) | Source | Location of Siltstone | Statistical Summary | | Comparison of Model | | |
|---|---|---|---|---|---|---|---|
| | | | Mean Bias | COV | RSE | AIC | BIC |
| $9.79 + 6.35e^{-0.796w}$ | Li et al. (2019) | Xinjiang, China | 0.1 | 1.26 | 0.46 | 92.84 | 99.54 |
| $4.4725w^{-1.45}$ | This Study | Wyoming, USA | 1.72 | 0.92 | 0.38 | 66.53 | 73.23 |

Note: $E$– Young's Modulus (GPa); COV– Coefficient of variation; w– Water content (%); RSE– Residual standard error; AIC– Akaike Information Criterion; BIC– Bayesian Information Criterion.

**Figure 6.12: Comparison of nonlinear models for *E* based on water content for siltstones.**

| Prediction Model for UCS (MPa) | Source | Location of Siltstone | Statistical Summary | | Comparison of Model | | |
|---|---|---|---|---|---|---|---|
| | | | Mean Bias | COV | RSE | AIC | BIC |
| $-0.0002n^2 + 0.28n + 18.82$ | Yasar et al. (2010) | Australia | 0.71 | 0.95 | 23.7 | 1287.8 | 1296.7 |
| $53.80(1 - \frac{n}{47.5})^{2.82}$ | This Study | World | 0.62 | 0.84 | 25.9 | 1069.7 | 1077.9 |
| $29.77(1 - \frac{n}{47.5})^{2.15}$ | This Study (All) | Wyoming, USA | 0.91 | 0.83 | 10.4 | 973.3 | 981.9 |
| $27.64 - 0.93\,n$ | This Study (Cretaceous) | Wyoming, USA | 1.06 | 0.86 | 14.7 | 414.6 | 420.3 |
| $48(1 - \frac{n}{47.5})^{3.8}$ | This Study (Triassic) | Wyoming, USA | 0.84 | 0.55 | 4.8 | 255.3 | 260.5 |

Note: UCS– Uniaxial compression test (MPa); COV– Coefficient of variation; w– Water content (%); RSE– Residual standard error; AIC– Akaike Information Criterion; BIC– Bayesian Information Criterion.

**Figure 6.13: Comparison of nonlinear models for UCS in terms of porosity for siltstones.**

*Porosity (n)*

Prediction equations for UCS in terms of porosity for siltstones were rarely developed and reported in the literature. Rzhevsky and Novick (1971) described a decreasing trend of UCS with porosity for carbonate and argillaceous rocks. Yasar et al. (2010) developed the prediction model for siltstones summarized in Table 6.4. Using the siltstone data from literature and Wyoming, Figure 6.18 showed that the UCS decreased with the increase in porosity, and a power model given by the equation shown in Figure 6.14 was established to describe this relationship. The RSE, AIC and BIC values for the literature model were higher than the two-power model developed in this study (Figures 6.14 and 6.15). A power model given by the equation shown in Figure 6.15 for Wyoming Siltstone only.

$$\widehat{UCS} = 53.80\left(1 - \frac{n}{47.5}\right)^{2.82}$$

**Figure 6.14: Equation. The predicted UCS for siltstone from literature and Wyoming.**

$$\widehat{UCS} = 29.77\left(1 - \frac{n}{47.5}\right)^{2.15}$$

**Figure 6.15: Equation. The predicted UCS for Wyoming siltstone.**

Figures 6.19a and 6.19b compare the UCS versus porosity for siltstones with geological ages of Cretaceous and Triassic, respectively. The linear and power function fitting the Cretaceous and Triassic periods is given by the equation shown in Figures 6.16 and 6.17, respectively. The linear fit in the Cretaceous period has $R^2$of 46 percent. RSE, AIC, and BIC values of equation in Figure 6.16 and Figure 6.17 are shown in Figure 6.13. The comparison of models showed that the literature model fitted the least followed by power models from all data and Wyoming only siltstone data. The AIC and BIC of models from the Cretaceous and Triassic periods were even lower as siltstones from specific locations and geological ages had similar properties which improved the goodness of correlation.

$$\widehat{UCS} = 27.64 - 0.93 \times n$$

**Figure 6.16: Equation. Predicted UCS for siltstone from Cretaceous age.**

$$\widehat{UCS} = 48 \times (1 - \frac{n}{47.5})^{3.8}$$

**Figure 6.17: Equation. Predicted UCS for siltstone from Triassic age.**

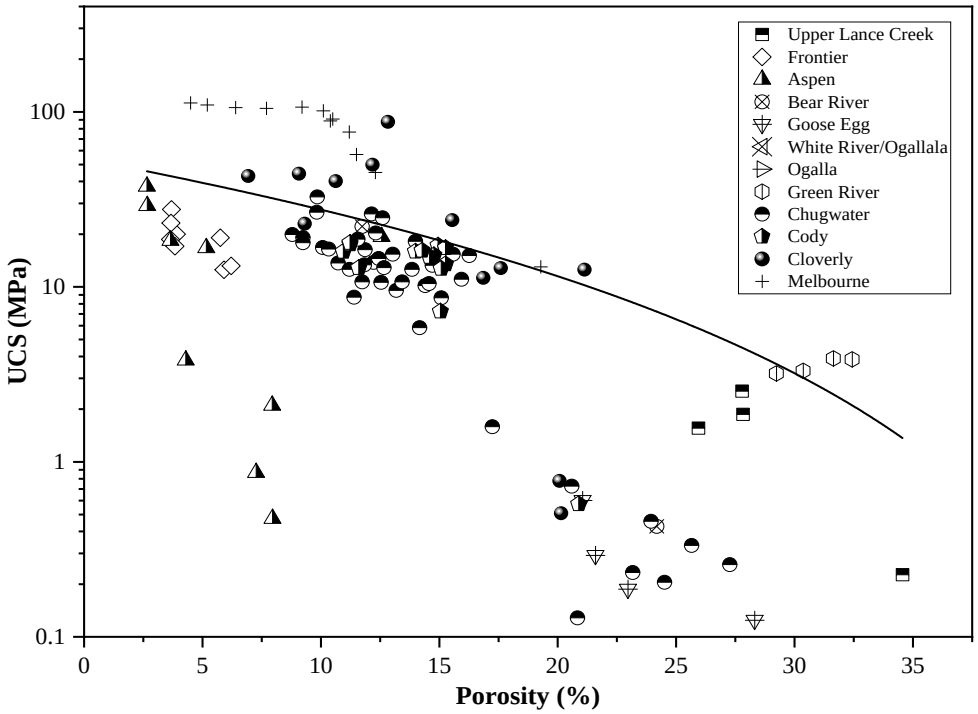


**Figure 6.18: UCS vs porosity for all siltstone data.**

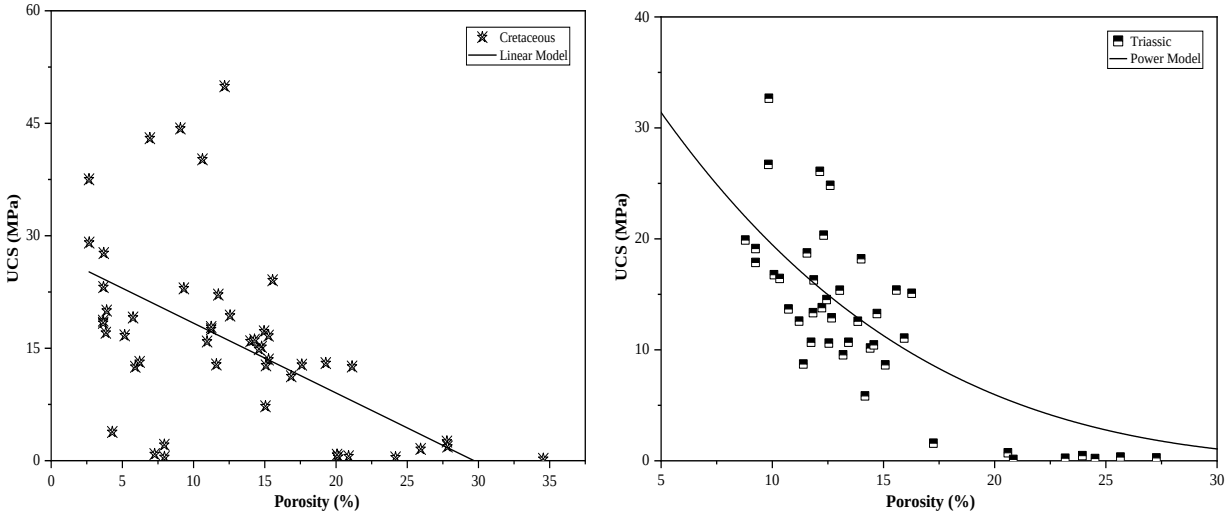


**Figure 6.19: (a) UCS vs porosity for Wyoming Siltstones with the geological ages of Cretaceous, and (b) Triassic.**

*Bulk Density ($\rho$)*

Figure 6.21 shows a positive relationship between UCS and $\rho$ of Wyoming Siltstones. Aspen Formation showed a sharp increase in UCS values from 0.47 MPa to 37.52 MPa with a minimal increase in $\rho$ from 2.33 g/cm$^3$ to 2.59 g/cm$^3$. Aspen Formation also showed an increase from 12.51 MPa to 27.68 MPa in UCS with the increase in $\rho$ from 2.51 g/cm$^3$ to 2.56 g/cm$^3$. In contrast, Green River Formation showed a slight decrease in UCS with the increase in $\rho$. Hence, the $\rho$ cannot be directly applied as a single variable to predict the UCS and the prediction model given by the equation in Figure 6.20 has a relatively low $R^2$ of 40 percent.

The prediction model has the RSE, AIC, and BIC values of 9.89, 961.03, and 969.88, respectively. The AIC and BIC values might increase or decrease when UCS vs $\rho$ data from other locations and formations of siltstones were included in the analysis. The RSE, AIC, and BIC values of UCS vs $\rho$, when compared to UCS vs $w$ and UCS vs $n$, were lower when all data were considered. When only Wyoming data were considered, AIC and BIC values from models based on water content and porosity were lower than that based on $\rho$.

$$\widehat{UCS} = 0.1582 \times \rho^{5.3966}$$

**Figure 6.20: Equation. the predicted UCS of Wyoming siltstones.**

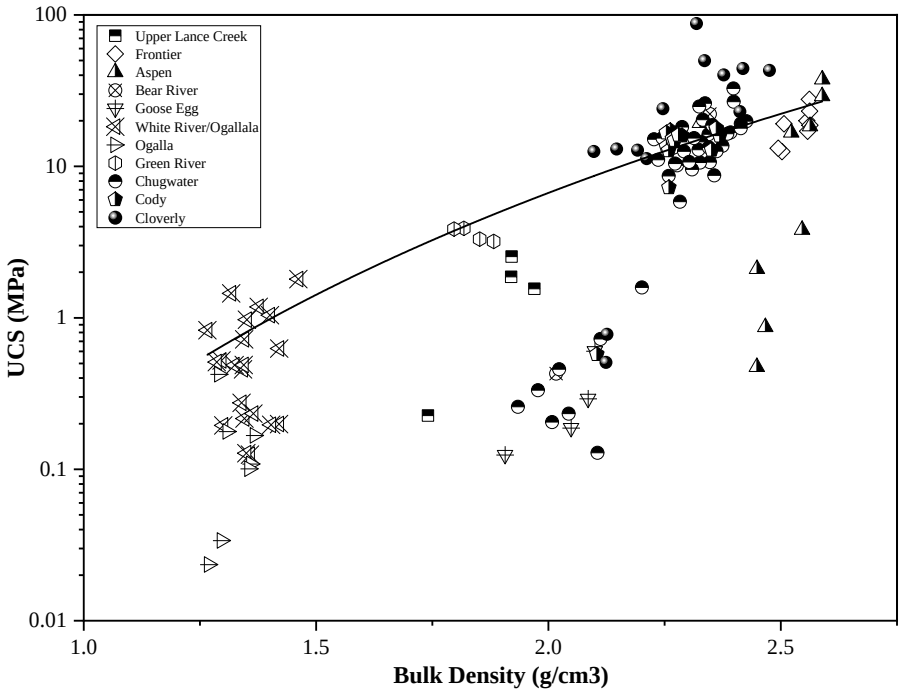


**Figure 6.21: UCS vs bulk density for Wyoming Siltstones.**

*Young's Modulus ($E$)*

An increase in the porosity of siltstone reduced Young's modulus and UCS. Figure 6.25 shows the decreasing exponential trend of Young's modulus with an increase in porosity given by the equation shown in Figure 6.22. The RSE, AIC, and BIC of the exponential model were 0.37, 61.89, and 68.59 respectively. These values were much less than the models for UCS vs porosity, hence $E$ correlated better than UCS with porosity.

$$\hat{E} = 0.564e^{-0.658\,n}$$

**Figure 6.22: Equation. Predicted Young's modulus of Wyoming siltstones.**

Comparing Young's modulus ($E$) with the $\rho$ of siltstone, we observed an exponential increase in $E$ with an increase in $\rho$. Figure 6.26 shows the increasing exponential trend of Young's modulus, in GPa, with an increase in $\rho$, in g/cm$^3$, given by the equation shown in Figure 6.23. The RSE, AIC, and BIC of the exponential model were 0.36, 62.54, and 69.24, respectively. These values were similar to the models for UCS vs $\rho$. Based on the statistical parameters, Young's modulus and UCS had a similar relationship with $\rho$.

$$\hat{E} = 0.0003e^{3.1359\rho}$$

**Figure 6.23: Equation. The predicted Young's modulus of Wyoming siltstones.**

Experimental data based on Wyoming Siltstone showed a linear relationship between $E$ in GPa and UCS in MPa as illustrated in Figure 6.27. The linear relationship can be described by the equation shown in Figure 6.24 with a coefficient of determination ($R^2$) of 86 percent. The RSE, AIC, and BIC values were 0.4789, 152.78, and 160.86, respectively.

$$\hat{E} = 0.0643 \times UCS + 0.0252$$

**Figure 6.24: Equation. The predicted Young's modulus of Wyoming siltstone in terms of UCS.**

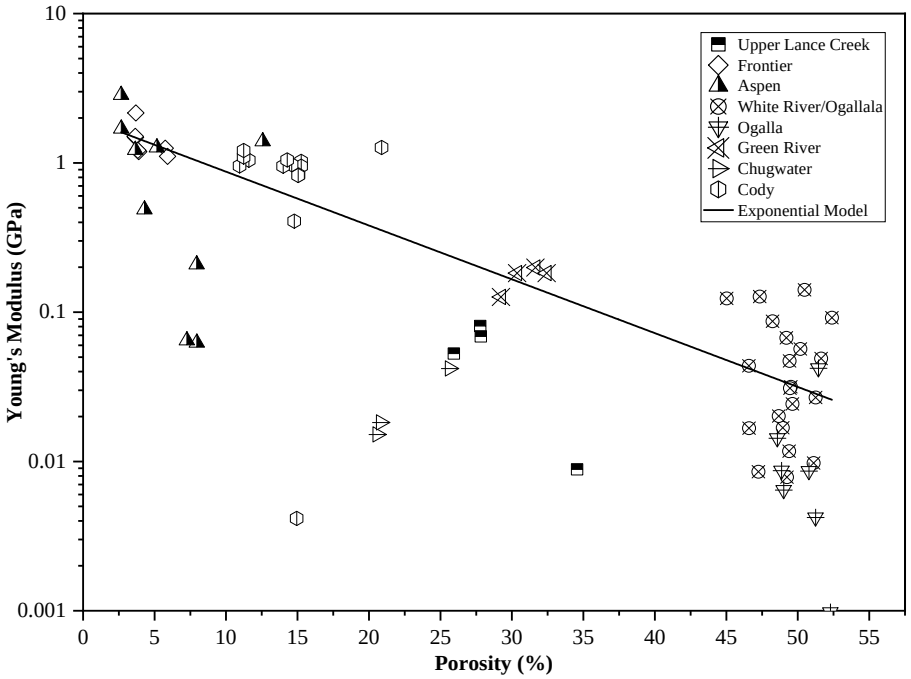


**Figure 6.25: Young's modulus vs porosity for Wyoming Siltstones.**

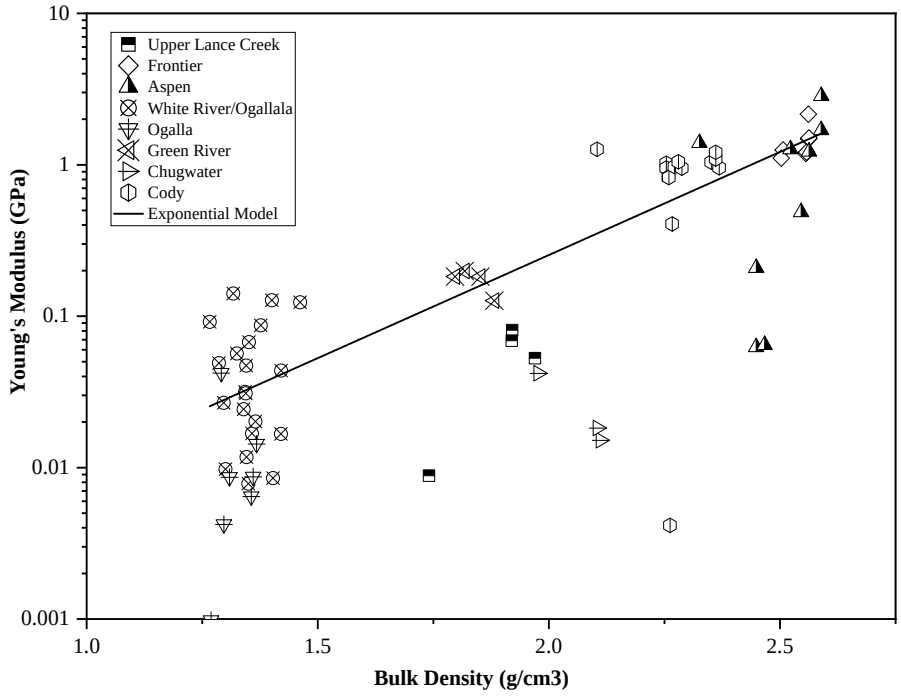


**Figure 6.26: Young's modulus vs bulk density for Wyoming Siltstones.**

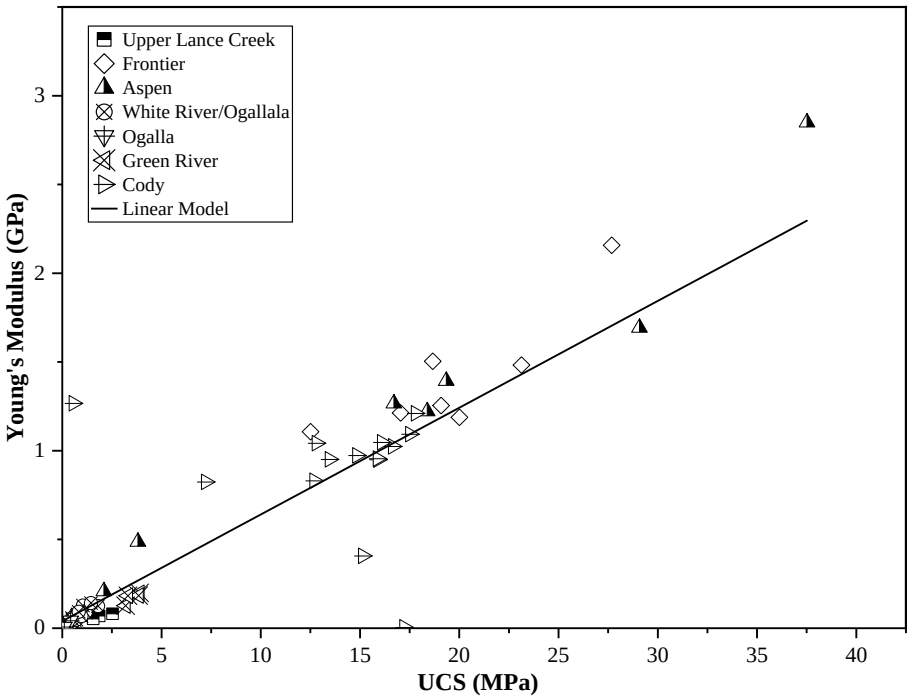


**Figure 6.27: Young's modulus vs UCS for Wyoming Siltstone.**

*Axial Strain at Peak Stress*

Figure 6.28 showed no apparent relationship between axial strain at peak stress (percent) and the UCS for Wyoming Siltstones. The axial strains at peak stress for the Cody, Upper Lance Creek, Frontier, Aspen, Bear River, Green River, Chugwater, and Cloverly Siltstones ranged from 1.8-2.5 percent, 3.6-4.5 percent, 1.6-2.4 percent, 0.8-2.2 percent, 1.8-4.8 percent, 2.3-4.91 percent, 2.2-2.9 percent, 1.9-5.5 percent, and 1.3-2.9 percent, respectively. Chugwater and Green River Siltstones showed a wide range of axial strains at failure whereas, Cody Siltstones showed a narrower range of axial strains at failure. Similar to UCS, the axial strain at peak stress (percent) showed no apparent relation with Young's modulus ($E$) as shown in Figure 6.29. White River/Ogallala Formations showed a wide variation of Young's modulus from 0.01 GPa to 0.14 GPa, when the axial strain rate changed from 1 percent to 3.5 percent whereas, the Cody Formation showed very little change in Young's modulus from 0.41 GPa to 1.27 GPa, when axial strain rate changed from 1.6 percent to 4.5 percent.

The difference in observed Young's modulus can be attributed to the mineral composition and physical properties of the individual formations. As this study did not focus on the mineral composition of siltstones, a clear description of the observed behavior cannot be made.

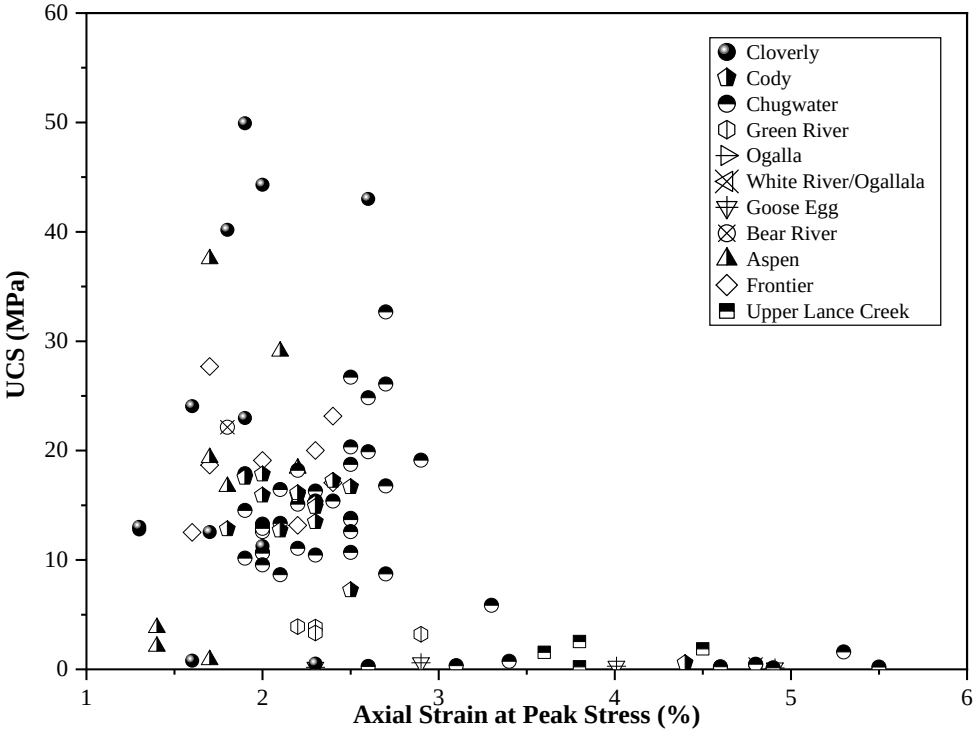


**Figure 6.28: UCS vs axial strain at peak stress for Wyoming Siltstone.**

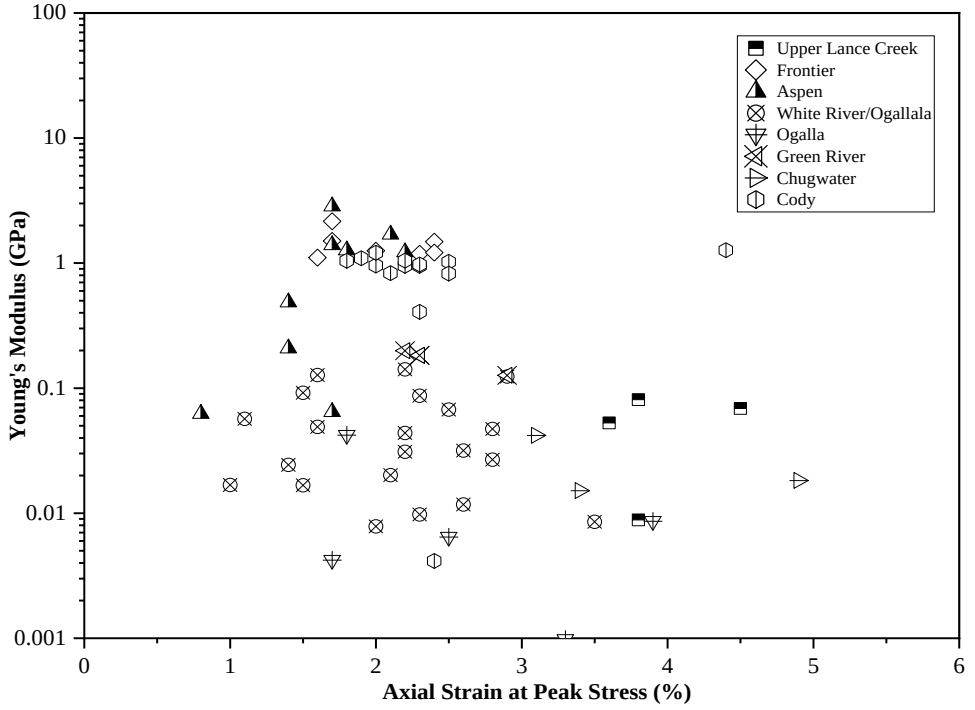


**Figure 6.29: Young's modulus vs axial strain at peak stress for Wyoming Siltstone.**

## 6.3 Mechanical Properties under Triaxial Compression

The analysis comprised all the literature data and tested Wyoming Siltstone data. Table 6.2 summarizes the geological age, formation, average depth, porosity, and water content of Wyoming Siltstone samples and samples from the literature.

*Confining Pressure and Porosity*

Triaxial compression tests conducted on Repetto Siltstones revealed that increasing the confining pressure ($\sigma_c$) at a constant temperature increased the peak strength (Handin et al. 1958). Similar observations have been made on sedimentary rocks by other researchers (Mogi 1971, Kumar et al. 2010, and Tang et al. 2018). In this study, the peak stress was plotted against the normalized confining pressure with porosity $\left(\frac{\sigma_c}{n}\right)$ in Figure 6.31. The test data showed that the peak stress increased with the increase in the ratio $\frac{\sigma_c}{n}$. This relationship can be described by a power model (Figure 6.30). The peak stress is in MPa and the ratio $\frac{\sigma_c}{n}$ in MPa/percent. The RSE, AIC and BIC values of the equation were 10.32, 289.15, and 294.07, respectively. The variation in data could be attributed to siltstone formations of different geological ages.

**Table 6.2: Summary of different siltstone formations for triaxial tests.**

| Formation | Avg Depth (m) | Avg n (Percent) | Avg *w* (Percent) | Confining Pressure (MPa) | Peak Stress (MPa) | Reference |
|---|---|---|---|---|---|---|
| Goose Egg | 4 | 21.13 | 0.57 | 1-10 | 31-42 | UW |
| Sundance | 9 | 26.07 | 5.32 | 1-10 | 9-23 | UW |
| Aspen/Bear River | 13 | - | - | - | - | UW |
| Pass Peak | 16 | - | - | - | - | UW |
| Wasatch | 20 | 33.17 | 22.25 | 0.3-10 | 0.8-11 | UW |
| White River | 22 | - | - | 0.1-0.7 | 1.4-2.7 | UW |
| Aspen | 11 | 3.25 | 1.48 | 1-20 | 137-222 | UW |
| Lance | Surface | 3.84 | 1.44 | 4-10 | 22-76 | UW |
| Bear River | 13 | 1.68 | 1.22 | 1-4 | 81-95 | UW |
| Arikaree | Surface | 12.98 | 2.65 | 4-10 | 45-82 | UW |
| Hanna | 57 | 4.25 | 1.65 | 4-10 | 57-93 | UW |
| Chugwater | Surface | 7.16 | 0.62 | 4-10 | 35-62 | UW |
| Ogallala | 27 | 42.92 | 21.29 | 0.3-0.4 | 0.4-0.6 | UW |
| Jurong | - | 0.18 | 0.22 | 1.25-10 | 143-367 | Diyuan Li et al. (2012) |
| Zhungdong | - | - | 2.8 | 5-40 | 77-236 | Li et al. (2019) |

Note: Avg– Average; *n*– Porosity (Percent); *w*–Water content (Percent); UW– University of Wyoming.

In Figure 6.32, Young's modulus was plotted against confining pressure with no visible trend. Unlike the peak strength, Young's modulus doesn't increase with an increase in confinement. In some formations like the White River, Aspen, and Bear River, a decrease in Young's modulus with an increase in confinement was observed.

$$\widehat{Peak\ Stress} = 39.09 \times \left(\frac{\sigma_c}{n}\right)^{0.68}$$

**Figure 6.30: Equation. The predicted peak stress for siltstone from literature and Wyoming.**

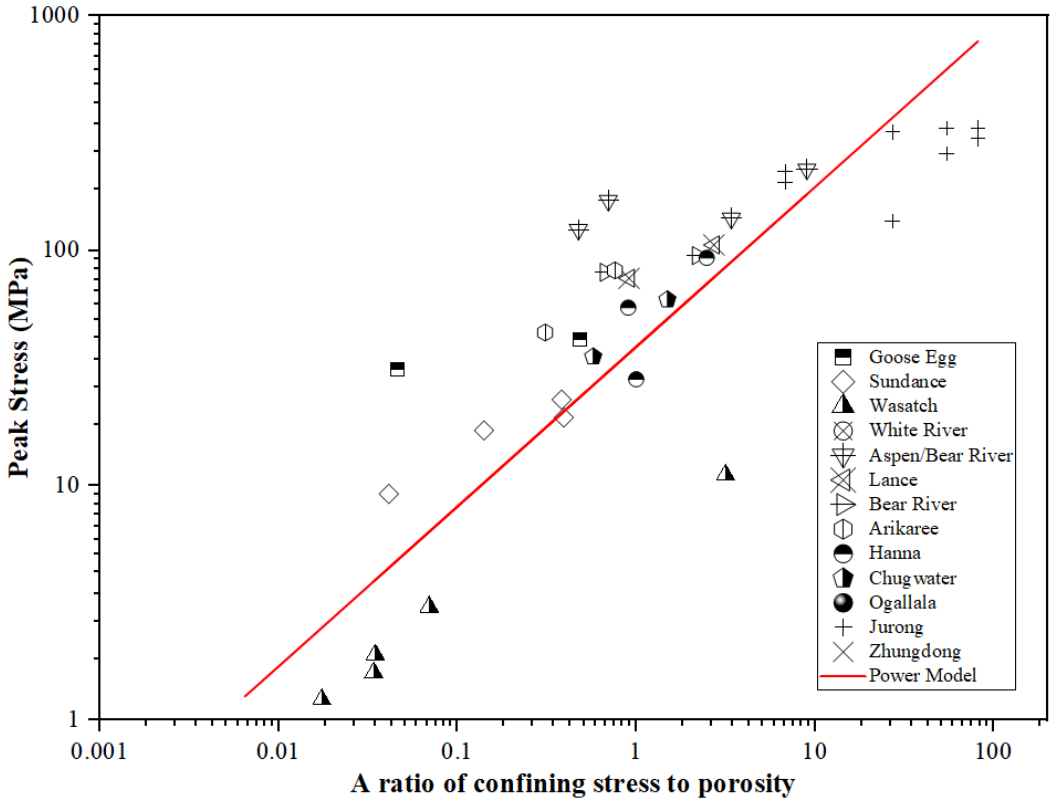


**Figure 6.31: Relationship between peak stress and the ratio of confining pressure to porosity.**

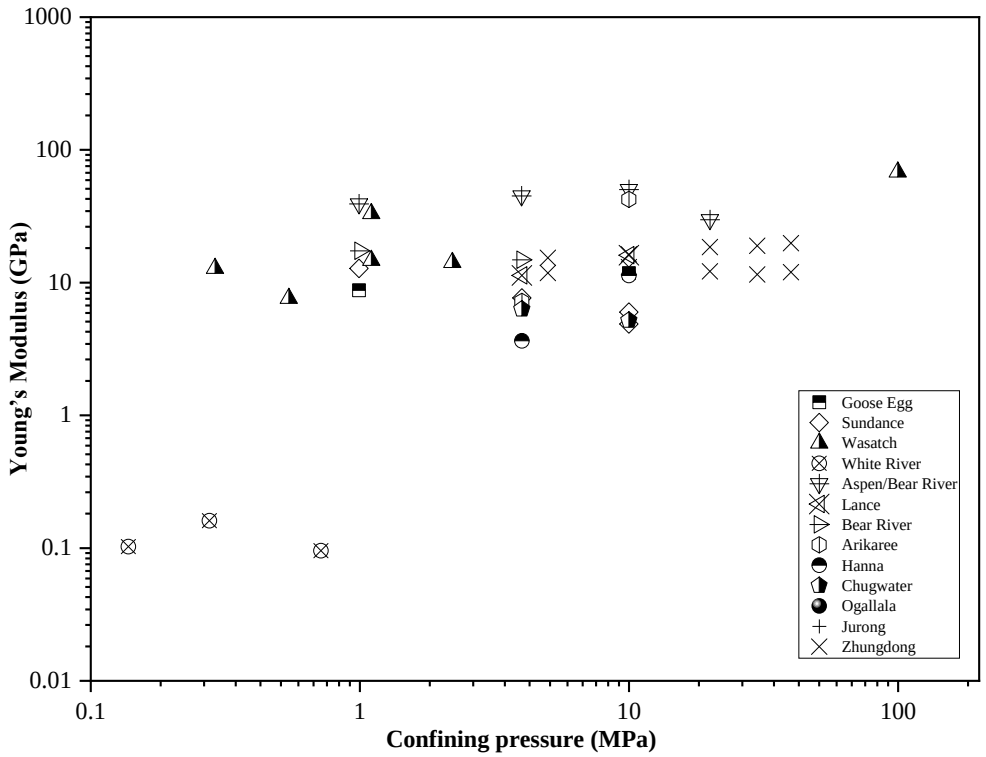


**Figure 6.32: The relationship between Young's modulus and the ratio of confining pressure to porosity.**

*Young's Modulus ($E$)*

Young's modulus decreased with the increase in rock porosity (Rzhevsky and Novick 1971). Figure 6.33 compares Young's modulus with the porosity of siltstones, and no apparent relationship can be observed. Wasatch, Sundance, Arikaree, and Hanna Siltstones showed an increase in Young's modulus with the increase in porosity while Bear River and Goose Egg Siltstones exhibited a decrease in Young's modulus with the increase in porosity. A comparison of Young's modulus to Poisson's ratio is shown in Figure 6.34. No relationship was observed between Young's modulus and Poisson's ratio for Wyoming Siltstone.

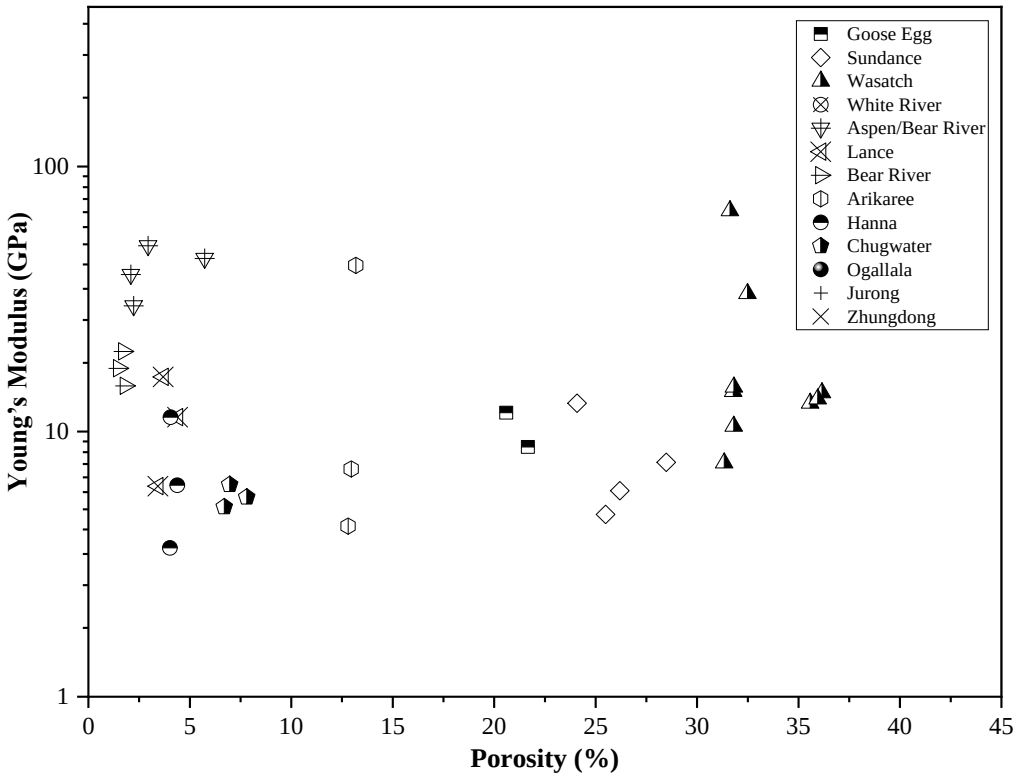


**Figure 6.33: Young's modulus vs porosity for siltstone.**

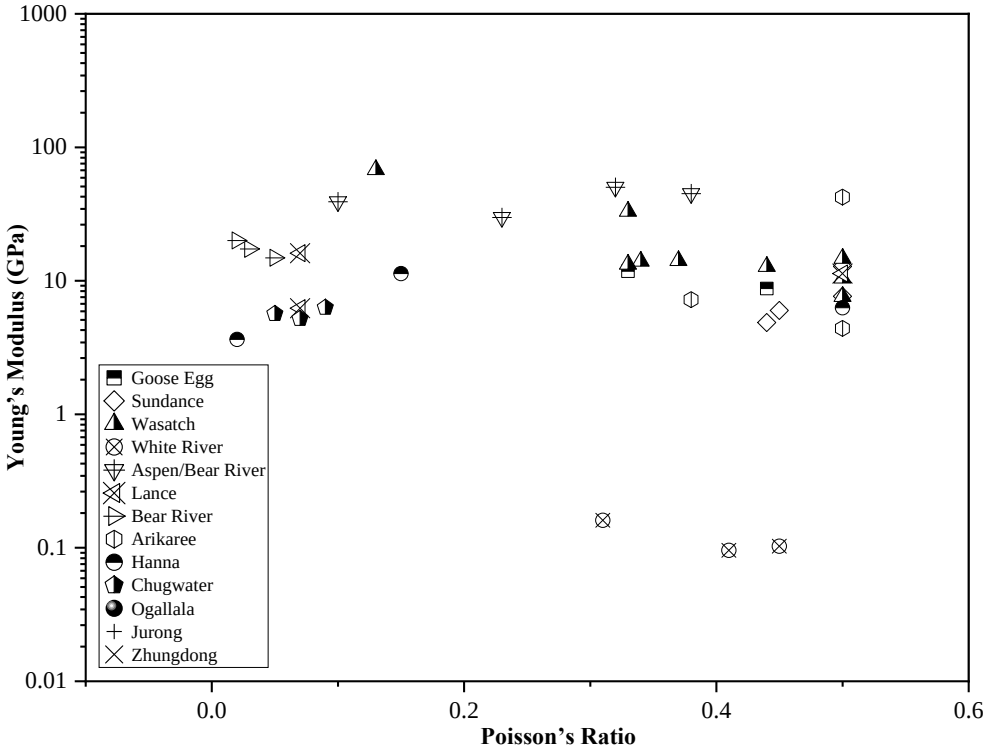


**Figure 6.34: Young's modulus vs Poisson's ratio for siltstone.**

*Cohesion & Internal Friction Angle (c & φ)*

Figure 6.37 shows that the cohesion decreased nonlinearly with the increase in porosity. A power equation (Figure 6.35) was developed to describe this relationship. Siltstones with porosity ranging from 0-5 percent exhibit a higher cohesion, and the cohesion of siltstones decreased gradually for porosity greater than 5 percent. To account for the effect of porosity on cohesion, the cohesion was normalized with the porosity and plotted against the water content in Figure 6.38 in an inverse relationship given by the equation shown in Figure 6.36.

$$\hat{C} = 32.17 \times n^{-0.674}$$

**Figure 6.35: Equation. The predicted cohesion for siltstone from literature and Wyoming.**

$$\frac{\hat{C}}{n} = 542.82e^{-0.614w}$$

**Figure 6.36: Equation. The normalized cohesion with respect to porosity for siltstone.**

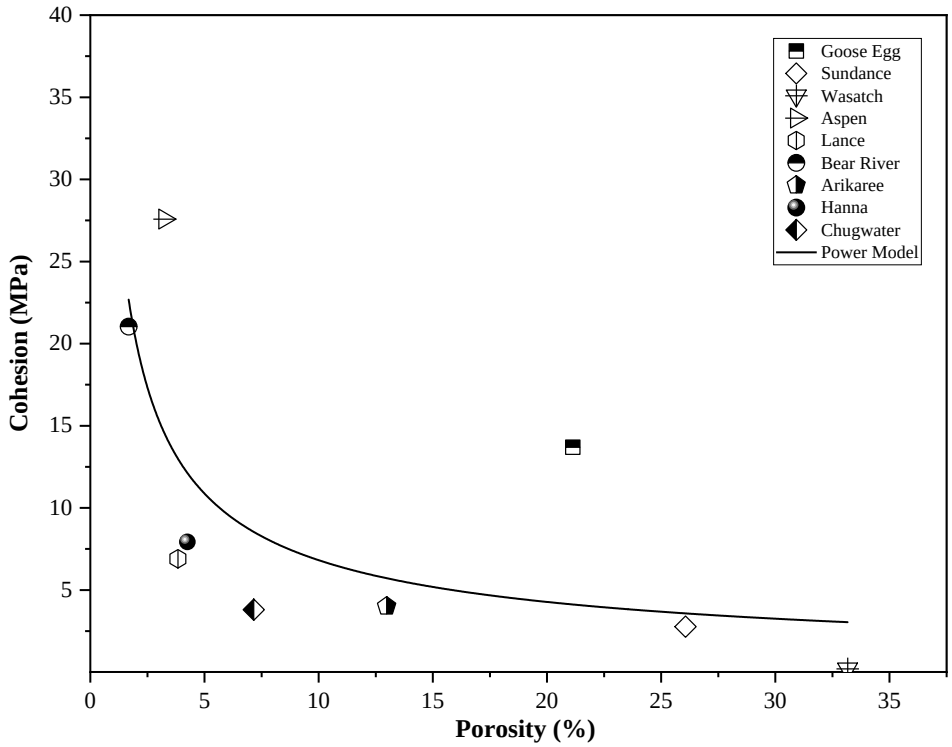


**Figure 6.37: Cohesion vs porosity for Wyoming Siltstones.**

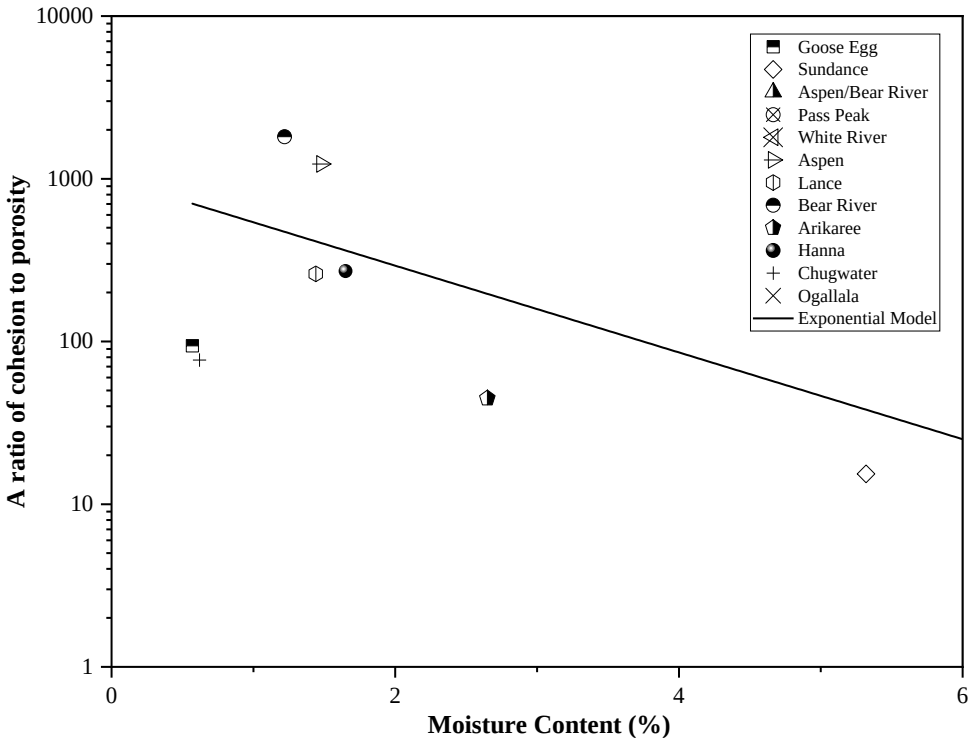


**Figure 6.38: The ratio of cohesion to porosity vs water content for siltstone.**

The RSE, AIC and BIC values of the equation in Figure 6.35 were 8.07, 66.86, and 67.45 and of equation in Figure 6.36 are 70.6, 131.36, and 131.59 respectively. The comparison of AIC and BIC suggested that cohesion better correlated to porosity alone and incorporating water content into the equation reduced the goodness of the fit. Hence, the equation in Figure 6.35 should be used to calculate cohesion from porosity for siltstones.

No relationship between the internal friction angle and porosity was observed in Figure 6.39. For siltstones with porosity ranging from 0 and 15 percent, the internal friction angles ranged from 35 and 50 degrees. When the porosity increased to 20 and 35 percent, the internal friction angle reduced to less than 20 degrees.

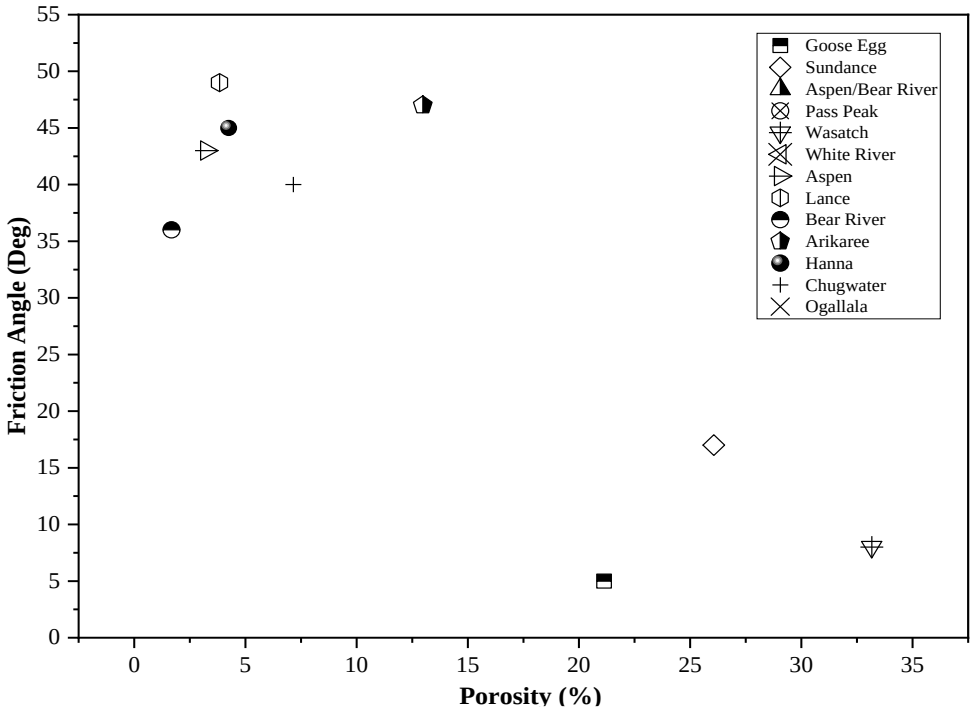


**Figure 6.39: Internal friction angle vs porosity for siltstone.**

# CHAPTER 7: MECHANICAL PROPERTIES OF SHALE UNDER UNIAXIAL AND TRIAXIAL CONDITIONS

Due to the layered structure, shale tends to split into thin layers along the laminations (fissile). Although geologically, shale is an argillaceous sedimentary rock, the classification for engineering purposes is not straightforward. Martin et al. (2016) provided a general geomechanical classification of argillaceous soil and rocks shown in Table 7.1. Underwood (1967) classified shales as “soil-like” and “rock-like” to distinguish between compacted shale and cemented shale, respectively.

Extensive research on shales for wellbore stability, reservoir simulation, and as a source of shale gas has been conducted in past decades. The mechanical properties (strength and Youngs modulus) of shales are of utmost interest in assessing borehole stability and hydrofracturing. Some studies have been made to study the geomechanical behavior of shale with temperature (Johnston 1987, and Masri et al. 2014) and creep behavior (Sone and Zoback 2013a, Sone and Zoback 2014). These studies are limited to a specific shale formation and a specific location. In addition, the mechanical properties of shales for civil infrastructure projects, including foundation, tunneling, and drilling, are not adequately quantified. Hence, this study focuses on the mechanical properties of shales from different formations and geological locations for a wide range of applications.

## 7.1 Research Methods and Analysis

A total of 33 shale samples from eight different locations in Wyoming were tested under both uniaxial and triaxial compression. Most shale samples were collected from depths of 13 to 33 m, while five surface samples were tested. Results from published literature on shales were collected for correlation analysis and the development of strength relationships. The mechanical properties of shales vary due to their anisotropic nature. Past research works have been conducted to study the effect of compaction, lithology, and diagenesis on the geomechanical properties of shales (Marsden et al. 1992, Horsrud et al. 1998, Dewhurst and Hennig 2003, Nygard et al. 2004, and Dewhurst et al. 2008). These shales have water content ranging from 5 percent to 22 percent and porosity from 12 percent to 38 percent. Akaike Information Criterion (AIC) (Akaike 1974) and Bayesian Information Criterion (BIC) (Schwarz 1978) were selected as the comparison criteria as they are widely used for nonlinear models that are proposed for describing the strength relationships.

## 7.2 Mechanical Properties under Uniaxial Compression

The UC test results described in this chapter were primarily based on unpublished test data of rock cores obtained from the state of Wyoming. The correlation analyses were conducted by considering shale test data from both literature and Wyoming and later considering only the Wyoming Shale data.

The literature data collected was from published papers for different formations of shales from different geographic locations. Most data are from USA, followed by China, Canada, and others. The type of shale encountered is a mix of soil-like and rock-like shales as defined by Underwood (1967). The number of tests for a specific formation of shale ranged from 1 to 161. The maximum porosity observed from the literature was 40 percent for Nigerian Shale, the maximum water content reported was 35 percent for Kansas Shale, and the maximum UCS was 318 MPa for Bowland Shale. Shales from Wyoming have a maximum porosity of 39 percent, maximum water content of 22 percent, and maximum UCS of 17 MPa. One of the factors for lower UCS of Wyoming Shale can be attributed to their depth of formation.

Wyoming Shales was collected from a shallow depth of below 30m, whereas shales from literature were mostly collected from deep mining and oil gas borings that run more than a couple hundred meters. The description of Wyoming and literature data used in the analysis are listed in Figure 7.1.
Shales UCS was related to physical properties such as water content, porosity, $\rho$, and $\beta$. Also, shale UCS was related to mechanical properties such as Young's modulus, Poisson's ratio, and axial strain at the peak stress.

*Water Content (w)*

It has been reported that the saturation of shales reduced the compressive strength by 90 percent and Young's modulus by 84 percent. The effect of water content on the mechanical properties of fine-grained sedimentary rocks has been reported by many researchers. An experimental study on coal mine Shale found that the increase in water content reduced compressive strength and Young's modulus but increased Poisson's ratio (Van Eeckhout 1976). Tandanand (1985) concluded that the compressive strength and tangent modulus of Illinois Shale decrease linearly with water content and lose most of their strength when the water content reaches 8 percent. Steiger and Leung (1992) found that the UCS of dry shales was 2-10

times greater than wet shales. Hsu and Nelson (1993) also reported a significant decrease in the compressive strength of clay shales in North America with the increase in water content. UCS and Young's modulus increase on desaturation and decrease on resaturation of the shale samples.

Lin & Lai (2013) reported a reduction in UCS and Young's modulus with the increase in water content on Barnett Shale. Similar to Van Eeckhout (1976), Lin & Lai (2013) also reported an increase in Poisson's ratio with the increase in water content. The reduction of Young's modulus and UCS of shales with the increase in the water content have also been reported by (Ghafoori 1995, Lashkaripour & Ghafoori 2002, Romana & Vasarhelyi 2007, Talal Al-Bazali 2012, and Cheng et al. 2015).

The reduction of compressive strength with an increase in water content can be attributed to the interaction of water with mineral surfaces altering their surface properties and the aid of pore water pressure, causing instability along the plane of weakness (Koncagul 1999). The relationships between water content vs UCS reported by various researchers and from this study are summarized in Figure 7.2.

| Prediction Model for UCS (MPa) | Source | Location of Shales | Model Comparison Criteria | | | |
|---|---|---|---|---|---|---|
| | | | RMSE | RSE | AIC | BIC |
| $86.976\ e^{-0.443w}$ | Talal AL-Bazali (2012) | Middle East | 37.79 | - | - | - |
| $82.279\ e^{-0.411w}$ | Lashkaripour et al. (2000) | - | 35.78 | 19.80 | 3922.7 | 3930.9 |
| $92.996\ e^{-0.602w}$ | Lashkaripour et al. (1993) | USA | 37.79 | - | - | - |
| $49.85\ e^{-2.523w} + 39.657$ | Fang et al. (2022) | China | 37.66 | - | - | - |
| $85.65\ e^{-0.358w}$ | Lashkaripour et al. (1993) | USA | 39.06 | - | - | - |
| $52.89\ e^{-0.342w}$ | Ghafoori et al. (1993) | Australia | 37.88 | - | - | - |
| $88.15\ \times\ 0.62^{w}$ | This Study | World | 19.73 | 4.4 | 2583.6 | 2595.9 |
| $6.25\ e^{-\frac{x}{7.66}}$ | This Study | Wyoming | 10.60 | 5.0 | 2908.3 | 2920.8 |

Note: UCS– Uniaxial compression test (MPa); COV– Coefficient of variation; w– Water content ( percent ); RSE– Residual standard error; AIC– Akaike Information Criterion; BIC– Bayesian Information Criterion.

**Figure 7.1: Prediction models for UCS of shales based on water content.**

Figure 7.4 compares the UCS with water content and illustrates the fitting of the power model proposed (Figure 7.2), from this study and the exponential model (Lashkaripour et al. 2000) from the literature. The root mean square error (RMSE), RSE, AIC, and BIC for the literature models and the proposed model are listed in Figure 7.1. RMSE is one of the most popular measures of estimating accuracy of predicted values of a proposed model. RMSE was chosen to describe the best model from literature as we cannot calculate individual AIC and BIC of many exponential equations for the same set of data. The lowest RMSE from literature was 37.78 based on the exponential model by Lashkaripour et al. (2000), and the proposed power model yields an RMSE of 19.73. The models from the literature were developed specifically for shales from a particular formation or location; however, the proposed model incorporates test data from all over the world including Wyoming. The RSE, AIC and BIC values for the proposed power model were lower than literature model suggesting a better prediction of UCS based on the proposed model.

Figure 7.5 shows an exponential model represented by the equation shown in Figure 7.3, for the UCS -water content relationship based on Wyoming Shale data only. The RSE, AIC, and BIC values of exponential model for data from Wyoming only were 4.0, 710.91, and 719.42. When fitting the exponential model with all data, the RSE, AIC, and BIC were higher than the power model, indicating that the power model provides the best prediction of UCS values of shale. This was because the formation and geological age of Wyoming Shales were similar, hence the relative scatterness of data was lower as indicated by the lower RSE, AIC, and BIC values but incorporating different formations and geological ages, the power model showed lower values of RSE, AIC, and BIC.

$$\widehat{UCS} = 88.15 \times 0.62^{w}$$

**Figure 7.2: Equation. The predicted UCS for shales from literature and Wyoming.**

$$\widehat{UCS} = 6.25\, e^{-\frac{w}{7.66}}$$

**Figure 7.3: Equation. The predicted UCS for Wyoming shale only.**

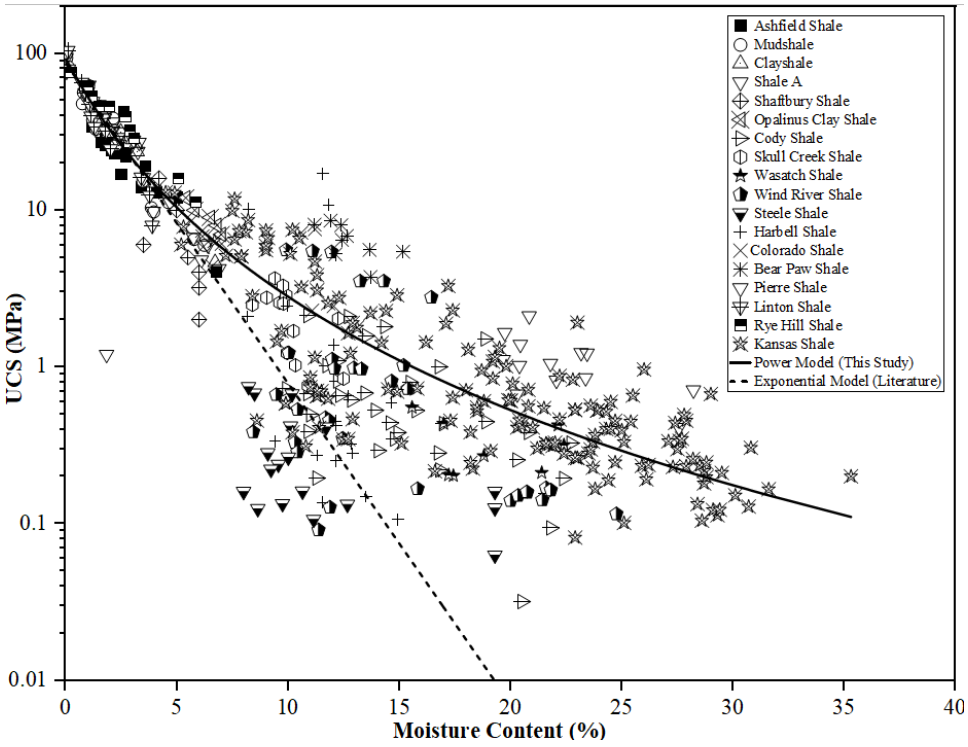


**Figure 7.4: UCS vs water content for all shales.**

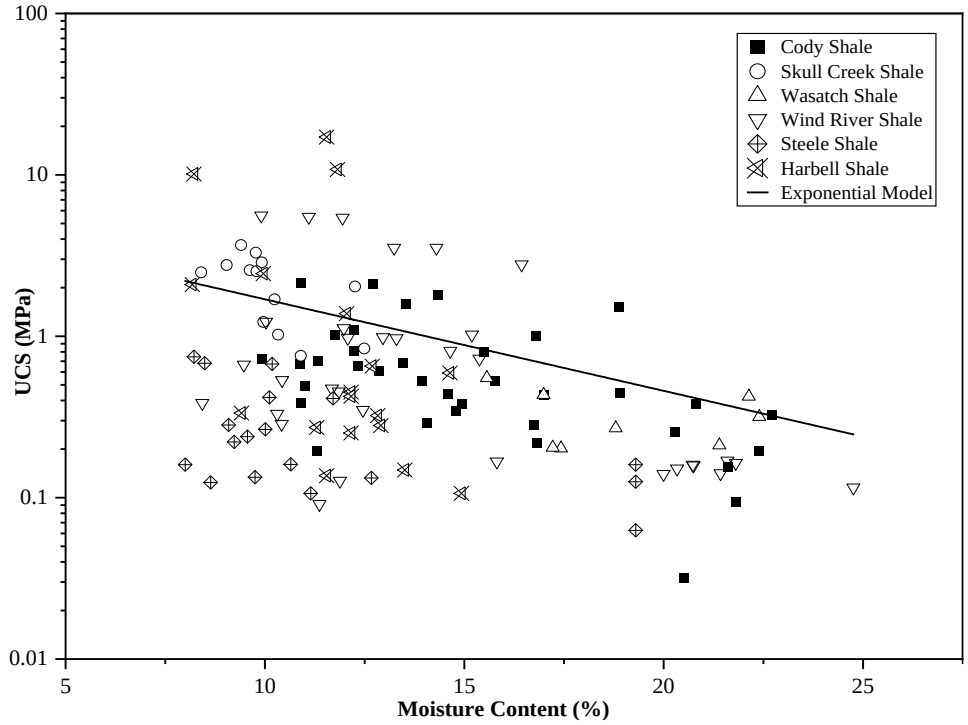


**Figure 7.5: UCS vs water content for Wyoming Shales.**

The relationship between Young's modulus and water content for Mud Shale studied by Fang et al. (2022) showed an exponential relationship. Young's modulus ($E$) of Mud Shale decreased by around 34 percent when the shale was saturated compared to the dry state. According to Chang et al. (2014), many factors like water content and porosity affecting the rock strength also affected Young's modulus. The study of Wyoming data and combined literature data represented in Figure 7.9 showed that the power model was the best fit model. The statistical summary and model comparison criteria are shown in Figure 7.6. The mean of Fang et al. (2022) was so low because of the constant 9.267 in the equation, it heavily over predicted Young's modulus in Wyoming Shales which have much lower values compared to the literature shales. The COV, however, was highest for the literature model and lowest for the power model, (Figure 7.7), developed for all shales. RSE, AIC and BIC values for the literature model were highest and lowest for the power model, the equation for Wyoming Shales only represented in the equation shown in Figure 7.8 and the data shown in Figure 7.10. Although the AIC and BIC values of the Wyoming Shale power model were negative, it's still the lowest and hence was the best model to estimate *E* from $w$.

| Prediction Model for $E$ (GPa) | Source | Location of Shales | Statistical Summary | | Model Comparison Criteria | | |
|---|---|---|---|---|---|---|---|
| | | | Mean Bias | COV | RSE | AIC | BIC |
| $5.086\ e^{-0.19w} + 9.267$ | Fang et al. (2022) | China | 0.1 | 1.74 | 0.34 | 45.7 | 52.1 |
| $28.121\ w^{-2.92}$ | This Study | World | 2.39 | 1.36 | 0.27 | 20.8 | 27.2 |
| $4.9896\ w^{-2.273}$ | This Study | Wyoming | 2.82 | 1.49 | 0.11 | -66.9 | -61.4 |

Note: $E$– Young's Modulus (GPa); COV– Coefficient of variation; w– Water content (percent ); RSE– Residual standard error; AIC– Akaike Information Criterion; BIC– Bayesian Information Criterion.

**Figure 7.6: Prediction models for Young's modulus of shale based on water content.**

$$\hat{E} = 28.121\ w^{-2.92}$$

**Figure 7.7: Equation. The predicted Young's modulus for shales from literature and Wyoming.**

$$\hat{E} = 4.9896\ w^{-2.273}$$

**Figure 7.8: Equation. The predicted Young's modulus for Wyoming shales only.**

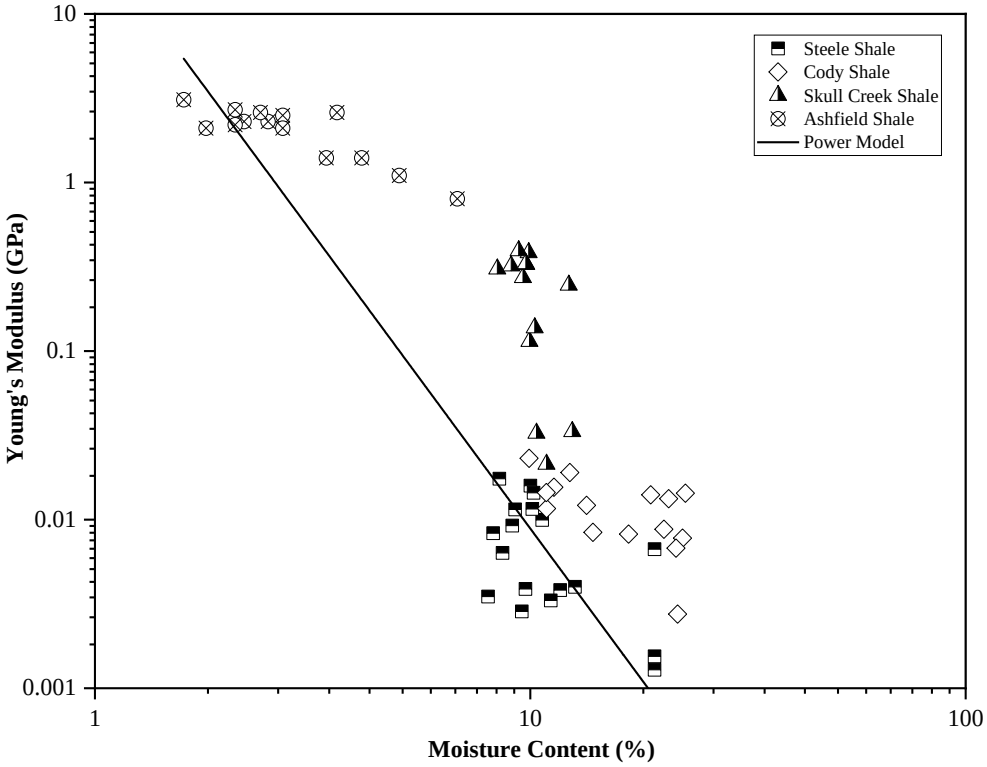


**Figure 7.9: Young's modulus vs water content for shales.**

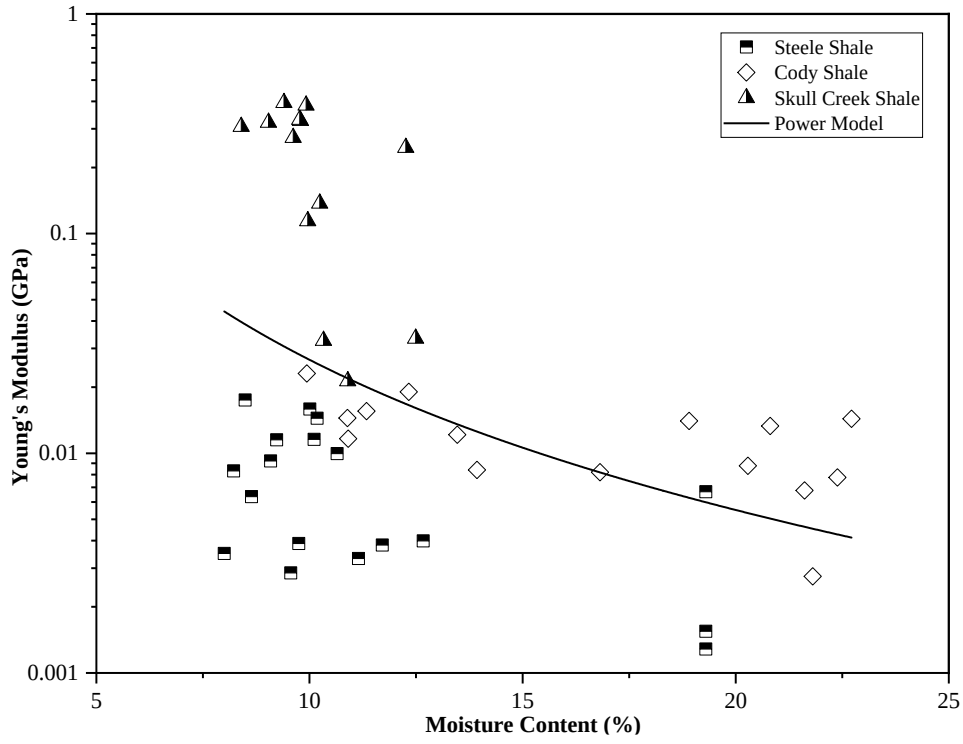


**Figure 7.10: Young's modulus vs water content for Wyoming Shales.**

*Porosity (n)*

Lashkaripour and Dusseault (1993) used a large set of published literature and lab data on shale with porosity of less than 20 percent and found a hyperbolic relationship between UCS and porosity. Horsrud (2001) conducted laboratory tests on shales with high porosity of 30-55 percent, Porosity showed an inverse nonlinear relationship with the strength of rocks. Kumar et al. (2012) found that porosity plays a critical role in the mechanical properties of shale. The prediction models describing the relationship between UCS and porosity for shale are summarized in Figure 7.13.

Figure 7.14 compares the UCS with the porosity along with the power model, represented by the equation shown in Figure 7.11, proposed in this study. The proposed model suggested that the mean UCS was 141 MPa for an “ideal” shale with zero porosity, and UCS decreases with the increase in porosity. The UCS approached zero when the porosity of shale reached about 50 percent. The RMSE, RSE, AIC, and BIC for the prediction models from the literature and the proposed model are summarized in Figure 7.13. The lowest RMSE of 20.60 was for the prediction model developed for all shales in this study, and the proposed model for Wyoming Shales only was higher at 34.43. The RSE, AIC, and BIC values for the proposed power model were lower than literature, suggesting a better prediction of UCS from the proposed power model.

Figure 7.15 shows a power model represented by the equation shown in Figure 7.12, for the UCS -porosity relationship based on Wyoming Shale data only. When fitting the power model (Wyoming only) with all data, the RSE, AIC, and BIC were lower than the power model (considering all data) as the scatteredness of data from Wyoming only was relatively low because all the shales were from a nearby location and similar geological age. The power model (considering all data) provided better results and was more applicable to a wider range of shale formations and geological ages.

$$\widehat{UCS} = 141.23\,(1 - \frac{n}{50})^{5.31}$$

**Figure 7.11: Equation. The predicted UCS for all shale data.**

$$\widehat{UCS} = 4.81\,(1 - \frac{n}{47.5})^{1.7}$$

**Figure 7.12: Equation. The predicted UCS for Wyoming shale only.**

| Prediction Model for UCS (MPa) | Source | Location of Shales | Model Comparison Criteria | | | |
|---|---|---|---|---|---|---|
| | | | RMSE | RSE | AIC | BIC |
| $1.001\ n^{-1.143}$ | Lashkaripour et al. (1993), from Chang et al. (2006) | Multiple | 45.83 | - | - | - |
| $243.6\ n^{-0.96}$ | Horsrud (2001) | Europe | 25.41 | 24.7 | 2614.7 | 2625.6 |
| $0.286\ n^{-1.762}$ | Horsrud (2001), from Chang et al. (2006) | Europe | 45.92 | - | - | - |
| $-0.4979\ n + 51.507$ | Anikoh et al. (2013) | Nigeria | 38.32 | - | - | - |
| $193.36\ n^{-1.143}$ | Lashkaripour et al. (1993) | Multiple | 30.16 | - | - | - |
| $141.23\ (1 - \frac{n}{50})^{5.31}$ | This Study | World | 20.60 | 20.6 | 2511.6 | 2522.5 |
| $4.81\ (1 - \frac{n}{47.5})^{1.7}$ | This Study | Wyoming | 34.43 | 2.2 | 550.8 | 560.3 |

Note: UCS– Uniaxial compression test; COV– Coefficient of variation; n– Porosity (%); RSE– Residual standard error; AIC– Akaike Information Criterion; BIC– Bayesian Information Criterion.

**Figure 7.13: Prediction models for UCS of shales based on porosity.**

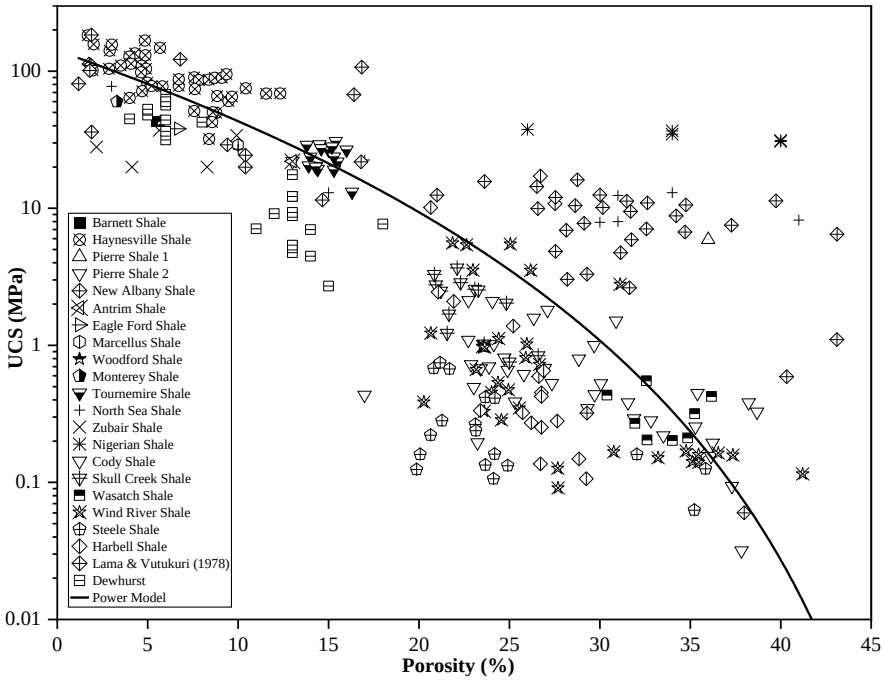


**Figure 7.14: UCS vs porosity for shale.**

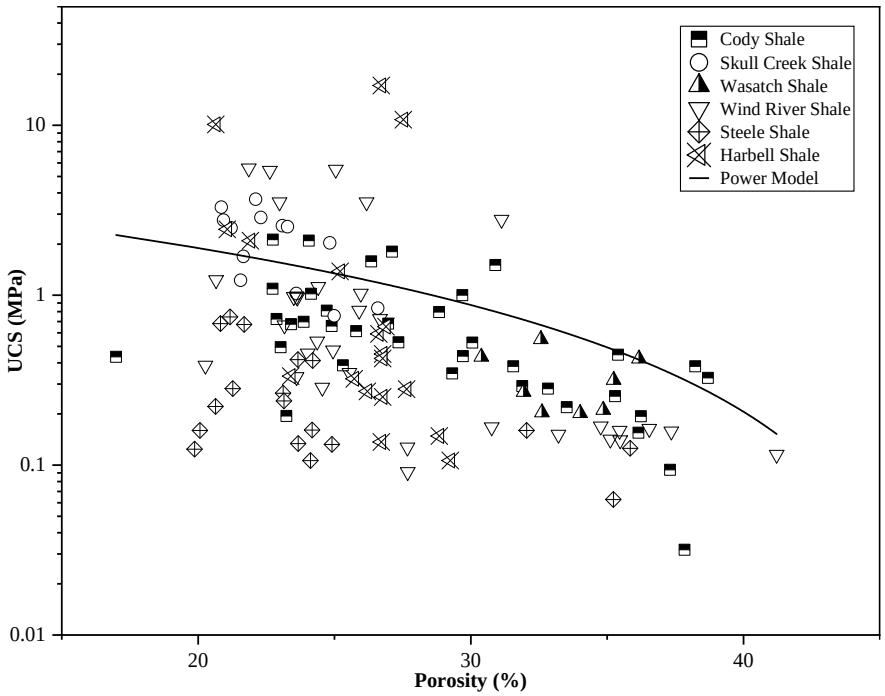


**Figure 7.15: UCS vs porosity for Wyoming Shale.**

Kumar (2012) observed a linear relationship between Young's modulus and porosity for four different shales with Young's modulus decreasing with an increase in porosity as the increase in porosity tends to weaken the rock matrix framework. Hui Li (2016) also concluded that the impact of porosity on Young's modulus is indeed significant. Figure 7.20 shows the comparison of models from the literature and this study for $E$ vs *n*. An exponential model for all shales and a power model observed for the shales from Wyoming only are shown in Figures 7.18 and 7.19 respectively.

The mean of Kumar et al. (2012) and Shukla et al. (2013) is very low because of the constants 67 and 73.45 respectively. The predicted value for Wyoming Shales from these models was very high compared to the measured value. The power model for data from literature and Wyoming and an exponential model for Wyoming Shales only have lower COV than the literature models. This suggests that these models predicted values of $E$ closer to the actual measured values. The model from combined shale data resulted in lower RSE, AIC, and BIC than the power model. We can thus say that the exponential model was better for the prediction of $E$ based on *n* for shales. $E$ vs *n* models for all shale and Wyoming Shale only from this study is given by the equations in Figures 7.16 and 7.17, respectively.

$$\hat{E} = 2065.8\, n^{-3.604}$$

**Figure 7.16: The predicted Young's modulus for all shale data.**

$$\hat{E} = 324.02\, e^{-0.344\, n}$$

**Figure 7.17: The predicted Young's modulus for Wyoming shale only.**

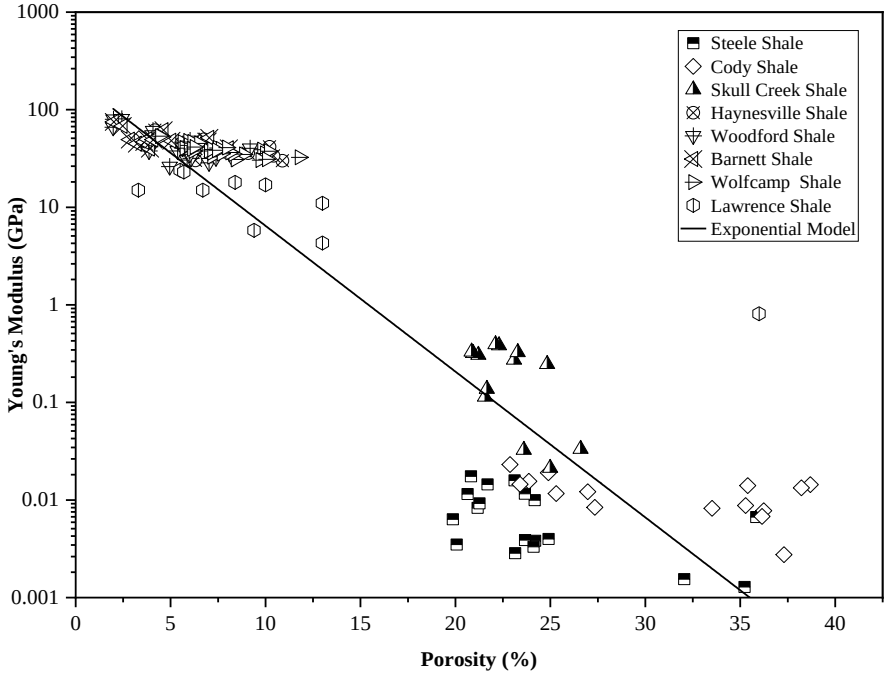


**Figure 7.18: Young's modulus vs porosity for shale.**

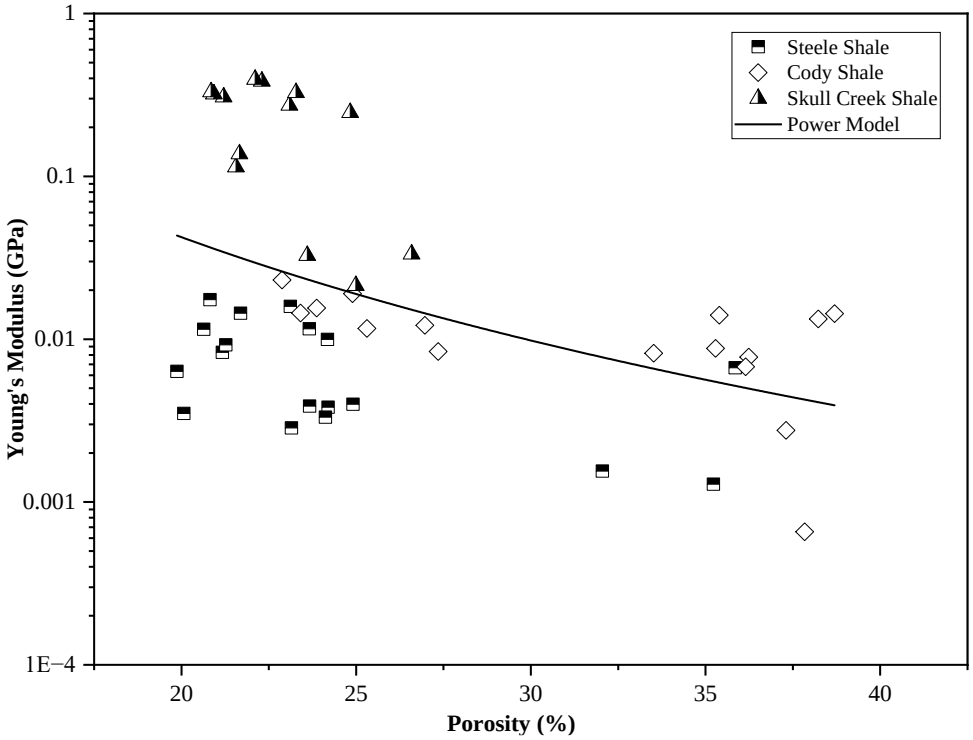


**Figure 7.19: Young's modulus vs porosity for Wyoming Shale.**

| Prediction Model for E (GPa) | Source | Location of Shales | Statistical Summary | | Model Comparison Criteria | | |
|---|---|---|---|---|---|---|---|
| | | | Mean Bias | COV | RSE | AIC | BIC |
| $67 - 3.8\,n$ | Kumar et al. (2012) | USA | 0.1 | 1.74 | - | - | - |
| $-4.43\,n + 73.45$ | Shukla et al. (2013) | USA | 0.1 | 1.76 | - | - | - |
| $2065.8\,n^{-3.604}$ | This Study | Wyoming | 2.78 | 1.48 | 7.35 | 181.4 | 185.2 |
| $324.02\,e^{-0.344\,n}$ | This Study | World | 2.32 | 1.52 | 6.78 | 177.3 | 181.0 |

Note: $E$– Young's Modulus (GPa); COV– Coefficient of variation; n– Porosity (%); RSE– Residual standard error; AIC– Akaike Information Criterion; BIC– Bayesian Information Criterion.

**Figure 7.20: Prediction models for Young's modulus of shales based on porosity.**

*Bedding Angle (β)*

Higgins et al. (2008) stated that bedding planes have a significant impact on the mechanical properties of bedded formation rocks. Test results from a series of UC tests indicated that the UCS values of shales first decreased and then increased when the $\beta$ of shales changed from 0 to 90 degrees (Fjaer et al. 2013, Jasmine et al. 2014). The effect of bedding planes on Colorado Shales has been studied by Wong et al. (2008) in terms of ultrasonic velocities. They concluded that samples parallel to the bedding plane have higher compressive and shear strength than samples perpendicular to the bedding plane. From a study on six different formations of shales, Willson et al. (2007) concluded that the UCS of shale is highest when the *β* equals 0 degree, intermediate when the *β* equals 90 degrees, and lowest when the *β* equals 60 degrees. Islam et al. (2013) concluded that shales drilled with $\beta$=90 degrees are much stronger and more brittle than those with $\beta$=0 degree. The experimental test results on Green River, Eagle Ford, and Mancos Shales at $\beta$=0 degree, 45 degrees and 90 degrees indicate that maximum compressive strength and Young's modulus are observed at *β* of 90 degrees and minimum properties at *β* of 45 degrees (Alqahtani et al. 2013).

Yan et al. (2017) found that the compressive strength varied substantially with *β* as the reduction in strength was up to 60.2 percent. They reported that the maximum compressive strength occurred at 0 degree bedding, compressive strength reduced from 0-60 degrees with the lowest at 60 degrees bedding and the compressive strength increased from 60-90 degrees. A similar finding was reported on Mancos Shale by Jin et al. (2015).

Figure 7.21 shows the effect of *β* on the UCS of shales. Marcellus, Boryeong, and Sichuan Formation shales showed similar trends as mentioned with the highest UCS at either 0 or 90 degrees and lowest at *β* of 60 degrees. Two shales from Longmaxi Shales also showed the highest UCS at either 0 or 90 degrees, but the lowest UCS was not at *β* of 60 degrees. The Longmaxi black Shale has high porosity and showed the lowest strength at *β* of 30 degrees. The lowest compressive strength of Longmaxi Formation shale was not conclusive as the test data for all *β* angles was not available. Apart from the general trend we observed that the most reduction in UCS was 43 percent for Sichuan Formation shales from 0 to 60 degrees whereas the least reduction was 9 percent for Longmaxi Formation shale. Boryeong Shale when tested multiple times at the same *β* showed the difference in the observed UCS. The difference between the compressive strengths observed could be because of the physical properties like porosity, water content, depth, and mineral composition (Islam et al., 2013).

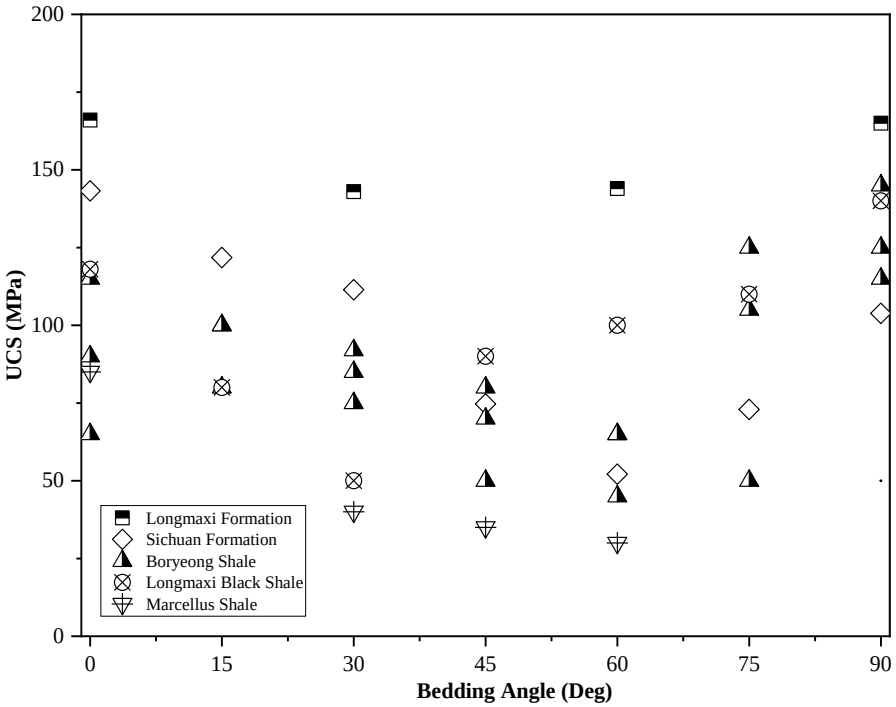


**Figure 7.21: UCS vs bedding angle (*β*) for shales.**

Higher Young's modulus was observed parallel to bedding planes as compared to perpendicular by Wu & Tan (2010) and Sone and Zoback (2013). Jin et al. (2015) reported an increase in Young's modulus with an increase in *β*. Figure 7.22 shows the relationship between Young's modulus and *β* for different formations of shale. Only Sichuan Formation shale showed an increasing trend with an increase in *β* as mentioned in the literature.

Young's modulus of Boryeong and Longmaxi black Shale showed a similar trend to that of the compressive strength with the highest value at 0 or 90 degrees and lowest in between 30-60 degrees. The Longmaxi Formation showed the least value of Young's modulus at *β* of 90 degrees. The possible reasons for this variation were water content, porosity, total carbonic content, and mineralogy.

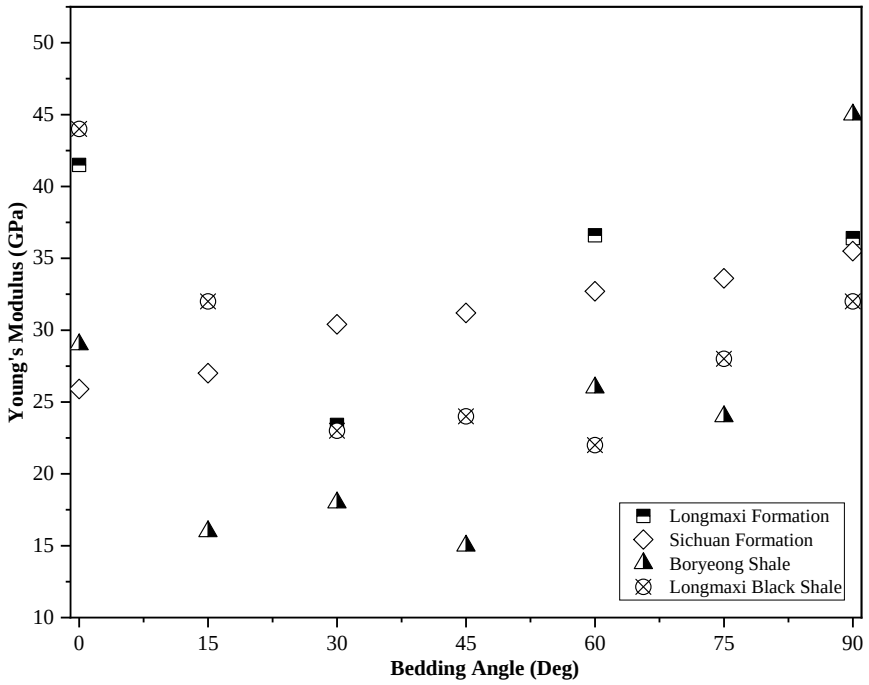


**Figure 7.22: Young's modulus vs bedding angle ($\beta$) for shale.**

*Poisson's Ratio ($\nu$)*

Lashkaripour et al. (1993) concluded there was no relationship between the UCS and Poisson's ratio of shale. Figure 7.23 similarly shows no relationship between UCS and Poisson's ratio.

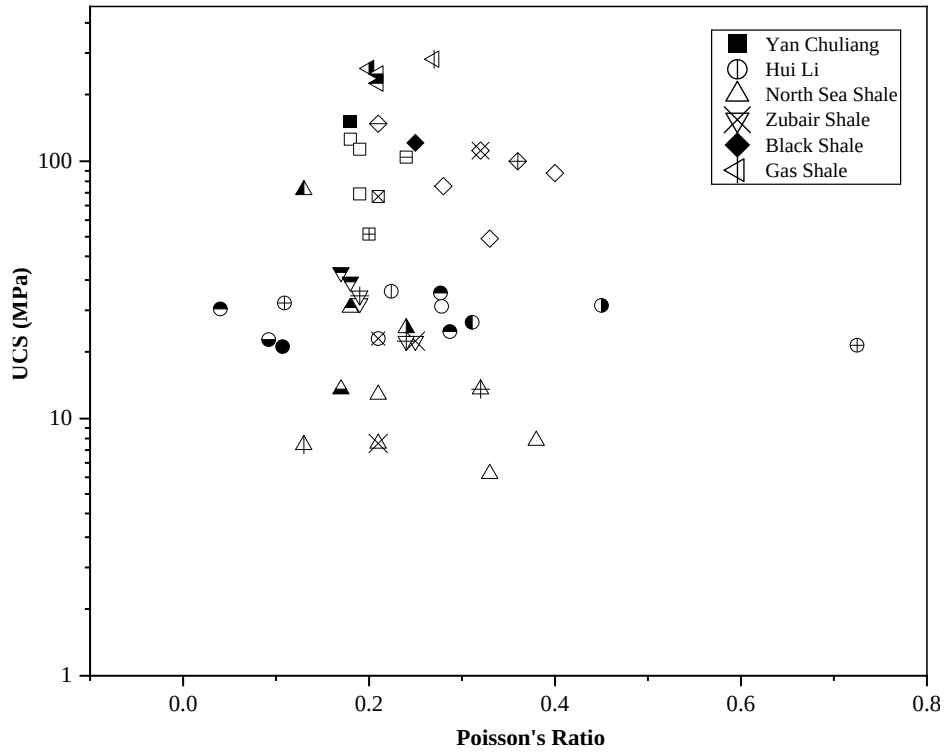


**Figure 7.23: UCS vs Poisson's ratio for shales.**

*Bulk density ($\rho$)*

Inoue and Ohami (1981) and Lashkiropour et al. (1993) have reported a poor relationship between UCS and $\rho$ for weak rocks like shale. Lashkiropour et al. (1993) further concluded that density is not a good indicator of UCS in shales as the density of minerals, such as quartz, illite, and montmorillonite, is relatively similar. The ratio of quartz to clay minerals in shales has been found as a factor influencing the strength of shale, and a higher ratio indicates a higher strength of shale (Hui Li et al. 2016). Considering all shale data, Figure 7.25 shows that the UCS of shales increased with the increase in density. The increasing trend can be approximated with an exponential model provided in the equation shown in Figure 7.24. Residual standard error, AIC, and BIC values were determined at 24.37, 1821.22, and 1831.07, respectively. This increasing relationship could be attributed to the ratio of quartz to clay mineral in shales. Due to the absence of measured mineralogy of the tested shales, a better prediction model to describe the relationship between UCS (MPa) and density of shales (g/cm$^3$) considering the shale mineralogy cannot be established.

$$UCS = 3.45\text{E} - 07 \times e^{7.4242\rho}$$

**Figure 7.24: Equation. The predicted UCS for all shale data.**

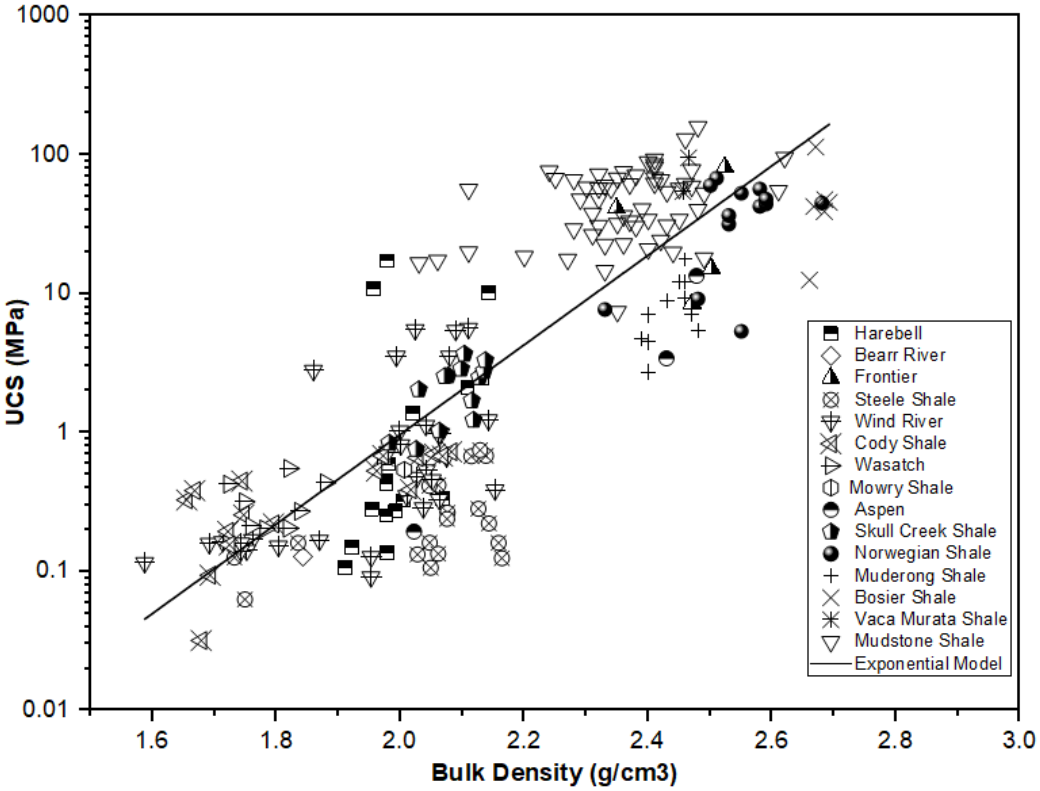


**Figure 7.25: UCS vs density for shale.**

Considering Wyoming Shale data, Figure 7.28 shows a similar exponential relationship between the UCS and $\rho$. The variation in UCS with respect to density could be attributed to the different types and formation depths of Wyoming Shales. Most shale from Wyoming was obtained from a relatively shallow depth of up to 30 m while the shale reported in the literature was collected from much deeper depths. The exponential model (Figure 7.26) has an RSE of 2.286, AIC of 480.10, and BIC of 488.09. Similarly, Figure 7.29 compares Young's modulus (GPa) and $\rho$ (g/cm$^3$) along with the power model given by the equation shown in Figure 7.27.

$$\widehat{UCS} = 0.000015 \times e^{5.354\rho}$$

**Figure 7.26: Equation. The predicted UCS for Wyoming shale only.**

$$\hat{E} = 0.00004 \times \rho^{8.801}$$

**Figure 7.27: Equation. The predicted Young's modulus for Wyoming shale only.**

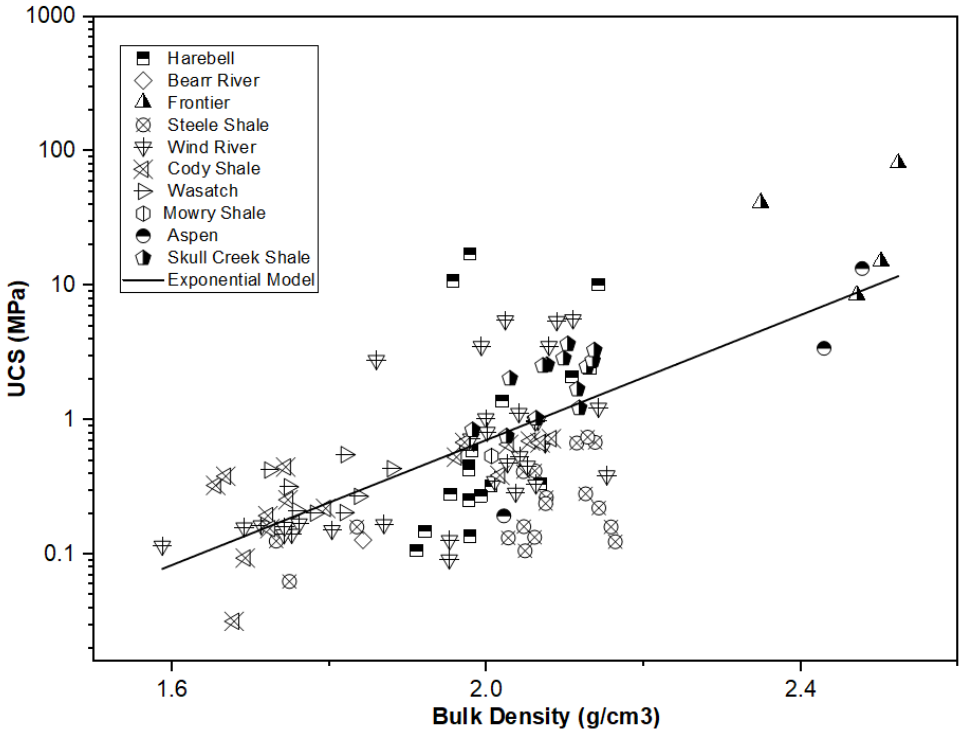


**Figure 7.28: UCS vs density for Wyoming Shales.**

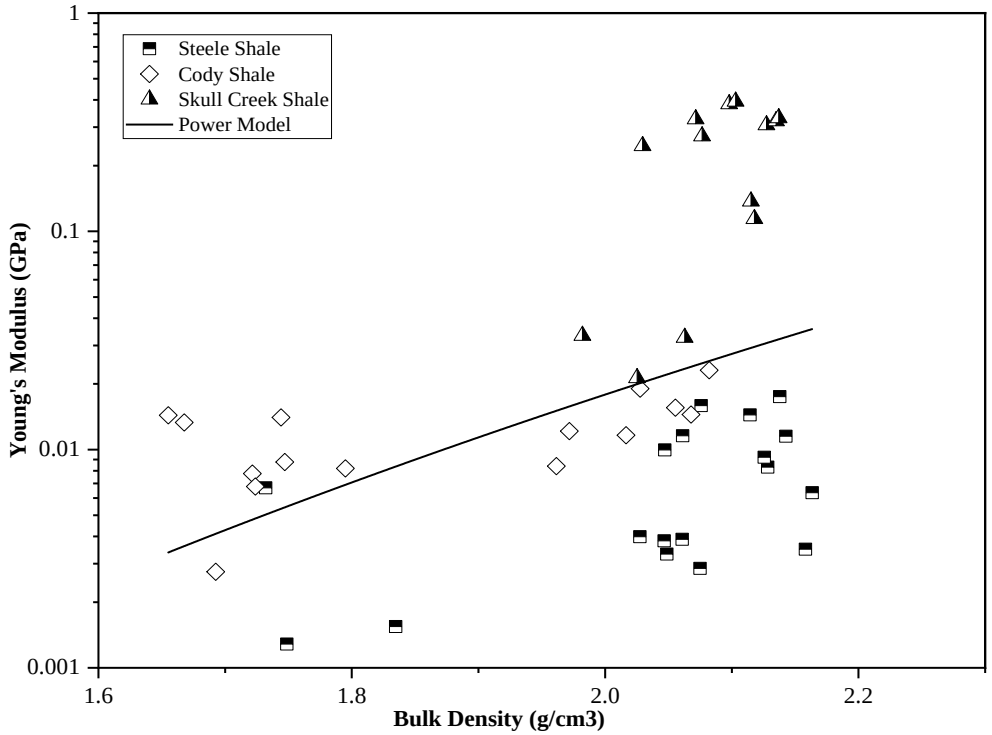


**Figure 7.29: Young's Modulus vs density for Wyoming Shales.**

*Young's Modulus (E) under Uniaxial Condition*

A linear relationship between Young's modulus ($E$) and UCS of shales has been observed by Lashkaripour & Dusseault (1993) and Franklin (1981). However, an exponential relationship between $E$ and UCS was reported for North Sea Shale (Horsrud 2001). Chang et al. (2006), using data from Horsrud (2001), illustrated a remarkably different trend with two empirical equations developed using a high porosity North Sea Shale and a strong compacted shale. The difference in trend observed with different shale types showed that the relationship between UCS and $E$ varied with the lithology and geology of the shales in consideration. The prediction equations describing the relationship between $E$ and UCS for shale are listed in Figure 7.33.

Figure 7.33 compares Young's modulus and UCS in a log plot along with a power model proposed given by the equation shown in Figure 7.30 from this study. The linear model for Wyoming Shales from this study had the lowest RMSE value followed by the power model from this study considering all data and Horsrud (2001). Comparing the Lashkaripour et al. (1993) linear model with the power model from this study we observe that the values of RSE, AIC, and BIC are smaller for the power model compared to the literature model.

The study of Wyoming Shale data only shows a similar trend. Figure 7.34 shows the fitting of a linear model given by the equation shown in Figure 7.31 on Wyoming Shale data only. $R^2$ value at 94 percent for Wyoming Shales test data. Residual standard error, AIC, and BIC values at 0.029, -195.1, and -189.6 respectively.

$$\hat{E} = 0.0699\, UCS^{1.3129}$$

**Figure 7.30: Equation. The predicted Young's modulus for all shale data.**

$$\hat{E} = 0.121\, UCS - 0.032$$

**Figure 7.31: Equation. The predicted Young's modulus for Wyoming shale only.**

| Prediction Model for $E$ (GPa) | Source | Location of Shales | Comparison of Model | | | |
|---|---|---|---|---|---|---|
| | | | RMSE | RSE | AIC | BIC |
| $0.365 \times UCS - 8.073$ | Lashkaripour et al. (1993) | Unknown | 16.93 | 11.11 | 2483.6 | 2494.9 |
| $0.102 \times UCS^{1.099}$ | Horsrud (2001) | Europe | 16.62 | - | - | - |
| $0.062 \times UCS^{1.40}$ | Chang et al. (2006) | Europe | 25.97 | - | - | - |
| $8.30 \times UCS^{1.40}$ | Zheng et al. (2020) after Chang et al. (2006) | China | - | - | - | - |
| $97.2\ UCS$ | Ghafoori et al. (1993) | Australia | - | - | - | - |
| $0.0699\ UCS^{1.3129}$ | This Study | World | 16.52 | 10.67 | 2457.8 | 2469.2 |
| $0.121\ UCS - 0.032$ | This Study | Wyoming | 15.53 | 0.029 | -195.1 | -189.6 |

Note: UCS– Uniaxial compression test (MPa); COV– Coefficient of variation; $E$– Young's Modulus (GPa); RSE– Residual standard error; AIC– Akaike Information Criterion; BIC– Bayesian Information Criterion; - – Unreasonable values or values can't be calculated.

**Figure 7.32: Prediction models describing the relationship between *E* and UCS for shales.**

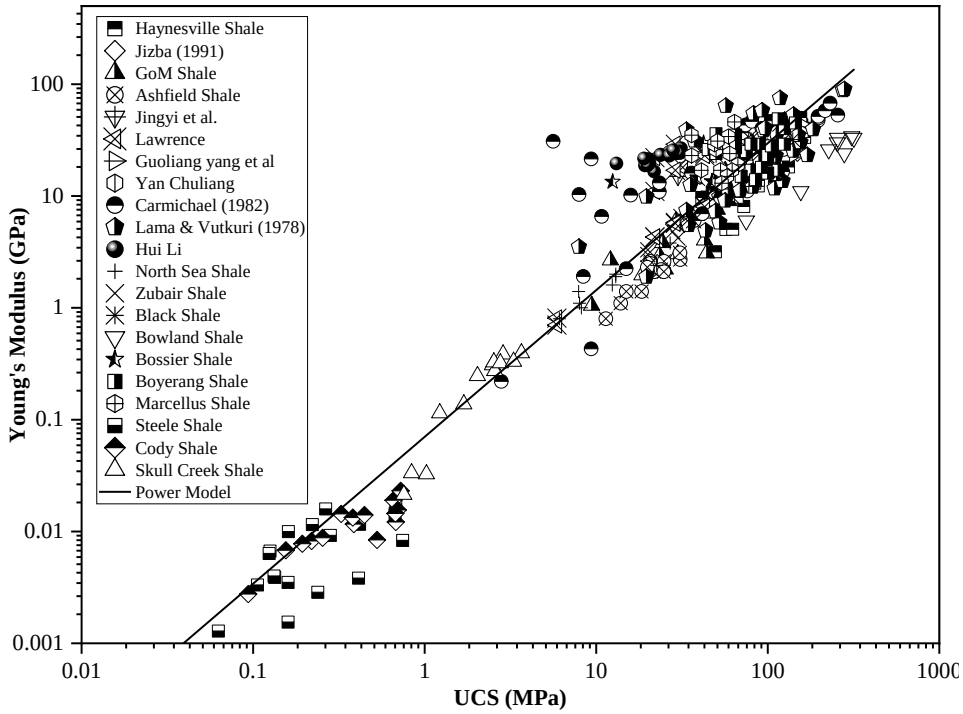


**Figure 7.33: Young's modulus vs UCS for shale.**

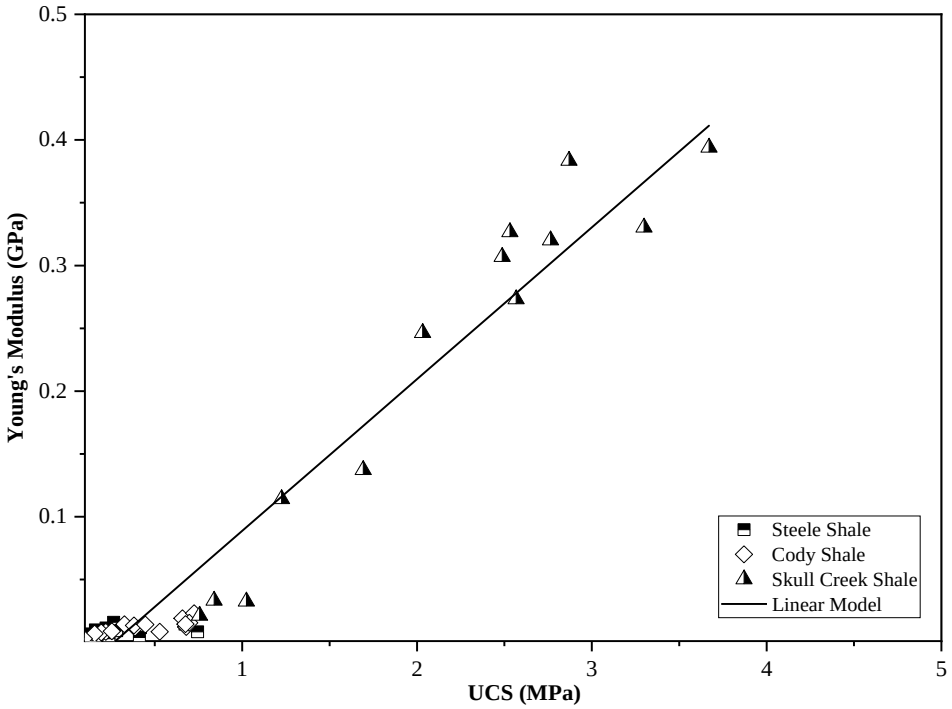


**Figure 7.34:Young's modulus vs UCS for Wyoming Shales.**

*Axial Strain at Peak Stress*

No apparent relationship was observed between the axial strain at peak stress (percent) and the UCS for shales included in the study. Figure 7.36 shows the comparison between UCS and axial strain at peak stress of Wyoming Shales. The linear fitting model with a relatively low $R^2$ of 15 percent suggested that the linear model cannot provide a relatively accurate UCS prediction based on the axial strain. Axial strains of Cody Shale, Skull Creek Shale, Wasatch Shale, Wind River Shale, Steele Shale, and Harbell Shale range from 2.7 to 8.5 percent, 1 to 3.9 percent, 2.5 to 4.6 percent, 1.3 to 11 percent, 2 to 13.5 percent and 0.8 to 5.5 percent, respectively. Wind River Shale and Steele Shale exhibited a broader range of axial strain at peak stress while the axial strains of Skull Creek Shale and Wasatch Shale are narrower.

Young's modulus (GPa) with axial strain at peak stress (percent) showed a power fitting given by the equation shown in Figure 7.35 and the data are shown in Figure 7.37. The Skull creek Shales from Wyoming showed a sharp decrease in Young's modulus with an increase in the axial strain at peak stress whereas in Steele Shale and Cody Shale the trend is not that apparent. The RSE, AIC, and BIC of the equation shown in Figure 7.35 for $E$ based on the axial strain at peak stress was 0.05, -139.40, and -133.85, respectively.

$$\hat{E} = 0.266\, x^{-2.106} \qquad (x = Axial\ strain\ at\ peak\ stress)$$

**Figure 7.35: Equation. The predicted Young's modulus of Wyoming shale.**

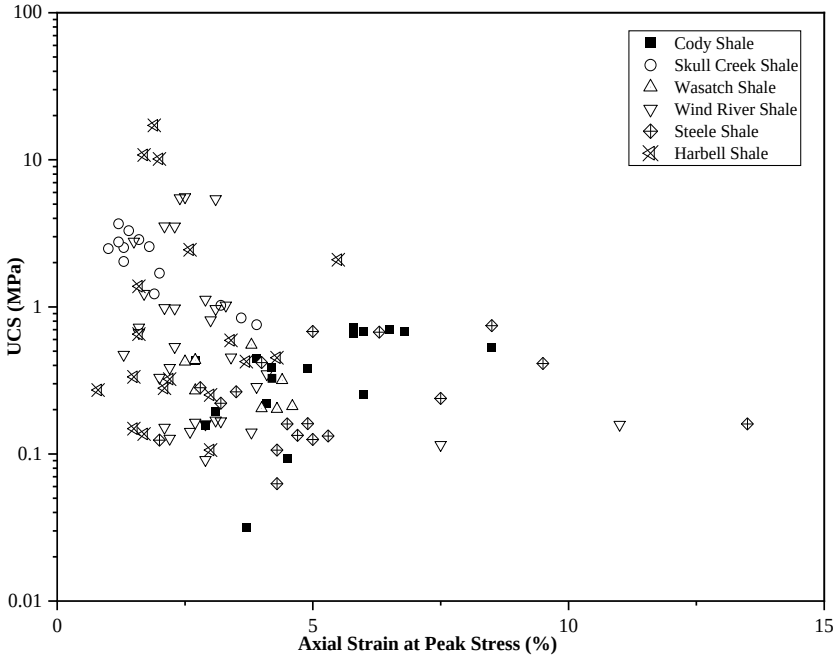


**Figure 7.36: UCS vs axial strain at peak stress for Wyoming Shales.**

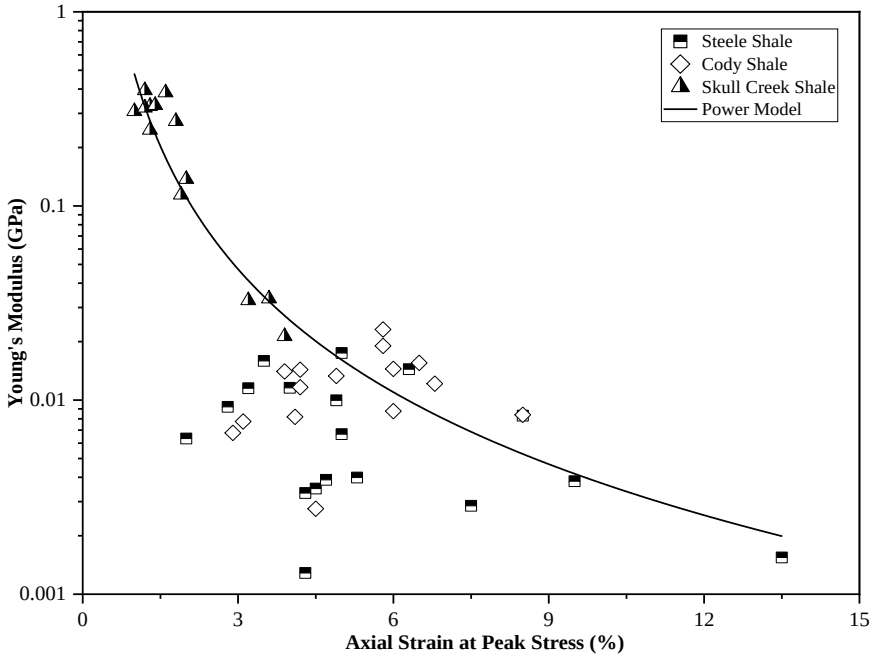


**Figure 7.37: Young's modulus vs axial strain at peak stress for Wyoming Shales.**

## 7.3 Mechanical Properties under Triaxial Compression

Triaxial test results described in this chapter are largely based on rock cores obtained from the state of Wyoming. Correlation analyses are conducted first considering shale data from

literature and Wyoming and later considering only Wyoming Shale data. Wyoming Shale samples did not have an apparent ***β***. The complete data from the literature and our lab used for the development of the correlation are shown in Table 7.1. Most of the shale data considered for analysis were from USA followed by China and France. Although most shales were from USA, they were from different formations.

Thirty-three triaxial tests were conducted on five formations of shales from Wyoming. The porosity and water content of Wyoming Shales ranged from 12.76 to 38.28 percent and 10.16 to 22.24 percent respectively. The porosity and water content of Wyoming Shales were much higher than shales from the literature, hence the confinement chosen for Wyoming Shales ranged from 0.14 to 10 MPa compared to 1 to 250 MPa for the literature shales. The peak strength obtained for Wyoming Shale ranged from 0.57 to 88.92 MPa which was much less compared to 14 to 584 MPa for literature shales. The higher peak stress of literature shales was because of the lower porosity and water content and higher range of confining pressure. Young's modulus and Poisson's ratio of Wyoming Shales were also lower than the literature values.

*Effect of bedding angle ($\beta$)*

Jasmine et al. (2014) defined ***β*** as the foliation angle with respect to the longitudinal direction of a rock specimen. They found that the shear failure of anisotropic shales under compression occurs along the bedding planes for 30 degree ≤ $\beta$ ≤ 75 degree, and hence, shales with bedding planes in this range exhibited the lowest compressive strength. Shales with $\beta$ = 0 and 90 degrees exhibited tensile failure and a higher compressive strength than that with other ***β*** angles. Similar observations have been made on shales by Cheng et al. (2017), Niandou et al. (1997), and Mese et al. (2001). Jung et al. (2016) studied the anisotropy of elastic parameters and strength of shale with Brazilian split testing and concluded that the highest compressive strength is at $\beta$ = 0 and 90 degrees. Figure 7.38 shows the normalized peak stress with confining pressure $\left(\frac{\sigma_p}{\sigma_c}\right)$ versus ***β*** for different shale formations. Higher normalized stresses were found to be at $\beta$ = 0 and 90 degrees and lower normalized stresses were observed in the range 30 degree ≤ $\beta$ ≤ 75 degree irrespective of the shale formation.

The normalized stress $\left(\frac{\sigma_p}{\sigma_c}\right)$ magnified by the porosity as $\left(\frac{\sigma_p}{\sigma_c} \times n\right)$ is compared against the ***β*** in Figure 7.39. The relationship between this normalized stress and porosity becomes more apparent with the highest strength at $\beta$ = 0 and 90 degrees and the lowest strength in the range

30 degree ≤ $\beta$ ≤ 75 degree. These comparisons further confirm the effect of $\beta$ on the compressive strength of anisotropic rocks like shale in addition to the effect of confinement and porosity.

**Table 7.1: Database of triaxial compression test results of shales from Wyoming and published literatures.**

| Sample ID | Formation | Location | No of Tests | Porosity (Percent) | Water Content (Percent) | Confining Pressure (MPa) | Peak Strength (MPa) | Young's Modulus (GPa) | Poisson's Ratio | References |
|---|---|---|---|---|---|---|---|---|---|---|
| 1 | Cody Shale | Wyoming, USA | 24 | 20.10-31.00 | 11.59-20.37 | 0.3-10 | 0.57-12.86 | 0.02-280.31 | 0.26-0.49 | This Study |
| 2 | Morrison Shale | Wyoming, USA | N/A | N/A | N/A | N/A | N/A | N/A | N/A | This Study |
| 3 | Undifferentiated | Wyoming, USA | 3 | 27.80-35.50 | 10.16 | 0.3-0.6 | 1.05-1.27 | 0.02-0.07 | 0.19 | This Study |
| 4 | Fort Union Shale | Wyoming, USA | 3 | 36.24-38.28 | 22.24 | 0.14-0.6 | 0.57-0.78 | N/A | N/A | This Study |
| 5 | Hanna Shale | Wyoming, USA | 3 | 12.76-13.20 | 5.01 | 4-10 | 81.67-88.92 | 5.38-9.83 | 0.12 | This Study |
| 6 | Coal Shale | Maryland, USA | 28 | 0.79 | N/A | 10-30 | 90-213 | 12-37.97 | N/A | Jin et al. (2015) |
| 7 | Longmaxi Formation | Sichuan, China | 8 | 4.00 | N/A | 15-25 | 192.5-220.2 | N/A | N/A | Guoliang Yang et al. (2020) |
| 8 | Pierre Shale | South Dakota, USA | 8 | 23.2 | N/A | 16-25 | 31.60-50.90 | N/A | N/A | Animul et al. (2013) |
| 9 | Tournemire Shale | Massif Central, France | 24 | 8.35 | N/A | 1-50 | 27-155 | 15 | N/A | Niadou et al. (1997) |
| 10 | Tournemire Shale | Massif Central, France | 12 | 8.35 | N/A | 5-20 | 62.63-106.76 | 11-15 | N/A | Masri et al. (2014) |
| 11 | Longmaxi Marine Shale | Chongquing, China | 16 | 4.45 | N/A | 20-100 | 173-584 | 21.3-32.3 | N/A | Yuan Li et al. (2018) |
| 12 | Bossier Shale | North America | 34 | 2.75 | N/A | 7-70 | 46-324.72 | N/A | N/A | Jasmine et al. (2014) |
| 13 | Longmaxi Black Shale | Schizu County, China | 20 | 4 | N/A | 20-60 | 90-340 | N/A | N/A | Song Yu et al. (2016) |
| 14 | Wilcox Shale | Louisiana, USA | 4 | 2.50 | N/A | 250 | 437.40-448.30 | N/A | N/A | Ibanez et al. (1993) |
| 15 | Vaca Murata Shale | Argentina | 14 | 5.00 | N/A | 7-138 | 138.71-482.38 | N/A | N/A | Jasmine et al. (2014) |
| 16 | Pierre-1 Outcrop | USA | 14 | 23.20 | N/A | 16-25 | 31.60-55.39 | 0.64-1.90 | 0.10-0.54 | Aminul Islam et al. (2013) |
| 17 | Opalinus Clay Shale | USA | 9 | 16.85 | N/A | 5-15 | 14-30 | N/A | N/A | Mohamadi (2015) |
| 18 | Tournemire Shale | USA | 30 | 8.00 | N/A | 1-50 | 24-110 | N/A | N/A | Mohamadi (2015) |
| 19 | Queenston Shale | Canada | 6 | N/A | 1.505 | 2.5-20 | 42.04-77.79 | 4.1-26.9 | 0.24-0.48 | Al-maamori et al. (2016) |
| 20 | Black Shale | Europe | 16 | N/A | N/A | 0.1-100 | 75-352 | N/A | N/A | Herrmann et al. (2018) |

Note: USA– United States of America.

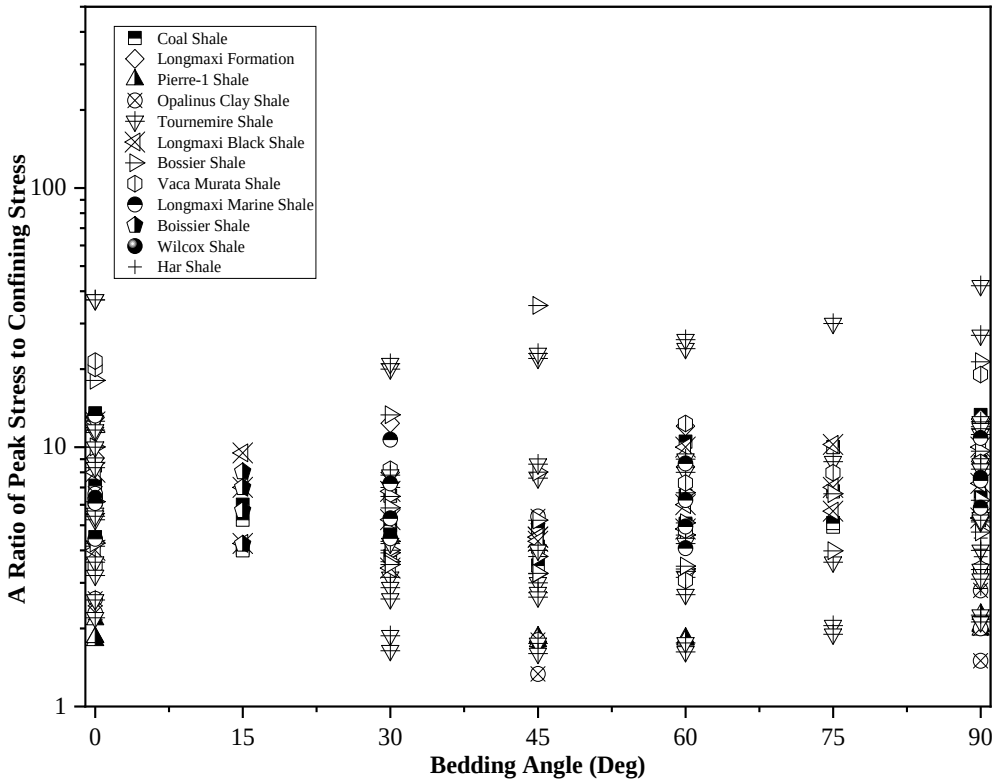


**Figure 7.38: Normalized $\frac{\sigma_p}{\sigma_c}$ vs bedding angle for shales.**

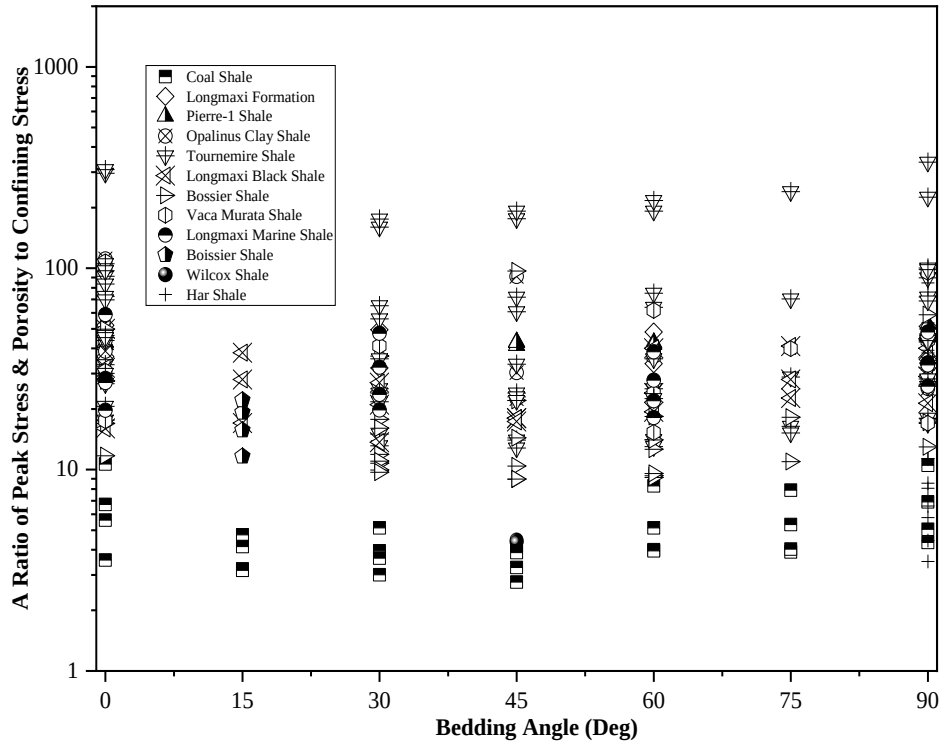


**Figure 7.39: Normalized $\frac{\sigma_p}{\sigma_c} \times n$ vs bedding angle for shales.**

*Cohesion (c) and internal friction angle (φ)*

Cohesion (*c*) and internal friction angle ($\varphi$) are important strength parameters of rocks. Figure 7.41 suggests that the cohesion of shales was inversely proportional to porosity. An exponential model (Figure 7.40) was established to describe this inverse relationship for predicting the cohesion (MPa) of shales using porosity (percent). Since cohesion is related to UCS via a friction factor (Dewhurst et al. 2008), the observed inverse relationship given by the equation shown in Figure 7.40 was expected. The porosity ranging from 3 to 13 percent showed a higher cohesion value as compared to the cohesion values for porosity greater than 13 percent.

$$c = 24.84e^{-0.136\phi}$$

**Figure 7.40: Equation. The predicted cohesion of shales.**

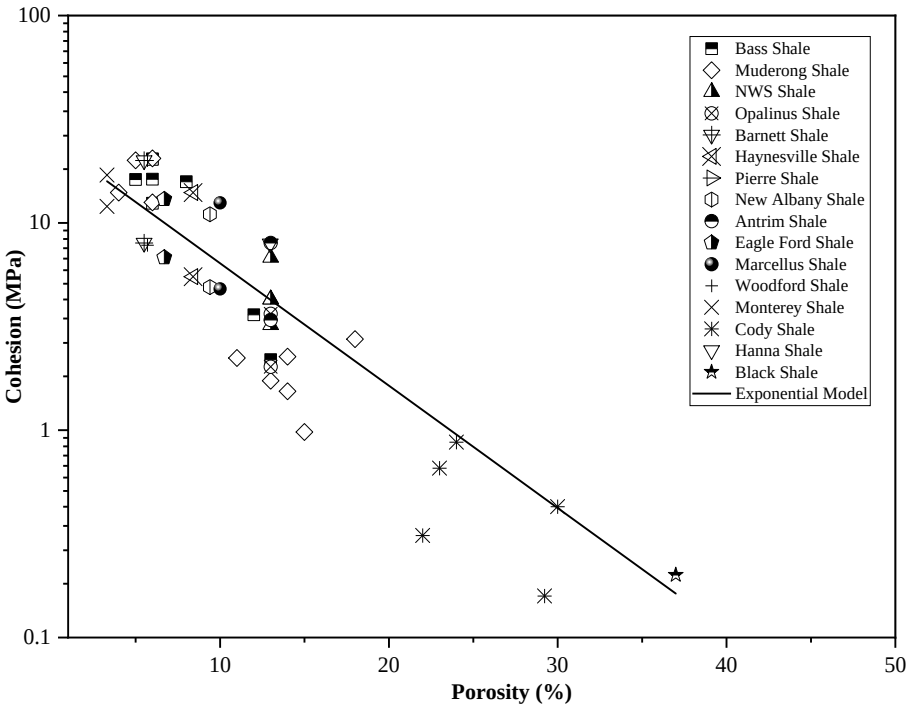


**Figure 7.41: The relationship between cohesion and porosity for shales.**

No effect of the internal friction angle on the measured physical properties was observed by Horsrud (2001) in North Sea Shales. Figure 7.43 compares the internal friction angle and porosity. For porosity ranging between 4 and 10 percent, a constant internal friction angle of about 23.4 degrees was observed except for the Hanna Shale. The relatively high internal friction angle of 45 degrees observed in Hanna Formation might be attributed to the size effect as 25 mm diameter Hanna Shale specimens versus 50 mm diameter specimens for other shale

formations are used in the testing. Cody Shale with the porosity ranging from 23 to 30 percent exhibited a linear relationship (Figure 7.42) for the internal friction angle ($\varphi$) in degree in terms of porosity ($n$) in percentage.

$$\hat{\varphi} = 1.01 \times n - 12.48$$

**Figure 7.42: Equation. The predicted internal friction angle of shales.**

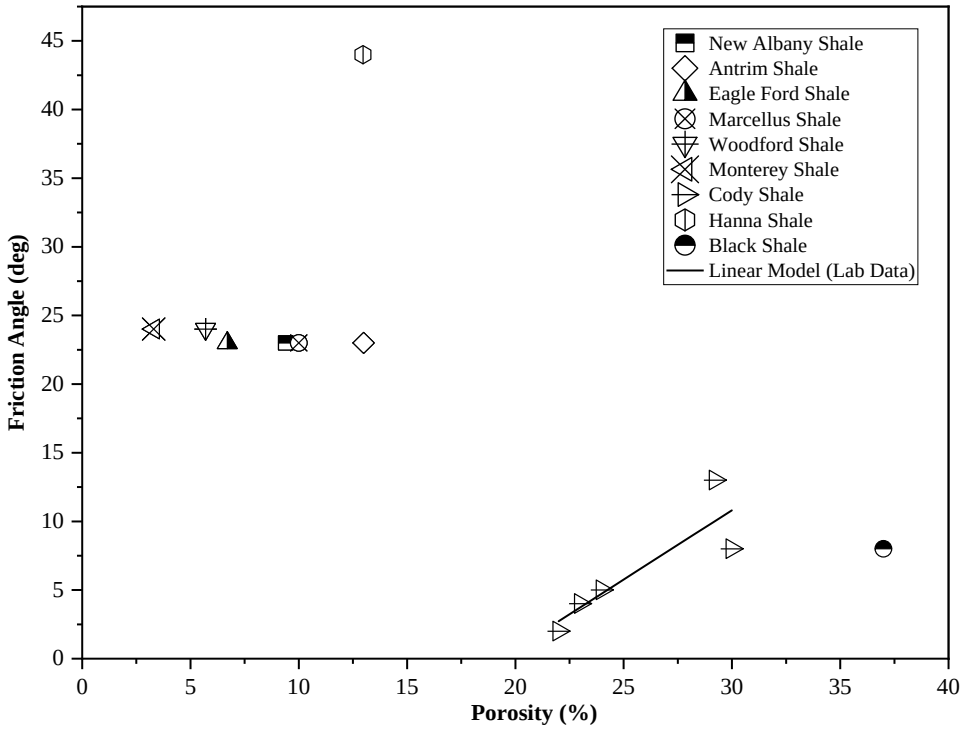


**Figure 7.43: Comparison of internal friction angle and porosity for shales.**

*Young's Modulus (E)*

Figure 7.45 shows that Young's modulus decreased with the increase in rock porosity. A power model (Figure 7.44) is fitted to define this relationship. Han et al. (2018) reported a gradual increase in Young's modulus with the increase in packing density and reduction of porosity in shale. The observed Young's moduli for shales below 30 GPa were comparable with the observation reported by Han et al. (2018) of 24.2 GPa for shales with a parallel bedding plane. The RSE of 6.786, AIC of 177.27, and BIC of 181.04 were observed for the proposed equation (Figure 7.44).

$$\hat{E} = 21.83 \times (0.93)^{n}$$

**Figure 7.44: Equation. The predicted Young's modulus of shales.**

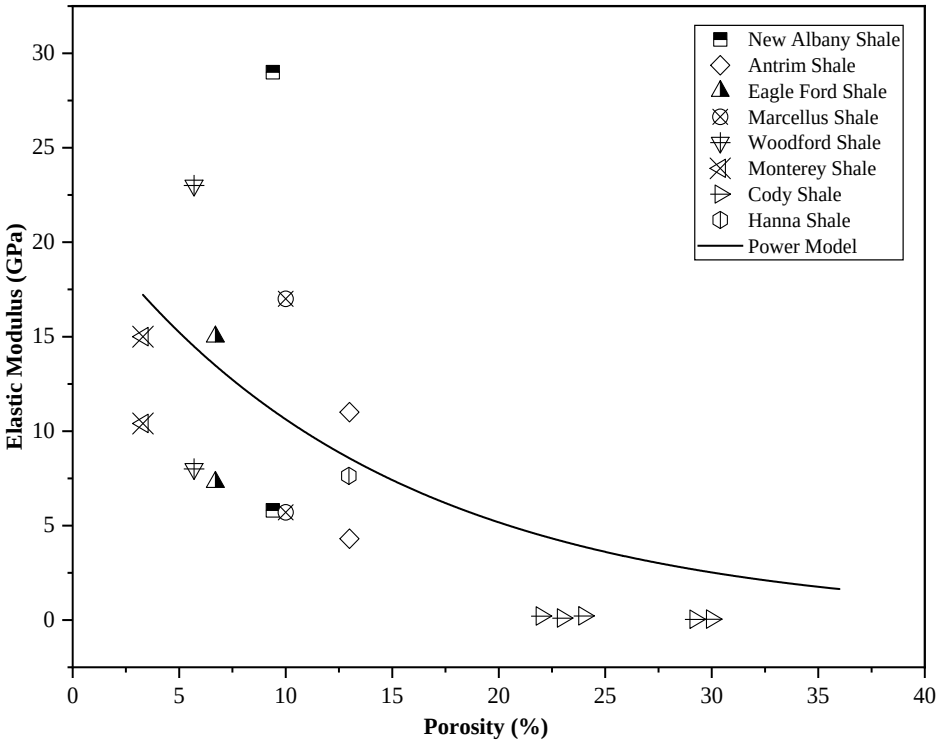


**Figure 7.45: Young's modulus vs porosity for shales.**

# CHAPTER 8: MECHANICAL PROPERTIES OF CLAYSTONE UNDER UNIAXIAL AND TRIAXIAL CONDITIONS

The study of the anisotropy effect on clay rocks by experimental investigation of mechanical properties has been conducted, especially on Callovo-Oxfordian Claystone (COX) and Opalinus clay. The investigations on COX by Zhang et al. (2012), Yang et al. (2013), and Belmokhtar (2017) reported that the deformability and strength of the clay rock depend on loading direction with respect to the bedding plane. The study by Naumann et al. (2007) and Amann et al. (2017) on opalinus clay also highlighted the effect of bedding planes on mechanical properties. Zhang et al. (2019) found that the elastic parameters increase at the beginning of loading and tend to be constant before peak failure.

The initial increase is attributed to the hardening effect of claystone. The effect due to claystone hardening has also been investigated (Plinninger et al. 2010, Hu et al. 2014). The mechanical properties and the effect of physical properties on the compressive strength of claystone have not been well published. Unlike other rock types, literature data on compressive strength of claystone is rarely available from laboratory tests. From a civil engineering perspective, since claystone is an important geomaterial supporting many civil infrastructures such as buildings, slopes, bridges, and tunnels, a comprehensive study of the mechanical properties of claystone from laboratory testing is essential.

## 8.1 Research Methods and Analysis

A total of 46 UC tests have been conducted on nine different claystone formations obtained from Wyoming. Five triaxial compression tests have been performed on claystone from three formations. All claystone samples were collected from depths less than 30 m. Literature data for the mechanical and physical properties of claystone cannot be found, and hence, the following correlation studies were conducted based only on Wyoming Claystone data. To evaluate and compare the prediction models, AIC, BIC, and RSE were determined using the statistical software RStudio version 2020.02.2 (R Core Team 2020).

## 8.2 Mechanical Properties under Uniaxial Compression

Correlation analyses were conducted by considering claystone test data from Wyoming as shown in Table 8.1. Ten different formations of claystone were tested. The average water content, porosity, $\rho$, axial strain, UCS, and Young's modulus for all ten formations of claystone are listed in Table 8.1. The average porosity of all claystone was less than 20 percent except for

the Ogallala Formation. Similarly, the average porosity for all formations was less than 30 percent except for Ogallala and Upper Lance Creek Formations. Three formations, Fort Union, Frontier and Goose Egg have higher densities compared to the other formations. The average UCS of the claystone ranged from 0.63 MPa to 5.30 MPa. The lowest UCS was observed in the Upper Lance Creek Formation with high porosity (32 percent) and water content (20 percent) as compared to other formations.

**Table 8.1: Database of uniaxial compressive test results of claystone from Wyoming.**

| Claystone Formation | Avg *w* (Percent) | Avg *n* (Percent) | Avg $\rho$ (g/cm3) | Axial Strain (Percent) | UCS (MPa) | Young's Modulus (GPa) |
|---|---|---|---|---|---|---|
| Aspen | 9.74 | 20.33 | 2.95 | 3.43 | 3.60 | 0.02 |
| Chugwater | 15.20 | 28.77 | 2.81 | 4.83 | 5.30 | 0.01 |
| Fort Union | 8.80 | 16.18 | 3.05 | 2.68 | 2.59 | 1.57 |
| Frontier | 3.47 | 7.98 | 3.21 | 1.90 | 1.50 | 0.23 |
| Goose Egg | 4.97 | 11.11 | 3.15 | 1.87 | 2.28 | 0.31 |
| Green River | 14.36 | 27.48 | 2.76 | 3.72 | 4.50 | 0.23 |
| Ogallala | 37.27 | 49.67 | 2.26 | 1.56 | 1.41 | 0.37 |
| Upper Lance Creek | 19.96 | 32.70 | 2.72 | 3.80 | 0.63 | - |
| Willwood | 16.42 | 29.55 | 2.76 | 2.23 | 2.99 | 0.05 |
| Wasatch | 15.16 | 27.01 | 2.83 | 2.37 | 2.73 | 0.74 |

Note: Avg– Average; *w*– Water content (percent); *n*– Porosity (percent); $\rho$ – Bulk density (g/cm3); UCS – Uniaxial compression test.

Claystone UCS was related to physical properties such as water content, porosity, and *ρ*, in addition to mechanical properties such as Young's modulus and axial strain at peak stress.

*Water content (w)*

The effect of water content on the compressive strength of Wyoming Claystone is illustrated in Figure 8.3. An exponential decreasing trend of UCS with increasing water content was observed for water contents less than 30 percent. The exponential relationship of UCS in MPa and water content ($w$) in percentage is described by the equation shown in Figure 8.1. Young's modulus (*E*) in GPa versus water content ($w$) in percentage is described by the equation shown in Figure 8.24. Figure 8.4 shows the exponential relationship between Young's modulus and water content. The statistical parameter for the proposed model for UCS vs w showed the Residual standard error of 8.613, AIC of 304.01, and BIC of 309.23. Statistical parameter for the proposed model of $E$ vs $w$ had a Residual standard error of 0.66, AIC of 73.87, and BIC of 78.54. Comparing the two models (Figures 8.1 and 8.2), Young's modulus had a better relationship with water content than UCS.

$$\widehat{UCS} = 28.71e^{-0.251w}$$

**Figure 8.1: Equation. The predicted UCS of Wyoming Claystone.**

$$\hat{E} = 1.7407e^{-0.273w}$$

**Figure 8.2: Equation. The predicted Young's modulus of Wyoming claystone.**

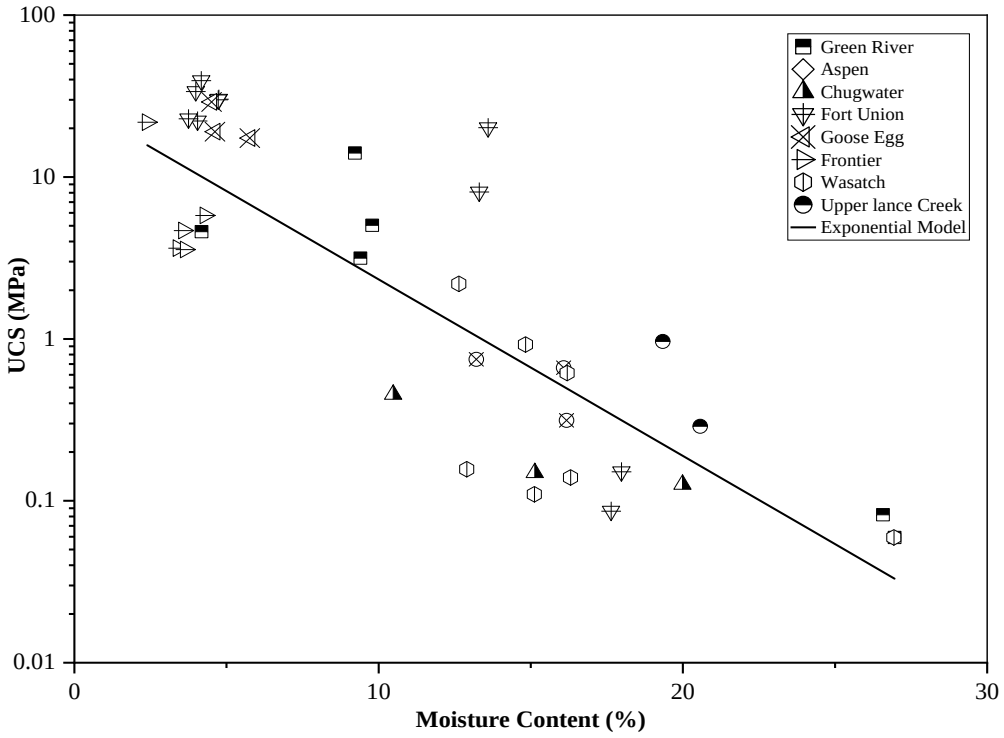


**Figure 8.3: UCS vs water content for Wyoming Claystone.**

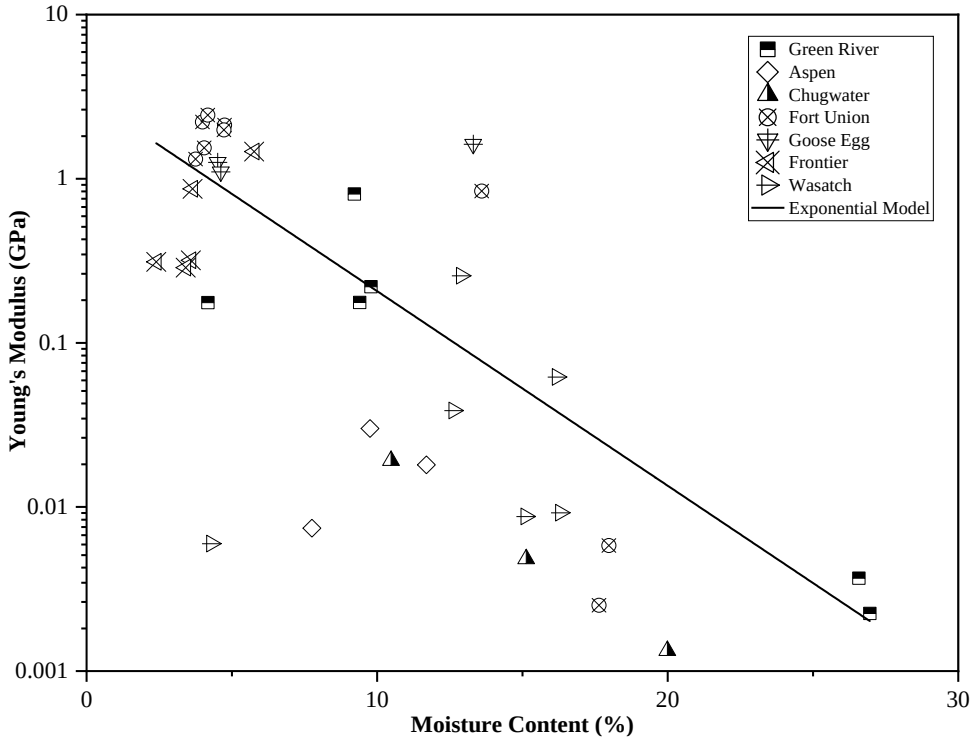


**Figure 8.4: Young's modulus vs water content for Wyoming Claystone.**

*Porosity (n)*

Figure 8.7 shows an inverse relationship between UCS and porosity for Wyoming Claystone. This linear relationship of UCS, in MPa, and porosity, in percent, is described by the equation shown in Figure 8.5. The statistical parameter for the proposed model showed a Residual standard error of 7.642, AIC of 293.97, and BIC of 299.18. The slightly lower AIC and BIC values of UCS vs porosity over UCS vs water content showed that the porosity was a more significant variable in predicting the UCS than water content. Figure 8.6 provides the relationship between Young's modulus, in GPa, and porosity and the data are shown in Figure 8.8. The statistical parameter for the proposed model showed the Residual standard error of 0.60, AIC of 68.07, and BIC of 72.73. Comparing the values of RSE, AIC, and BIC of equations shown in Figures 8.5 and 8.6, we find that Young's modulus related much better to porosity than UCS.

$$\widehat{UCS} = 62.29\, e^{-0.17n}$$

**Figure 8.5: Equation. The predicted UCS of Wyoming claystone.**

$$\hat{E} = 3.3678e^{-0.174n}$$

**Figure 8.6: Equation. The predicted Young's modulus of Wyoming claystone.**

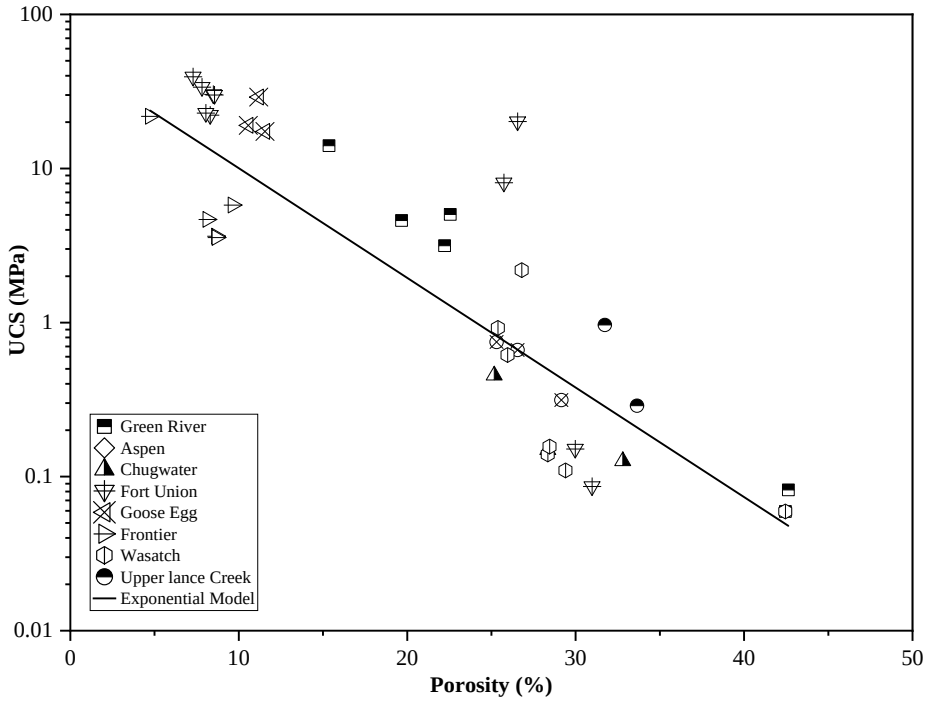


**Figure 8.7: UCS vs porosity for Wyoming Claystone.**

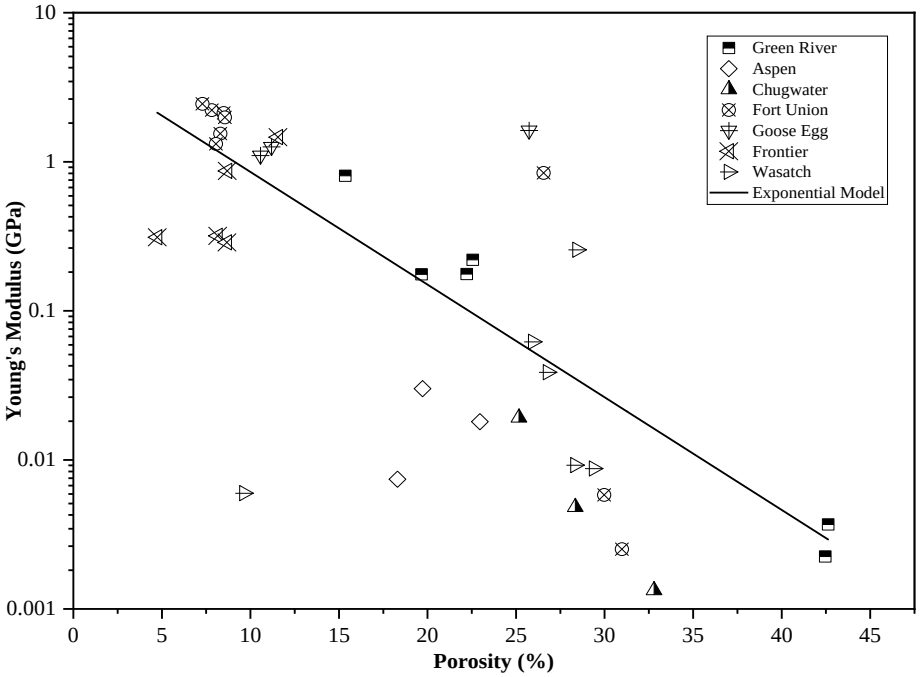


**Figure 8.8: Young's modulus vs porosity for Wyoming Claystone.**

*Bulk density ($\rho$)*

Figure 8.9 shows the linear relationship between UCS and $\rho$. Similarly, Figure 8.10 showed the relation between Young's modulus and $\rho$ for claystone. The $\rho$ showed no relation with UCS and Young's modulus as no prediction model could be developed.

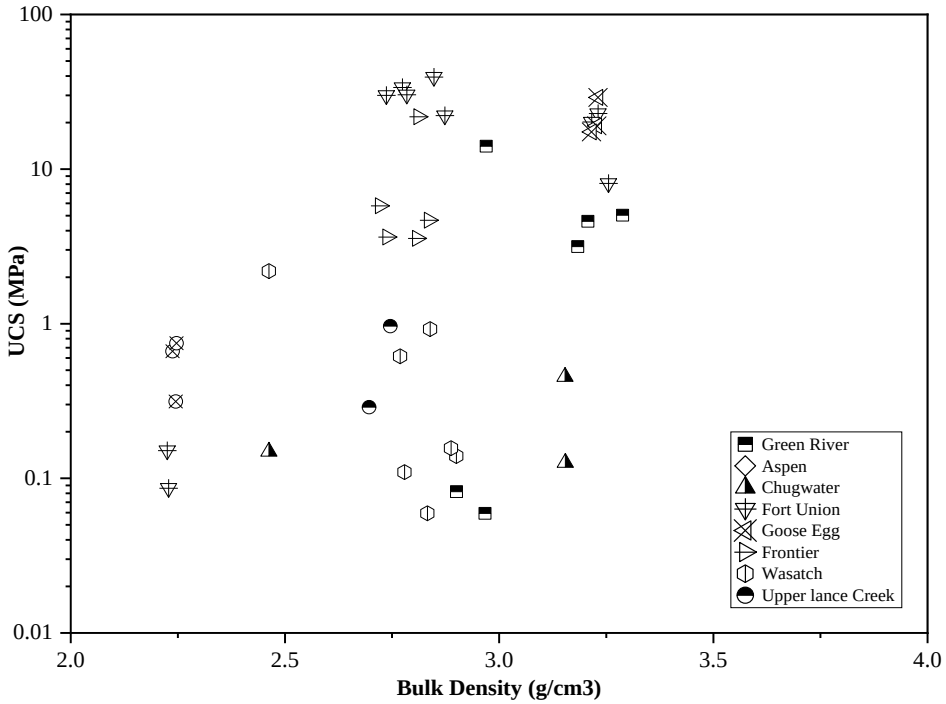


**Figure 8.9: UCS vs bulk density for Wyoming Claystone.**

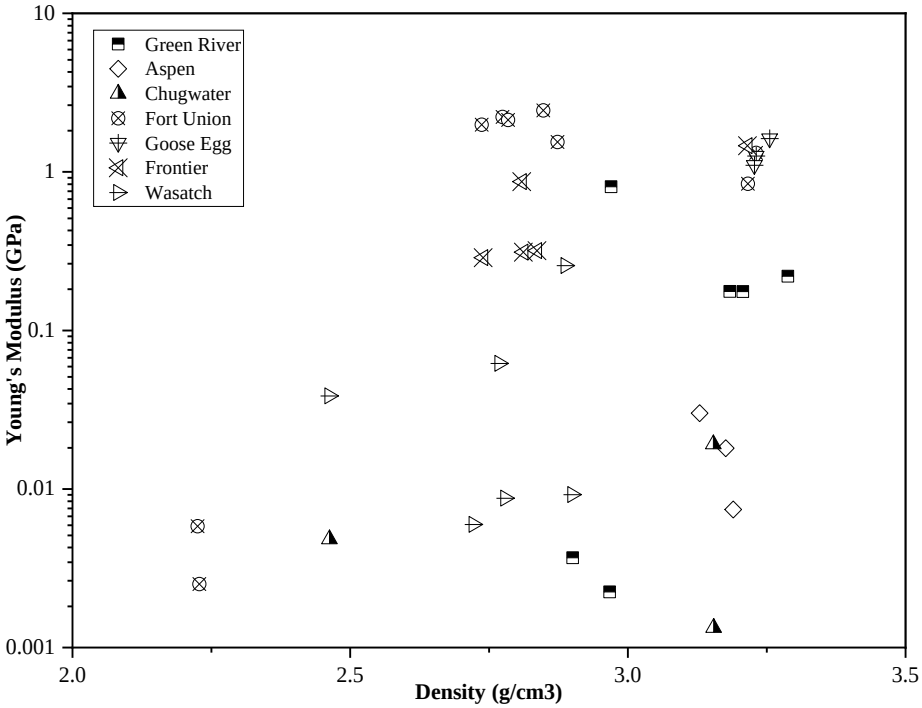


**Figure 8.10: Young's modulus vs bulk density for Wyoming Claystone.**

*Young's modulus (E)*

In this study, a linear trend was observed for claystone as shown in Figure 8.12. The relationship between $E$ and UCS is described by the equation shown in Figure 8.11 with the $R^2$ of 96 percent. The R-squared value of 96 percent showed that there was a strong relationship between Young's modulus (GPa) and the UCS (MPa).

$$\hat{E} = 0.0654 \times UCS + 0.0287$$

**Figure 8.11: Equation. The predicted Young's modulus of Wyoming claystone.**

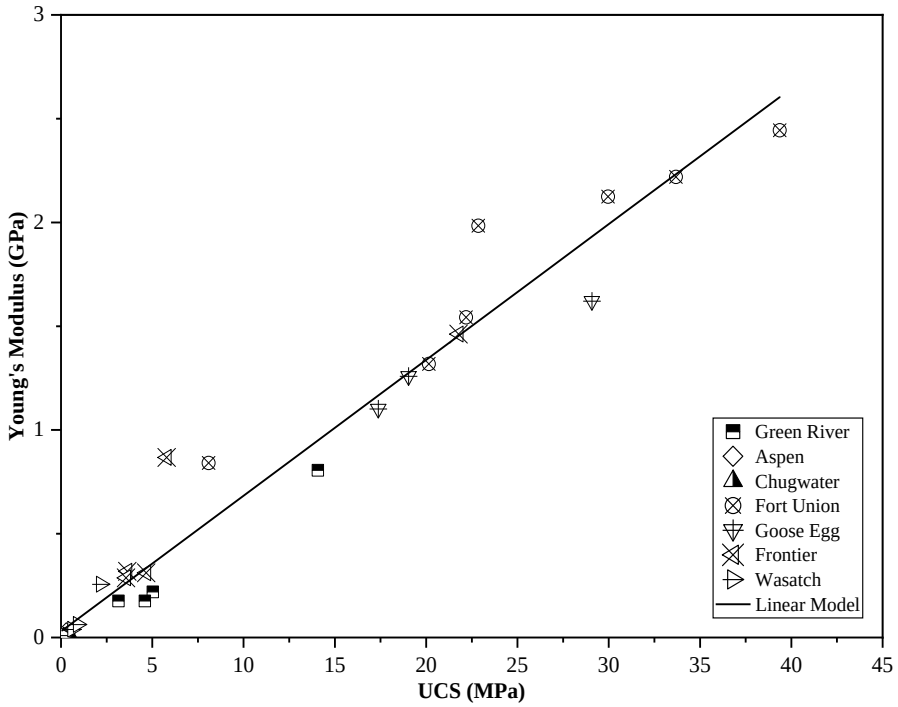


**Figure 8.12: Young's modulus Vs UCS for Wyoming Claystone.**

*Axial Strain at Peak Stress*

Figure 8.13 shows no apparent relationship between UCS and the axial strain at peak stress (in percentage) for claystone. Figure 8.14 shows the relationship between Young's modulus (GPa) and axial strain at the peak stress (in percentage). There seemed to be no apparent relationship between UCS and the axial strain at peak stress of claystone. Similarly, Figure 8.14 shows no apparent relationship between Young's modulus and axial strain at the peak stress for claystone and no correlation could be developed.

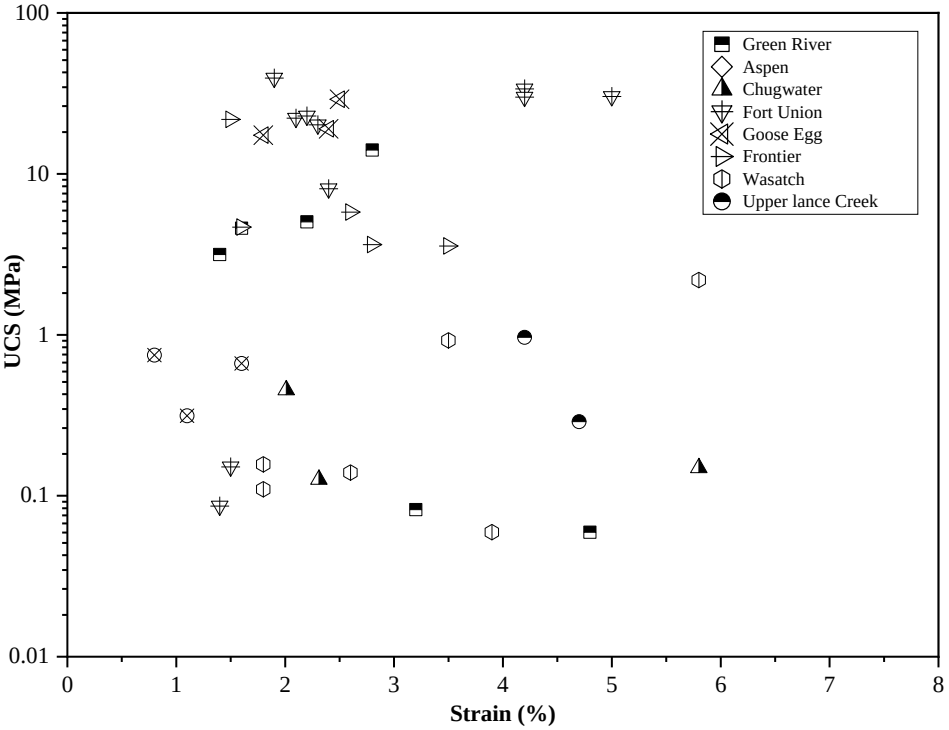


**Figure 8.13: UCS vs peak strain for Wyoming Claystone.**

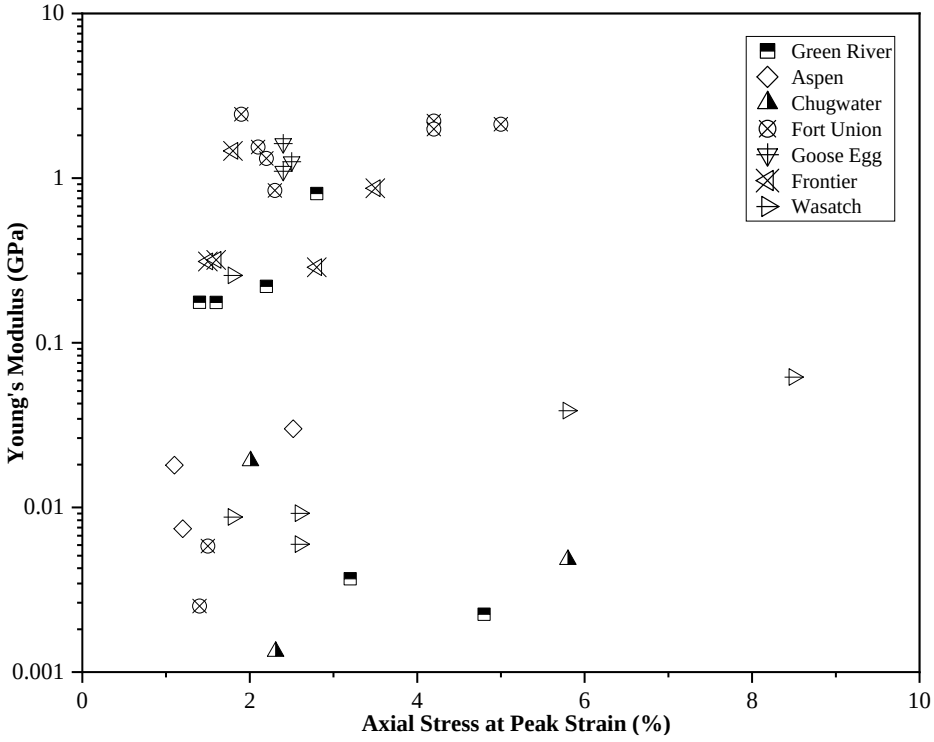


**Figure 8.14: Young's modulus vs peak strain for Wyoming Claystone.**

## 8.3 Mechanical Properties under Triaxial Compression

The triaxial test results summarized in this chapter were based on rock cores obtained from Wyoming. Five triaxial tests were performed in the laboratory on three claystone formations, and the test results are summarized in Table 8.2. No triaxial test data on claystone could be found in published literature. Due to the limited triaxial test data on claystone, similar correlation analysis to develop prediction models cannot be performed.

**Table 8.2: Database of triaxial compression test results of claystone from laboratory.**

| Claystone Formation | Avg $w$ (percent) | Avg $n$ (percent) | Confining Pressure (MPa) | Peak Stress (MPa) | Avg $E$ (GPa) |
|---|---|---|---|---|---|
| Ogallala | 15.90 | 28.00 | 0.32-0.56 | 1-1.27 | 0.01-0.017 |
| Wind River | 7.85 | 5.13 | 4-10 | 51-70 | 3.58-4.57 |
| Hanna | 6.58 | 7.65 | 4 | 51 | 3.90-4.49 |

Note: Avg– Average; $w$– Water content (percent); $n$– Porosity (percent); $\rho$ – Bulk density (g/cm3); UCS– Uniaxial compression test; $E$– Young's Modulus.

# CHAPTER 9: MECHANICAL PROPERTIES OF CARBONATE ROCKS UNDER UNIAXIAL AND TRIAXIAL CONDITIONS

## 9.1 Research Methods and Analysis

Three limestones and one dolostone sample from Wyoming were tested for uniaxial and triaxial compression tests. The four samples were collected from the surface for testing. The limestone samples have water contents ($w$) ranging from 1.84 percent to 2.18 percent and the porosity ($n$) ranges from 1.86 percent to 12.20 percent. Whereas the dolostone sample had water contents of 1.41 percent and porosity ($n$) of 8.29 percent.

Other carbonate rocks collected from literature in addition to limestone data collected from the historical WYDOT database are summarized in Figure 9.3 and Figure 9.11 for uniaxial and triaxial compression tests respectively. Carbonate rocks from the literature included limestone, dolomite, gypsum, chalk, and marble. The proposed models were compared with other models from the literature based on the RMSE and MAD values.

## 9.2 Mechanical Properties under Uniaxial Compression

An experimental study was carried out on 3 limestones and one dolostone formations from Wyoming, USA in addition to other data collected from literature, to examine the effect of physical properties on the UCS of carbonate rocks. A summary of the UC test results is given in Figure 9.3. Additional test results of Madison Limestone were collected from a historical rock database developed by the Wyoming Department of Transportation (WYDOT). Various formations collected from literature were utilized to better understand the mechanical behaviors of carbonate rocks from different regions of the world. The recommended model for the true mean of UCS is power in terms of the porosity ($n$ in percentage) as shown in Figure 9.2 and given by the equation shown in Figure 9.1 based on the training dataset that contains 178 data points.

$$\widehat{UCS} = 60.251\,(1 - 0.02\,n)^{1.67}$$

**Figure 9.1: Equation. The predicted UCS of carbonate rocks.**

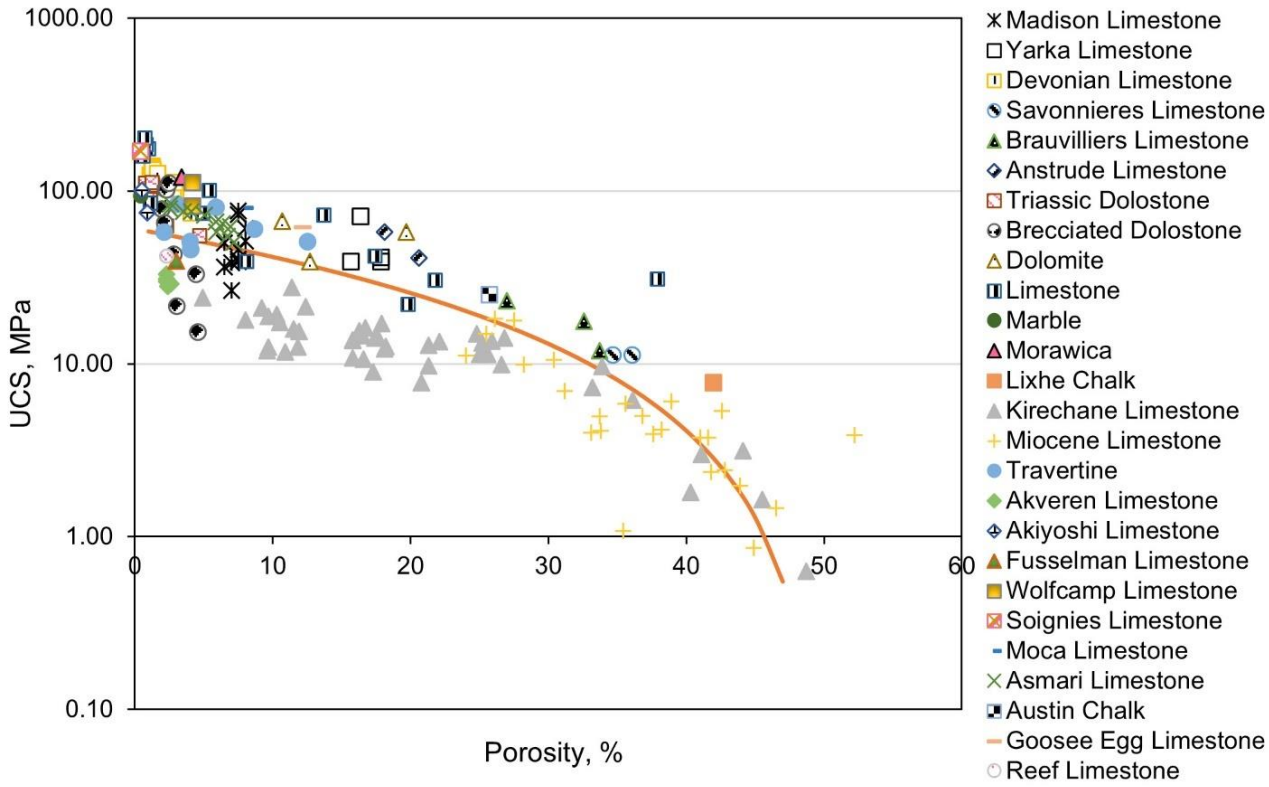


**Figure 9.2: Relationship between UCS and rock porosity.**

The negative power trend in porosity on predicting UCS (Figure 9.1) was consistent with past findings that explain the weakening effect of pores on the rock's compressive strength because pores are considered weak points within the rock matrix that induces stress concentration (Ludovico-Marques et al. 2012). Figure 9.4 summarizes several relationships developed for predicting UCS based on specific carbonate rock formations reported in the literature. According to the independent testing dataset that contained 76 data points and included formations from literature and Wyoming, the proposed equation for UCS prediction fitted the testing dataset better than other equations according to the lowest RMSE and MAD values summarized in Figure 9.4.

| Formation, (Location) | n, % | $\rho_{dry}$, $g/cm^3$ | UCS, MPa | *E*, GPa | Reference |
|---|---|---|---|---|---|
| Madison Limestone | 6.50-8.00 | 2.493-2.534 | 26.65-76.65 | NA | Rock Spring uplift- WY study |
| Yarka Limestone | 15.70-17.90 | 2.300-2.360 | 38.70-71.00 | 6.20-8.40 | Palchik (2010) |
| Devonian Limestone | 1.14-4.12 | 2.611-2.731 | 74.20-138.10 | 16.68-46.23 | Zarif and Turgul (2003) |
| Savonnieres Limestone | 30.60-36.10 | 1.721-1.820 | 11.20-17.00 | NA | Moh'd (2009) |
| Brauvilliers Limestone | 27.00-33.70 | 1.766-1.959 | 11.90-23.20 | NA | |
| Anstrude Limestone | 18.10-21.90 | 2.114-2.218 | 41.10-58.10 | NA | |
| Kirechane Limestone | 4.90-33.90 | 1.352-2.699 | 7.32-24.06 | NA | Ceryan et al. (2013) |
| Miocene Limestone | 11.40-52.20 | 1.363-2.405 | 0.63-27.6 | 0.47-10.30 | Vasarhelyi. (2005) |
| Akveren Limestone | 2.20-2.60 | 2.220-2.330 | 28.00-33.00 | 49.00-58.69 | Kurtulus et al. (2015) |
| Akiyoshi Limestone | 0.50-0.90 | 2.710-2.720 | 75.00-101.00 | NA | Kawakita et al. (1981) |
| Asmari Limestone | 2.04-7.21 | 2.410-2.700 | 50.40-84.20 | NA | Jamshidi et al. (2017) |
| Indiana Limestone | 14.80 | NA | 61.00 | NA | Walton et al. (2017) |
| Reef Limestone | 2.30 | 2.590 | 42.00 | NA | Liu et al. (2021) |
| Triassic Dolostone | 0.76-4.70 | 2.620-2.800 | 47.29-112.00 | 2.38-18.80 | Pappalardo (2015) |
| Brecciated Dolostone | 1.40-4.60 | 2.570-2.720 | 15.18-109.65 | 2.67-18.09 | |
| Weathered Limestone | 8.10 | 2.280 | 39.00 | 37.00 | Verwaal and Mulder (1993) |
| Artificial fine grained Gypsum rock | 35.00 | 1.800 | 8.00 | 2.00 | |
| Medium grained Calcarenite | 50.10 | 1.340 | 6.00 | NA | |
| Detrital Limestone | 19.80 | 1.720 | 22.00 | 9.00 | |
| Fine grained Limestone | 37.90 | 2.150 | 31.00 | 12.00 | |
| | 15.70 | 1.940 | 57.00 | 24.00 | |
| Weathered Dolomite | 12.70 | 2.030 | 39.00 | 38.00 | |
| Weathered Limestone | 8.10 | 2.280 | 39.00 | 37.00 | |
| Fine grained Dolomite | 10.70 | 2.310 | 67.00 | 32.00 | |
| Fine grained Marble | 0.40 | 2.440 | 94.00 | 49.00 | |
| Fresh micritic fine grained Limestone | 5.40 | 2.420 | 101.00 | 26.00 | |
| Fine grained micritic Limestone | 4.90 | 2.70 | 74.00 | 52.00 | |
| Coarse crystalline Limestone | 1.10 | 2.340 | 85.00 | 59.00 | |
| Medium grained Limestone | 3.80 | 2.550 | 174.00 | 59.00 | |
| | 1.00 | 2.190 | 176.00 | 78.00 | |
| | 0.60 | 2.580 | 159.00 | 76.00 | |

**Figure 9.3: Summary of UC test results of carbonate rocks from literature and this study.**

| Formation, (Location) | n, % | $\rho_{dry}$, g/cm$^3$ | UCS, MPa | *E*, GPa | Reference |
|---|---|---|---|---|---|
| | 0.70 | 2.660 | 203.00 | 80.00 | |
| Fine grained Limestone | 0.50 | 2.510 | 163.00 | 69.00 | |
| Crystalline Limestone | 0.80 | 2.680 | 186.00 | 70.00 | |
| Morawica | 3.40 | 2.648 | 120.00 | 58.00 | Fabre and Gustkiewicz (1997) |
| Tonnerre Limestone | 13.70 | 2.642 | 72.40 | 19.30 | |
| Chauvigny Limestone | 17.40 | 2.583 | 42.00 | 16.30 | |
| Lavoux Limestone | 21.80 | 2.652 | 30.40 | 13.80 | |
| Louny Gauze | 26.00 | 2.669 | 58.00 | 9.20 | |
| Lixhe Chalk | 42.00 | 2.643 | 7.70 | 3.80 | |
| Travertine | 2.15-13.27 | 1.295-2.401 | 45.40-112.30 | NA | Kahraman et al. (2005) |
| Danian Chalk | 43.05 | 1.53 | 11.00 | NA | Blanton (1981) |
| Austin Chalk | 25.75 | 2.03 | 25.00 | NA | |
| Devonian Limestone | 2.30 | 2.670 | 78.45 | NA | Handin and Hanger (1957) |
| Fusselman Limestone | 3.00 | 2.547 | 39.23 | NA | |
| Wolfcamp Limestone | 4.20 | 2.625 | 110.82 | NA | |
| Soignies Limestone | 0.40 | 2.700 | 170.00 | NA | Descamps and Tshibang (2011) |
| | 0.40 | 2.700 | 139.00 | 13.20 | |
| Moca Limestone | 8.00 | 2.652 | 79.00 | NA | |
| Sorcy Limestone | 30.00 | 2.350 | 47.00 | NA | |
| Big horn Dolostone | 8.29 | NA | 23.13 | 3.09 | This study |
| Jefferson Limestone | 1.55 | 2.500 | 11.33 | 6.72 | |
| Goose Egg Limestone | 12.20 | 2.560 | 61.27 | 32.55 | |

Note: NA– Unavailable; D– Specimen diameter (mm); n– Porosity (%); *w*– water content (%); UCS– Unconfined compressive strength (MPa); *E*– Young's modulus (GPa).

**Figure 9.3 (Continued): Summary of UC test results of carbonate rocks from literature and this study.**

| Rock type | Reference | Model from literature | Model from literature | | This study | |
|---|---|---|---|---|---|---|
| | | | RMSE | MAD | RMSE | MAD |
| Carbonate rocks | Farquhar et al. (1994) | $UCS = 174.8\, e^{-9.3\, n}$ | 48.64 | 37.15 | 29.29 | 21.8 |
| Carbonate rocks, n<0.3 | Hebib et al. (2017) | $UCS = -28.56 \ln(n)$ | 23.79 | 17.64 | 31.16 | 25.72 |
| Dolomite | Hatzor and Palchik (2000) | $UCS = \frac{\pi \times E^{0.25}}{n\%^{0.45} \times \sqrt{d_m}}$ | 51.51 | 49.08 | 27.96 | 22.49 |
| Gypsum (2 data points) | Yilmaz (2010) | $UCS = 16.68 \times e^{-0.8193\, w\%} + 24$ | 33.69 | 33.68 | 4.24 | 3.04 |
| Limestone | Chang et al. (2006) | $UCS = 13.8 \times E^{0.51}$ | 24.30 | 28.79 | 24.3 | 27.02 |
| Dolomite | | $UCS = 25.1 \times E^{0.34}$ | 23.92 | 19.21 | 27.96 | 22.49 |
| Limestone & Dolomite | | $UCS = 276 \times (1 - 3 \times n)^2$ | 103.84 | 69.73 | 22.33 | 13.70 |
| Carbonate rocks with 0.05<n<0.2 and 30<UCS<150 | | $UCS = 143.8 \times e^{-6.95\, n}$ | 46.90 | 40.03 | 33.10 | 26.77 |
| Carbonate rocks with 0.05<n<0.2 and 30<UCS<150 | | $UCS = 135.9 \times e^{-4.8\, n}$ | 44.95 | 51.12 | 26.77 | 33.10 |
| Carbonate rocks | M.Beiki et al. (2013) | $UCS = -7.7 \ln(n) + 74.5$ | 32.71 | 26.07 | 26.39 | 17.48 |

Note: NA–Unavailable; UCS–Unconfined compressive strength (MPa); w–water content (%), n–rock porosity (%), RMSE-Root Mean Square Error; MAD-Mean Absolute Deviation.

**Figure 9.4: Assessment of prediction equations for UCS based on the testing dataset.**

*Young's Modulus*

The relationship between Young's modulus and porosity according to the training dataset is shown in Figure 9.6. The plot illustrated a power decrease in mean *E* as the porosity increased according to the training dataset that contained 79 data points from literature and Wyoming. Other studies related to predicted *E* are summarized in Figure 9.7. According to the testing dataset that contained 66 data points, the proposed equation shown in Figure 9.5 had lower RMSE and MAD compared to those from the literature except for the model of Farquhar et al. (1994) where the statistical comparison was very similar, indicating a better prediction of Young's modulus for most of the models.

$$\hat{E}(GPa) = 30.31\ (1 - 0.02\ n)^{1.82}$$

**Figure 9.5: Equation. The predicted Young's modulus of carbonate rocks.**

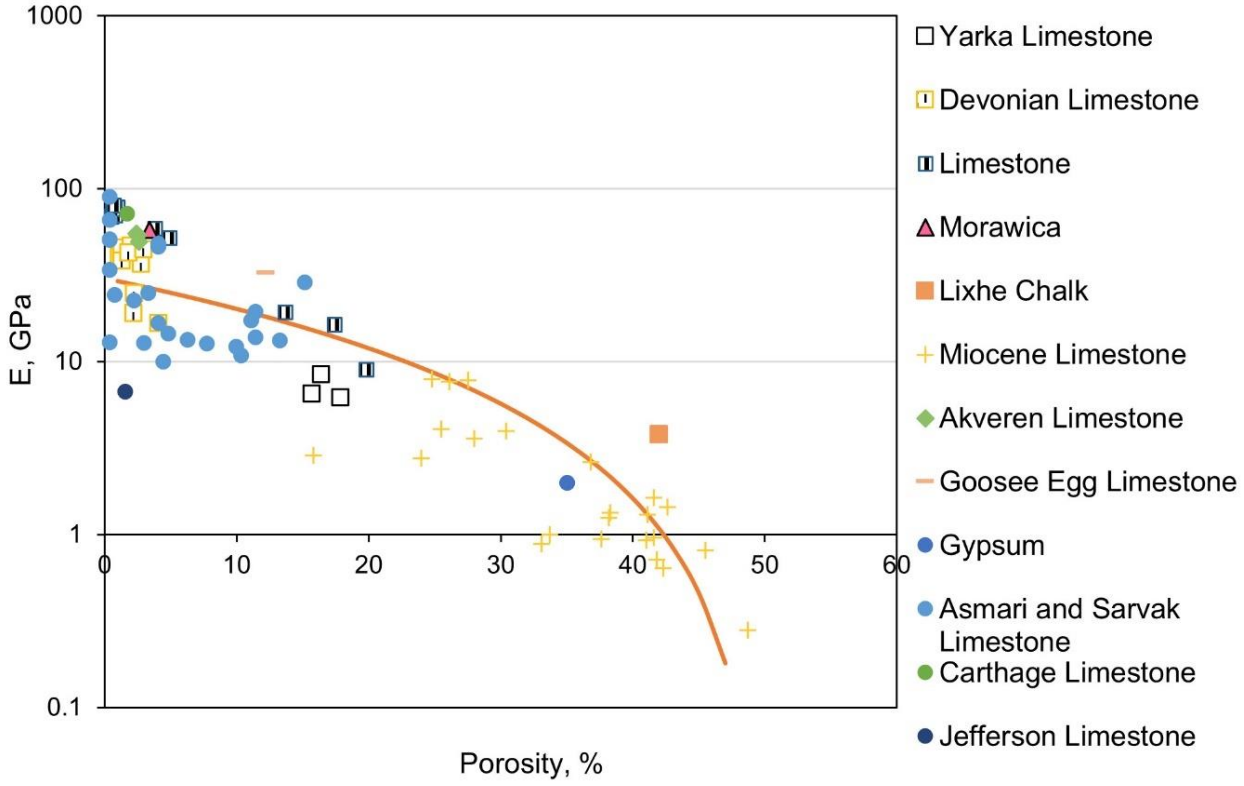


**Figure 9.6: Relationship between Young's modulus and rock porosity.**

| Rock type | Reference | Model from literature | Model from literature | | This study model | |
|---|---|---|---|---|---|---|
| | | | RMSE | MAD | RMSE | MAD |
| Carbonate rocks | M.Beiki et al. (2013) | $E = 69.05\, e^{-6\, n}$ | 20.02 | 14.87 | 15.80 | 10.72 |
| Carbonate rocks, n<0.3 | Ameen et al. (2009) | $E = 86.094\, e^{-5.34\, n}$ | 35.94 | 31.95 | 18.89 | 14.89 |
| Carbonate rocks, n<0.3 | Asef et al. (2010) | $E = \left(\frac{UCS}{2.94} \times n^{0.088}\right)^{1.2}$ | 13.49 | 19.47 | 10.72 | 15.80 |
| Carbonate rocks | Farquhar et al. (1994) | $E = 36.6\ (0.91)^{n\%}$ | 15.21 | 10.35 | 15.80 | 10.71 |

Note: NA–Unavailable; UCS–Unconfined compressive strength (MPa); w–water content (%); n–rock porosity (%); RMSE-Root Mean Square Error; MAD-Mean Absolute Deviation.

**Figure 9.7: Assessment of Young's modulus predictions based on the testing dataset.**

## 9.3 Mechanical Properties under Triaxial Compression

Figure 9.11 includes a summary of the triaxial compression test results of carbonate rocks from this study and literature. The effect of porosity on rock strength was further demonstrated with the comparison of porosity and the failure parameters, cohesion ($c$), and internal friction angle ($\varphi$), derived for the Mohr-Coulomb criterion as shown in Figure 9.8. The internal friction angle decreased with increasing porosity indicating that the porosity had a significant effect on the rock failure. A similar decreasing trend was observed between porosity and cohesion. However, because of other factors that are not available in this study, such as minerology, geological process (cementation), and compaction, a larger variation was observed between porosity and cohesion.

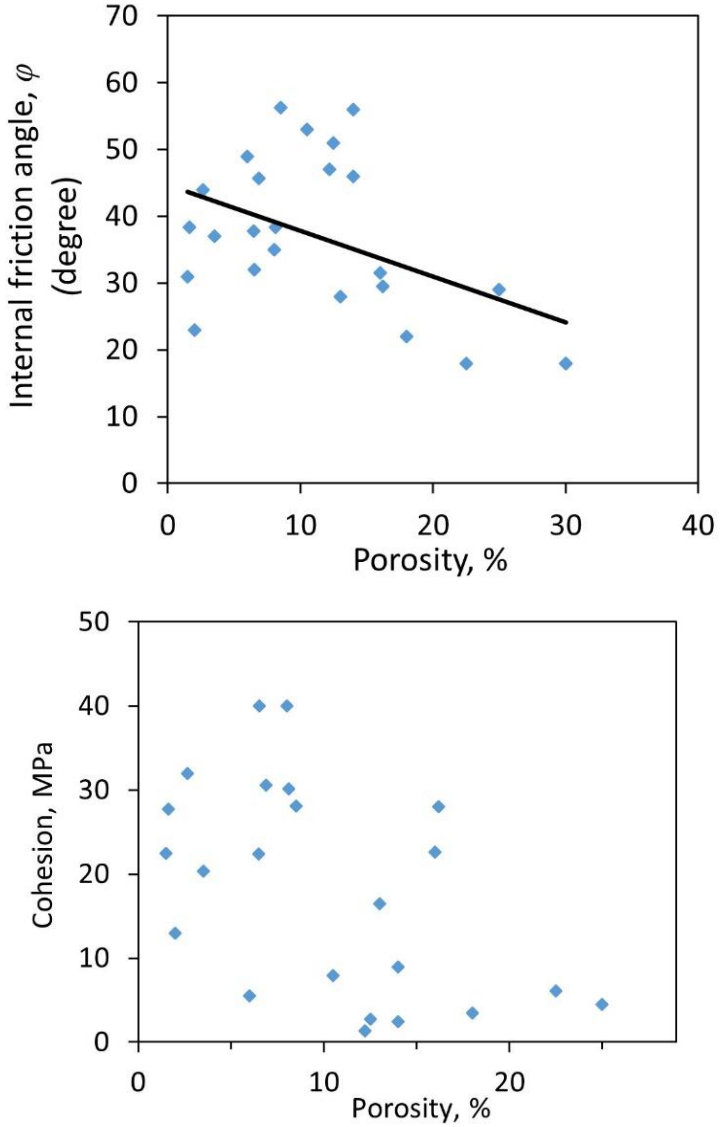


**Figure 9.8: Comparison of the porosity effect on the internal friction angle and cohesion.**

Figure 9.9 contains a linear model to capture the relationship between *n* in percentage, $\sigma_3$ in MPa, and the true mean $\sigma_1$ in MPa based on the training dataset that contained 250 data points from literature and Wyoming. The relationship is shown in Figure 9.10.

$$\widehat{\sigma_1} = 252.74 - 8.50\, n + 2.29\, \sigma_3$$

**Figure 9.9: Equation. The predicted peak compressive strength of carbonate rocks.**

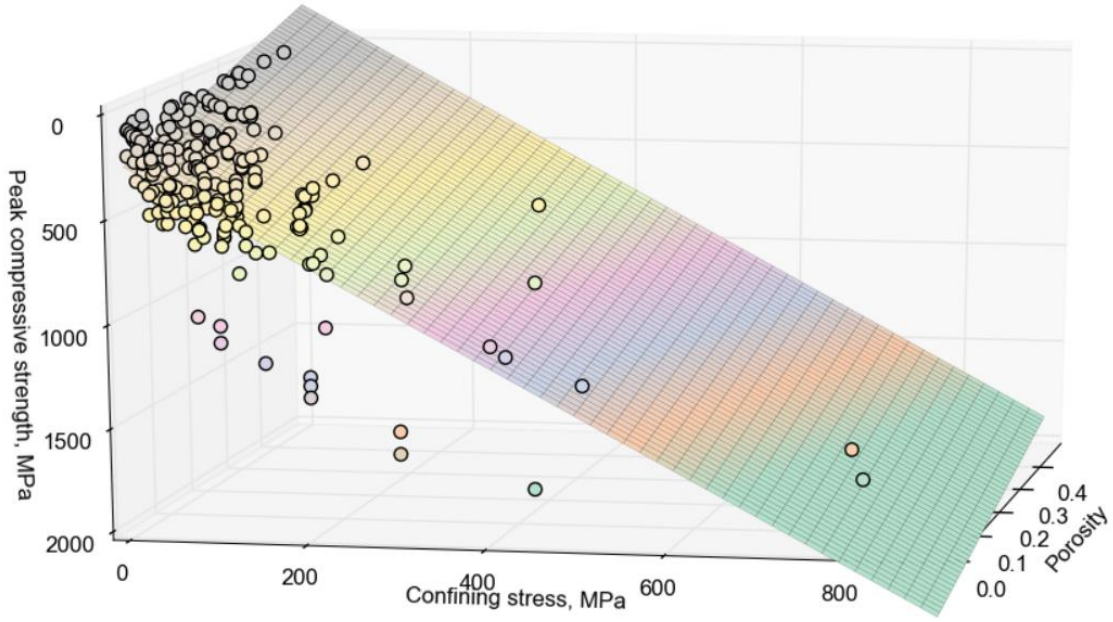


**Figure 9.10: Relationship between the peak compressive strength and the porosity and confining pressure.**

The mean $\sigma_1$ decreased with the increase in *n*. An increase in the internal surface area per unit rock volume resulting from a higher n decreased the predicted integrity of the rock and hence reduced its strength (Atapour and Mortazavi 2018a). On the other hand, the mean $\sigma_1$ generally increased with an increase in the confining pressure $(\sigma_3)$ due to the strengthening effect of confinement on compressive strength. Statistical results indicated that both *n* and $\sigma_3$ were significant predictors of mean $\sigma_1$.

| Formation, (Location) | n, % | $\sigma_3$, MPa | $\sigma_1$, MPa | Reference |
|---|---|---|---|---|
| Soignies Limestone | 0.40 | 2-90 | 206.00-443.00 | Descamps and Tshibangu (2007) |
| Soignies Limestone | 0.40 | 30-90 | 265.00-428.00 | Descamps and Tshibangu (2011) |
| Moca Limestone | 8.00 | 10-40 | 140.00-220.00 | |
| Sorcy Limestone | 29.50 | 5-10 | 47.00-71.00 | |
| Saint Maximin Limestone | 37.00 | 3-6 | 20.00-25.00 | Baud et al. (2009) |
| Salem/Indiana Limestone | 16.90 | 25-400 | 87.00-544.00 | Chitty et al. (1994) |
| Tavel Limestone | 10.40 | 10-50 | 221.00-313.00 | Vajdova et al. (2004) |
| Indiana Limestone | 13.40 | 5-10 | 45.00-62.00 | Vajdova et al. (2004) and (2012) |
| Indiana Limestone | 19.40 | 7-69 | 65.50-174.40 | Schwartz (1964) |
| White Tavel Limestone | 14.70 | 20-85 | 181.33-430.00 | Nicolas et al. (2016) and (2017) |
| Comiso Limestone | 10.10 | 7-30 | 123.23-214.41 | Castagna et al. (2018) |
| Solnhofen Limestone | 3.00 | 10-50 | 336.00-478.00 | Baud et al. (2000) |
| Solnhofen Limestone | 4.80 | 17-81 | 277.00-491.00 | Byerlee (1968) |
| Solnhofen Limestone | 5.90 | 100-800 | 530.00-1730.00 | Edmond and Peterson (1972) |
| Solnhofen Limestone | 1.70 | 20-500 | 493.00-1264.00 | Heard (1960) |
| Solnhofen Limestone | 4.80 | 0.1-98 | 270.76-490.33 | Byerlee (1968) |
| Intact Solnhofen Limestone | 3.70-5.50 | 6-195 | 311.00-703.00 | Mogi (2007) |
| Oak Hall Limestone | 0.30 | 18-220 | 388.00-1000.00 | Byerlee (1968) |
| Indiana Limestone | 0.15 | 2-50 | 75.00-173.00 | Walton et al. (2017) |
| Benxi Limestone | NA | 5-20 | 90-180 | Liu et al. (2018) |
| Maokou Limestone | 0.09 | 4-12 | 80.90-170.00 | Zhao et al. (2017) |
| Reef Limestone | 0.02 | 1-8 | 63.00-181.00 | Liu et al. (2021) |
| Xuzhou Limestone | NA | 5-30 | 110.00-157.00 | Meng et al. (2020) |
| Comiso Limestone | 0.10 | 7-50 | 123.23-214.41 | Castagna et al. (2018) |
| Karst Limestone | NA | 5-25 | 131.00-288.00 | Wang et al. (2019) |
| Majella Grainstone | 30.00 | 5-21 | 32-46 | Baud et al. (2009) |
| Georgia Marble | 2.70 | 7-69 | 83.00-228.00 | Schwartz (1964) |
| Carrara Marble | 1.10 | 50-800 | 270.00-1530.00 | Fredrich et al. (1989) |
| Carrara Marble | 1.10 | 1.72-34.5 | 80.31-247.99 | Gerogiannopoulous (1976) |
| Carrara Marble | 1.10 | 5-450 | 100.00-770.00 | Fredrich et al. (1989) |
| Wombeyan Marble | 0.90 | 0.1-98 | 69.73-332.45 | Paterson (1958) |

**Figure 9.11: Summary of triaxial compression test results of carbonate rocks from this study and literature.**

| Formation, (Location) | n, % | $\sigma_3$, MPa | $\sigma_1$, MPa | Reference |
|---|---|---|---|---|
| Blair Dolomite | 0.90 | 50-450 | 549.00-1760.00 | Handin et al. (1967) |
| Cold pressed Aragonite | 10.60-22.30 | 10-195 | 84.00-661.00 | Renner and Rummel (1996) |
| Cold pressed Calcite | 6.90-16.20 | 10-150 | 89.00-500.00 | |
| Cold pressed Solnhofen Limestone | 7.40-15.80 | 10-150 | 96.00-485.00 | |
| Gypsum | 0.50 | 2-95 | 19.80-83.00 | Brantut et al. (2011) |
| Big Horn Dolostone | 8.29 | 4-10 | 38.55-79.56 | This study |
| Madison Limestone | 2.60-7.90 | 1-10 | 31.67-38.6 | |
| Goose Egg Limestone | 12.00-12.40 | 1-2 | 62.98-67.01 | |
| Jefferson Limestone | 1.90-2.10 | 4-10 | 52.76-146.71 | |

Note: NA– Unavailable; D– Specimen diameter (mm); n– Porosity (%); w– water content (%); $\sigma_3$– Confining pressure (MPa); $\sigma_1$– Compressive Strength (MPa); *E*– Young's modulus (GPa); c-Cohesion (MPa); $\varphi$– Internal friction angle in degree.

**Figure 9.11 (Continued): Summary of triaxial compression test results of carbonate rocks from this study and literature.**

# CHAPTER 10: SUMMARY, CONCLUSIONS AND RECOMMENDATIONS

## 10.1 Summary

This study was aimed at understanding the mechanical and deformation behaviors and quantifying the mechanical properties of Wyoming bedrocks to improve the design and construction of transportation infrastructures in the state. To accomplish this objective, fifty samples were tested under different confining pressures. Tested rock samples were mostly sandstone (30 percent), siltstone (23 percent), shale (14 percent), and others (33 percent). Bedrocks in Wyoming were from different geological ages, and a conscious effort was made to include samples from different ages. The tested samples were mostly from Cretaceous (27 percent), Eocene (13 percent), Paleogene (11 percent), and others. The rock samples were from all three geological rock types: Sedimentary (86 percent), Igneous (11 percent), and Metamorphic (3 percent). The rock samples were obtained as surface boulders (48 percent) and rock cores from subsurface drilling (52 percent). The rock specimens prepared for testing were either 25mm or 50mm in diameter with a height-to-diameter ratio of two.

Uniaxial and triaxial compression tests were conducted using GCTS RTR-1500 rapid triaxial rock testing equipment for hard rocks and GeoJac triaxial equipment for soft and soil-like rocks. The physical properties like water content, porosity, and specific gravity of tested specimens were measured before compression testing. Laboratory compressive tests were performed to measure the stress and strains of each rock specimen.

Elastic properties (Young's modulus and Poisson's ratio) were determined from the linear stress-strain relationship of the rock under compression. Shear strength parameters, such as cohesion and internal friction angle, were determined from the Mohr-Coulomb criterion constructed from a series of Mohr's circles. The nonlinear HB criterion was also applied to determine the tensile strength and material constant ($m_i$) for each rock sample. This research focused on presenting the results of laboratory tests and correlation analyses to relate mechanical properties to physical properties of sandstone, claystone, shale, limestone, and siltstone. An extensive study was conducted to compile available test data on sandstone, shale, claystone, limestone, and siltstone from the literature for correlation analyses.

## 10.2 Conclusions

An extensive experimental study was conducted to study the effects of physical properties and environmental conditions on the mechanical behaviors of Wyoming bedrocks under different loading conditions. The empirical equations developed from this study for predicting UCS, *E* and strength parameters in a SI unit system and English unit system are summarized in Figure 10.1 and Figure 10.2, respectively.

| Rock Type | Developed Equation | Test Condition | Data Source |
|---|---|---|---|
| Sandstone | $\widehat{UCS}(MPa) = 109.87 - 2.39\,n - 9.12\,w - 33.74\,d_m$ | UC | World |
| | $\hat{E}(GPa) = 0.15\,UCS + 1.38$ | UC | World |
| Shale | $\widehat{UCS}(MPa) = 88.15 \times 0.62^{w}$ | UC | World |
| | $\widehat{UCS}(MPa) = 4.81\,(1 - \frac{n}{47.5})^{1.7}$ | UC | Wyoming |
| | $\hat{E}(GPa) = 28.12\,w^{-2.92}$ | UC | World |
| | $\hat{E}(GPa) = 324.02\,e^{-0.344n}$ | UC | World |
| | $\hat{E}(GPa) = 0.12\,UCS - 0.032$ | UC | Wyoming |
| | $\hat{E}(GPa) = 0.00004 \times \rho^{8.801}$ | UC | Wyoming |
| | $\hat{c}\,(MPa) = 24.84e^{-0.136n}$ | Triaxial | World |
| | $\hat{\varphi}\,(Degree) = 1.01 \times n - 12.48$ | Triaxial | World |
| Claystone | $\widehat{UCS}\,(MPa) = 28.71e^{-0.251w}$ | UC | Wyoming |
| | $\widehat{UCS}\,(MPa) = 62.29\,e^{-0.17n}$ | UC | Wyoming |
| | $\hat{E}\,(GPa) = 1.74e^{-0.273w}$ | UC | Wyoming |
| | $\hat{E}\,(GPa) = 3.378e^{-0.174n}$ | UC | Wyoming |
| | $\hat{E}\,(GPa) = 0.065 \times UCS + 0.029$ | UC | Wyoming |
| Siltstone | $\widehat{UCS}\,(MPa) = 39.18 \times 0.83^{w}$ | UC | Wyoming |
| | $\widehat{UCS}\,(MPa) = 29.77(1 - \frac{n}{47.5})^{2.15}$ | UC | Wyoming |
| | $\widehat{UCS}(MPa) = 0.16 \times \rho^{5.3966}$ | UC | Wyoming |
| | $\hat{E}(GPa) = 4.47w^{-1.45}$ | UC | Wyoming |
| | $\hat{E}(GPa) = 0.56e^{-0.658n}$ | UC | Wyoming |
| | $\hat{E}(GPa) = 0.064 \times UCS + 0.025$ | UC | Wyoming |
| | $\hat{E}(GPa) = 0.0003e^{3.1359\rho}$ | UC | Wyoming |
| | $\hat{c}\,(MPa) = 32.17 \times n^{-0.674}$ | Triaxial | Wyoming |
| | $\frac{\hat{c}}{n}\,(MPa) = 542.82e^{-0.614w}$ | Triaxial | Wyoming |
| Carbonate rocks | $\widehat{UCS}(MPa) = 60.25\,(1 - 0.02\,n)^{1.67}$ | UC | World |
| | $\hat{E}(GPa) = 30.31\,(1 - 0.02\,n)^{1.82}$ | UC | World |

Note: $UCS$ – Uniaxial Compressive Strength (MPa); n– Porosity (%); w–Water content (%); $d_m$– Mean grain size (mm); $E$–Young's modulus (GPa); $\rho$–dry density (g/cc); $c$–Cohesion (MPa); $\varphi$–Internal friction angle (degree); UC–Uniaxial Compression; World–Data for rocks collected from all over the world including Wyoming; Wyoming– Data are for Wyoming rocks only.

**Figure 10.1: Developed prediction equations for UCS, *E* and strength parameters from this study in SI unit system.**

| Rock Type | Developed Equation | Test Condition | Data Source |
|---|---|---|---|
| Sandstone | $\widehat{UCS}(MPa) = 109.87 - 2.39\,n - 9.12\,w - 33.74\,d_m$ | UC | World |
| | $\hat{E}(GPa) = 0.15\,UCS + 1.38$ | UC | World |
| Shale | $\widehat{UCS}(MPa) = 88.15 \times 0.62^{w}$ | UC | World |
| | $\widehat{UCS}(MPa) = 4.81\,(1 - \frac{n}{47.5})^{1.7}$ | UC | Wyoming |
| | $\hat{E}(GPa) = 28.12\,w^{-2.92}$ | UC | World |
| | $\hat{E}(GPa) = 324.02\,e^{-0.344n}$ | UC | World |
| | $\hat{E}(GPa) = 0.12\,UCS - 0.032$ | UC | Wyoming |
| | $\hat{E}(GPa) = 0.00004 \times \rho^{8.801}$ | UC | Wyoming |
| | $\hat{c}\,(MPa) = 24.84e^{-0.136n}$ | Triaxial | World |
| | $\hat{\varphi}\,(Degree) = 1.01 \times n - 12.48$ | Triaxial | World |
| Claystone | $\widehat{UCS}\,(MPa) = 28.71e^{-0.251w}$ | UC | Wyoming |
| | $\widehat{UCS}\,(MPa) = 62.29\,e^{-0.17n}$ | UC | Wyoming |
| | $\hat{E}\,(GPa) = 1.74e^{-0.273w}$ | UC | Wyoming |
| | $\hat{E}\,(GPa) = 3.378e^{-0.174n}$ | UC | Wyoming |
| | $\hat{E}\,(GPa) = 0.065 \times UCS + 0.029$ | UC | Wyoming |
| Siltstone | $\widehat{UCS}\,(MPa) = 39.18 \times 0.83^{w}$ | UC | Wyoming |
| | $\widehat{UCS}\,(MPa) = 29.77(1 - \frac{n}{47.5})^{2.15}$ | UC | Wyoming |
| | $\widehat{UCS}(MPa) = 0.16 \times \rho^{5.3966}$ | UC | Wyoming |
| | $\hat{E}(GPa) = 4.47w^{-1.45}$ | UC | Wyoming |
| | $\hat{E}(GPa) = 0.56e^{-0.658n}$ | UC | Wyoming |
| | $\hat{E}(GPa) = 0.064 \times UCS + 0.025$ | UC | Wyoming |
| | $\hat{E}(GPa) = 0.0003e^{3.1359\rho}$ | UC | Wyoming |
| | $\hat{c}\,(MPa) = 32.17 \times n^{-0.674}$ | Triaxial | Wyoming |
| | $\frac{\hat{c}}{n}\,(MPa) = 542.82e^{-0.614w}$ | Triaxial | Wyoming |
| Carbonate rocks | $\widehat{UCS}(MPa) = 60.25\,(1 - 0.02\,n)^{1.67}$ | UC | World |
| | $\hat{E}(GPa) = 30.31\,(1 - 0.02\,n)^{1.82}$ | UC | World |

Note: $UCS$ – Uniaxial Compressive Strength (MPa); n– Porosity (%); w–Water content (%); $d_m$– Mean grain size (mm); $E$–Young's modulus (GPa); $\rho$–dry density (g/cc); $c$–Cohesion (MPa); $\varphi$–Internal friction angle (degree); UC–Uniaxial Compression; World–Data for rocks collected from all over the world including Wyoming; Wyoming– Data are for Wyoming rocks only.

**Figure 10.2: Developed prediction equations for UCS, *E* and strength parameters from this study in English unit system.**

The main findings drawn from this study for each rock type were described as follows:

*Sandstone*

1) The UCS of sandstone was linearly related to water content ($w$), porosity ($n$), and mean grain size ($d_m$).
2) The $n$ and confining pressure significantly affected the triaxial compressive strength of dry sandstones.
3) A linear relationship between Young's modulus ($E$) and UCS was observed.

*Shale*

1) The UCS of shale decreased with the increase in $w$ and $n$. It was found that the UCS was lowest when the bedding angle ($\beta$) was between 30-60 degrees and highest when the $\beta$ was either 0 or 90 degrees. The UCS increased with the increase in bulk density ($\rho$) of shales. Axial strain at peak stress for shale showed no relationship with UCS.
2) $E$ of shale decreased with the increase in $w$. A negative relationship between $E$ and $n$ of shale was observed. $E$ increased with the increase in UCS. For Wyoming shales, some data showed that $E$ increased with the increase in $\beta$. Most data showed that the lowest $E$ occurred in shales with $\beta$ between 30-60 degrees and the highest $E$ in shales with the $\beta$ at either 0 or 90 degrees. $E$ had a decreasing trend with the axial strain at peak stress.
3) A linear relationship was observed between the peak stress and confining pressure for all $\beta$ angles 0, 15, 30, 45, 60, 75, and 90 degrees. No relationship was observed between the ratio of peak stress to confining pressure versus $n$ for $\beta$ of 0, 15, 30, 45, 60, 75, and 90 degrees. The effect of $\beta$ on rock strength was similarly observed in the triaxial test condition. The lowest peak stress occurred at the $\beta$ between 30-60 degrees and the highest peak stress at the $\beta$ of either 0 or 90 degrees.
4) No relationship was observed between $E$ and the ratio of confining pressure to $n$ for $\beta$ of 0, 15, 30, 45, 60, 75, and 90 degrees. $E$ decreased with the increase in $n$ for the triaxial condition.
5) Regarding shear strength parameters, the cohesion decreased with the increase in $n$. No relationship was observed between the internal friction angle and $n$ for shale data from literature. However, an increasing trend between internal friction angle and $n$ was observed in Cody shale.

*Claystone*

1) For Wyoming claystone, UCS decreased with the increase in $w$. UCS decreased exponentially with the $n$. No apparent relationship was observed between UCS and $\rho$ as well as the axial strain at peak stress.
2) A linear relationship was observed between $E$ and UCS. $E$ decreased exponentially with the increase in $w$ and $n$. No relationship was observed between $E$ and the $\rho$ as well as the axial strain at peak stress.

*Siltstone*

1) UCS decreased with the increase in $w$. The power relationships between UCS and $w$ for both all siltstone data and Wyoming data were determined. The relationship between UCS and $w$ was improved when siltstones from individual geological ages were used in the analysis. The negative relationships between UCS and $n$ for both all siltstone data and Wyoming siltstone data were determined. The relationship between UCS and $n$ was improved when siltstones were analyzed from individual geological ages. A positive power relationship between UCS and $\rho$ was determined. No relationship was observed between UCS and axial strain at peak stress.
2) $E$ decreased with the increase in $w$, and a negative relationship between E and $n$ was determined. The linear relationship between $E$ and UCS was determined. The positive relationship between $E$ and $\rho$ could be described by an exponential model. No relationship was observed between $E$ and axial strain at peak stress.
3) The peak stress under triaxial compression condition had a positive relationship with the normalized confining pressure with $n$.
4) Cohesion ($c$) decreased with the increase in $n$. The ratio of $c$ to $n$ also decreased with $w$. Internal friction angle showed no relationship with $n$.
5) No relationship was observed between $E$ and $n$ as well as confining pressure.

*Carbonate rocks*

1) The UCS of carbonate rocks was negatively related to $n$.
2) A significant effect of $n$ and confining pressure on the triaxial compressive strength was observed.
3) A negative relationship between $E$ and $n$ was observed.

## 10.3 Future Studies

This study focused on the strength properties of rocks at their in-situ water conditions. The rock samples obtained were either surface boulders or rock cores from shallow depths (around 30 m). The effect of water saturation had not been considered in this study. Sedimentary rocks like shale and claystone were known to exhibit lower strength properties at higher water saturation, and hence, studying the behaviors of these bedrocks at different saturations can be a point of interest.

The mineral composition of rocks affected their shear and compressive strengths. The percentage of clay content and clay fraction in the overall composition of shale and claystone have been found to significantly alter the strength and deformation behaviors of these rocks. The mineral composition of rocks can be quantified in a future study to understand the anisotropic effect on the rock strength. No apparent bedding was noticed on Wyoming rocks, but it has been found that the rock strength was highly influenced by the degree of bedding. A future study on Wyoming shales, sandstones, and claystone with different bedding planes should be considered.

There is a lack of research regarding the mechanical properties of claystone and siltstone in terms of their physical properties. The shear and compressive strengths of claystone and siltstone from Wyoming were very low compared to the strengths of rocks reported in literature. Additional research on different claystone and siltstone formations will help to populate more test data and help better understand their mechanical behaviors.

## REFERENCES


Abbas, A. K., Flori, R. E., and Alsaba, M. (2018) "Estimating rock mechanical properties of the Zubair shale formation using a sonic wireline log and core analysis." *Journal of Natural Gas Science and Engineering* 53: 359-369.

Adhikari, P., Ng, K. W., Gebreslasie, Y.Z., Wulff, S. S., and Sullivan, T. A. (2020) "Geomaterial classification criteria for design and construction of driven steel H-piles." *Canadian Geotechnical Journal* 57, no. 4: 616-621.

Akaike, H. (1974) "A new look at the statistical model identification. IEEE Transactionson Automatic Control, 19 (6), 716–723." Math. Rev. 423716.

Al-Maamori, H. M. S., El Naggar, M. H., Micic, S., and Lo, K. Y. (2016) "Influence of lubricant fluids on swelling behaviour of Queenston shale in southern Ontario." *Canadian Geotechnical Journal* 53, no. 7: 1059-1080.

Alqahtani, A. A., Mokhtari, M., Tutuncu, A. N., and Sonnenberg, S. (2013) "Effect of mineralogy and petrophysical characteristics on acoustic and mechanical properties of organic rich shale." *In SPE/AAPG/SEG Unconventional Resources Technology Conference*.

Amann, F., Wild, K. M., Loew, S., Yong, S., Thoeny, R., and Frank, E. (2018) "Geomechanical behaviour of Opalinus Clay at multiple scales: results from Mont Terri rock laboratory (Switzerland)." Mont Terri Rock Laboratory, 20 Years: Two Decades of Research and Experimentation on Claystones for Geological Disposal of Radioactive Waste: 153-173.

Ambrose, J., Zimmerman, R. W., and Suarez-Rivera, R. (2014) "Failure of shales under triaxial compressive stress." *In 48th US Rock Mechanics/Geomechanics Symposium*.

Ambrose, J. (2014) "Failure of anisotropic shales under triaxial stress conditions."

Ameen, M. S., Smart, B. G. D., Somerville, J. Mc., Hammilton, S., and Naji, N. A. (2009) "Predicting rock mechanical properties of carbonates from wireline logs (A case study: Arab-D reservoir, Ghawar field, Saudi Arabia)." *Marine and Petroleum Geology* 26, no. 4: 430-444.

American Association of State Highway and Transportation Officials. (2017). AASHTO LRFD Bridge Design Specifications, 8th Edition, U.S. Customary Units, Washington, D.C.

Anikoh, G. A., and Olaleye, B. M. (2013) "Estimation of strength properties of shale from some of its physical properties using developed mathematical models." *The International Journal of Engineering and Science* 2, no. 4: 1-5.

Asef, M. R., and Farrokhrouz. M. (2010) "Governing parameters for approximation of carbonates UCS." *Electron J Geotech Eng* 15, no. 2010: 1581-1592.

ASTM D4543-08. (2008) "Standard practices for preparing rock core as cylindrical test specimens and verifying conformance to dimensional and shape tolerances." Annual Book of ASTM Standards.

ASTM D7012-14e1. (2014) "Standard Test Methods for Compressive Strength and Elastic Moduli of Intact Rock Core Specimens under Varying States of Stress and Temperatures". West Conshohocken, PA.

Atapour, H., and Mortazavi, A. (2018) "The effect of grain size and cement content on index properties of weakly solidified artificial sandstones." *Journal of Geophysics and Engineering* 15, no. 2: 613-619.

Bandyopadhyay, A., and Abdullah, H. (2013) "A laboratory study of strong and weak sandstones." *In Oral presentation given at the Seventh International Conference on Case Histories in Geotechnical Engineering*, Chicago, vol. 29.

Barton, N. (1973) "Review of a new shear-strength criterion for rock joints." *Engineering geology* 7, no. 4: 287-332.

Barton, N., and Choubey, V. (1977) "The shear strength of rock joints in theory and practice." *Rock mechanics* 10: 1-54.

Baud, P., Vinciguerra, S., David, C., Cavallo, A., Walker, E., and Reuschlé, T. (2009) "Compaction and failure in high porosity carbonates: Mechanical data and microstructural observations." *Pure and Applied Geophysics* 166: 869-898.

Baud, P., Schubnel, A., and Wong, T. (2000) "Dilatancy, compaction, and failure mode in Solnhofen limestone." *Journal of Geophysical Research: Solid Earth* 105, no. B8: 19289-19303.

Baud, P., Reuschlé, T., Ji, Y., Cheung, C. S. N., and Wong, T. (2015) "Mechanical compaction and strain localization in Bleurswiller sandstone." *Journal of Geophysical Research: Solid Earth* 120, no. 9: 6501-6522.

Beiki, M., Majdi, A., and Givshad, A. D. (2013) "Application of genetic programming to predict the uniaxial compressive strength and elastic modulus of carbonate rocks." *International Journal of Rock Mechanics and Mining Sciences* 63: 159-169.

Belmokhtar, M., Delage, P., Ghabezloo, S., Tang, A., Menaceur, H., and Conil, N. (2017) "Poroelasticity of the Callovo–Oxfordian claystone." *Rock Mechanics and Rock Engineering* 50: 871-889.

Bésuelle, P. (2001) "Evolution of strain localisation with stress in a sandstone: brittle and semi-brittle regimes." *Physics and Chemistry of the Earth, Part A: Solid Earth and Geodesy* 26, no. 1-2: 101-106.

Bian, K., Liu, J., Zhang, W., Zheng, X., Ni, S., and Liu, Z. (2019) "Mechanical behavior and damage constitutive model of rock subjected to water-weakening effect and uniaxial loading." *Rock Mechanics and Rock Engineering* 52: 97-106.

Bieniawski, Z. T. (1989) “Engineering rock mass classifications: a complete manual for engineers and geologists in mining, civil, and petroleum engineering.” John Wiley & Sons.

Blanton, T. L. (1981) "Deformation of chalk under confining pressure and pore pressure." *Society of Petroleum Engineers Journal* 21, no. 01: 43-50.

Brantut, N., Schubnel, A., and Guéguen, Y. (2011) "Damage and rupture dynamics at the brittle-ductile transition: The case of gypsum." *Journal of Geophysical Research: Solid Earth* 116, no. B1.

Broch, E., and Franklin, J. A. (1972) "The point-load strength test." *In International Journal of Rock Mechanics and Mining Sciences & Geomechanics Abstracts*, vol. 9, no. 6, pp. 669-676. Pergamon.

Brown, E. T., and Hoek, E. (1968) “Underground excavations in rock.” CRC Press, 1980.

Byerlee, James D. "Brittle-ductile transition in rocks." *Journal of Geophysical Research* 73, no. 14: 4741-4750.

Cai, X., Zhou, Z., Zang, H., and Song, Z. (2020) "Water saturation effects on dynamic behavior and microstructure damage of sandstone: phenomena and mechanisms." *Engineering Geology* 276: 105760.

Carter, J. P., and Kulhawy, F. H. (1988) “Analysis and design of drilled shaft foundations socketed into rock.” No. EPRI-EL-5918. *Electric Power Research Inst*., Palo Alto, CA (USA); Cornell Univ., Ithaca, NY (USA). Geotechnial Engineering Group.

Castagna, A., Ougier-Simonin, A., Benson, P. M., Browning, J., Walker, R. J., Fazio, M., and Vinciguerra, S. (2018) "Thermal damage and pore pressure effects of the Brittle-Ductile transition in comiso limestone." *Journal of Geophysical Research: Solid Earth* 123, no. 9: 7644-7660.

Ceryan, N., Okkan, U., and Kesimal, A. (2013) "Prediction of unconfined compressive strength of carbonate rocks using artificial neural networks." *Environmental earth sciences* 68: 807-819.

Chang, C., Zoback, M. D., and Khaksar, A. (2006) "Empirical relations between rock strength and physical properties in sedimentary rocks." *Journal of Petroleum Science and Engineering* 51, no. 3-4: 223-237.

Chang, Y., Raghunathan, V. K., Garland, S. P., Morgan, J. T., Russell, P., and Murphy, C. J. (2014) "Automated AFM force curve analysis for determining elastic modulus of

biomaterials and biological samples." *Journal of the mechanical behavior of biomedical materials* 37: 209-218.

Chatterjee, R., and Mukhopadhyay, M. (2002) "Petrophysical and geomechanical properties of rocks from the oilfields of the Krishna-Godavari and Cauvery Basins, India." *Bulletin of Engineering Geology and the Environment* 61: 169-178.

Chen, P., Tang, S., Liang, X., Zhang, Y., and Tang, C. (2021) "The influence of immersed water level on the short-and long-term mechanical behavior of sandstone." *International Journal of Rock Mechanics and Mining Sciences* 138: 104631.

Cheng, J., Wan, Z., Zhang, Y., Li, W., Peng, S. S., and Zhang, P. (2015) "Experimental study on anisotropic strength and deformation behavior of a coal measure shale under room dried and water saturated conditions." *Shock and Vibration* 2015.

Cheng, P., Tian, H., Xiao, X., Gai, H., Li, T., and Wang, X. (2017) "Water distribution in overmature organic-rich shales: implications from water adsorption experiments." *Energy & Fuels* 31, no. 12: 13120-13132.

Chitty, D. E., Blouin, S. E., Sun, X., and Kim, K. (1994) "Laboratory investigation and analysis of the strength and deformation of joints and fluid flow in Salem limestone."

Cho, J., Kim, H., Jeon, S., and Min, K. (2012) "Deformation and strength anisotropy of Asan gneiss, Boryeong shale, and Yeoncheon schist." *International journal of rock mechanics and mining sciences* 50: 158-169.

Chuanliang, Y., Jingen, D., Lianbo, H., Zijian, C., Xinjiang, Y., Hai, L., Qiang, T., and Baohua, Y. (2015) "Brittle failure of shale under uniaxial compression." *Arabian Journal of Geosciences* 8: 2467-2475.

Davarpanah, S. M., Bar, N., Török, Á., Tarifard, A., and Vásárhelyi, B. (2020) "Determination of Young's Modulus and Poisson's Ratio for Intact Stratified Rocks and their Relationship with Uniaxial Compressive Strength." *Australian Geomechanics Journal* 55, no. 4: 101-118.

Descamps, F., and Tshibangu, J. P. (2007) "Modelling the limiting envelopes of rocks in the octahedral plane." *Oil & Gas Science and Technology-Revue de l'IFP* 62, no. 5: 683-694.

Descamps, F., Tshibangu, J. P., Ramos da Silva, M., Schroeder, C., and Verbrugge, J. (2011) "Behaviour of carbonated rocks under true triaxial compression." *In 12th ISRM Congress*.

Dewhurst, D. N., Siggins, A. F., Kuila, U., Clennell, M. B., Raven, M. D., and Nordgard-Bolas, H. M. (2008) "Elastic, geomechanical and petrophysical properties of shales." *In The 42nd US Rock Mechanics Symposium (USRMS).*

Dewhurst, D. N., Henning, A. L., and Kovack, G. E. (2003) "Mechanics of Top Seal Leakage in the Carnarvon Basin, Australian Northwest Shelf." In First EAGE International Conference on Fault and Top Seals-What do we know and where do we go?, pp. cp-97. *European Association of Geoscientists & Engineers*.

Edmond, J. M., and Paterson, M. S. (1972) "Volume changes during the deformation of rocks at high pressures." *In International Journal of Rock Mechanics and Mining Sciences & Geomechanics Abstracts*, vol. 9, no. 2, pp. 161-182. Pergamon.

Egert, R., Seithel, R., Kohl, T., and Stober, I. (2018) "Triaxial testing and hydraulic–mechanical modeling of sandstone reservoir rock in the Upper Rhine Graben." *Geothermal Energy* 6, no. 1: 1-22.

Eremin, M. (2020) "Influence of the porosity on the uniaxial compressive strength of sandstone samples." *Procedia Structural Integrity* 25: 465-469.

Erguler, Z. A., and Ulusay, R. (2009) "Water-induced variations in mechanical properties of clay-bearing rocks." *International Journal of Rock Mechanics and Mining Sciences* 46, no. 2: 355-370.

Fabre, D., and Gustkiewicz, J. (1997) "Poroelastic properties of limestones and sandstones under hydrostatic conditions." *International Journal of Rock Mechanics and Mining Sciences* 34, no. 1: 127-134.

Fang, S., Xiong, H., Wang, B., Ma, L., Rao, X., and Wu, Y. (2021) "The influence of infill well-caused fracture interference on shale gas production and recovery: A comprehensive numerical simulation study." In Asia Pacific Unconventional Resources Technology Conference, Virtual, 16–18 November 2021, pp. 1680-1693. *Unconventional Resources Technology Conference* (URTeC).

Farquhar, R. A., Somerville, J. M., and Smart, B. G. D. (1994) "Porosity as a geomechanical indicator: an application of core and log data and rock mechanics." *In European Petroleum Conference*.

Fattahpour, V., Baudet, B. A., Moosavi, M., Mehranpour, M., and Ashkezari, A. (2014) "Effect of grain characteristics and cement content on the unconfined compressive strength of artificial sandstones." *International Journal of Rock Mechanics and Mining Sciences* 72: 109-116.

Fjær, E., and Nes, O. (2014) "The impact of heterogeneity on the anisotropic strength of an outcrop shale." *Rock Mechanics and Rock Engineering* 47: 1603-1611.

Forbes, E. (2011) "Shear, selective and temperature responsive flocculation: A comparison of fine particle flotation techniques." *International Journal of Mineral Processing* 99, no. 1-4: 1-10.

Franklin, J. A. (1981) "A shale rating system and tentative applications to shale performance." *Transportation Research Record* 790, no. 3: 2-12.

Fredrich, J. T., Evans, B., and Wong, T. (1989) "Micromechanics of the brittle to plastic transition in Carrara marble." *Journal of Geophysical Research: Solid Earth* 94, no. B4: 4129-4145.

Geng, J., and Cao, L. (2020) "Failure analysis of water-bearing sandstone using acoustic emission and energy dissipation." *Engineering Fracture Mechanics* 231: 107021.

Gerogiannopoulos, N. (1976) "A Critical State Approach to Rock Mechanics."

Ghafoori, M., Carter, J. P., and Airey, D. W. (1993) "Anisotropic behavior of Ashfield shale in the direct shear test." *In Proc Int Symp on Geotechnical Engineering of Hard Soils–Soft Rocks*. AA Balkema, Rotterdam, pp. 509-515.

Ghafoori, M. (1995) "Engineering behaviour of Ashfield shale."

Gong, F., Si, X., Li, X., and Wang, S. (2019) "Dynamic triaxial compression tests on sandstone at high strain rates and low confining pressures with split Hopkinson pressure bar." *International Journal of Rock Mechanics and Mining Sciences* 113: 211-219.

Goodman, R. E. (1989). “Introduction.” In Rock Mechanics, Second Edition, John Wiley and Sons, Inc., New York, NY, p. 562.

Goodman, R. E. (1980) “Introduction to Rock Mechanics”, John Wiley & Sons, New York, 478p.

Griffith, A. (1924) "The theory of rupture." *In First Int. Cong. Appl. Mech*, pp. 55-63.

Han, S., Cheng, Y., Gao, Q., Yan, C., and Han, Z. (2018) "Experimental study of the effect of liquid nitrogen pretreatment on shale fracability." *Journal of Natural Gas Science and Engineering* 60: 11-23.

Handin, J., and Hager Jr, R. V. (1958) "Experimental deformation of sedimentary rocks under confining pressure: tests at high temperature." *AAPG Bulletin* 42, no. 12: 2892-2934.

Handin, J., and Hager, R. V. (1957) "Experimental deformation of sedimentary rocks under confining pressure: Tests at room temperature on dry samples." *AAPG Bulletin* 41, no. 1: 1-50.

Handin, J., HC and Heard, and Magouirk, J. N. (1967) "Effects of the intermediate principal stress on the failure of limestone, dolomite, and glass at different temperatures and strain rates." *Journal of geophysical research* 72, no. 2: 611-640.

Hawkins, A. B., and McConnell, B. J. (1992) "Sensitivity of sandstone strength and deformability to changes in moisture content." *Quarterly Journal of Engineering Geology* 25, no. 2: 115-130.

Heap, M. J. (2019) "The influence of sample geometry on the permeability of a porous sandstone." *Geoscientific Instrumentation, Methods and Data Systems* 8, no. 1: 55-61.

Heard, H. C. (1960) "Transition from brittle fracture to ductile flow in Solenhofen limestone as a function of temperature, confining pressure, and interstitial fluid pressure."

Hebib, R., Belhai, D., and Alloul, B. (2017) "Estimation of uniaxial compressive strength of North Algeria sedimentary rocks using density, porosity, and Schmidt hardness." *Arabian Journal of Geosciences* 10: 1-13.

Herrmann, J., Rybacki, E., Sone, H., and Dresen, G. (2018) "Deformation experiments on Bowland and Posidonia Shale—part I: strength and Young's modulus at ambient and in situ pc–T conditions." *Rock Mechanics and Rock Engineering* 51: 3645-3666.

Higgins, S., Goodwin, S., Donald, A., Bratton, T., and Tracy, G. (2008) "Anisotropic stress models improve completion design in the Baxter Shale." *In SPE Annual Technical Conference and Exhibition*.

Hoek, E., and Brown, E. T. (1997) "Practical estimates of rock mass strength." *In Int. J. Mech. Min. Sci. Geomech. Abstr*, vol. 34, no. 8.

Hoek, E., and Martin, C. D. (2014) "Fracture initiation and propagation in intact rock–a review." *Journal of Rock Mechanics and Geotechnical Engineering* 6, no. 4: 287-300.

Hoek, E., and Brown, E. T. (2019) "The Hoek–Brown failure criterion and GSI–2018 edition." *Journal of Rock Mechanics and Geotechnical Engineering* 11, no. 3: 445-463.

Hoek, E., and Marinos, P. (2000) "Predicting tunnel squeezing problems in weak heterogeneous rock masses." *Tunnels and tunnelling international* 32, no. 11: 45-51.

Horsrud, P., Sønstebø, E. F., and Bøe, R. (1998) "Mechanical and petrophysical properties of North Sea shales." *International Journal of Rock Mechanics and Mining Sciences* 35, no. 8: 1009-1020.

Horsrud, P. (2001) "Estimating mechanical properties of shale from empirical correlations." *SPE Drilling & Completion* 16, no. 02: 68-73.

Hossain, M. S., and Lane, D. S. (2015) "Development of a catalog of resilient modulus values for aggregate base for use with the mechanistic-empirical pavement design guide (MEPDG). " No. FHWA/VCTIR 15-R13. Virginia Center for Transportation Innovation and Research.

Hsu, S., and Nelson, P. P. (1993) "Characterization of cretaceous clay-shales in North America." *Geot. Eng. of Hard Soils-Soft Rocks*. Anagnostopoulos et al (eds. Balkema. Pp 139-146.

Hu, D. W., Zhang, F., Shao, J., and Gatmiri, B. (2014) "Influences of mineralogy and water content on the mechanical properties of argillite." *Rock mechanics and rock engineering* 47: 157-166.

Hu, D. W., Zhang, F., and Shao, J. F. (2014) "Experimental study of poromechanical behavior of saturated claystone under triaxial compression." *Acta Geotechnica* 9: 207-214.

Hua, W., Li, J., Dong, S., and Pan, X. (2019) "Experimental study on mixed mode fracture behavior of sandstone under water–rock interactions." *Processes* 7, no. 2 (2019): 70.

Huang, S., He, Y., Liu, G., Lu, Z., and Xin, Z. (2021) "Effect of water content on the mechanical properties and deformation characteristics of the clay-bearing red sandstone." *Bulletin of Engineering Geology and the Environment* 80: 1767-1790.

Huang, Z., Gu, Q., Wu, Y., Wu, Y., Li, S., Zhao, K., and Zhang, R. (2021) "Effects of confining pressure on acoustic emission and failure characteristics of sandstone." *International Journal of Mining Science and Technology* 31, no. 5: 963-974.

Ibanez, W. D., and Kronenberg, A. K. (1993) "Experimental deformation of shale: Mechanical properties and microstructural indicators of mechanisms." *In International journal of rock mechanics and mining sciences & geomechanics abstracts*, vol. 30, no. 7, pp. 723-734. Pergamon.

Inoue, M., and Ohomi, M. (1981) "Relation between uniaxial compressive strength and elastic wave velocity of soft rock." *In ISRM International Symposium.*

Islam, M. A., and Skalle, P. (2013) "An experimental investigation of shale mechanical properties through drained and undrained test mechanisms." *Rock Mechanics and Rock Engineering* 46: 1391-1413.

Islam, M. A., Yunsi, M., Qadri, SM. T., Shalaby, M. R., and Haque, AKM. E. (2021) "Three-dimensional structural and petrophysical modeling for reservoir characterization of the Mangahewa formation, Pohokura Gas-Condensate Field, Taranaki Basin, New Zealand." *Natural Resources Research* 30: 371-394.

Jaeger, J. C. (1979) "Cook., NGW Fundamentals of Rock Mechanics." Loydon, methuen.

Jaeger, J. C., and Cook, N. G. W. (1976) "Fundamentals of Rock Mechanics 2nd ed., 585." Halsted, London.

Jaeger, J. C., Cook, N. G. W., and Zimmerman, R. W. (2007) "Fundamentals of rock mechanics, 4th edn Blackwell." Maiden, MA.

Jamshidi, A., Zamanian, H., and Sahamieh, R. Z. (2018) "The effect of density and porosity on the correlation between uniaxial compressive strength and P-wave velocity." *Rock mechanics and Rock engineering* 51: 1279-1286.

Jin, X., Shah, S. N., Roegiers, J., and Zhang, B. (2015) "An integrated petrophysics and geomechanics approach for fracability evaluation in shale reservoirs." *SPE Journal* 20, no. 03: 518-526.

Jin, Z., Nie, H., Liu, Q., Zhao, J., and Jiang, T. (2018) "Source and seal coupling mechanism for shale gas enrichment in upper Ordovician Wufeng Formation-Lower Silurian Longmaxi Formation in Sichuan Basin and its periphery." *Marine and Petroleum Geology* 97: 78-93.

Johnston, D. H. (1987) "Physical properties of shale at temperature and pressure." *Geophysics* 52, no. 10: 1391-1401.

Jung, D. H., Kang, C., Nam, J. E., Jeong, H., and Lee, J. S. (2016) "Surface diffusion directed growth of anisotropic graphene domains on different copper lattices." *Scientific reports* 6, no. 1: 1-7.

Kahraman, S. A. İ. R., Gunaydin, O., and Fener, M. (2005) "The effect of porosity on the relation between uniaxial compressive strength and point load index." *International Journal of Rock Mechanics and Mining Sciences* 42, no. 4: 584-589.

Kawakita, M., and Kinoshita, S. (1981) "The dynamic fracture properties of rocks under confining pressure." *Memoirs of the Faculty of Engineering, Hokkaido University* 15, no. 4: 467-478.

Kegang, L., Lin, M., Xiangxing, L., and Shoujian, P. (2016) "Effect of Drying-Wetting Cycles on Triaxial Compression Mechanical Properties of Sandstone." *Journal of Engineering Science & Technology Review* 9, no. 3.

Kim, E., Stine, M. A., Davi Bastos Martins de Oliveira, and Hossein, C. (2017) "Correlations between the physical and mechanical properties of sandstones with changes of water content and loading rates." *International Journal of Rock Mechanics and Mining Sciences* 100: 255-262.

Koncagül, E. C., and Santi, P. M. (1999) "Predicting the unconfined compressive strength of the Breathitt shale using slake durability, Shore hardness and rock structural properties." *International Journal of Rock Mechanics and Mining Sciences* 36, no. 2: 139-153.

Kumar, S., and Pandey, S. K. (2010) "Trace fossils from the Nagaur Sandstone, Marwar Supergroup, Dulmera area, Bikaner district, Rajasthan, India." *Journal of Asian Earth Sciences* 38, no. 3-4: 77-85.

Kumar, V., Sondergeld, C. H., and Rai, C. S. (2012) "Nano to macro mechanical characterization of shale." *In SPE annual technical conference and exhibition*.

Kurtulus, C. E. N. G., Cakir, S., and Yoğurtcuoğlu, A. (2016) "Ultrasound Study of Limestone Rock Physical and Mechanical Properties." *Soil Mechanics & Foundation Engineering* 52, no. 6.

Lama, R. D., and Vutukuri, V. S. (1978) “Handbook on mechanical properties of rocks-testing techniques and results-volume iii”. Vol. 3, no. 2.

Lashkaripour, G. R., and Dusseault, M. B. (2020) "A statistical study on shale properties: Relationships among principal shale properties." *In Probabilistic Methods in Geotechnical Engineering*, pp. 195-200. CRC Press.

Lashkaripour, G. R., and Ajalloeian, R. (2000) "The effect of water content on the mechanical behaviour of fine-grained sedimentary rocks." *In ISRM International Symposium.*

Li, B., Liu, J., Bian, K., Ai, F., Hu, X., Chen, M., and Liu, Z. (2019) "Experimental study on the mechanical properties weakening mechanism of siltstone with different water content." *Arabian Journal of Geosciences* 12: 1-14.

Li, D., Sun, Z., Zhu, Q., and Peng, K. (2019) "Triaxial loading and unloading tests on dry and saturated sandstone specimens." *Applied Sciences* 9, no. 8: 1689.

Li, H., Li, H., Wang, K., and Liu, C. (2018) "Effect of rock composition microstructure and pore characteristics on its rock mechanics properties." *International Journal of mining science and technology* 28, no. 2: 303-308.

Li, H., Sun, R., Lee, W., Dong, K., and Guo, R. (2016) "Assessing risk in chinese shale gas investments abroad: Modelling and policy recommendations." *Sustainability* 8, no. 8: 708.

Li, Y., Zhang, K., and Wu, X. (2018) "Study of ultrasonic wave characteristics of shale in triaxial compression tests." *Journal of Geophysics and Engineering* 15, no. 5: 2183-2193.

Lin, Q., Cao, P., Mao, S., Ou, C., and Cao, R. (2020) "Fatigue behaviour and constitutive model of yellow sandstone containing pre-existing surface crack under uniaxial cyclic loading." *Theoretical and Applied Fracture Mechanics* 109: 102776.

Lin, S., and Lai, B. (2013) "Experimental investigation of water saturation effects on Barnett Shale's geomechanical behaviors." *In SPE Annual Technical Conference and Exhibition*.

Liping, W., Ning, L., Jilin, Q., Yanzhe, T., and Shuanhai, X. (2019) "A study on the physical index change and triaxial compression test of intact hard rock subjected to freeze-thaw cycles." *Cold Regions Science and Technology* 160: 39-47.

Liu, D., Liu, C., Kang, Y., Guo, B., and Jiang, Y. (2018) "Mechanical behavior of Benxi Formation limestone under triaxial compression: a new post-peak constitutive model and experimental validation." *Bulletin of Engineering Geology and the Environment* 77: 1701-1715.

Liu, H., Zhu, C., Zheng, K., Ma, C., and Yi, M. (2021) "Crack initiation and damage evolution of micritized framework reef limestone in the South China Sea." *Rock Mechanics and Rock Engineering* 54: 5591-5601.

Lu, Y., Wang, L., Sun, X., and Wang, J. (2017) "Experimental study of the influence of water and temperature on the mechanical behavior of mudstone and sandstone." *Bulletin of Engineering Geology and the Environment* 76: 645-660.

Ludovico-Marques, M., Chastre, C., and Vasconcelos, G. (2012) "Modelling the compressive mechanical behaviour of granite and sandstone historical building stones." *Construction and Building Materials* 28, no. 1: 372-381.

Małkowski, P., Ostrowski, L., and Brodny, J. (2018) "Analysis of Young's modulus for Carboniferous sedimentary rocks and its relationship with uniaxial compressive strength using different methods of modulus determination." *Journal of Sustainable Mining* 17, no. 3: 145-157.

Marsden, J. R., Holt, R. M., Nakken, S. J., and Raaen, A. M. (1992) "Mechanical and petrophysical characterization of highly stressed mudstones." *In Rock Characterization: ISRM Symposium,* Eurock'92, Chester, UK, 14–17 September 1992, pp. 51-56. Thomas Telford Publishing.

Martin, C. D., and Chandler, N. A. (1994) "The progressive fracture of Lac du Bonnet granite." In *International journal of rock mechanics and mining sciences & geomechanics abstracts*, vol. 31, no. 6, pp. 643-659. Pergamon.

Martin, E. LO., Pittet, B., Gutiérrez-Marco, J., Vannier, J., El Hariri, K., Lerosey-Aubril, R., Moussa Masrour et al. (2016) "The lower Ordovician Fezouata Konservat-Lagerstätte from Morocco: age, environment and evolutionary perspectives." *Gondwana Research* 34: 274-283.

Masoumi, H., Horne, J., and Timms, W. (2017) "Establishing empirical relationships for the effects of water content on the mechanical behavior of Gosford sandstone." *Rock Mechanics and Rock Engineering* 50: 2235-2242.

Masri, M., Sibai, M., Shao, J., and Mainguy, M. (2014) "Experimental investigation of the effect of temperature on the mechanical behavior of Tournemire shale." *International Journal of Rock Mechanics and Mining Sciences* 70: 185-191.

Meng, Q., Wang, C., Liu, J., Zhang, M., Lu, M., and Wu, Y. (2020) "Physical and micro-structural characteristics of limestone after high temperature exposure." *Bulletin of Engineering Geology and the Environment* 79: 1259-1274.

Mese, A., and Tutuncu, A. (2001) "Mechanical, acoustic, and failure properties of shales." In DC Rocks 2001, *The 38th US Symposium on Rock Mechanics (USRMS).*

Mogi, K. (1971) "Fracture and flow of rocks under high triaxial compression." *Journal of Geophysical Research* 76, no. 5: 1255-1269.

Mogi, K. (2006) "Experimental rock mechanics. " Vol. 3. CRC Press.

Moh'd, B. K. (2009) "Compressive strength of vuggy oolitic limestones as a function of their porosity and sound propagation." *Jordan J Earth Environ Sci* 2, no. 1: 18-25.

Mohamadi, M. (2015) "Experimental and Constitutive Investigation of the Thermo-Hydro-Mechanical Behavior of Shales: A Case Study of the Colorado Clay Shale." PhD diss., University of Calgary (Canada).

Mokwa, R. L., and Brooks, H. (2008) "Axial capacity of piles supported on intermediate geomaterials." No. FHWA/MT-08-008/8117-32. Montana. Dept. of Transportation. Research Programs.

Nasseri, M. H. B., Rao, K. S., and Ramamurthy, T. (2003) "Anisotropic strength and deformational behavior of Himalayan schists." *International Journal of Rock Mechanics and Mining Sciences* 40, no. 1: 3-23.

Naumann, M., Hunsche, U., and Schulze, O. (2007) "Experimental investigations on anisotropy in dilatancy, failure and creep of Opalinus Clay." *Physics and Chemistry of the Earth*, Parts A/B/C 32, no. 8-14: 889-895.

Ng, K. W., Garder, J., and Sritharan, S. (2015) "Investigation of ultra high performance concrete piles for integral abutment bridges." *Engineering Structures* 105: 220-230.

Ng, K. W., and Sullivan, T. (2017) "Case studies to demonstrate challenges of driven piles on rock." *Geotechnical Research* 4, no. 2: 82-93.

Ng, K. W., Adhikari, P., and Gebreslasie, Y. Z. (2019) "Development of load and resistance factor design procedures for driven piles on soft rocks in Wyoming." No. WY-1902F. *Wyoming. Dept. of Transportation*.

Niandou, H., Shao, J. F., Henry, J. P., and Fourmaintraux, D. (1997) "Laboratory investigation of the mechanical behaviour of Tournemire shale." *International Journal of Rock Mechanics and Mining Sciences* 34, no. 1: 3-16.

Nicolas, A., Fortin, J., Regnet, J. B., Verberne, B. A., Plümper, O., Dimanov, A., Spiers, C. J., and Guéguen, Y. (2017) "Brittle and semibrittle creep of Tavel limestone deformed at room temperature." *Journal of Geophysical Research: Solid Earth* 122, no. 6: 4436-4459.

Nicolas, A., Fortin, J., Regnet, J. B., Dimanov, A., and Guéguen, Y. (2016) "Brittle and semi-brittle behaviours of a carbonate rock: influence of water and temperature." *Geophysical Journal International* 206, no. 1: 438-456.

Noël, C., Baud, P., and Violay, M. (2021) "Effect of water on sandstone's fracture toughness and frictional parameters: Brittle strength constraints." *International Journal of Rock Mechanics and Mining Sciences* 147: 104916.

Nygård, R., Gutierrez, M., Gautam, R., and Høeg, K. (2004) "Compaction behavior of argillaceous sediments as function of diagenesis." *Marine and Petroleum Geology* 21, no. 3: 349-362.

Palchik, V. (2010) "Mechanical behavior of carbonate rocks at crack damage stress equal to uniaxial compressive strength." *Rock mechanics and rock engineering* 43: 497-503.

Palchik, V., and Hatzor, Y. H. (2000) "Correlation between mechanical strength and microstructural parameters of dolomites and limestones in the Judea group, Israel." *Israel Journal of Earth Sciences* 49, no. 2: 65-79.

Pappalardo, G. (2015) "Correlation between P-wave velocity and physical–mechanical properties of intensely jointed dolostones, Peloritani mounts, NE Sicily." *Rock mechanics and rock engineering* 48: 1711-1721.

Paterson, M. S. (1958) "Experimental deformation and faulting in Wombeyan marble." *Geological Society of America Bulletin* 69, no. 4: 465-476.

Plinninger, R. J. (2010) "Hardrock abrasivity investigation using the Rock Abrasivity Index (RAI)." Williams, et al., (Eds.), Geologically Active, Taylor & Francis, London: 3445-3452.

Prakoso, W. A., and Kulhawy, F. H. (2011) "Effects of testing conditions on intact rock strength and variability." *Geotechnical and Geological Engineering* 29: 101-111.

Qi, Y., Ju, Y., Yu, K., Meng, S., and Qiao, P. (2022) "The effect of grain size, porosity and mineralogy on the compressive strength of tight sandstones: A case study from the eastern Ordos Basin, China." *Journal of Petroleum Science and Engineering* 208: 109461.

R Core Team, and R Core Team. (2020) "European environment agency."

Renner, J., and Rummel, F. (1996) "The effect of experimental and microstructural parameters on the transition from brittle failure to cataclastic flow of carbonate rocks." *Tectonophysics* 258, no. 1-4: 151-169.

Rohde, J., and Feng, H. (1990) "Analysis of the variability of unconfined compression tests of rock." *Rock Mechanics and Rock Engineering* 23: 231-236.

Romana, M., and Vasarhelyi, B. (2007) "A discussion on the decrease of unconfined compressive strength between saturated and dry rock samples." *In 11th ISRM Congress*.

Roshan, H., Masoumi, H., and Regenauer-Lieb, K. (2017) "Frictional behaviour of sandstone: a sample-size dependent triaxial investigation." *Journal of Structural Geology* 94: 154-165.

Rzhevsky, V., and Novik, G. (1971) "The Physics of rocks. 320 str." *Mir Publischers. Moskva* .

Schwartz, A. E. (1964) "Failure of rock in the triaxial shear test." *In The 6th US Symposium on Rock Mechanics (USRMS)*.

Schwarz, G. (1978) "Estimating the dimension of a model." *The annals of statistics* : 461-464.

Shukla, P., Kumar, V., Curtis, Sondergeld, C. H., and Rai, C. S. (2013) "Nanoindentation studies on shales." *In 47th us rock mechanics/geomechanics symposium*.

Sirdesai, N. N., Gupta, T., Singh, T. N., and Ranjith, P. G. (2018) "Studying the acoustic emission response of an Indian monumental sandstone under varying temperatures and strains." *Construction and Building Materials* 168: 346-361.

Sone, H., and Zoback, M. D. (2013) "Mechanical properties of shale-gas reservoir rocks—Part 2: Ductile creep, brittle strength, and their relation to the elastic modulus." *Geophysics* 78, no. 5: D393-D402.

Sone, H., and Zoback, M. D. (2014) "Viscous relaxation model for predicting least principal stress magnitudes in sedimentary rocks." *Journal of Petroleum Science and Engineering* 124: 416-431.

Song, Y., Liu, Z., Meng, Q., Xu, J., Sun, P., Cheng, L., and Zheng, G. (2016) "Multiple controlling factors of the enrichment of organic matter in the upper cretaceous oil shale sequences of the songliao basin, NE China: implications from geochemical analysis." *Oil Shale* 33, no. 2.

Steiger, R. P., and Leung, P. K. (1992) "Quantitative determination of the mechanical properties of shales." *SPE drilling engineering* 7, no. 03: 181-185.

Al-Bazali, T. (2013) "The impact of water content and ionic diffusion on the uniaxial compressive strength of shale." *Egyptian Journal of Petroleum* 22, no. 2: 249-260.

Tandanand, S. (1985) "Moisture adsorption rate and strength degradation of Illinois shales." *In The 26th US Symposium on Rock Mechanics (USRMS).*

Tang, S. B., Yu, C. Y., Heap, M. J., Chen, P. Z., and Ren, Y. G. (2018) "The influence of water saturation on the short-and long-term mechanical behavior of red sandstone." *Rock Mechanics and Rock Engineering* 51: 2669-2687.

Tang, S. (2018) "The effects of water on the strength of black sandstone in a brittle regime." *Engineering Geology* 239: 167-178.

Thuro, K., Plinninger, R. J., Zäh, S., and Schütz, S. (2001) "Scale effects in rock strength properties. Part 1: Unconfined compressive test and Brazilian test." *In ISRM regional symposium,* EUROCK, pp. 169-174.

Tien, Y. M., Kuo, M. C., and Juang, C. H. (2006) "An experimental investigation of the failure mechanism of simulated transversely isotropic rocks." *International journal of rock mechanics and mining sciences* 43, no. 8: 1163-1181.

Underwood, B. J., and Ekstrand, B. R. (1967) "Effect of distributed practice on paired-associate learning." *Journal of Experimental Psychology* 73, no. 4p2: 1.

Vajdova, V., Baud, P., and Wong, T. (2004) "Compaction, dilatancy, and failure in porous carbonate rocks." *Journal of Geophysical Research: Solid Earth* 109, no. B5.

Vajdova, V., Baud, P., Wu, L., and Wong, T. (2012) "Micromechanics of inelastic compaction in two allochemical limestones." *Journal of Structural Geology* 43: 100-117.

Van E., Edward, M. (1976) "The mechanisms of strength reduction due to moisture in coal mine shales." *In International Journal of Rock Mechanics and Mining Sciences & Geomechanics Abstracts*, vol. 13, no. 2, pp. 61-67. Pergamon.

Vásárhelyi, B. (2005) "Technical note statistical analysis of the influence of water content on the strength of the Miocene limestone." *Rock Mech. Rock Eng* 38, no. 1: 69-76.

Verwaal, W., and Mulder, A. (1993) "Estimating rock strength with the Equotip hardness tester." *In International Journal of Rock Mechanics and Mining Sciences and Geomechanics Abstracts*, vol. 30, no. 6, pp. 659-662. Elsevier Science.

Walton, G., Hedayat, A., Kim, E., and Labrie, D. (2017) "Post-yield strength and dilatancy evolution across the brittle–ductile transition in Indiana limestone." *Rock Mechanics and Rock Engineering* 50: 1691-1710.

Wang, F., Cao, P., Wang, Y., Hao, R., Meng, J., and Shang, J. (2020) "Combined effects of cyclic load and temperature fluctuation on the mechanical behavior of porous sandstones." *Engineering Geology* 266: 105466.

Wang, M., Guo, Z., Jiao, C., Lu, S., Li, J., Xue, H., Li, J., Li, J., and Chen, G. (2019) "Exploration progress and geochemical features of lacustrine shale oils in China." *Journal of Petroleum Science and Engineering* 178: 975-986.

Wang, Q., Chen, J., Guo, J., Luo, Y., Wang, H., and Liu, Q. (2019) "Acoustic emission characteristics and energy mechanism in karst limestone failure under uniaxial and triaxial compression." *Bulletin of Engineering Geology and the Environment* 78: 1427-1442.

Wang, Y., and Cui, F. (2018) "Energy evolution mechanism in process of Sandstone failure and energy strength criterion." *Journal of Applied Geophysics* 154: 21-28.

Wasantha, P. L. P., Ranjith, P. G., Permata, G., and Bing, D. (2018) "Damage evolution and deformation behaviour of dry and saturated sandstones: insights gleaned from optical measurements." *Measurement* 130: 8-17.

Wasantha, P. LP, and Ranjith, P. G. (2014) "Water-weakening behavior of Hawkesbury sandstone in brittle regime." *Engineering Geology* 178: 91-101.

Willson, S. M., Edwards, S. T., Crook, A., Bere, A., Moos, D., Peska, P., and Last, N. (2007) "Assuring stability in extended-reach wells—analyses, practices, and mitigations." *In SPE/IADC Drilling Conference*.

Wong, R. C. K., Schmitt, D. R., Collis, D., and Gautam, R. (2008) "Inherent transversely isotropic elastic parameters of over-consolidated shale measured by ultrasonic waves and their comparison with static and acoustic in situ log measurements." *Journal of Geophysics and Engineering* 5, no. 1: 103-117.

Wu, B., and Tan, C. P. (2010) "Effect of shale bedding plane failure on wellbore stability-example from analyzing stuck-pipe wells." *In 44th US Rock Mechanics Symposium and 5th US-Canada Rock Mechanics Symposium*.

Wu, G., Wang, y., Swift, g., and Chen, J. (2013) "Laboratory investigation of the effects of temperature on the mechanical properties of sandstone." *Geotechnical and Geological Engineering* 31: 809-816.

Wu, J., Feng, M., Yu, B., Zhang, W., Ni, X., and Han, G. (2018) "Experimental investigation on dilatancy behavior of water-saturated sandstone." *International Journal of Mining Science and Technology* 28, no. 2: 323-329.

Xu, F., Yang, C., Guo, Y., Wang, T., Wang, L., and Zhang, P. (2017) "Effect of confining pressure on the mechanical properties of thermally treated sandstone." *Current science* 112, no. 6: 1101-1106.

Xu, H., Zhou, W., Xie, R., Da, L., Xiao, C., Shan, Y., and Zhang, H. (2016) "Characterization of rock mechanical properties using lab tests and numerical interpretation model of well logs." *Mathematical Problems in Engineering*.

Yagiz, S. (2009) "Assessment of brittleness using rock strength and density with punch penetration test." *Tunnelling and underground space technology* 24, no. 1: 66-74.

Yan, C., Deng, J., Cheng, Y., Li, M., Feng, Y., and Li, X. (2017) "Mechanical properties of gas shale during drilling operations." *Rock Mechanics and Rock Engineering* 50: 1753-1765.

Yang, D., Chanchole, S., Valli, P., and Chen, L. (2013) "Study of the anisotropic properties of argillite under moisture and mechanical loads." *Rock mechanics and rock engineering* 46: 247-257.

Yang, G., Bi, J., Li, X., Liu, J., and Feng, Y. (2020) "SHPB testing and analysis of bedded shale under active confining pressure." *Journal of Engineering* 2020: 1-8.

Yang, S-Q., and Jing, H-W. (2013) "Evaluation on strength and deformation behavior of red sandstone under simple and complex loading paths." *Engineering Geology* 164: 1-17.

Yang, S-Q., and Jing, H-W. (2011) "Strength failure and crack coalescence behavior of brittle sandstone samples containing a single fissure under uniaxial compression." *International Journal of Fracture* 168: 227-250.

Yang, S-Q., Huang, Y-W., and Tang, J-Z. (2020) "Mechanical, acoustic, and fracture behaviors of yellow sandstone specimens under triaxial monotonic and cyclic loading." *International Journal of Rock Mechanics and Mining Sciences* 130: 104268.

Yang, S-Q. (2016) "Experimental study on deformation, peak strength and crack damage behavior of hollow sandstone under conventional triaxial compression." *Engineering Geology* 213: 11-24.

Yaşar, E., Ranjith, P. G., and Perera, M. S. A. (2010) "Physico-mechanical behaviour of southeastern Melbourne sedimentary rocks." *International Journal of Rock Mechanics and Mining Sciences* 47, no. 3: 481-487.

Yilmaz, I. (2010) "Influence of water content on the strength and deformability of gypsum." *International Journal of Rock Mechanics and Mining Sciences* 47, no. 2: 342-347.

Yu, C., Tang, S., Duan, D., Zhang, Y., Liang, Z., Ma, K., and Ma, T. (2019) "The effect of water on the creep behavior of red sandstone." *Engineering Geology* 253: 64-74.

Zarif, I. H., and Tuğrul, A. (2003) "Aggregate properties of Devonian limestones for use in concrete in Istanbul, Turkey." *Bulletin of Engineering Geology and the Environment* 62: 379-388.

Zhang, C-L., Komischke, M., Kröhn, M., Rogalski, A., and Zehle, B. (2019) “Experimental study of the mechanical behaviour of the sandy facies of Opalinus Clay at Mont-Terri. LT-A programme within the Mont-Terri-Project. No. GRS—555”. *Gesellschaft für Anlagen-und Reaktorsicherheit* (GRS) gGmbH.

Zhang, F., Xie, S. Y., Hu, D. W., Shao, J-F., and Gatmiri, B. (2012) "Effect of water content and structural anisotropy on mechanical property of claystone." *Applied Clay Science* 69: 79-86.

Zhang, Q., Zhu, H., Zhang, L., and Ding, X. (2011) "Study of scale effect on intact rock strength using particle flow modeling." *International Journal of Rock Mechanics and Mining Sciences* 48, no. 8: 1320-1328.

Zhao, K., Yang, D., Zeng, P., Huang, Z., Wu, W., Li, B., and Teng, T. (2021) "Effect of water content on the failure pattern and acoustic emission characteristics of red sandstone." *International Journal of Rock Mechanics and Mining Sciences* 142: 104709.

Zhao, Y., Zhang, L., Wang, W., Wan, W., Li, S., Ma, W., and Wang, Y. (2017) "Creep behavior of intact and cracked limestone under multi-level loading and unloading cycles." *Rock Mechanics and Rock Engineering* 50: 1409-1424.

Zheng, S., Yao, Y., Elsworth, D., Liu, D., and Cai, Y. (2020) "Dynamic fluid interactions during CO2-ECBM and CO2 sequestration in coal seams. Part 2: CO2-H2O wettability." *Fuel* 279: 118560.

Zhou, H., Chen, J., Lu, J., Jiang, Y., and Meng, F. (2018) "A new rock brittleness evaluation index based on the internal friction angle and class I stress–strain curve." *Rock Mechanics and Rock Engineering* 51: 2309-2316.